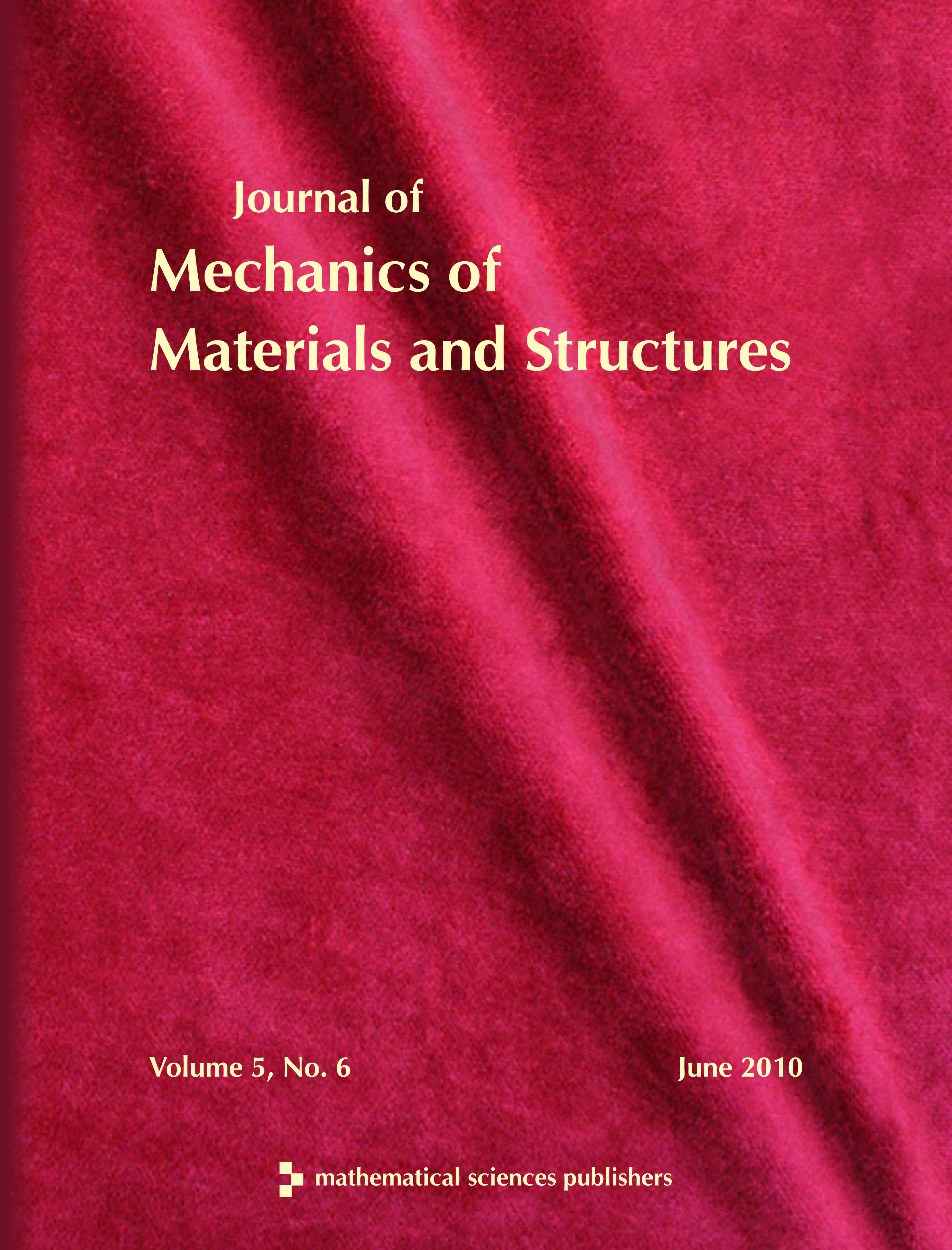

Journal of
Mechanics of Materials and Structures

Volume 5, No. 6 June 2010

mathematical sciences publishers

JOURNAL OF MECHANICS OF MATERIALS AND STRUCTURES

http://www.jomms.org

Founded by Charles R. Steele and Marie-Louise Steele

Cover design: Alex Scorpan Cover photo: Ev Shafrir

See inside back cover or http://www.jomms.org for submission guidelines.

JoMMS (ISSN 1559-3959) is published in 10 issues a year. The subscription price for 2010 is US $500/year for the electronic version, and $660/year (+ $60 shipping outside the US) for print and electronic. Subscriptions, requests for back issues, and changes of address should be sent to Mathematical Sciences Publishers, Department of Mathematics, University of California, Berkeley, CA 94720–3840.

JoMMS peer-review and production is managed by EditFLOW™ from Mathematical Sciences Publishers.

PUBLISHED BY
mathematical sciences publishers
http://www.mathscipub.org
A NON-PROFIT CORPORATION
Typeset in LaTeX

JOURNAL OF MECHANICS OF MATERIALS AND STRUCTURES
Vol. 5, No. 6, 2010

A SEMIANALYTICAL SOLUTION FOR THE BENDING OF CLAMPED LAMINATED DOUBLY CURVED OR SPHERICAL PANELS

KASRA BIGDELI AND MOHAMMAD MOHAMMADI AGHDAM

A semianalytical solution is presented for bending of moderately thick fully clamped laminated doubly curved panels using the extended Kantorovich method (EKM). The panel is subjected to uniform and nonuniform distributed loading and cut from a rectangular platform. Based on the first-order shear deformation theory, five highly coupled second-order partial differential equations in terms of displacement components are derived. Assuming separable functions for panel displacements together with the EKM converts the governing equations into double sets of ordinary differential equations with constant coefficients in terms of x and y. The resulting ODE systems are then solved iteratively until a level of prescribed convergence is achieved. Closed-form solutions can be presented for ODE systems in each iteration. Efficiency and rapid convergence of the solution technique are examined using several examples. Predictions of both deflection and stress resultants show very good agreement with other available results in the literature. It is also shown that the same formulation and solution method can be used to obtain results for spherical and cylindrical panels and rectangular plates.

1. Introduction

Since fabrication of composite materials such as graphite/epoxy, boron/epoxy, Kevlar/epoxy and graphite/PEEK started, high-tech industries have become interested in using them as structural materials. Thus laminated composites have replaced metallic alloys in many applications, offering, among their beneficial features, light weight, high stiffness and strength.

Panels can generally bear much higher loads than plates, due to the geometric coupling between the membrane and flexure forces in panels. This coupling is material-independent and only occurs in panels due to the curved geometry. Material asymmetry in composite structures, either panels or plates, may also cause another type of coupling between the membrane and flexure forces which can occur in composite plates as well as composite panels. Thus, advanced laminated composite panels are currently being used in aircraft, space vehicles, ships and other structures where excellent structural performance is needed. Particularly, spherical panels are used wherever a high external pressure is applied on the panel, such as pressure vessel caps and ceilings.

The efficient use of laminated panels relies on the accurate prediction of their behavior under various types of loading. This depends on the level of accuracy of the modeling theory which normally leads to a system of coupled PDEs and also solution technique. An efficient procedure to solve systems of PDEs, known as the extended Kantorovich method (EKM), was initially introduced in [Kerr 1968] to obtain highly accurate approximate closed-form solutions for torsion of isotropic beams with rectangular cross-section. In the EKM, the idea of the Kantorovich method [Kantorovich and Krylov 1958],

---

Keywords: bending analysis, doubly curved panel, laminated composite, extended Kantorovich method, EKM.

which transforms a partial differential equation into a couple of ordinary differential equations, is further developed into an iterative scheme to improve accuracy.

The EKM has been widely used to obtain highly accurate approximate solutions for several 2D elasticity problems of rectangular plates in such applications as the bending of thin plates [Kerr and Alexander 1968; Dalaei 1995], eigenvalue problems [Kerr 1969], free vibration [Aghdam et al. 2009; Dalaei and Kerr 1996], buckling [Yuan and Jin 1998], bending of thick plates [Aghdam et al. 1996; Yuan et al. 1998; Aghdam and Falahatgar 2003], bending of variable thickness plates [Fariborz and Pourbohloul 1989] and free-edge strength analysis [Kim et al. 2000]. Recently, the EKM has been used to solve problems in other geometries, such as annular sector plates [Aghdam and Mohammadi 2009] and cylindrical panels [Alijani and Aghdam 2009; Alijani et al. 2008; Abouhamze et al. 2007].

This study presents an EKM-based semianalytical solution for the bending of clamped laminated doubly curved panels. Based on first-order deformation theory (FSDT) and considering initial curvature effects [Toorani and Lakis 2000], governing equations in the form of five highly coupled second-order PDEs are derived. The EKM is employed to convert them to two sets of five ODEs with constant coefficients in terms of x and y. An exact closed-form solution is presented for each ODE system, ensuring the computational effort in applying this method is generally lower than for numeric methods. Rapid convergence and good accuracy of the solution is shown through examples and comparisons with other analytical and numerical methods. The effects of length-to-thickness ratio and radius-to-length ratio on stress resultant and displacement components are also investigated. We also show how the method can be used for the analysis of rectangular plates and cylindrical panels by assuming infinite values for one or both radii of curvatures.

2. Governing equations

A laminated doubly curved panel of rectangular platform with total thickness of h is considered. A curvilinear coordinate system (x, y, z) is used to describe the geometry of the panel, as shown in Figure 1. The radii of curvature of the panel are R_x and R_y, and the lengths of the panel are a and b, along the x and y directions, respectively.

According to the FSDT assumptions, the three-dimensional displacement field is

$$u_x(x, y, z) = u_0(x, y) + z\beta_1(x, y), \quad u_y(x, y, z) = v_0(x, y) + z\beta_2(x, y), \quad u_z(x, y, z) = w_0(x, y), \quad (1)$$

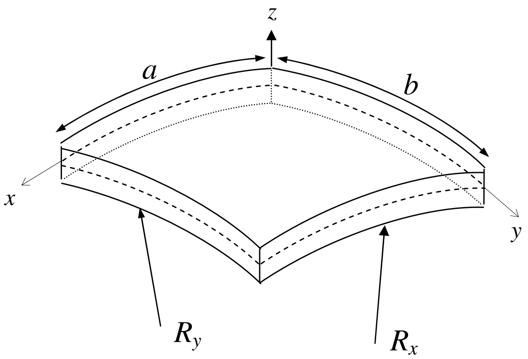

Figure 1. Doubly curved panel geometry.

where u_i $(i = x, y, z)$ are the displacement components of the panel along the analogous directions, u_0, v_0 and w_0 stand for the displacements of mid-surface, and β_1 and β_2 represent rotations about y and x, respectively. (For formulas (1)–(3) see [Reddy 2004].)

The strain-displacement relationships of the panel can be expressed as

$$\begin{gathered}\varepsilon_1 = \frac{1}{1+z/R_x}(\varepsilon_1^0 + z\varepsilon_1^1), \quad \varepsilon_2 = \frac{1}{1+z/R_y}(\varepsilon_2^0 + z\varepsilon_2^1), \quad \varepsilon_4 = \frac{1}{1+z/R_y}\varepsilon_4^0, \quad \varepsilon_5 = \frac{1}{1+z/R_x}\varepsilon_5^0, \\ \varepsilon_6 = \frac{1}{1+z/R_x}(\omega_1^0 + z\omega_1^1) + \frac{1}{1+z/R_y}(\omega_2^0 + z\omega_2^1),\end{gathered} \tag{2}$$

where ε_1 and ε_2 are the normal strains along the x and y axes, ε_6 is the shear strain in the xy-plane, ε_4 and ε_5 stand for the transverse shear strains in the yz- and xz-planes, respectively. Also, ε_i^0, ω_i^0, ε_i^1 $(i = 1, 2)$ and $\omega_i^1 (i = 1, 2)$ represent the in-plane normal strains, in-plane shear strains, changes in the curvature and the torsions of the mid-plane surface. ε_i^0 $(i = 4, 5)$ denote the transverse shear strains of the reference surface in y-z and x-z planes.

The relationship between the reference surface strains and the displacement components is

$$\begin{gathered}\varepsilon_1^0 = \frac{\partial u_0}{\partial x} + \frac{w_0}{R_x}, \quad \varepsilon_2^0 = \frac{\partial v_0}{\partial y} + \frac{w_0}{R_y}, \quad \varepsilon_4^0 = \frac{\partial w_0}{\partial y} - \frac{v_0}{R_y} + \beta_2, \quad \varepsilon_5^0 = \frac{\partial w_0}{\partial x} - \frac{u_0}{R_x} + \beta_1, \\ \varepsilon_1^1 = \frac{\partial \beta_1}{\partial x}, \quad \varepsilon_2^1 = \frac{\partial \beta_2}{\partial y}, \quad \omega_1^0 = \frac{\partial v_0}{\partial x}, \quad \omega_2^0 = \frac{\partial u_0}{\partial y}, \quad \omega_1^1 = \frac{\partial \beta_2}{\partial x}, \quad \omega_2^1 = \frac{\partial \beta_1}{\partial y}.\end{gathered} \tag{3}$$

For simplicity we rewrite this in matrix form:

$$\{\varepsilon\} = [d]\{u\}, \tag{4}$$

where $\{u\} = \langle u_0, v_0, w_0, \beta_1, \beta_2\rangle^T$ is the displacement vector, $\{\varepsilon\} = \langle \varepsilon_1^0, \omega_1^0, \varepsilon_5^0, \varepsilon_2^0, \omega_2^0, \varepsilon_4^0, \varepsilon_1^1, \omega_1^1, \varepsilon_2^1, \omega_2^1\rangle^T$ is the strain vector and the operator matrix $[d]_{10\times 5}$ is given by

$$[d] = \begin{bmatrix} \frac{\partial}{\partial x} & 0 & \frac{-1}{R_x} & 0 & \frac{\partial}{\partial y} & 0 & 0 & 0 & 0 & 0 \\ 0 & \frac{\partial}{\partial x} & 0 & \frac{\partial}{\partial y} & 0 & \frac{-1}{R_y} & 0 & 0 & 0 & 0 \\ \frac{1}{R_x} & 0 & \frac{\partial}{\partial x} & \frac{1}{R_y} & 0 & \frac{\partial}{\partial y} & 0 & 0 & 0 & 0 \\ 0 & 0 & 1 & 0 & 0 & 0 & \frac{\partial}{\partial x} & 0 & 0 & \frac{\partial}{\partial y} \\ 0 & 0 & 0 & 0 & 0 & 1 & 0 & \frac{\partial}{\partial x} & \frac{\partial}{\partial y} & 0 \end{bmatrix}^T. \tag{5}$$

The constitutive equations, that is, the relationship between strain components and stress resultants, including transverse shear deformations and initial curvature effects, can be written as

$$\{F\} = [P]\{\varepsilon\} \tag{6}$$

(see [Toorani and Lakis 2000]), where $\{F\} = \langle N_x, N_{xy}, Q_x, N_y, N_{yx}, Q_y, M_x, M_{xy}, M_y, M_{yx}\rangle^T$ is the stress resultant vector, and the stiffness matrix $[P]$ is defined as

$$[P] = \begin{bmatrix} G_{11} & G_{16} & 0 & A_{12} & A_{16} & 0 & H_{11} & H_{16} & B_{12} & B_{16} \\ G_{61} & G_{66} & 0 & A_{62} & A_{66} & 0 & H_{61} & H_{66} & B_{62} & B_{66} \\ 0 & 0 & K_s G_{55} & 0 & 0 & K_s A_{54} & 0 & 0 & 0 & 0 \\ A_{21} & A_{26} & 0 & G'_{22} & G'_{26} & 0 & B_{21} & B_{26} & H'_{22} & H'_{26} \\ A_{61} & A_{66} & 0 & G'_{62} & G'_{66} & 0 & B_{61} & B_{66} & H'_{62} & H'_{66} \\ 0 & 0 & K_s A_{45} & 0 & 0 & K_s G'_{44} & 0 & 0 & 0 & 0 \\ H_{11} & H_{16} & 0 & B_{12} & B_{16} & 0 & J_{11} & J_{16} & D_{12} & D_{16} \\ H_{61} & H_{66} & 0 & B_{62} & B_{66} & 0 & J_{61} & J_{66} & D_{62} & D_{66} \\ B_{21} & B_{26} & 0 & H'_{22} & H'_{26} & 0 & D_{21} & D_{26} & J'_{22} & J'_{26} \\ B_{61} & B_{66} & 0 & H'_{62} & H'_{66} & 0 & D_{61} & D_{66} & J'_{62} & J'_{66} \end{bmatrix} \tag{7}$$

(see [Reddy 2004]), where K_s is the shear correction factor and

$$\begin{gathered} G_{ij} = A_{ij} + a'_1 B_{ij} + a'_2 D_{ij} + a'_2 E_{ij}, \quad G'_{ij} = A_{ij} + b'_1 B_{ij} + b'_2 D_{ij} + b'_3 E_{ij}, \\ H_{ij} = B_{ij} + a'_1 D_{ij} + a'_2 E_{ij} + a'_3 F_{ij}, \quad H'_{ij} = B_{ij} + b'_1 D_{ij} + b'_2 E_{ij} + b'_3 F_{ij}, \\ J_{ij} = D_{ij} + a'_1 E_{ij} + a'_2 F_{ij} + a'_3 C_{ij}, \quad J'_{ij} = D_{ij} + b'_1 E_{ij} + b'_2 F_{ij} + b'_3 C_{ij}, \\ a'_1 = \frac{1}{R_y} - \frac{1}{R_x}, \quad a'_2 = \frac{1}{R_x}\Big(\frac{1}{R_x} - \frac{1}{R_y}\Big), \quad a'_3 = \frac{1}{R_x^2 R_y}, \\ b'_1 = \frac{1}{R_x} - \frac{1}{R_y}, \quad b'_2 = \frac{1}{R_y}\Big(\frac{1}{R_y} - \frac{1}{R_x}\Big), \quad b'_3 = \frac{1}{R_y^2 R_x}, \end{gathered} \tag{8}$$

with (for $i, j = 1, 2, 4, 5, 6$)

$$\begin{aligned} A_{ij} &= \sum_{k=1}^{N} (\bar{Q}_{ij})_k (h_k - h_{k-1}), & B_{ij} &= \frac{1}{2}\sum_{k=1}^{N} (\bar{Q}_{ij})_k (h_k^2 - h_{k-1}^2), \\ D_{ij} &= \frac{1}{3}\sum_{k=1}^{N} (\bar{Q}_{ij})_k (h_k^3 - h_{k-1}^3), & E_{ij} &= \frac{1}{4}\sum_{k=1}^{N} (\bar{Q}_{ij})_k (h_k^4 - h_{k-1}^4), \\ F_{ij} &= \frac{1}{5}\sum_{k=1}^{N} (\bar{Q}_{ij})_k (h_k^5 - h_{k-1}^5), & C_{ij} &= \frac{1}{6}\sum_{k=1}^{N} (\bar{Q}_{ij})_k (h_k^6 - h_{k-1}^6), \end{aligned} \tag{9}$$

the $\bar{Q}_{ij}$ being defined by

$$\begin{aligned} \bar{Q}_{11} &= Q_{11} m^4 + 2(Q_{12} + 2Q_{66}) + Q_{22} n^4, \\ \bar{Q}_{12} &= (Q_{11} + Q_{22} - 4Q_{66}) m^2 n^2 + Q_{12}(m^4 + n^4), \\ \bar{Q}_{22} &= Q_{11} n^4 + 2(Q_{12} + 2Q_{66}) m^2 n^2 + Q_{22} m^4, \end{aligned}$$

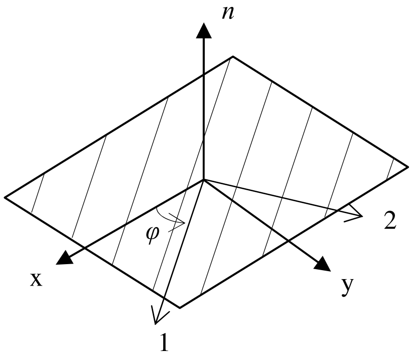

Figure 2. An orthotropic layer.

$$\begin{aligned}
\bar{Q}_{45} &= (Q_{55} - Q_{44})mn, \\
\bar{Q}_{16} &= (Q_{11} - Q_{12} - 2Q_{66})m^3n + (Q_{12} - Q_{22} + 2Q_{66})mn^3, \\
\bar{Q}_{26} &= (Q_{11} - Q_{12} - 2Q_{66})mn^3 + (Q_{12} - Q_{22} + 2Q_{66})m^3n, \\
\bar{Q}_{44} &= Q_{44}m^2 + Q_{55}n^2, \\
\bar{Q}_{55} &= Q_{44}n^2 + Q_{55}m^2, \\
\bar{Q}_{66} &= (Q_{11} + Q_{22} - 2Q_{12} - 2Q_{66})m^2n^2 + Q_{66}(m^4 + n^4),
\end{aligned} \tag{10}$$

for $m = \cos\varphi$, $n = \sin\varphi$, and

$$\begin{aligned}
Q_{11} &= E_{11}/(1 - \nu_{12}\nu_{21}), & Q_{44} &= G_{23}, \\
Q_{12} &= E_{11}\nu_{12}/(1 - \nu_{12}\nu_{21}), & Q_{55} &= G_{13}, \\
Q_{22} &= E_{22}/(1 - \nu_{12}\nu_{21}) & Q_{66} &= G_{12}.
\end{aligned} \tag{11}$$

Here $E_{\alpha\alpha}$, $G_{\alpha\beta}$ and $\nu_{\alpha\beta}$ ($\alpha, \beta = 1, 2$) represent the Young's moduli, rigidity moduli, and Poisson ratios, respectively, along the principal directions, and the orientation angle φ is measured counterclockwise from the x-axis to the 1-axis (fiber orientation) as shown in Figure 2.

The matrices $[B]$, $[E]$ and $[C]$ vanish in the case of symmetrically laminated composites. Note that, unlike the conventional constitutive equations in general use [Reddy 2004], here we consider also initial curvature effects. Therefore, the shear forces and torsional moments are not generally equal, i.e., $N_{xy} \neq N_{yx}$ and $M_{xy} \neq M_{yx}$.

To obtain equations of equilibrium, Hamilton's principle is applied to the FSDT displacement field [Toorani and Lakis 2000]. Neglecting time-dependent terms in the resulting equations, one obtains the static form of the equilibrium equations as

$$[E]\{F\} = \{q\}, \tag{12}$$

where the vector $\{q\} = \{0, 0, q(x, y), 0, 0\}^T$ is the external force vector and the matrix $[E]$, usually called the equilibrium operator, is defined as

$$[E]=\begin{bmatrix} \frac{\partial}{\partial x} & 0 & \frac{1}{R_x} & 0 & \frac{\partial}{\partial y} & 0 & 0 & 0 & 0 & 0 \\ 0 & \frac{\partial}{\partial x} & 0 & \frac{\partial}{\partial y} & 0 & \frac{1}{R_y} & 0 & 0 & 0 & 0 \\ \frac{-1}{R_x} & 0 & \frac{\partial}{\partial x} & \frac{-1}{R_y} & 0 & \frac{\partial}{\partial y} & 0 & 0 & 0 & 0 \\ 0 & 0 & -1 & 0 & 0 & 0 & \frac{\partial}{\partial x} & 0 & 0 & \frac{\partial}{\partial y} \\ 0 & 0 & 0 & 0 & 0 & -1 & 0 & \frac{\partial}{\partial x} & \frac{\partial}{\partial y} & 0 \end{bmatrix}. \tag{13}$$

Substitution of (4) into (6) in conjunction with (12) leads to five second-order PDEs in terms of five unknown displacement and rotation components. The final governing system of equations may be written in matrix form as

$$[S]\{u\}=\{q\}, \tag{14}$$

where the square matrix $[S]_{5\times5}=[E][P][d]$, called the fundamental matrix, comprises the geometric and material properties of the panel; its entries are defined in Appendix A. In the case of clamped structures, all displacements and rotations must vanish at the boundaries:

$$u_0(x,y)=v_0(x,y)=w_0(x,y)=\beta_1(x,y)=\beta_2(x,y)=0 \quad \text{at } x=0,\ a \ \text{ and at } y=0,b. \tag{15}$$

3. Application of the EKM

To apply the EKM to the governing equations (14), the first step is to assume all displacement components to be products of single-term separable functions. For economy we write this in matrix form as

$$\begin{Bmatrix} u_0(x,y) \\ v_0(x,y) \\ w_0(x,y) \\ \beta_1(x,y) \\ \beta_2(x,y) \end{Bmatrix} = \begin{Bmatrix} \xi_1(x)\times\psi_1(y) \\ \xi_2(x)\times\psi_2(y) \\ \xi_3(x)\times\psi_3(y) \\ \xi_4(x)\times\psi_4(y) \\ \xi_5(x)\times\psi_5(y) \end{Bmatrix} = [\psi]\times[\xi]\times\{1\}, \tag{16}$$

where the square matrices $[\xi]_{5\times5}$, $[\psi]_{5\times5}$ and $\{1\}_{5\times1}$ are defined by

$$[\psi]=\begin{bmatrix} \psi_1 & & & & \\ & \psi_2 & & 0 & \\ & & \psi_3 & & \\ & 0 & & \psi_4 & \\ & & & & \psi_5 \end{bmatrix}, \quad [\xi]=\begin{bmatrix} \xi_1 & & & & \\ & \xi_2 & & 0 & \\ & & \xi_3 & & \\ & 0 & & \xi_4 & \\ & & & & \xi_5 \end{bmatrix}, \quad \{1\}=\begin{bmatrix} 1 \\ 1 \\ 1 \\ 1 \\ 1 \end{bmatrix}. \tag{17}$$

Introducing (16) into (14) leads to the new form of the governing equations as

$$[S][\psi][\xi]\{1\}=-\{q\}. \tag{18}$$

It is essential to rewrite the clamped boundary condition in terms of $\psi_i(y)$ and $\xi_i(x)$. Substituting (16) into (15) results in the new form of the boundary conditions for clamped panels as

$$\xi_i(0) = \xi_i(a) = \psi_i(0) = \psi_i(b) = 0, \quad i = 1, \dots, 5. \tag{19}$$

Following the main idea of the weighted residuals method, all the governing equations should be multiplied by an appropriate weighting function, which in this case, in view of Hamilton's principle, is $\psi_i(y)$ for the i-th equation. Multiplying the governing equations (18) by the appropriate functions leads to

$$[\psi][S][\psi][\xi] = [\psi]\{q\}. \tag{20}$$

The next step is to integrate over the length of the panel in the y direction. Performing the integration results in the first system of ODEs:

$$[X]\{\xi\} = \{J\}, \tag{21}$$

where the matrices $[X] = \int_0^b [\psi][S][\psi]dy$ and $\{J\} = \int_0^b [\psi]\{q\}dy$. are presented in Appendix B. Thus, assuming the first set of $\psi_i(y)$ as the initial guess functions, $[X]$ and $\{J\}$ can be calculated. Any analytical or numerical solution for (21) leads to the first approximate displacement and rotation functions in the x direction, i.e., $\xi_i(x)$, $i = 1, \dots, 5$.

Closed-form solutions can be found for the system of simultaneous ODEs (21), using standard techniques [Wylie and Barret 1985]. The solution consists of particular and homogenous parts:

$$\begin{Bmatrix} \xi_1 \\ \xi_2 \\ \xi_3 \\ \xi_4 \\ \xi_5 \end{Bmatrix} = \begin{bmatrix} 1 & 1 & 1 & \cdots & 1 \\ \alpha_1 & \alpha_2 & \alpha_3 & \cdots & \alpha_{10} \\ \beta_1 & \beta_2 & \beta_3 & \cdots & \beta_{10} \\ \chi_1 & \chi_2 & \chi_3 & \cdots & \chi_{10} \\ \delta_1 & \delta_2 & \delta_3 & \cdots & \delta_{10} \end{bmatrix}_{5\times 10} \begin{Bmatrix} A_1 e^{\lambda_1 x} \\ A_2 e^{\lambda_2 x} \\ A_3 e^{\lambda_3 x} \\ \vdots \\ A_{10} e^{\lambda_{10} x} \end{Bmatrix}_{10\times 1} + \begin{Bmatrix} \xi_{p1}(x) \\ \xi_{p2}(x) \\ \xi_{p3}(x) \\ \xi_{p4}(x) \\ \xi_{p5}(x) \end{Bmatrix}, \tag{22}$$

where the $\xi_{ip}(x)$ are particular parts of the solution that depend on the type of external load. For instance, in the case of uniform loading, all the $\xi_{ip}(x)$ are constants. They can be obtained by substituting $d_x = 0$ in the matrix $[X]$ of (21) and using the equality

$$\{\xi_p\}_{5\times 1} = ([X]|_{d_x=0})^{-1} \times \{J\}. \tag{23}$$

The homogenous part of the solution is comprised of exponential functions multiplied by appropriate constant coefficients. To obtain the λ_i in (22), one solves the characteristic equation

$$\det [X] = 0, \tag{24}$$

which amounts to a polynomial equation

$$H_1\lambda^{10} + H_2\lambda^8 + H_3\lambda^6 + H_4\lambda^4 + H_5\lambda^2 + H_6 = 0, \tag{25}$$

in which d_x is replaced by λ. Once the λ_i are calculated, it is possible to determine α_i, β_i, χ_i and δ_i, by replacing d_x by λ_i:

$$\left.\begin{bmatrix} X_{21} & X_{22} & X_{23} & X_{24} & X_{25} \\ X_{31} & X_{32} & X_{33} & X_{34} & X_{35} \\ X_{41} & X_{42} & X_{43} & X_{44} & X_{45} \\ X_{51} & X_{52} & X_{53} & X_{54} & X_{55} \end{bmatrix}\right|_{dx=\lambda_i} \times \begin{Bmatrix} 1 \\ \alpha_i \\ \beta_i \\ \chi_i \\ \delta_i \end{Bmatrix} = \begin{Bmatrix} 0 \\ 0 \\ 0 \\ 0 \\ 0 \end{Bmatrix}. \tag{26}$$

Finally, the boundary conditions (19) lead to the determination of the constant coefficients A_i:

$$\begin{pmatrix} 1 & 1 & 1 & 1 & 1 & 1 & 1 & 1 & 1 & 1 \\ \alpha_1 & \alpha_2 & \alpha_3 & \alpha_4 & \alpha_5 & \alpha_6 & \alpha_7 & \alpha_8 & \alpha_9 & \alpha_{10} \\ \beta_1 & \beta_2 & \beta_3 & \beta_4 & \beta_5 & \beta_6 & \beta_7 & \beta_8 & \beta_9 & \beta_{10} \\ \chi_1 & \chi_2 & \chi_3 & \chi_4 & \chi_5 & \chi_6 & \chi_7 & \chi_8 & \chi_9 & \chi_{10} \\ \delta_1 & \delta_2 & \delta_3 & \delta_4 & \delta_5 & \delta_6 & \delta_7 & \delta_8 & \delta_9 & \delta_{10} \\ e^{\lambda_1 a} & e^{\lambda_2 a} & e^{\lambda_3 a} & e^{\lambda_4 a} & e^{\lambda_5 a} & e^{\lambda_6 a} & e^{\lambda_7 a} & e^{\lambda_8 a} & e^{\lambda_9 a} & e^{\lambda_{10} a} \\ \alpha_1 e^{\lambda_1 a} & \alpha_2 e^{\lambda_2 a} & \alpha_3 e^{\lambda_3 a} & \alpha_4 e^{\lambda_4 a} & \alpha_5 e^{\lambda_5 a} & \alpha_6 e^{\lambda_6 a} & \alpha_7 e^{\lambda_7 a} & \alpha_8 e^{\lambda_8 a} & \alpha_9 e^{\lambda_9 a} & \alpha_{10} e^{\lambda_{10} a} \\ \beta_1 e^{\lambda_1 a} & \beta_2 e^{\lambda_2 a} & \beta_3 e^{\lambda_3 a} & \beta_4 e^{\lambda_4 a} & \beta_5 e^{\lambda_5 a} & \beta_6 e^{\lambda_6 a} & \beta_7 e^{\lambda_7 a} & \beta_8 e^{\lambda_8 a} & \beta_9 e^{\lambda_9 a} & \beta_{10} e^{\lambda_{10} a} \\ \chi_1 e^{\lambda_1 a} & \chi_2 e^{\lambda_2 a} & \chi_3 e^{\lambda_3 a} & \chi_4 e^{\lambda_4 a} & \chi_5 e^{\lambda_5 a} & \chi_6 e^{\lambda_6 a} & \chi_7 e^{\lambda_7 a} & \chi_8 e^{\lambda_8 a} & \chi_9 e^{\lambda_9 a} & \chi_{10} e^{\lambda_{10} a} \\ \delta_1 e^{\lambda_1 a} & \delta_2 e^{\lambda_2 a} & \delta_3 e^{\lambda_3 a} & \delta_4 e^{\lambda_4 a} & \delta_5 e^{\lambda_5 a} & \delta_6 e^{\lambda_6 a} & \delta_7 e^{\lambda_7 a} & \delta_8 e^{\lambda_8 a} & \delta_9 e^{\lambda_9 a} & \delta_{10} e^{\lambda_{10} a} \end{pmatrix} \times \begin{pmatrix} A_1 \\ A_2 \\ A_3 \\ A_4 \\ A_5 \\ A_6 \\ A_7 \\ A_8 \\ A_9 \\ A_{10} \end{pmatrix} = \begin{pmatrix} -\xi_{1p} \\ -\xi_{2p} \\ -\xi_{3p} \\ -\xi_{4p} \\ -\xi_{5p} \\ -\xi_{1p} \\ -\xi_{2p} \\ -\xi_{3p} \\ -\xi_{4p} \\ -\xi_{5p} \end{pmatrix}.$$

Subsequently, a similar procedure in the x direction results in the second set of ODEs:

$$[Y]\{\psi\} = \{K\}, \tag{27}$$

where the matrices $[Y] = \int_0^a [\xi][S][\xi]dx$ and $\{K\} = \int_0^a [\xi]\{q\}dx$ are defined in Appendix C. The same process can be used to obtain closed-form solutions for (27) which lead to the approximate functions for$\psi_i(y)$. At this point, the first iteration for solution of governing equations (18) is completed. Again, the new set of $\psi_i(y)$ is used to calculate coefficients of (21). This cyclic procedure should be continued successively, until a predefined level of accuracy is achieved. Results show that three to four iterations are usually enough to obtain the converged solution.

4. Results and discussion

In order to examine the efficiency and applicability of the solution, we consider examples of laminated panels and plates subjected to uniform and nonuniform loadings. The mechanical properties of two orthotropic materials used in this study are tabulated in Table 1, where E_1 and E_2 are the Young's moduli of the material in x and y directions, ν_{12} is the Poisson's ratio in the xy-plane, G_{12} stands for the in-plane shear modulus, and G_{13} and G_{23} are the transverse shear moduli in the xz- and yz-planes. The

	E_1 (GPa)	E_1/E_2	E_1/G_{13}	E_1/G_{12}	E_1/G_{23}	ν_{12}
Material I	175.78	25	50	50	125	0.25
Material II	147.66	15	35	35	42	0.3

Table 1. Material properties.

shear correction factor is taken as $K_s = \frac{5}{6}$ [Chaudhuri and Kabir 1993]. The results are then compared with others results in the literature. Moreover, many results including displacement components as well as stress resultants are presented to show the effects of various parametric ratios on the static response of the panel. The following dimensionless terms are used in all results presented in this study:

$$W^* = \frac{10^3 E_2 h^3 w_0}{q a^4}, \qquad M^* = \frac{10^3 M_1}{q a^2}, \qquad \beta^* = \frac{10^2 E_2 h^3}{q a^3} \beta_1. \tag{28}$$

The dimensionless deflection (W^*) and moment (M^*) are computed at the center point ($a/2$, $b/2$) of the panel, while the dimensionless rotation ($b*$) is reported at the point ($a/4$, $b/2$). The stacking sequence of the panel is taken as [0/90/0] unless explicitly noted.

It should be noted that unlike the traditional weighted residual methods, the EKM does not require the initial guess functions to meet boundary conditions. To illustrate this, arbitrary initial guess functions for all cases are taken as $\psi_i(y) = y^2 \sin(y\pi/i)$, $i = 1, \dots, 5$, which clearly do not satisfy the clamped boundary conditions (19). However, the solution obtained satisfies the boundary conditions once the first iteration is accomplished.

4.1. ***Laminated spherical panel.*** The first example deals with a clamped symmetrically laminated spherical panel ($R_x = R_y = R$) subjected to a uniform distributed load. The span lengths of the panel are taken as $a = b = 812.8$ mm, and the panel is made of material type I. For the described panel with the radius to side length ratio of $R/a = 10$ and the side length to thickness ratio of $a/h = 10$, the first four iterations of deflection functions $\psi_3(y)$ and $\xi_3(x)$ are illustrated in Figure 3. Note the good convergence rate of the method apparent in these graphs. After the second iteration, both $\xi_3(x)$ and $\psi_3(y)$ overlap completely. The predictions for dimensionless deflection, moment and rotation, tabulated in Table 2, left, also show the rapid convergence of the solution: the last two iterations differ by no more than 0.07% in dimensionless deflection, moment and rotation.

Table 2, right, compares, for a laminated spherical panel ($R/a = a/h = 10$) with symmetric lamination [0/90/0] and asymmetric lamination [0/90], the results of the present study and those of the double

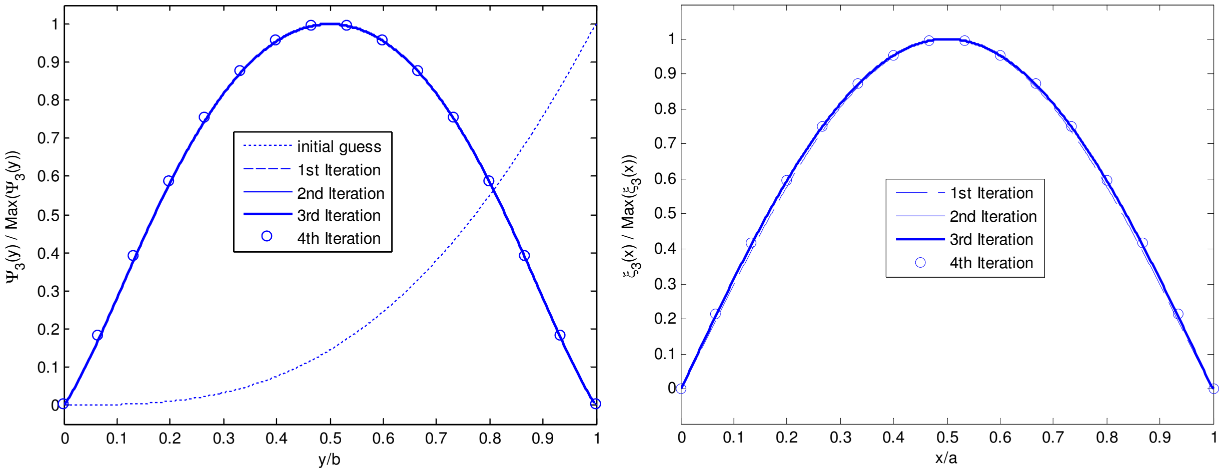

Figure 3. First four iterations for ψ_3 (left) and ξ_3 (right).

Iteration	W^*	M^*	β^*
1	4.5973	36.6842	0.3452
2	4.5012	35.9860	0.3332
3	4.4956	35.9494	0.3329
4	4.4925	35.9274	0.3327

Lamin.	Method	W^*	M^*	β^*
[0/90/0]	EKM	4.49	35.92	0.333
	DF	4.73	35.89	0.322
[0/90]	EKM	5.97	31.86	1.023
	DF	5.58	31.70	1.030

Table 2. First four iterations for spherical panel (left) and comparison of end result with those of the double Fourier method of [Chaudhuri and Kabir 1993] (right). In both cases, $a/h = R/a = 10$.

Fourier series analysis reported in [Chaudhuri and Kabir 1993]. The predictions for dimensionless deflection, moment and rotation are in agreement with Chaudhuri and Kabir's. However, it seems that the results of their double Fourier series technique are slightly inaccurate, since the analytical solution based on Navier's approach for dimensionless deflection of a similar panel with simply supported (SS1) edges is 10.11 [Reddy 2004], while the double Fourier series technique results in 10.53. Note also that the solution based on the double Fourier series needs about 100 terms to converge, while the solution presented here usually converges after the third iteration.

Figure 4, left, plots the dimensionless displacement W^*, moment M^* and rotation β^* versus the length to thickness ratio (a/h) of a moderately deep, symmetrically laminated cross-ply ($R/a = 10$) spherical panel. For thin panels ($a/h > 40$), both dimensionless deflection and rotation are constant. Included in the figure are also results of the double Fourier series method [Chaudhuri and Kabir 1993].

Variations of the dimensionless displacement W^*, moment M^* and rotation β^* with respect to radius to side length ratio (R/a) for symmetrically laminated moderately thick ($a/h = 10$) spherical panels are depicted in Figure 4, right. No variations of the dimensionless parameters (W^*, M^* and β^*) can be seen for the case of shallow shells ($R/a > 20$).

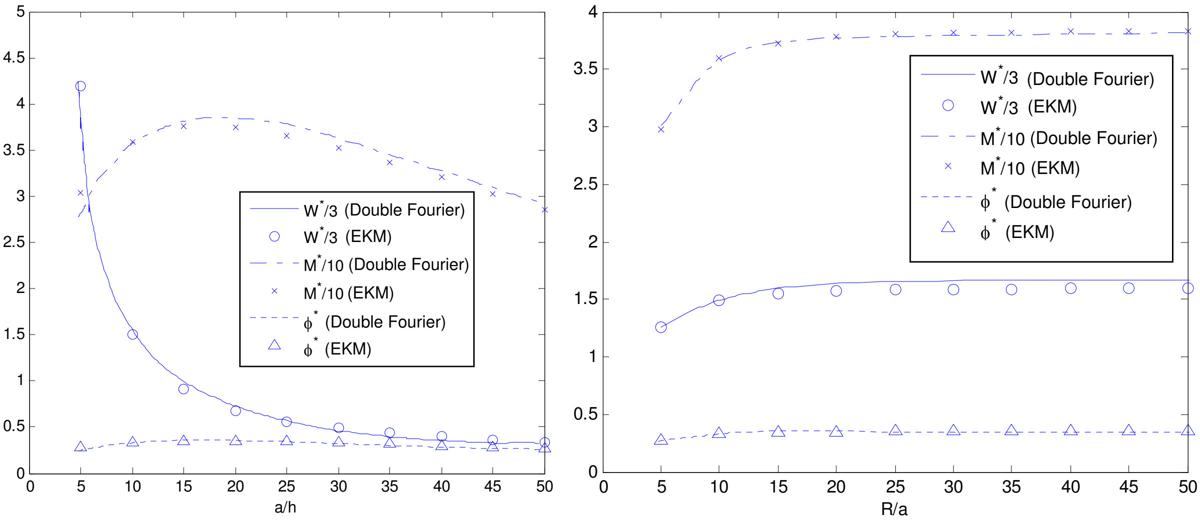

Figure 4. Dimensionless deflection, moment and rotation as functions of thickness (left) and curvature (right).

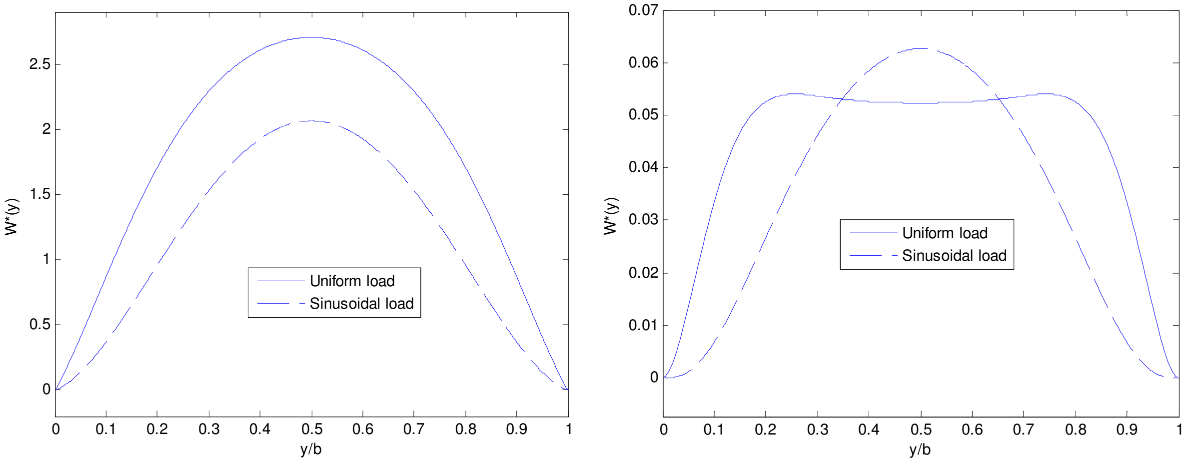

Figure 5. Dimensionless deflection of the spherical panel along the centerline $x/a = 0.5$. Left: $R/a = 3$ and $a/h = 10$; right: $R/a = 3$ and $a/h = 100$.

The next example investigates the static response of the laminated spherical panel to nonuniform loading. The geometric parameters of the panel are taken as $R/a = 3$ and $a/h = 10$, and the material is type I. Figure 5, left, shows the dimensionless deflection along the centerline ($x/a = 0.5$) of the panel subjected to a uniformly distributed load of q_0 and a sinusoidal load $q_0 \sin(\pi\, x/a) \sin(\pi\, y/b)$. The deflection is greater under the uniform load than under the sinusoidal load. However, this is not always the case: Figure 5, right, shows the dimensionless deflection of a spherical panel with geometric parameters $R/a = 3$ and $a/h = 100$, where the maximum deflection is higher under a sinusoidal load.

To study the effects of the loading distribution on the static response, dimensionless deflection, we give in Tables 3 and 4 the moment and rotation of spherical panels with different geometric parameters and laminations. We see that that as the panel gets thinner and deeper, it is more easily deflected under a sinusoidal load than under a uniform load.

4.2. ***Orthotropic spherical panel.*** This example investigates sensitivity of the static response of a single-layer orthotropic spherical panel to degree of orthotropy (E_1/E_2). Except for E_1/E_2 ratio, other mechanical properties of the panel are the same as material type I. In order to show the effect of the degree of orthotropy on the static response of the panel, the dimensionless displacement W^*, moment M^* and rotation β^* versus degree of orthotropy (E_1/E_2) are plotted in Figure 6. It is obvious that changes in the degree of orthotropy result in significant changes of the static response of the panel. It can easily be seen that dimensionless deflection and rotation decrease as degree of orthotropy (E_1/E_2) increases while increasing degree of orthotropy leads to increasing of dimensionless moment.

4.3. ***Laminated cylindrical panel.*** We now turn to cylindrical panels, introduced first as the limit of doubly curved panels as one radius of curvature increases. Thus we take $R_x = 10^8$ m in this section. Table 5 shows the dimensionless central deflections of clamped cylindrical panels made of material I with constant curvature ratio of 10 ($R_y/a = 10$), various thickness ratios and various laminations under uniform loading. Analogous results obtained using the commercial finite element software code ANSYS are also included in the table, showing good agreement with our solution.

		$a/h = 10$			$a/h = 20$			$a/h = 50$		
R/a		W^*	M^*	β^*	W^*	M^*	β^*	W^*	M^*	β^*
2	UL	1.715	12.544	0.120	0.518	8.299	0.082	0.092	1.696	0.021
	SL	1.413	13.039	0.112	0.469	9.809	0.084	0.104	3.619	0.029
3	UL	2.715	20.917	0.196	0.943	16.332	0.156	0.209	4.918	0.052
	SL	2.069	18.774	0.164	0.774	15.764	0.138	0.203	6.661	0.056
5	UL	3.777	29.876	0.278	1.535	27.664	0.260	0.492	13.140	0.129
	SL	2.783	24.768	0.218	1.185	23.711	0.210	0.421	13.206	0.116
10	UL	4.493	35.927	0.333	2.049	37.524	0.351	1.018	28.653	0.271
	SL	3.263	28.819	0.254	1.536	30.492	0.272	0.800	24.476	0.218
20	UL	4.715	37.805	0.350	2.231	41.023	0.382	1.356	38.646	0.362
	SL	3.409	30.061	0.266	1.661	32.887	0.294	1.039	31.558	0.283

Table 3. Dimensionless deflection, moment and rotation for symmetrically laminated [0/90/0] spherical panels, under uniform loading (UL) and sinusoidal loading (SL).

		$a/h = 10$			$a/h = 20$			$a/h = 50$		
R/a		W^*	M^*	β^*	W^*	M^*	β^*	W^*	M^*	β^*
2	UL	1.723	10.598	0.113	0.523	7.116	0.080	0.092	1.259	0.020
	SL	1.387	11.138	0.106	0.477	8.677	0.083	0.107	3.129	0.030
3	UL	2.688	17.689	0.184	0.956	14.395	0.154	0.217	4.246	0.053
	SL	2.010	15.969	0.153	0.781	14.025	0.136	0.209	5.967	0.057
5	UL	3.685	25.113	0.258	1.556	24.641	0.256	0.521	12.217	0.134
	SL	2.667	20.895	0.202	1.182	21.051	0.205	0.432	12.055	0.117
10	UL	4.345	30.043	0.307	2.075	33.560	0.345	1.069	26.966	0.282
	SL	3.103	24.168	0.234	1.524	27.001	0.264	0.814	22.478	0.221
20	UL	4.545	31.547	0.322	2.259	36.731	0.377	1.416	36.349	0.375
	SL	3.237	25.168	0.244	1.644	29.097	0.285	1.054	28.986	0.285

Table 4. Dimensionless deflection, moment and rotation for symmetrically laminated [0/90/90/0] spherical panels. under uniform loading (UL) and sinusoidal loading (SL).

Lamination	$a/h =$	10	20	30	40	50
[30/−30/30/−30]	EKM	4.560	2.490	2.053	1.867	1.754
	ANSYS	4.563	2.496	2.062	1.890	1.783
[45/−45/45/−45]	EKM	4.510	2.488	2.016	1.785	1.626
	ANSYS	4.542	2.514	2.062	1.846	1.704
[0/90/0]	EKM	4.702	2.215	1.674	1.445	1.303
	ANSYS	4.711	2.215	1.674	1.439	1.299

Table 5. Dimensionless central deflection of cylindrical panels with constant curvature ratio of $R/a = 10$ and various thickness ratios and laminations: comparison of present method with results obtained using commercial finite-element code (ANSYS).

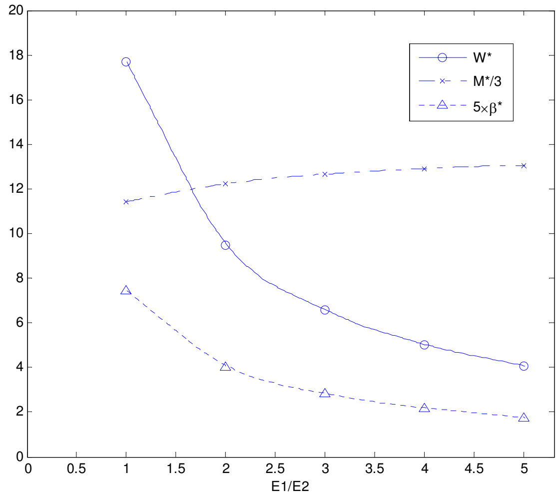

Figure 6. Variation of dimensionless deflection, moment and rotation to degree of orthotropy.

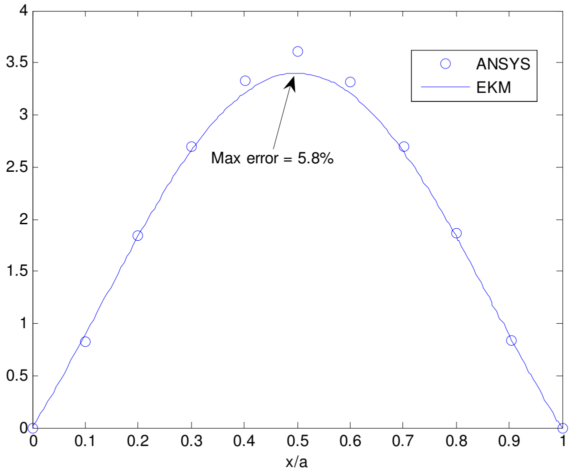

Figure 7. Dimensionless deflection of cylindrical panel along the straight center line.

The next example is a clamped symmetrically laminated cylindrical panel subjected to sinusoidal loading. The material properties of the panel are shown in Table 1 under type I and the geometric parameters are $R_y = 3\,\mathrm{m}$, $a = b = 0.3\,\mathrm{m}$ and $h = 0.03\,\mathrm{m}$. A sinusoidal loading distribution is assumed along both curved and straight axes as $q(x, y) = \sin(\pi\, x/a)\sin(\pi\, y/b)$. The dimensionless deflection of the panel along straight axis x is plotted in Figure 7; close agreement can be seen between the present method and the results from ANSYS. This suggests that the method provides a stable and valid solution even as one radius of curvature tends to infinity.

4.4. ***Laminated rectangular plate.*** The next case mimics that of laminated rectangular plates by assuming very large values for both radii of the panel, say $R_x = R_y = 10^8$ m. The mechanical properties of the panel are shown in Table 1 under type II. The dimensionless deflections of plates with different aspect

a/h	$b/a=$	1.0	1.2	1.4	1.6	1.8	2.0
10	EKM	5.20	5.96	6.31	6.42	6.42	6.35
	LMT	5.17	5.93	6.29	6.41	6.40	6.33
100	EKM	2.33	2.49	2.52	2.48	2.44	2.41
	LMT	2.28	2.44	2.46	2.43	2.38	2.35

Table 6. Dimensionless deflection of plates with different aspect ratios: comparison between the present method and results from [Chandrashekhara et al. 1990] obtained with the Lagrange multiplier technique.

Lamination	$a/h=$	10	20	30	40	50
[30/−30/30/−30]	EKM	4.599	2.535	2.122	1.971	1.899
	ANSYS	4.605	2.531	2.117	1.966	1.896
[45/−45/45/−45]	EKM	4.615	2.614	2.203	2.049	1.974
	ANSYS	4.626	2.610	2.200	2.043	1.969
[0/90/0]	EKM	4.809	2.308	1.797	1.613	1.527
	ANSYS	4.830	2.311	1.799	1.615	1.524

Table 7. Dimensionless central deflection of rectangular plates with various thickness ratios and laminations: comparison between the present method and results obtained from ANSYS.

ratios and thickness-to-side-length ratios are reported in Table 6. Predictions of the EKM are compared with corresponding results achieved by the Lagrange multipliers technique (LMT) [Chandrashekhara et al. 1990], again showing good agreement.

Finally, dimensionless central deflections of square plates made of material I with various thickness ratios and laminations obtained using the presented solution along with analogous results obtained using ANSYS are reported in Table 7.

Again, if we take infinite values for both radii ($R_x = R_y = \infty$), no divergence appears to occur. This suggests the validity and stability of the EKM for solving for the bending of laminated doubly curved panels even in the limit when both axes are straight.

5. Conclusion

We have presented an accurate semianalytical solution procedure for the bending of clamped doubly curved panels, using the extended Kantorovich method. Assuming the displacement functions to be products of two sets of separable functions, the governing PDEs are converted to two systems of ODEs with constant coefficients, each of which can be solved in closed form. Successive solution of the ODE systems results in convergence to the final solution of the problem. Unlike other weighted residual methods, this approach accepts arbitrary initial guess functions, not necessarily satisfying the boundary conditions. Examples are given of panels with different length-to-thickness and radius-to-length ratios, subjected to both uniform and nonuniform loading. In each case rapid convergence and high accuracy are observed, and the results agree with existing numerical and analytical solutions. The method also performs well in predicting displacement components and stress resultants. Finally, for the case of cylindrical panels ($R_x = \infty$) and rectangular plates ($R_x = R_y = \infty$), we check that the procedure remains functional and valid.

Appendix A: Coefficients of the fundamental matrix S of (14)

The matrix is symmetric. Set $d_x = \dfrac{\partial}{\partial x}$, $d_y = \dfrac{\partial}{\partial y}$, $d_x^2 = \dfrac{\partial^2}{\partial x^2}$, $d_y^2 = \dfrac{\partial^2}{\partial y^2}$.

$$S_{11} = G_{11}d_x^2 + 2A_{16}d_xd_y + G'_{66}d_y^2 - K_sG_{55}/R_x^2$$

$$S_{12} = G_{61}d_x^2 + A_{66}d_xd_y + A_{21}d_xd_y + G'_{26}d_y^2 - K_sA_{45}/R_xR_y$$

$$S_{13} = \left(\frac{K_sG_{55} + G_{11}}{R_x} + \frac{A_{12}}{R_y}\right)d_x + \left(\frac{K_sA_{54} + A_{61}}{R_x} + \frac{G'_{62}}{R_y}\right)d_y$$

$$S_{14} = H_{11}d_x^2 + H'_{66}d_y^2 + K_sG_{55}/R_x + 2B_{16}d_xd_y$$

$$S_{15} = H_{16}d_x^2 + H'_{62}d_y^2 + K_sA_{54}/R_x + (B_{66} + B_{12})d_xd_y$$

$$S_{22} = G_{66}d_x^2 + 2A_{26}d_xd_y + G'_{22}d_y^2 - K_sG'_{44}/R_y^2$$

$$S_{23} = \left(\frac{K_sA_{45} + A_{62}}{R_y} + \frac{G_{61}}{R_x}\right)d_x + \left(\frac{K_sG'_{44} + G'_{22}}{R_y} + \frac{A_{21}}{R_x}\right)d_y$$

$$S_{24} = H_{61}d_x^2 + H'_{26}d_y^2 + K_sA_{45}/R_y + (B_{66} + B_{12})d_xd_y$$

$$S_{25} = H_{66}d_x^2 + H'_{22}d_y^2 + K_sG'_{44}/R_y + 2B_{26}d_xd_y$$

$$S_{33} = -K_s(G_{55}d_x^2 + 2A_{45}d_xd_y + G'_{44}d_y^2) + \frac{G_{11}}{R_x^2} + \frac{2A_{12}}{R_xR_y} + \frac{G'_{22}}{R_y^2}$$

$$S_{34} = \left(\frac{H_{11}}{R_x} - K_sG_{55} + \frac{B_{12}}{R_y}\right)d_x + \left(\frac{H'_{26}}{R_y} - K_sA_{45} + \frac{B_{16}}{R_x}\right)d_y$$

$$S_{35} = \left(\frac{H_{16}}{R_x} - K_sA_{45} + \frac{B_{26}}{R_y}\right)d_x + \left(\frac{H'_{22}}{R_y} - K_sG'_{44} + \frac{B_{12}}{R_x}\right)d_y$$

$$S_{44} = J_{11}d_x^2 + 2D_{16}d_xd_y + J'_{66}d_y^2 - K_sG_{55}$$

$$S_{45} = J_{16}d_x^2 + (D_{12} + D_{66})d_xd_y + J'_{26}d_y^2 - K_sA_{54}$$

$$S_{55} = J_{66}d_x^2 + 2D_{26}d_xd_y + J'_{22}d_y^2 - K_sG'_{44}$$

Appendix B: Coefficients of the fundamental matrix X of (21)

Set $I_{ij} = \displaystyle\int_0^b \psi_i(y)\psi_j(y)\,dy$, $I'_{ij} = \displaystyle\int_0^b \psi_i(y)\frac{d\psi_j(y)}{dy}dy$, $I''_{ij} = \displaystyle\int_0^b \psi_i(y)\frac{d^2\psi_j(y)}{dy^2}dy$, and

$$\{J\} = \left\langle 0, 0, -\int_0^b q(x, y)\psi_3(y)dy, 0, 0\right\rangle^T.$$

$$
\begin{aligned}
X_{11} &= G_{11} I_{11} d_x^2 + 2A_{16} I'_{11} d_x + G'_{66} I''_{11} - K_s G_{55} I_{11}/R_x^2 \\
X_{12} &= G_{61} I_{12} d_x^2 + (A_{21} + A_{66}) I'_{12} d_x + G'_{26} I''_{12} - K_s A_{45} I_{12}/R_x R_y \\
X_{13} &= \left(\frac{K_s G_{55} + G_{11}}{R_x} + \frac{A_{12}}{R_y} \right) I_{13} d_x + \left(\frac{K_s A_{54} + A_{61}}{R_x} + \frac{G'_{62}}{R_y} \right) I'_{13} \\
X_{14} &= H_{11} I_{14} d_x^2 + H'_{66} I''_{14} + K_s G_{55} I_{14}/R_x + 2 I'_{14} B_{16} d_x \\
X_{15} &= H_{16} I_{15} d_x^2 + H'_{62} I''_{15} + K_s A_{54} I_{15}/R_x + I'_{15} (B_{66} + B_{12}) d_x \\
X_{21} &= G_{61} I_{21} d_x^2 + (A_{21} + A_{66}) I'_{21} d_x + G'_{26} I''_{21} - K_s A_{45} I_{21}/R_x R_y \\
X_{22} &= G_{66} I_{22} d_x^2 + 2A_{26} I'_{22} d_x + G'_{22} I''_{22} - K_s G'_{44} I_{22}/R_y^2 \\
X_{23} &= \left(\frac{K_s A_{45} + A_{62}}{R_y} + \frac{G_{61}}{R_x} \right) I_{23} d_x + \left(\frac{K_s G'_{44} + G'_{22}}{R_y} + \frac{A_{21}}{R_x} \right) I'_{23} \\
X_{24} &= H_{61} I_{24} d_x^2 + H'_{26} I''_{24} + K_s A_{45} I_{24}/R_y + I'_{24} (B_{66} + B_{12}) d_x \\
X_{25} &= H_{66} I_{25} d_x^2 + H'_{22} I''_{25} + K_s G'_{44} I_{25}/R_y + 2 I'_{25} B_{26} d_x \\
X_{31} &= \left(\frac{K_s G_{55} + G_{11}}{R_x} + \frac{A_{12}}{R_y} \right) I_{31} d_x + \left(\frac{K_s A_{54} + A_{61}}{R_x} + \frac{G'_{62}}{R_y} \right) I'_{31} \\
X_{32} &= \left(\frac{K_s A_{45} + A_{62}}{R_y} + \frac{G_{61}}{R_x} \right) I_{32} d_x + \left(\frac{K_s G'_{44} + G'_{22}}{R_y} + \frac{A_{21}}{R_x} \right) I'_{32} \\
X_{33} &= -K_s (G_{55} I_{33} d_x^2 + 2A_{45} I'_{33} d_x + G'_{44} I''_{33}) + \left(\frac{G_{11}}{R_x^2} + \frac{2A_{12}}{R_x R_y} + \frac{G'_{22}}{R_y^2} \right) I_{33} \\
X_{34} &= \left(\frac{H_{11}}{R_x} - K_s G_{55} + \frac{B_{12}}{R_y} \right) I_{34} d_x + \left(\frac{H'_{26}}{R_y} - K_s A_{45} + \frac{B_{16}}{R_x} \right) I'_{34} \\
X_{35} &= \left(\frac{H_{16}}{R_x} - K_s A_{45} + \frac{B_{26}}{R_y} \right) I_{35} d_x + \left(\frac{H'_{22}}{R_y} - K_s G'_{44} + \frac{B_{12}}{R_x} \right) I'_{35} \\
X_{41} &= H_{11} I_{41} d_x^2 + H'_{66} I''_{41} + K_s G_{55} I_{41}/R_x + 2 I'_{41} B_{16} d_x \\
X_{42} &= H_{61} I_{42} d_x^2 + H'_{26} I''_{42} + K_s A_{45} I_{42}/R_y + I'_{42} (B_{66} + B_{12}) d_x \\
X_{43} &= \left(\frac{H_{11}}{R_x} - K_s G_{55} + \frac{B_{12}}{R_y} \right) I_{43} d_x + \left(\frac{H'_{26}}{R_y} - K_s A_{45} + \frac{B_{16}}{R_x} \right) I'_{43} \\
X_{44} &= J_{11} I_{44} d_x^2 + 2D_{16} I'_{44} d_x + J'_{66} I''_{44} - K_s G_{55} I_{44} \\
X_{45} &= J_{16} I_{45} d_x^2 + (D_{12} + D_{66}) I_{45} d_x + J'_{26} I''_{45} - K_s A_{54} I_{45} \\
X_{51} &= H_{16} I_{51} d_x^2 + H'_{62} I''_{51} + K_s A_{54} I_{51}/R_x + I'_{51} (B_{66} + B_{12}) d_x \\
X_{52} &= H_{66} I_{52} d_x^2 + H'_{22} I''_{52} + K_s G'_{44} I_{52}/R_y + 2 I'_{52} B_{26} d_x \\
X_{53} &= \left(\frac{H_{16}}{R_x} - K_s A_{45} + \frac{B_{26}}{R_y} \right) I_{53} d_x + \left(\frac{H'_{22}}{R_y} - K_s G'_{44} + \frac{B_{12}}{R_x} \right) I'_{53} \\
X_{54} &= J_{16} I_{54} d_x^2 + (D_{12} + D_{66}) I_{54} d_x + J'_{26} I''_{45} - K_s A_{54} I_{45} \\
X_{55} &= J_{66} I_{55} d_x^2 + 2D_{26} I'_{55} d_x + J'_{22} I''_{55} - K_s G'_{44} I_{55}
\end{aligned}
$$

Appendix C: Coefficients of the fundamental matrix Y of (27)

Set $L_{ij} = \int_0^a \xi_i(x)\xi_j(x)\,dx$, $L'_{ij} = \int_0^a \xi_i(x)\dfrac{d\xi_j(x)}{dx}dx$, $L''_{ij} = \int_0^a \xi_i(x)\dfrac{d^2\xi_j(x)}{dx^2}dx$, and

$$\{K\} = \left\langle 0, 0, -\int_0^a q(x, y)\xi_3(x)dx, 0, 0\right\rangle^T.$$

$$Y_{11} = G_{11}L''_{11} + 2A_{16}L'_{11}d_y + G'_{66}L_{11}d_y^2 - K_sG_{55}L_{11}/R_x^2$$

$$Y_{12} = G_{61}L''_{12} + (A_{66} + A_{21})L'_{12}d_y + G'_{26}L_{12}d_y^2 - K_sA_{45}L_{12}/R_xR_y$$

$$Y_{13} = \left(\frac{K_sG_{55} + G_{11}}{R_x} + \frac{A_{12}}{R_y}\right)L'_{13} + \left(\frac{K_sA_{54} + A_{61}}{R_x} + \frac{G'_{62}}{R_y}r\right)L_{13}d_y$$

$$Y_{14} = H_{11}L''_{14} + H'_{66}L_{14}d_y^2 + K_sG_{55}L_{14}/R_x + 2L'_{14}B_{16}d_y$$

$$Y_{15} = H_{16}L''_{15} + H'_{62}L_{15}d_y^2 + K_sA_{54}L_{15}/R_x + L'_{15}(B_{66} + B_{12})d_y$$

$$Y_{21} = G_{61}L''_{21} + (A_{66} + A_{21})L'_{21}d_y + G'_{26}L_{21}d_y^2 - K_sA_{45}L_{21}/R_xR_y$$

$$Y_{22} = G_{66}L''_{22} + 2A_{26}L'_{22}d_y + G'_{22}L_{22}d_y^2 - K_sG'_{44}L_{22}/R_y^2$$

$$Y_{23} = \left(\frac{K_sA_{45} + A_{62}}{R_y} + \frac{G_{61}}{R_x}\right)L'_{23} + \left(\frac{K_sG'_{44} + G'_{22}}{R_y} + \frac{A_{21}}{R_x}\right)L_{23}d_y$$

$$Y_{24} = H_{61}L''_{24} + H'_{26}L_{24}d_y^2 + K_sA_{45}L_{24}/R_y + L'_{24}(B_{66} + B_{12})d_y$$

$$Y_{25} = H_{66}L''_{25} + H'_{22}L_{25}d_y^2 + K_sG'_{44}L_{25}/R_y + 2L'_{25}B_{26}d_y$$

$$Y_{31} = \left(\frac{K_sG_{55} + G_{11}}{R_x} + \frac{A_{12}}{R_y}\right)L'_{31} + \left(\frac{K_sA_{54} + A_{61}}{R_x} + \frac{G'_{62}}{R_y}\right)L_{31}d_y$$

$$Y_{32} = \left(\frac{K_sA_{45} + A_{62}}{R_y} + \frac{G_{61}}{R_x}\right)L'_{32} + \left(\frac{K_sG'_{44} + G'_{22}}{R_y} + \frac{A_{21}}{R_x}\right)L_{32}d_y$$

$$Y_{33} = -K_s(G_{55}L''_{33} + 2A_{45}L'_{33}d_y + G'_{44}L_{33}d_y^2) + \left(\frac{G_{11}}{R_x^2} + \frac{2A_{12}}{R_xR_y} + \frac{G'_{22}}{R_y^2}\right)L_{33}$$

$$Y_{34} = \left(\frac{H_{11}}{R_x} - K_sG_{55} + \frac{B_{12}}{R_y}\right)L'_{34} + \left(\frac{H'_{26}}{R_y} - K_sA_{45} + \frac{B_{16}}{R_x}\right)L_{34}d_y$$

$$Y_{35} = \left(\frac{H_{16}}{R_x} - K_sA_{45} + \frac{B_{26}}{R_y}\right)L'_{35} + \left(\frac{H'_{22}}{R_y} - K_sG'_{44} + \frac{B_{12}}{R_x}\right)L_{35}d_y$$

$$Y_{41} = H_{11}L''_{41} + H'_{66}L_{41}d_y^2 + K_sG_{55}L_{41}/R_x + 2L'_{41}B_{16}d_y$$

$$Y_{42} = H_{61}L''_{42} + H'_{26}L_{42}d_y^2 + K_sA_{45}L_{42}/R_y + L'_{42}(B_{66} + B_{12})d_y$$

$$Y_{43} = \left(\frac{H_{11}}{R_x} - K_sG_{55} + \frac{B_{12}}{R_y}\right)L'_{43} + \left(\frac{H'_{26}}{R_y} - K_sA_{45} + \frac{B_{16}}{R_x}\right)L_{43}d_y$$

$$Y_{44} = J_{11}L''_{44} + 2D_{16}L'_{44}d_y + J'_{66}L_{44}d_y^2 - K_sG_{55}L_{44}$$

$$Y_{45} = J_{16}L''_{45} + (D_{12} + D_{66})L'_{45}d_y + J'_{26}L_{45}d_y^2 - K_sA_{54}L_{45}$$

$$\begin{aligned}
Y_{51} &= H_{16}L''_{51} + H'_{62}L_{51}d_y^2 + K_sA_{54}L_{51}/R_x + L'_{51}(B_{66}+B_{12})d_y\\
Y_{52} &= H_{66}L''_{52} + H'_{22}L_{52}d_y^2 + K_sG'_{44}L_{52}/R_y + 2L'_{52}B_{26}d_y\\
Y_{53} &= \left(\frac{H_{16}}{R_x} - K_sA_{45} + \frac{B_{26}}{R_y}\right)L'_{53} + \left(\frac{H'_{22}}{R_y} - K_sG'_{44} + \frac{B_{12}}{R_x}\right)L_{53}d_y\\
Y_{54} &= J_{16}L''_{54} + (D_{12}+D_{66})L'_{54}d_y + J'_{26}L_{54}d_y^2 - K_sA_{54}L_{54}\\
Y_{55} &= J_{66}L''_{55} + 2D_{26}L'_{55}d_y + J'_{22}L_{55}d_y^2 - K_sG'_{44}L_{55}
\end{aligned}$$

References

[Abouhamze et al. 2007] M. Abouhamze, M. M. Aghdam, and F. Alijani, “Bending analysis of symmetrically laminated cylindrical panels using the extended Kantorovich method”, *Mech. Adv. Mater. Struct.* **14**:7 (2007), 523–30.

[Aghdam and Falahatgar 2003] M. M. Aghdam and S. R. Falahatgar, “Bending analysis of thick laminated plates using extended Kantorovich method”, *Comput. Struct.* **62**:3–4 (2003), 279–83.

[Aghdam and Mohammadi 2009] M. M. Aghdam and M. Mohammadi, “Bending analysis of thick orthotropic sector plates with various loading and boundary conditions”, *Comput. Struct.* **88** (2009), 212–218.

[Aghdam et al. 1996] M. M. Aghdam, M. Shakeri, and S. J. Fariborz, “Solution to the Reissner plate with clamped edges”, *J. Eng. Mech.* (*ASCE*) **122**:7 (1996), 679–82.

[Aghdam et al. 2009] M. M. Aghdam, F. Alijani, K. Bigdeli, and F. BakhtiariNejad, “Free vibration Analysis of functionally graded thin plates using the extended Kantorovich method, ICCST/07”, in *Proc. 7th Int. Conf. on Composite Science and Technology*, Sharjah, UAE, 2009.

[Alijani and Aghdam 2009] F. Alijani and M. M. Aghdam, “A semi-analytical solution for stress analysis of moderately thick laminated cylindrical panels with various boundary conditions”, *Comput. Struct.* **89** (2009), 543–550.

[Alijani et al. 2008] F. Alijani, M. M. Aghdam, and M. Abouhamze, “Application of the extended Kantorovich method to the bending of clamped cylindrical panels”, *Eur. J. Mech. A Solids* (2008), 378–388.

[Chandrashekhara et al. 1990] K. Chandrashekhara, A. H. Yahyavi, and E. R. Rao, “Bending of cross-ply laminated clamped plates using Lagrange multipliers”, *Comput. Struct.* **15** (1990), 169–179.

[Chaudhuri and Kabir 1993] R. A. Chaudhuri and H. R. H. Kabir, “Sensitivity to the response of moderately thick cross-ply doubly curved panels to lamination and boundary constraints, II: application”, *Int. J. Solids Struct.* **30** (1993), 273–86.

[Dalaei 1995] M. Dalaei, “Analysis of clamped rectangular orthotropic plates subjected to a uniform lateral load”, *Int. J. Mech. Sci.* **37** (1995), 527–35.

[Dalaei and Kerr 1996] M. Dalaei and A. D. Kerr, “Natural vibration analysis of clamped rectangular orthotropic plates”, *J. Sound Vib.* **189** (1996), 399–406.

[Fariborz and Pourbohloul 1989] S. J. Fariborz and A. Pourbohloul, “Application of the extended Kantorovich method to the bending of variable thickness plates”, *Comput. Struct.* **31**:3 (1989), 957–65.

[Kantorovich and Krylov 1958] L. V. Kantorovich and V. I. Krylov, *Approximate methods of higher analysis*, Translated from the 3rd Russian edition by C. D. Benster, Interscience, New York and Noordhoff, Groningen, 1958.

[Kerr 1968] A. D. Kerr, “An extension of the Kantorovich method”, *Quart. Appl. Math.* **26** (1968), 219–29.

[Kerr 1969] A. D. Kerr, “An extended Kantorovich method for the solution of eigenvalue problems”, *Int. J. Solids Struct.* **5** (1969), 559–72.

[Kerr and Alexander 1968] A. D. Kerr and H. Alexander, “An application of the extended Kantorovich method to the stress analysis of a clamped rectangular plate”, *Acta. Mech.* **6** (1968), 180–96.

[Kim et al. 2000] H. S. Kim, M. Cho, and G. I. Kim, “Free-edge strength analysis in composite laminates by the extended Kantorovich method”, *Comput. Struct.* **49**:2 (2000), 229–35.

[Reddy 2004] J. N. Reddy, *Mechanics of laminated component plates and shells theory and analysis*, 2nd ed., CRC Press, 2004.

[Toorani and Lakis 2000] M. H. Toorani and A. A. Lakis, "General equations of anisotropic plates and shells including transverse shear deformation, rotary inertia and initial curvature effects", *J. Sound Vib.* **237**:4 (2000), 561–615.

[Wylie and Barret 1985] C. R. Wylie and L. C. Barret, *Advanced engineering mathematics*, 5th ed., McGraw-Hill, New York, 1985.

[Yuan and Jin 1998] S. Yuan and Y. Jin, "Computation of elastic buckling loads of rectangular thin plates using the extended Kantorovich method", *Comput. Struct.* **66**:6 (1998), 861–7.

[Yuan et al. 1998] S. Yuan, J. Yan, and F. W. Williams, "Bending analysis of Mindlin plates by extended Kantorovich method", *J. Eng. Mech.* (*ASCE*) **124** (1998), 1339–45.

Received 15 Dec 2009. Revised 16 Jun 2010. Accepted 3 Jul 2010.

KASRA BIGDELI: `bigdeli@aut.ac.ir`
Thermoelasticity Center of Excellency, Department of Mechanical Engineering, Amirkabir University of Technology,
Hafez Ave, Tehran 15914, Iran
Current address: School of Engineering, The University of British Columbia at Okanagan, 3333 University Way,
Kelowna, BC, V1V 1V7, Canada

MOHAMMAD MOHAMMADI AGHDAM: `aghdam@aut.ac.ir`
Thermoelasticity Center of Excellency, Department of Mechanical Engineering, Amirkabir University of Technology,
Hafez Ave, Tehran 15914, Iran
http://me.aut.ac.ir/M.Aghdam.htm

JOURNAL OF MECHANICS OF MATERIALS AND STRUCTURES
Vol. 5, No. 6, 2010

ANALYTICAL SOLUTION FOR A CONCENTRATED FORCE ON THE FREE SURFACE OF A COATED MATERIAL

ZHIGEN WU, YIHUA LIU, CHUNXIAO ZHAN AND MEIQIN WANG

Based on the general solution of the displacement method for isotropic plane problems, the analytical solution for the plane problem of coated materials subjected to an arbitrary concentrated force on the free surface has been derived explicitly by using the image point method. The displacement functions are assumed to be the infinite series of the harmonic functions defined in the local coordinate systems with their origins placed at different image points. The harmonic functions corresponding to the higher-order image points can be deduced from those to the lower-order points by the recurrence formulae presented in this paper, and the first two harmonic functions are the displacement functions for the solution of a semi-infinite plane subjected to a concentrated force on the free surface. The theoretical formulae have been confirmed by numerical, finite-element-based, results in a special coated material.

1. Introduction

With the wide application of film-coated and surface-treated materials in engineering structures, the stress and failure analysis of coated materials have been the focus of attention. To obtain interfacial stresses for the evaluation of the cohesive strength, there are commonly three approaches: analytical, numerical, and experimental. In the last two decades, some numerical studies [Djabella and Arnell 1993; Hiroyuki et al. 1994b; Hiroyuki et al. 1994a; Kouitat-Njiwa and von Stebut 2003] and experimental methods [Masayuki et al. 1994; Takuma et al. 2000] have been developed. However, accurate stress results at the interface cannot be obtained easily by numerical or experimental methods for reasons of the thin coating or surface layer. Therefore, an analytical solution for coated materials is desirable.

For coated materials with a thin surface layer, the analytical solution of the stress field cannot be deduced easily by the theoretical method due to the difficulty in satisfying boundary and interface conditions. In recent years, the image point method has been applied to the construction of stress or displacement functions and the analytical solutions of coated materials for some cases have been obtained. The image point method is a technique that uses the superposition of known solutions to construct the solution of other complicated problems, and the relevant stress or displacement functions are expressed in the form corresponding to the loading point or image points. To our knowledge, this method was first employed by Mindlin [1936], who dealt with the fundamental solution for a single force applied in the interior of a semi-infinite solid, and the solution may be called a half-space nucleus of strain. Subsequently, Mindlin and Cheng [1950] provided many fundamental solutions for nuclei of strain in the half-space solid. Rongved [1955] found the theoretical solution of a point force acting in the interior of one of the two jointed half-spaces. Dundurs and Hetényi [1965] presented the fundamental solution for a point

---

Keywords: analytical solution, coated material, image point method, displacement method, interface.
Work supported by the Anhui Provincial Natural Science Foundation under Grant No. 090414157.

force applied in the interior of one of the two elastic half-spaces jointed by a sliding contact interface. Phan-Thien [1983] considered the case of an elastic half-space with a fixed boundary. Hasegawa *et al.* [1992] investigated Green's function for the axisymmetric problem of a bimaterial elastic solid. Recently, Ma and Lin [2001; 2002b] researched Green's functions for an isotropic elastic half-plane and bimaterial subjected to forces and dislocations, and nearly all kinds of image singularities for both half-plane and bimaterial were discussed in considerable detail. In these studies, one reflection face exists and the image point is a single point as far from the face as the object point. If there are two parallel reflection faces, the object point will lead to infinite image points by reciprocal reflections. Therefore, the image point method can be also extended to solve the problem with two parallel faces, and the related stress or displacement functions are constructed in the form of infinite series about the image points. For example, by taking the two interfaces as reflection faces, Aderogba [2003] established a theorem to generate the Airy stress function for trimaterials comprised of two semi-infinite planes separated by a thick layer due to a point force applied in or near the intermediate layer. By adopting the interface and surface as the reflection faces, Xu and Mutoh [2003a; 2003b] derived the analytical solutions for both two- and three-dimensional problems of coated semi-infinite bodies subjected to a concentrated force on the surface. By introducing two series image points, Li and Xu [2004; 2007] obtained the fundamental solutions for a coated semi-infinite plane subjected to a concentrated force in the interior of the coating layer and substrate as well as at the interface. Most recently, Yang and Xu [2009] deduced the three-dimensional analytical solution of coated materials with concentrated forces in the interior of the coating layer.

In the literature above, the image method was applied to isotropic materials. In fact, this method can also be applied to anisotropic materials. For example, Willis [1970] and Barnett and Lothe [1974] considered Green's functions for the two-dimensional deformation of an anisotropic elastic half-space subjected to a line force and/or a line dislocation inside it. Ting [1992] discussed in detail the image singularities of Green's functions for an anisotropic elastic half-space and bimaterials subjected to line forces and line dislocations based on Stroh's formalism. It should be mentioned that the locations of image singularities of Green's functions for the half-plane depend on anisotropic elastic constants and there are at most nine image points located at different positions with respect to the object point. Therefore, it is difficult to apply the conventional image method to obtain the solution of the anisotropic problem with two reflection faces directly. Nevertheless, recently, some particular mathematical approaches were employed by fewer researchers to treat certain layered half-planes with complex material constants. For instance, by using the Lekhnitskii formalism for anisotropic elastic materials and the Fourier-transformation technique, Ma and Lin [2002a] obtained the analytical solutions for stresses in the anisotropic layered half-plane subjected to concentrated forces and edge dislocations in the thin layer or in the half-plane. Applying the Fourier transform method and the series expansion technique, an effective analytic methodology was developed by Ma and Lee [2009] to construct the full-field explicit solutions for a transversely isotropic magnetoelectroelastic layered half-plane subjected to generalized line forces and edge locations. In these problems, the complete solutions consist of the simplest solutions for the infinite medium with applied loadings, and the physical meaning of these simplest solutions is the image method.

In this paper, in order to obtain the explicit analytical solution for coated materials subjected to an arbitrary concentrated force on the free surface, we make use of the general solution of the displacement method as well as the image point method to construct the displacement functions in terms of infinite series of harmonic functions. According to the free boundary and interface continuity conditions, the

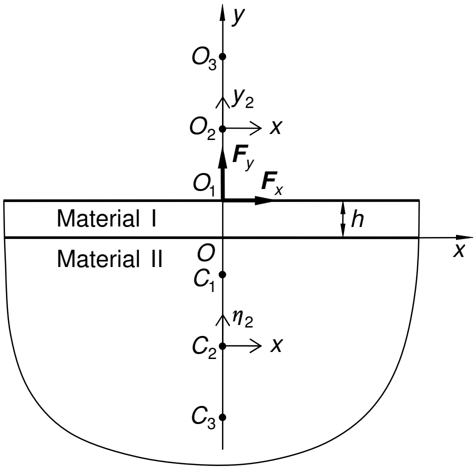

Figure 1. Analytical model of a coated material.

recurrence formulae for the harmonic functions are derived and all harmonic functions can be determined from the initial harmonic functions, which correspond to the first-order image point and are the displacement functions for the semi-infinite plane subjected to a concentrated force on the free surface.

2. Analytical model

The coated material is modeled as a surface layer with thickness h bonded perfectly to a half-plane, as shown in Figure 1. An arbitrary concentrated force is decomposed into a normal force F_x and a tangential force F_y applied at the point O_1 on the free surface of the surface layer. The surface layer and half-plane materials are numbered I and II, respectively; their shear moduli and Poisson's ratios are μ_{I}, μ_{II}, ν_{I}, and ν_{II}. We place the origin O of the global coordinate system on the interface just beneath the loading point O_1 and the x-axis along the interface. By use of the reciprocal reflections of the loading point O_1 on the interface and free surface, infinite image points will be produced on the xy-plane, i.e., the image points O_k $(k = 1, 2, 3, \ldots)$ in the upper half-plane and C_k $(k = 1, 2, 3, \ldots)$ in the lower half-plane. Introducing the local coordinates (x, y_k) and (x, η_k) with their origins located at O_k and C_k, respectively, the relationships between the local and global coordinates can be expressed as

$$y_k = y - (2k-1)h, \quad \eta_k = y + (2k-1)h, \quad k = 1, 2, 3, \ldots. \tag{1}$$

The displacement and traction continuity conditions on the interface can be represented as

$$u_{\mathrm{I}} = u_{\mathrm{II}}, \quad v_{\mathrm{I}} = v_{\mathrm{II}}, \quad \sigma_{y\mathrm{I}} = \sigma_{y\mathrm{II}}, \quad \tau_{xy\mathrm{I}} = \tau_{xy\mathrm{II}}, \quad \text{at } y = 0, \tag{2}$$

and the free surface condition can be written as

$$\sigma_{y\mathrm{I}} = 0, \quad \tau_{xy\mathrm{I}} = 0, \quad \text{at } y = h, \tag{3}$$

where subscript I and II refer to materials I and II, respectively.

3. Derivation of theoretical formulae

The general solution of the displacement method for isotropic plane problems can be obtained from [Wu and Liu 2008] as

$$2\mu u = \frac{\partial\Phi}{\partial x} + y\frac{\partial\Psi}{\partial x}, \quad 2\mu v = \frac{\partial\Phi}{\partial y} + y\frac{\partial\Psi}{\partial y} - \kappa\Psi, \tag{4}$$

$$\begin{gathered}\sigma_x = \frac{\partial^2\Phi}{\partial x^2} + y\frac{\partial^2\Psi}{\partial x^2} + \frac{\kappa-3}{2}\frac{\partial\Psi}{\partial y}, \quad \sigma_y = \frac{\partial^2\Phi}{\partial y^2} + y\frac{\partial^2\Psi}{\partial y^2} - \frac{\kappa+1}{2}\frac{\partial\Psi}{\partial y}, \\ \tau_{xy} = \frac{\partial^2\Phi}{\partial x\partial y} + y\frac{\partial^2\Psi}{\partial x\partial y} - \frac{\kappa-1}{2}\frac{\partial\Psi}{\partial x},\end{gathered} \tag{5}$$

where Φ and Ψ are the two displacement functions which are harmonic, μ is the shear modulus, $\kappa = 3-4\nu$ for plane strain and $(3-\nu)/(1+\nu)$ for plane stress, and ν is Poisson's ratio.

Substituting (4) and (5) into (2) and (3), respectively, one has

$$\begin{gathered}\Gamma\Phi_{\mathrm{I}} = \Phi_{\mathrm{II}}, \quad \Gamma\left(\frac{\partial\Phi_{\mathrm{I}}}{\partial y} - \kappa_{\mathrm{I}}\Psi_{\mathrm{I}}\right) = \frac{\partial\Phi_{\mathrm{II}}}{\partial y} - \kappa_{\mathrm{II}}\Psi_{\mathrm{II}}, \\ \frac{\partial^2\Phi_{\mathrm{I}}}{\partial y^2} - \frac{\kappa_{\mathrm{I}}+1}{2}\frac{\partial\Psi_{\mathrm{I}}}{\partial y} = \frac{\partial^2\Phi_{\mathrm{II}}}{\partial y^2} - \frac{\kappa_{\mathrm{II}}+1}{2}\frac{\partial\Psi_{\mathrm{II}}}{\partial y}, \quad \frac{\partial\Phi_{\mathrm{I}}}{\partial y} - \frac{\kappa_{\mathrm{I}}-1}{2}\Psi_{\mathrm{I}} = \frac{\partial\Phi_{\mathrm{II}}}{\partial y} - \frac{\kappa_{\mathrm{II}}-1}{2}\Psi_{\mathrm{II}}, \quad \text{at } y=0,\end{gathered} \tag{6}$$

where $\Gamma = \mu_{\mathrm{II}}/\mu_{\mathrm{I}}$, and

$$\frac{\partial^2\Phi_{\mathrm{I}}}{\partial y^2} + h\frac{\partial^2\Psi_{\mathrm{I}}}{\partial y^2} - \frac{\kappa_{\mathrm{I}}+1}{2}\frac{\partial\Psi_{\mathrm{I}}}{\partial y} = 0, \quad \frac{\partial\Phi_{\mathrm{I}}}{\partial y} + h\frac{\partial\Psi_{\mathrm{I}}}{\partial y} - \frac{\kappa_{\mathrm{I}}-1}{2}\Psi_{\mathrm{I}} = 0, \quad \text{at } y=h. \tag{7}$$

In order to solve the displacement functions Φ_{I}, Ψ_{I}, Φ_{II}, and Ψ_{II}, assume that these functions can be written in series form as

$$\begin{aligned}\Phi_{\mathrm{I}} &= \sum_{k=1}^{\infty}\left[A_k(x, y_k) + \phi_k(x, \eta_k)\right], \quad \Phi_{\mathrm{II}} = \sum_{k=1}^{\infty} B_k(x, y_k), \\ \Psi_{\mathrm{I}} &= \sum_{k=1}^{\infty}\left[a_k(x, y_k) + \psi_k(x, \eta_k)\right], \quad \Psi_{\mathrm{II}} = \sum_{k=1}^{\infty} b_k(x, y_k),\end{aligned} \tag{8}$$

where A_k, ϕ_k, a_k, ψ_k, B_k, and b_k are harmonic functions with respect to x and y_k or η_k. Considering the remote stress condition (the stresses should vanish at infinite), all functions on the right in (8) must be singular at their corresponding origins. Since there is no stress singularity in the material II, the displacement functions of the material II cannot contain any term related to the image points in the lower half-plane.

From (1), it is easy to find that

$$\frac{\partial}{\partial y} = \frac{\partial}{\partial y_k}, \quad \frac{\partial}{\partial y} = \frac{\partial}{\partial \eta_k}. \tag{9}$$

Substituting (8) into (6) and using (9), one obtains, at $y = 0$,

$$\begin{aligned}
&\Gamma\phi_k(x,\eta_k) = B_k(x,y_k) - \Gamma A_k(x,y_k),\\
&\Gamma\left[\frac{\partial\phi_k(x,\eta_k)}{\partial\eta_k} - \kappa_{\mathrm{I}}\psi_k(x,\eta_k)\right] = \frac{\partial B_k(x,y_k)}{\partial y_k} - \kappa_{\mathrm{II}} b_k(x,y_k) - \Gamma\left[\frac{\partial A_k(x,y_k)}{\partial y_k} - \kappa_{\mathrm{I}} a_k(x,y_k)\right],\\
&\frac{\partial^2\phi_k(x,\eta_k)}{\partial\eta_k^2} - \frac{\kappa_{\mathrm{I}}+1}{2}\frac{\partial\psi_k(x,\eta_k)}{\partial\eta_k} = \frac{\partial^2 B_k(x,y_k)}{\partial y_k^2} - \frac{\kappa_{\mathrm{II}}+1}{2}\frac{\partial b_k(x,y_k)}{\partial y_k} - \frac{\partial^2 A_k(x,y_k)}{\partial y_k^2} + \frac{\kappa_{\mathrm{I}}+1}{2}\frac{\partial a_k(x,y_k)}{\partial y_k},\\
&\frac{\partial\phi_k(x,\eta_k)}{\partial\eta_k} - \frac{\kappa_{\mathrm{I}}-1}{2}\psi_k(x,\eta_k) = \frac{\partial B_k(x,y_k)}{\partial y_k} - \frac{\kappa_{\mathrm{II}}-1}{2} b_k(x,y_k) - \frac{\partial A_k(x,y_k)}{\partial y_k} + \frac{\kappa_{\mathrm{I}}-1}{2} a_k(x,y_k). \qquad (10)
\end{aligned}$$

These equations are of the form $L(x,\eta_k) = R(x,y_k)$ (L and R being the left and right sides of the equation, respectively). Because (10) is valid only on the interface where the local coordinate values satisfy $y_k = -\eta_k = -(2k-1)h$, we have the interchange laws

$$\frac{\partial L}{\partial\eta_k} = -\frac{\partial R}{\partial y_k}, \qquad \int L\,\mathrm{d}\eta_k = -\int R\,\mathrm{d}y_k. \tag{11}$$

Applying (11) to (10), we obtain

$$\begin{aligned}
B_k(x,y_k) &= \frac{\Gamma(\kappa_{\mathrm{I}}+1)}{\Gamma\kappa_{\mathrm{I}}+1}A_k(x,y_k) + \Gamma\left[\frac{\kappa_{\mathrm{I}}^2(\Gamma-1)}{2(\Gamma\kappa_{\mathrm{I}}+1)} - \frac{\Gamma\kappa_{\mathrm{I}}-\kappa_{\mathrm{II}}}{2(\Gamma+\kappa_{\mathrm{II}})}\right]\int a_k(x,y_k)\,\mathrm{d}y_k,\\
b_k(x,y_k) &= \frac{\Gamma(\kappa_{\mathrm{I}}+1)}{\Gamma+\kappa_{\mathrm{II}}}a_k(x,y_k),
\end{aligned}\tag{12}$$

$$\begin{aligned}
\phi_k(x,\eta_k) &= -\frac{\kappa_{\mathrm{I}}(\Gamma-1)}{\Gamma\kappa_{\mathrm{I}}+1}A_k(x,y_k) + \left[\frac{\kappa_{\mathrm{I}}^2(\Gamma-1)}{2(\Gamma\kappa_{\mathrm{I}}+1)} - \frac{\Gamma\kappa_{\mathrm{I}}-\kappa_{\mathrm{II}}}{2(\Gamma+\kappa_{\mathrm{II}})}\right]\int a_k(x,y_k)\,\mathrm{d}y_k,\\
\psi_k(x,\eta_k) &= \frac{2(\Gamma-1)}{\Gamma\kappa_{\mathrm{I}}+1}\frac{\partial A_k(x,y_k)}{\partial y_k} - \frac{\kappa_{\mathrm{I}}(\Gamma-1)}{\Gamma\kappa_{\mathrm{I}}+1}a_k(x,y_k), \quad \text{at } y_k = -\eta_k.
\end{aligned}\tag{13}$$

Equations (12) and (13) show that the four harmonic functions B_k, b_k, ϕ_k, and ψ_k can be calculated by using the other two ones, A_k and a_k. In (13), $y_k = -\eta_k$ means that y_k on the right side should be replaced by $-\eta_k$ to obtain ϕ_k and ψ_k.

Substituting the values of Φ_{I} and Ψ_{I} from (8) into (7), using the relation (9), and considering the symmetric relations of the image points O_{k+1} and C_k about the free surface, we have

$$\begin{aligned}
&\frac{\partial^2 A_{k+1}(x,y_{k+1})}{\partial y_{k+1}^2} + h\frac{\partial^2 a_{k+1}(x,y_{k+1})}{\partial y_{k+1}^2} - \frac{\kappa_{\mathrm{I}}+1}{2}\frac{\partial a_{k+1}(x,y_{k+1})}{\partial y_{k+1}}\\
&\qquad\qquad = -\left[\frac{\partial^2\phi_k(x,\eta_k)}{\partial\eta_k^2} + h\frac{\partial^2\psi_k(x,\eta_k)}{\partial\eta_k^2} - \frac{\kappa_{\mathrm{I}}+1}{2}\frac{\partial\psi_k(x,\eta_k)}{\partial\eta_k}\right],\\
&\frac{\partial A_{k+1}(x,y_{k+1})}{\partial y_{k+1}} + h\frac{\partial a_{k+1}(x,y_{k+1})}{\partial y_{k+1}} - \frac{\kappa_{\mathrm{I}}-1}{2}a_{k+1}(x,y_{k+1})\\
&\qquad\qquad = -\left[\frac{\partial\phi_k(x,\eta_k)}{\partial\eta_k} + h\frac{\partial\psi_k(x,\eta_k)}{\partial\eta_k} - \frac{\kappa_{\mathrm{I}}-1}{2}\psi_k(x,\eta_k)\right], \quad \text{at } y = h, \qquad (14)
\end{aligned}$$

and

$$\begin{aligned}&\frac{\partial^2 A_1(x,y_1)}{\partial y_1^2}+h\frac{\partial^2 a_1(x,y_1)}{\partial y_1^2}-\frac{\kappa_{\mathrm{I}}+1}{2}\frac{\partial a_1(x,y_1)}{\partial y_1}=0,\\&\frac{\partial A_1(x,y_1)}{\partial y_1}+h\frac{\partial a_1(x,y_1)}{\partial y_1}-\frac{\kappa_{\mathrm{I}}-1}{2}a_1(x,y_1)=0,\quad \text{at } y=h.\end{aligned}\tag{15}$$

Equation (14) is in the form $L(x, y_{k+1}) = R(x, \eta_k)$. On the free surface $y = h$, the local coordinate values satisfy $y_{k+1} = -\eta_k = -2kh$; thus we can get the interchange laws in the form

$$\frac{\partial L}{\partial y_{k+1}}=-\frac{\partial R}{\partial \eta_k},\qquad \int L\,\mathrm{d}y_{k+1}=-\int R\,\mathrm{d}\eta_k.\tag{16}$$

Applying (16) to (14), one has

$$\begin{aligned}&A_{k+1}(x,y_{k+1})=\kappa_{\mathrm{I}}\phi_k(x,\eta_k)+2h\frac{\partial\phi_k(x,\eta_k)}{\partial\eta_k}+2h^2\frac{\partial\psi_k(x,\eta_k)}{\partial\eta_k}-\frac{\kappa_{\mathrm{I}}^2-1}{2}\int\psi_k(x,\eta_k)\,\mathrm{d}\eta_k,\\&a_{k+1}(x,y_{k+1})=-2\frac{\partial\phi_k(x,\eta_k)}{\partial\eta_k}-2h\frac{\partial\psi_k(x,\eta_k)}{\partial\eta_k}+\kappa_{\mathrm{I}}\psi_k(x,\eta_k),\quad \text{at } \eta_k=-y_{k+1}.\end{aligned}\tag{17}$$

From (17), we find that the harmonic functions A_{k+1} and a_{k+1} can be obtained from ϕ_k and ψ_k. In (17), $\eta_k = -y_{k+1}$ means that η_k on the right side should be replaced by $-y_{k+1}$ to obtain A_{k+1} and a_{k+1}. Equation (17) shows that the harmonic functions corresponding to the order $k + 1$ can be deduced from the ones to the order k. Therefore, if the functions A_1 and a_1 are given, all functions on the right in (8) can be derived by using (12), (13), and (17).

To determine the functions A_1 and a_1, one should consider simultaneously (15) and the condition of a concentrated force applied at the point O_1 on the free surface. It is not difficult to find that the solutions for the normal and tangential concentrated forces on the free surface of a semi-infinite plane satisfy these conditions. Considering the parallel translation of the coordinate system, the functions A_1 and a_1 for the normal and tangential forces can be found, respectively, as

$$\begin{aligned}&A_1(x,y_1)=\frac{F_y}{2\pi}\left[\left(\frac{\kappa_{\mathrm{I}}-1}{2}y_1-h\right)\ln(x^2+y_1^2)+(\kappa_{\mathrm{I}}-1)x\arctan\frac{y_1}{x}\right],\\&a_1(x,y_1)=\frac{F_y}{2\pi}\ln(x^2+y_1^2),\quad \text{for normal force},\end{aligned}\tag{18}$$

$$\begin{aligned}&A_1(x,y_1)=\frac{F_x}{\pi}\left[\left(\frac{\kappa_{\mathrm{I}}+1}{2}y_1-h\right)\arctan\frac{y_1}{x}-\frac{(\kappa_{\mathrm{I}}+1)}{4}x\ln(x^2+y_1^2)\right],\\&a_1(x,y_1)=\frac{F_x}{\pi}\arctan\frac{y_1}{x},\quad \text{for tangential force}.\end{aligned}\tag{19}$$

It is easy to demonstrate that (18) and (19) are all harmonic functions and satisfy (15) as well as the condition of the concentrated force applied at the point O_1. To this time, all harmonic functions appearing on the right in (8) can be derived through the recurrence as shown in (12), (13), (17), and (18) or (19). Therefore, the analytical solution for coated materials subjected to an arbitrary concentrated force on the free surface is obtained explicitly.

4. Numerical results

For a verification of the correctness of the above theoretical formulae, the stresses along the interface of a coated material (Figure 2) have been numerically analyzed by ABAQUS based on the displacement finite element method concerning the plane strain analysis. Since the thickness of the surface layer is very thin, it can be considered as a thin film bonded to the free surface of a semi-infinite plane. In Figure 2, the height and width of the substrate are taken as one and two hundred times the thickness of the film, respectively. Although half of the analytical model can be selected for the numerical calculation due to the symmetry and anti-symmetry of the problem, the whole model was till treated for the numerical analysis to obtain the accurate numerical results of the nodes at and near the symmetric axis y. The finite element mesh, containing 6200 elements and 18841 nodes, is shown in Figure 3. The material constants are $E_{\mathrm{I}} = 546\,\mathrm{GPa}$, $E_{\mathrm{II}} = 206\,\mathrm{GPa}$, and $\nu_{\mathrm{I}} = \nu_{\mathrm{II}} = 0.3$, respectively.

Tables 1–4 compare the theoretical and FEM results of the stress components along the interface for the normal and tangential concentrated forces, respectively, where $n = k$ means that the orders of the image point from one to k are considered in the analytical solution. From these tables it can be observed that the higher the order of the image point is considered, the better the theoretical results agree with the FEM ones, and the convergence rates are all very rapid. From Table 1 it can be found that the maximum of the stress component σ_y is about 0.513892 MPa for the theoretical result and 0.517178 MPa for the FEM one at $x = 0$, and the relative error is 0.64%. Table 2 shows that the minimum of the stress component τ_{xy} is about -0.166807 MPa for the theoretical result and -0.168955 MPa for the FEM one at $x = 0.6$ mm, and the relative error is 1.27%. Table 3 indicates that the minimum of the stress component σ_y is about

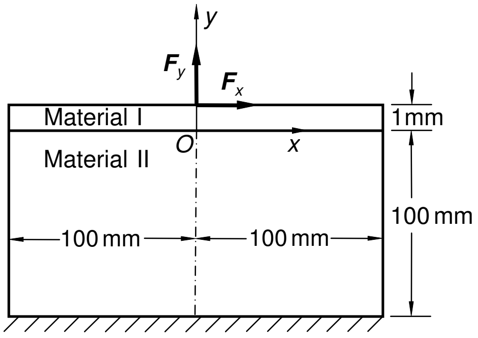

Figure 2. Model for FEM calculation.

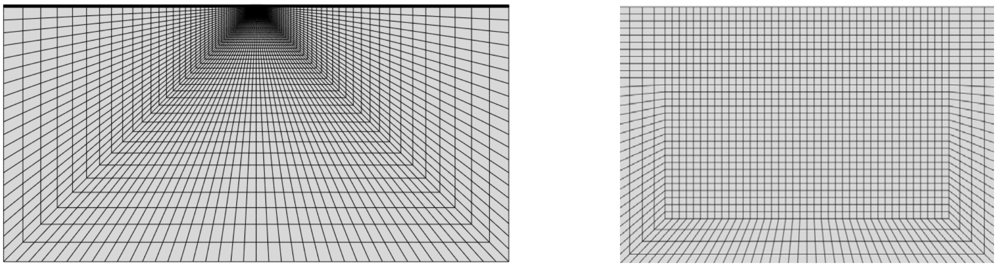

Figure 3. Mesh division for FEM (right: zoom near the loading point).

	σ_y/MPa				
x/mm	$n=1$	$n=2$	$n=3$	$n=4$	FEM
0.0	0.377616	0.470810	0.502243	0.513892	0.517178
0.2	0.348280	0.439538	0.470597	0.482151	0.486965
0.4	0.277906	0.363634	0.393600	0.404869	0.412302
0.6	0.199702	0.277057	0.305294	0.316106	0.324809
0.8	0.134947	0.202128	0.228126	0.238330	0.246878
1.0	0.088676	0.144976	0.168376	0.177853	0.185658
1.2	0.057885	0.103544	0.124148	0.132810	0.138807
1.4	0.037974	0.073918	0.091680	0.099476	0.105742
1.6	0.025168	0.052719	0.067721	0.074633	0.080256
1.8	0.016876	0.037494	0.049923	0.055961	0.061005
2.0	0.011439	0.026542	0.036652	0.041853	0.046368
2.31919	0.006252	0.015088	0.022140	0.026092	0.029827
2.69364	0.003101	0.007558	0.011908	0.014714	0.017624
3.13291	0.001306	0.003164	0.005508	0.007284	0.009394
3.64824	0.000355	0.000952	0.002031	0.003028	0.004437
4.25279	−0.000101	0.000031	0.000472	0.000978	0.001850

Table 1. Normal stress σ_y along the interface for the case of $F_x = 0$ and $F_y = 1\,\text{N}$.

	τ_{xy}/MPa				
x/mm	$n=1$	$n=2$	$n=3$	$n=4$	FEM
0.0	0.000000	0.000000	0.000000	0.000000	0.000000
0.2	−0.078466	−0.086408	−0.088172	−0.088660	−0.090259
0.4	−0.126963	−0.141976	−0.145389	−0.146345	−0.148621
0.6	−0.140036	−0.160574	−0.165427	−0.166807	−0.168955
0.8	−0.130309	−0.154459	−0.160467	−0.162210	−0.163999
1.0	−0.111587	−0.137409	−0.144241	−0.146276	−0.147799
1.2	−0.091997	−0.117795	−0.125111	−0.127359	−0.128753
1.4	−0.074835	−0.099318	−0.106796	−0.109176	−0.110524
1.6	−0.060862	−0.083188	−0.090546	−0.092981	−0.094314
1.8	−0.049829	−0.069566	−0.076578	−0.078995	−0.080316
2.0	−0.041206	−0.058242	−0.064744	−0.067084	−0.068366
2.31919	−0.031160	−0.044170	−0.049661	−0.051781	−0.052963
2.69364	−0.023304	−0.032496	−0.036728	−0.038501	−0.039528
3.13291	−0.017365	−0.023419	−0.026333	−0.027663	−0.028471
3.64824	−0.012977	−0.016778	−0.018529	−0.019392	−0.019936
4.25279	−0.009781	−0.012140	−0.013028	−0.013478	−0.013750

Table 2. Shear stress τ_{xy} along the interface for the case of $F_x = 0$ and $F_y = 1\,\text{N}$.

−0.143830 MPa for the theoretical result and −0.143788 MPa for the FEM one at $x = 0.6\,\text{mm}$, and the relative error is 0.03%. In Table 4, the maximum of the stress component τ_{xy} is about 0.101641 MPa for the theoretical result and 0.102782 MPa for the FEM one at $x = 1.2\,\text{mm}$, and the relative error is 1.11%.

			σ_y/MPa		
x/mm	$n = 1$	$n = 2$	$n = 3$	$n = 4$	FEM
0.0	0.000000	0.000000	0.000000	0.000000	0.000000
0.2	−0.069656	−0.076721	−0.078337	−0.078804	−0.077114
0.4	−0.111162	−0.124505	−0.127639	−0.128552	−0.127132
0.6	−0.119821	−0.138045	−0.142507	−0.143830	−0.143788
0.8	−0.107958	−0.129342	−0.134879	−0.136558	−0.137641
1.0	−0.088676	−0.111488	−0.117807	−0.119778	−0.121405
1.2	−0.069462	−0.092198	−0.098999	−0.101193	−0.102991
1.4	−0.053163	−0.074696	−0.081694	−0.084038	−0.085851
1.6	−0.040268	−0.059879	−0.066827	−0.069253	−0.071031
1.8	−0.030376	−0.047714	−0.054414	−0.056860	−0.058592
2.0	−0.022878	−0.037874	−0.044183	−0.046595	−0.048302
2.31919	−0.014500	−0.026062	−0.031579	−0.033851	−0.035506
2.69364	−0.008354	−0.016731	−0.021256	−0.023285	−0.024818
3.13291	−0.004091	−0.009919	−0.013416	−0.015124	−0.016489
3.64824	−0.001295	−0.005342	−0.007950	−0.009318	−0.010482
4.25279	−0.000429	−0.002494	−0.004460	−0.005532	−0.006493

Table 3. Normal stress σ_y along the interface for the case of $F_x = 1\,\mathrm{N}$ and $F_y = 0$.

			τ_{xy}/MPa		
x/mm	$n = 1$	$n = 2$	$n = 3$	$n = 4$	FEM
0.0	−0.022910	−0.025870	−0.026507	−0.026780	−0.028217
0.2	−0.007212	−0.009495	−0.010030	−0.010127	−0.011164
0.4	0.027875	0.027507	0.027271	0.027240	0.027283
0.6	0.061111	0.063535	0.063761	0.063833	0.064659
0.8	0.081337	0.086962	0.087769	0.087976	0.089110
1.0	0.088676	0.097452	0.098904	0.099268	0.100444
1.2	0.087486	0.099000	0.101107	0.101641	0.102782
1.4	0.081859	0.095488	0.098213	0.098918	0.100030
1.6	0.074469	0.089522	0.092791	0.093660	0.094766
1.8	0.066781	0.082613	0.086326	0.087346	0.088465
2.0	0.059502	0.075575	0.079624	0.080775	0.081943
2.31919	0.049356	0.065027	0.069393	0.070705	0.071945
2.69364	0.039863	0.054403	0.058853	0.060276	0.061562
3.13291	0.031491	0.044462	0.048753	0.050214	0.051528
3.64824	0.024433	0.035721	0.039673	0.041093	0.042405
4.25279	0.018685	0.028395	0.031935	0.033254	0.034533

Table 4. Shear stress τ_{xy} along the interface for the case of $F_x = 1\,\mathrm{N}$ and $F_y = 0$.

Tables 1–4 illustrate that the analytical results really converge to FEM ones and that enough accuracy of the analytical solution can be achieved only considering the first four image points for this coated material. Figures 4 and 5 provide the numerical calculations based on the analytical solution ($n = 4$) for

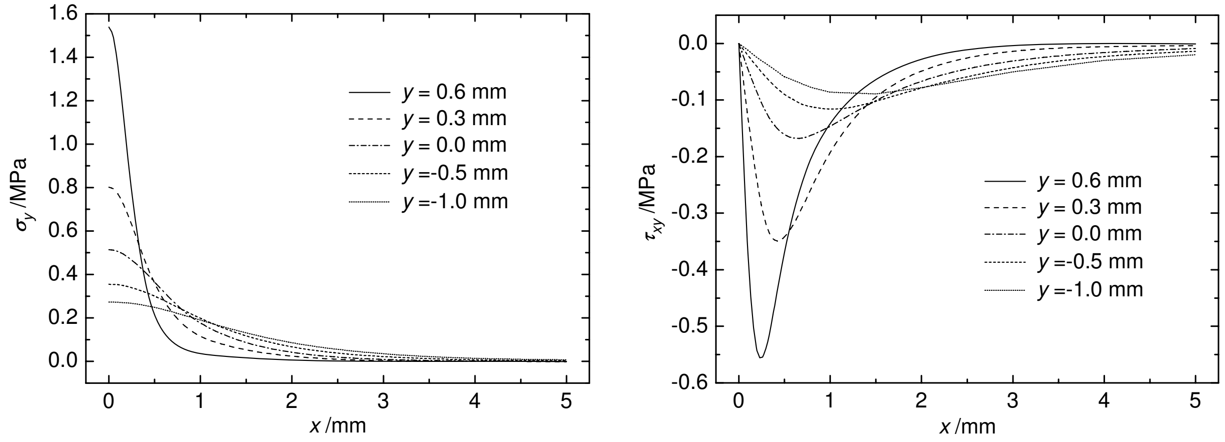

Figure 4. Analytical solutions of stress components at different values of y for the case of $F_x = 0$ and $F_y = 1\,\text{N}$: σ_y (left) and τ_{xy} (right).

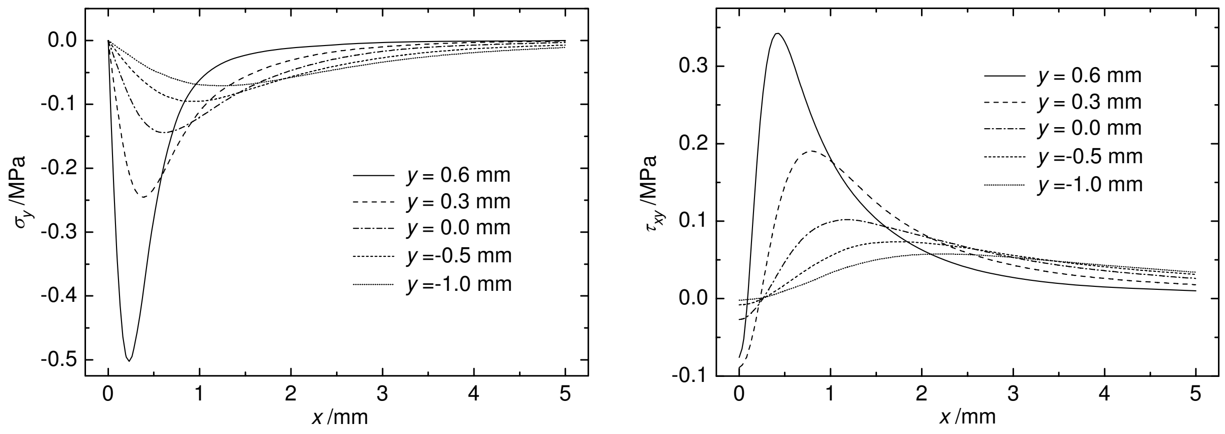

Figure 5. Analytical solutions of stress components at different values of y for the case of $F_x = 1\,\text{N}$ and $F_y = 0$: σ_y (left) and τ_{xy} (right).

the stress components at different locations for the cases of $F_x = 0$ and $F_y = 1\,\text{N}$ as well as $F_x = 1\,\text{N}$ and $F_y = 0$, respectively.

On the other hand, to maintain the accuracy of the analytical solution, the different orders of image points should be needed for the various matches of material constants. Given $\nu_{\text{I}} = \nu_{\text{II}} = 0.3$ and $E_{\text{I}} = 546\,\text{GPa}$, Figure 6 displays the required image point order to obtain the results with the relative error below 2.5%. It can be found that the larger the difference of the material constants is, the more image points are needed.

5. Conclusions

In this paper, we derived the analytical solution for the plane problem of the coated material subjected to an arbitrary concentrated force on the free surface by using the general solution of the displacement

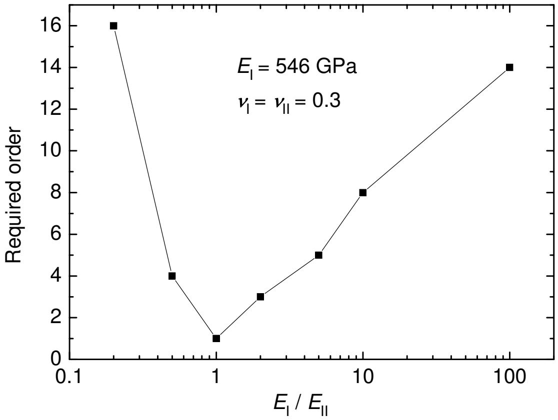

Figure 6. Image point order required for various Young's modulus ratios.

method as well as the image point method. This solution is given explicitly as the summation of the harmonic functions corresponding to each image point, and the harmonic functions corresponding to the higher-order image points can be determined from those to the lower-order ones through the recurrence. The numerical results verified the correctness and rapid convergence of the analytical solution obtained in this paper. The enough accurate theoretical results can be obtained only by considering image points of the first several order.

References

[Aderogba 2003] K. Aderogba, "An image treatment of elastostatic transmission from an interface layer", *J. Mech. Phys. Solids* **51**:2 (2003), 267–279.

[Barnett and Lothe 1974] D. Barnett and J. Lothe, "An image force theorem for dislocations in anisotropic bicrystals", *J. Phys. F Metal Phys.* **4**:10 (1974), 1618–1635.

[Djabella and Arnell 1993] H. Djabella and R. Arnell, "Finite element comparative study of elastic stresses in single, double layer and multilayered coated systems", *Thin Solid Films* **235**:1-2 (1993), 156–162.

[Dundurs and Hetényi 1965] J. Dundurs and M. Hetényi, "Transmission of force between two semi-infinite solids", *J. Appl. Mech.* (*ASME*) **32** (1965), 671–674.

[Hasegawa et al. 1992] H. Hasegawa, V.-G. Lee, and T. Mura, "Green's functions for axisymmetric problems of dissimilar elastic solids", *J. Appl. Mech.* (*ASME*) **59**:2 (1992), 312–320.

[Hiroyuki et al. 1994a] K. Hiroyuki, I. Masahiro, T. Tohru, and K. Hiroki, "Approximate expression for stress distribution in film subjected to indentation by spherical indenter : the case of a very thin film", *Trans. Soc. Mech. Eng. A* **60**:570 (1994), 416–420.

[Hiroyuki et al. 1994b] K. Hiroyuki, I. Masahiro, T. Tohru, and K. Hiroki, "Elasto-plastic finite-element analysis of stress distribution in a film-substrate system indented by a spherical indenter in relation to evaluation of fracture strength of films", *Trans. Soc. Mech. Eng. A* **60**:570 (1994), 409–415.

[Kouitat-Njiwa and von Stebut 2003] R. Kouitat-Njiwa and J. von Stebut, "Boundary element numerical analysis of elastic indentation of a sphere into a bi-layer material", *Int. J. Mech. Sci.* **45**:2 (2003), 317–324.

[Li and Xu 2007] Y. Li and J.-Q. Xu, "Fundamental solution for bonded materials with a free surface parallel to the interface. Part II: Solutions of concentrated force acting at the interior of the substrate and the case when the force acting at the interface", *Int. J. Solids Struct.* **44**:10 (2007), 3317–3327.

[Li et al. 2004] Y. Li, J.-Q. Xu, and L. Fu, “Fundamental solution for bonded materials with a free surface parallel to the interface. Part I: Solution of concentrated forces acting at the inside of the material with a free surface”, *Int. J. Solids Struct.* **41**:24-25 (2004), 7075–7089.

[Ma and Lee 2009] C.-C. Ma and J.-M. Lee, “Theoretical analysis of generalized loadings and image forces in a planar magnetoelectroelastic layered half-plane”, *J. Mech. Phys. Solids* **57**:3 (2009), 598–620.

[Ma and Lin 2001] C.-C. Ma and R.-L. Lin, “Image singularities of Green’s functions for an isotropic elastic half-plane subjected to forces and dislocations”, *Math. Mech. Solids* **6**:5 (2001), 503–524.

[Ma and Lin 2002a] C.-C. Ma and R.-L. Lin, “Full-field analysis of a planar anisotropic layered half-plane for concentrated forces and edge dislocations”, *Proc. Royal Soc. London A Math. Phys. Eng. Sci.* **458**:2026 (2002), 2369–2392.

[Ma and Lin 2002b] C.-C. Ma and R.-L. Lin, “Image singularities of Green’s functions for isotropic elastic bimaterials subjected to concentrated forces and dislocations”, *Int. J. Solids Struct.* **39**:20 (2002), 5253–5277.

[Masayuki et al. 1994] T. Masayuki, I. Takeshi, K. Ken, and A. Masao, “Asymmetric three-point bending of a laminated beam containing a delamination”, *Trans. Soc. Mech. Eng. A* **60**:578 (1994), 2266–2272.

[Mindlin 1936] R. Mindlin, “Force at a point in the interior of a semi-infinite solid”, *J. Appl. Phys.* **7** (May 1936), 195–202.

[Mindlin and Cheng 1950] R. Mindlin and D. H. Cheng, “Nuclei of strain in the semi-infinite solid”, *J. Appl. Phys.* **21** (September 1950), 926–930.

[Phan-Thien 1983] N. Phan-Thien, “On the image system for the Kelvin-state”, *J. Elasticity* **13** (1983), 231–235.

[Rongved 1955] L. Rongved, “Force interior to one of two jointed semi-infinite solids”, pp. 1–13 in *Proceedings of the 2nd Midwestern Conference on Solid Mechanics*, 1955.

[Takuma et al. 2000] M. Takuma, N. Shinke, T. Kubo, and A. Yonekura, “Evaluation on fracture characteristics of thin ceramic film with scratch testing”, *Trans. Soc. Mech. Eng. A* **66**:651 (2000), 2074–2078.

[Ting 1992] T. C. T. Ting, “Image singularities of green’s functions for anisotropic elastic half-spaces and bimaterials”, *Quarterly J. Mech. Appl. Math.* **45**:1 (1992), 119–139.

[Willis 1970] J. Willis, “Stress fields produced by dislocations in anisotropic media”, *Philos. Mag.* **21** (May 1970), 931–949.

[Wu and Liu 2008] Z. Wu and Y. Liu, “Analytical solution for the singular stress distribution due to V-notch in an orthotropic plate material”, *Eng. Fract. Mech.* **75**:8 (2008), 2367–2384.

[Xu and Mutoh 2003a] J.-Q. Xu and Y. Mutoh, “Analytical solution for interface stresses due to concentrated surface force”, *Int. J. Mech. Sci.* **45**:11 (2003), 1877–1892.

[Xu and Mutoh 2003b] J.-Q. Xu and Y. Mutoh, “A normal force on the free surface of a coated material”, *J. Elasticity* **73** (2003), 147–164.

[Yang and Xu 2009] Z. Yang and J.-Q. Xu, “Three-dimensional solution of concentrated forces in semi-infinite coating materials”, *Int. J. Mech. Sci.* **51**:6 (2009), 424–433.

Received 4 Jan 2010. Revised 3 May 2010. Accepted 3 Jun 2010.

ZHIGEN WU: `zhigenwu@126.com`
Hefei University of Technology, School of Civil Engineering, Hefei, 230009, China

YIHUA LIU: `liuyhfut@yahoo.cn`
Hefei University of Technology, School of Civil Engineering, Hefei, 230009, China

CHUNXIAO ZHAN: `zhcxhfut@yahoo.cn`
Hefei University of Technology, School of Civil Engineering, Hefei, 230009, China

MEIQIN WANG: `wang_meiqin@yahoo.cn`
Hefei University of Technology, School of Civil Engineering, Hefei, 230009, China

JOURNAL OF MECHANICS OF MATERIALS AND STRUCTURES
Vol. 5, No. 6, 2010

ON THE NONLINEAR DYNAMICS OF OVAL CYLINDRICAL SHELLS

SYED MUHAMMAD IBRAHIM, BADRI PRASAD PATEL AND YOGENDRA NATH

The nonlinear periodic response characteristics of symmetrically and nonsymmetrically excited oval cylindrical shells are investigated using the first order shear deformation theory based finite strip method. The periodic solutions of the governing second order equations of motion are obtained using the shooting technique coupled with Newmark time marching and the arc length continuation algorithm. The effect of ovality parameter and loading locations on the steady state frequency response and modal participation factors is studied. For circular shells ($\zeta = 0.0$), travelling waves emanating at loading point but moving in opposite directions for certain range of forcing frequency are brought out. For the symmetrically excited oval shell with $\zeta = 0.6$, due to 1:1 internal resonance between the AS/SS and SA/AA modes, a secondary branch with traveling wave response emanates from the primary one through a symmetry breaking bifurcation. For the nonsymmetrically excited oval shells ($\zeta = 0.6$), either waves moving in anticlockwise direction or those originating near the major axis and moving in opposite directions in the top and bottom halves of the shell are observed for certain forcing frequency ranges.

A list of symbols can be found on page 907.

1. Introduction

Large amplitude vibrations occur frequently in thin shells and panels used in the aerospace industry, as they are subjected to high acoustic and aerodynamic excitations. For the study of such vibrations, a linear model (usually the first approximation to the actual system) is often inadequate. In particular, the nonlinear forced response analysis of closed circular cylindrical shells still remains an active and challenging area of research [Moussaoui and Benamar 2002; Amabili and Païdoussis 2003; Amabili 2008].

Shells with variable curvature, especially oval and elliptical cylindrical shells, are used in nuclear fusion reactors, heat exchangers, aerospace and underwater structures due to special external shape or internal storage requirements. Noncircularity may also be introduced while fabricating circular shells. The variable stiffness along the circumference of a shell due to noncircularity leads to the coupling of modes with different circumferential wave numbers of a corresponding perfect circular shell and influences the dynamic characteristics significantly. The asymmetric free vibration modes of perfect circular cylindrical shells are not spatially fixed, due to axisymmetric geometry, but noncircular shells with doubly symmetric cross-section have spatially fixed free vibration modes, categorised as AS, SA, SS, AA, the first and second letters indicating symmetry or antisymmetry about the major and minor axes, respectively.

Studies relating to the linear static and dynamic, buckling and nonlinear static analyses of shells with noncircular cross-sections have been reviewed in [Soldatos 1999]. Investigations on the nonlinear

---

Keywords: noncircular shell, nonlinear, periodic, shooting, travelling wave, internal resonance.
The authors are grateful to DST, India (Project No. SR/S3/MERC/46/2005) for financial support.

vibration characteristics of oval and elliptical shells are quite limited. Using the Galerkin method, Pandalai and Sathyamoorthy [1970] investigated large amplitude flexural vibrations of simply supported thin oval rings and finite oval cylindrical shells using one axisymmetric and one asymmetric term in the approximation of transverse displacement, and a softening type behaviour was found. Using the Bubnov–Galerkin method, the nonlinear free vibration of thin-walled elastic cylindrical shell of elliptic cross-section was analysed in [Kozarov and Mladenov 1979] using a single term approximation of all the three displacements (axial, circumferential, radial) and predicted hardening behaviour. The studies [Pandalai and Sathyamoorthy 1970; Kozarov and Mladenov 1979] are based on approximate analytical solutions that may affect the accuracy of the results. Patel et al. [2002; 2003] investigated the nonlinear free flexural vibration behaviour of the isotropic/laminated orthotropic noncircular rings using the finite element approach and Newmark time marching scheme and reported softening nonlinearity. The nonlinear forced vibration analysis of oval cylindrical shells with different support conditions has been carried out in [Ibrahim et al. 2008a; 2008b] employing the direct time integration approach and only part of the stable branches of the frequency response curves could be captured. Further, it is observed that in the direct integration approach, the convergence to a steady state solution is very slow. In addition, the steady state response can not be ascertained in the direct time integration approaches.

Periodic solutions of nonlinear systems can be obtained by the shooting method. Unlike frequency domain methods, the number of equations does not depend on the number of harmonics. Steady state solutions can be reached in significantly fewer iterations than with direct time integration methods. The shooting method also yields the monodromy matrix, which can be used to predict the stability of the solution. In the traditional shooting approach, the dynamical equations of motion are transformed into first order equations [Nayfeh and Balachandran 1994; Padmanabhan and Singh 1995; Sundararajan and Noah 1997; Ribeiro 2004; 2008], thus increasing computational time as the number of equations is doubled and the banded nature of system of equations is destroyed. This issue is quite important, particularly for systems with many degrees of freedom such as the ones resulting from finite element discretisation. Note that a few-degrees-of-freedom model of a continuous system may not capture a priori unknown modal interactions/phenomena. To the best of the authors' knowledge, the complete frequency response characteristics of oval cylindrical shells have not been dealt with in the literature, nor are there results on the participation of different modes, effect of loading location, internal resonance between AS/SS and SA/AA modes and travelling wave response of noncircular cylindrical shells.

The modified shooting technique coupled with the Newmark time marching and arc length continuation algorithm [Patel et al. 2009; Ibrahim et al. 2009; 2010] is employed to investigate the steady state periodic response of the oval cylindrical shells excited in the neighbourhood of the first AS, SA, SS, and AA linear free vibration modes. The analysis is carried out using the finite strip method based on first order shear deformation theory. The effect of the ovality parameter and loading locations on the steady-state frequency response and modal participation factors is studied. Participation of AS and SS modes in the primary branch of symmetrically excited shells and participation of AS, SA, SS, and AA modes in asymmetrically excited shells is brought out. For symmetrically excited shells, a secondary branch corresponding to significant participation of SA/AA modes in addition to AS/SS modes due to one-to-one internal resonance is reported for the first time. For a certain forcing frequency range, shell response includes waves travelling from the loading point in two opposite directions or in the same direction, depending on the forcing frequency.

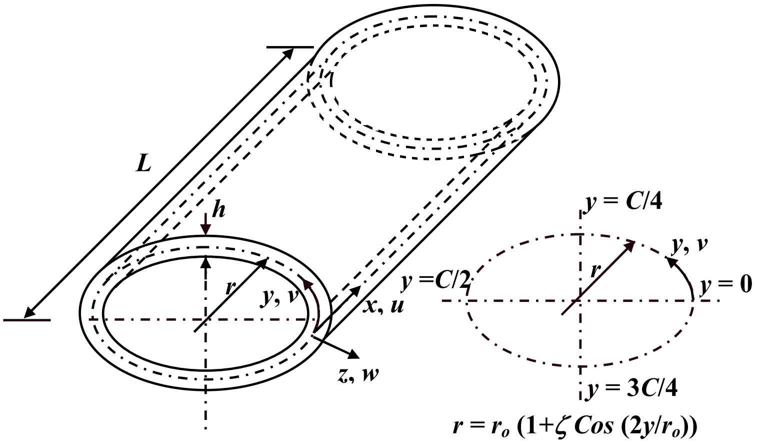

Figure 1. Coordinate system and geometry of oval shell.

2. Formulation

The geometry and coordinate system of the oval cylindrical shell are shown in Figure 1. The coordinates x, y and z having origin at the mid-surface of the shell are considered along the meridional, circumferential and thickness directions, respectively. The displacements u, v, w at a point (x, y, z), employing the first order shear deformation theory, are expressed as

$$\begin{aligned} u(x, y, z, t) &= u_0(x, y, t) + z\theta_x(x, y, t), \\ v(x, y, z, t) &= v_0(x, y, t) + z\theta_y(x, y, t), \\ w(x, y, z, t) &= w_0(x, y, t). \end{aligned} \tag{1}$$

The displacement field variables u_0, v_0, w_0, θ_x and θ_y are represented as the superposition of trigonometric functions in the meridional coordinate x as

$$\begin{aligned} u_0(x, y, t) &= \sum_{i=1}^{M} u_0^i(y, t) U_i(x), \\ v_0(x, y, t) &= \sum_{i=1}^{M} v_0^i(y, t) V_i(x), \\ w_0(x, y, t) &= \sum_{i=1}^{M} w_0^i(y, t) W_i(x), \\ \theta_x(x, y, t) &= \sum_{i=1}^{M} \theta_x^i(y, t) \Theta_{xi}(x), \\ \theta_y(x, y, t) &= \sum_{i=1}^{M} \theta_y^i(y, t) \Theta_{yi}(x), \end{aligned} \tag{2}$$

where the trigonometric functions $U_i(x)$, $V_i(x)$, $W_i(x)$, $\Theta_x i(x)$ and $\Theta_y i(x)$ satisfying all the boundary conditions for movable simply supported shell at its two ends are taken as in [Soedel 1993]:

$$U_i(x) = \cos(i\pi x/L), \quad V_i(x) = \sin(i\pi x/L), \quad W_i(x) = \sin(i\pi x/L),$$
$$\Theta_{xi}(x) = \cos(i\pi x/L), \quad \Theta_{yi}(x) = \sin(i\pi x/L).$$

For the other boundary conditions, these functions can be chosen appropriately.

The strain-displacement relations are based on kinematic approximations of Sanders type: (i) small strains, (ii) moderately large rotations; and (iii) thin shell ($z/r << 1$) such that $1 + z/r \approx 1$. However, transverse shear deformation is important due to smaller wavelength of the deformation shape to thickness ratio. The Green's strains are written in terms of the midsurface deformations as

$$\boldsymbol{\varepsilon} = \begin{Bmatrix} \boldsymbol{\varepsilon}_p^L \\ \mathbf{0} \end{Bmatrix} + \begin{Bmatrix} z\boldsymbol{\varepsilon}_b \\ \boldsymbol{\varepsilon}_s \end{Bmatrix} + \begin{Bmatrix} \boldsymbol{\varepsilon}_p^{NL} \\ \mathbf{0} \end{Bmatrix}, \tag{3}$$

where $\mathbf{0}$ is the 2×1 null vector, and

$$\boldsymbol{\varepsilon}_p^L = \begin{Bmatrix} \dfrac{\partial u_0}{\partial x} \\ \dfrac{\partial v_0}{\partial y} + \dfrac{w_0}{r} \\ \dfrac{\partial u_0}{\partial y} + \dfrac{\partial v_0}{\partial x} \end{Bmatrix}, \quad \boldsymbol{\varepsilon}_b = \begin{Bmatrix} \dfrac{\partial \theta_x}{\partial x} \\ \dfrac{\partial \theta_y}{\partial y} \\ \dfrac{\partial \theta_x}{\partial y} + \dfrac{\partial \theta_y}{\partial x} \end{Bmatrix}, \quad \boldsymbol{\varepsilon}_s = \begin{Bmatrix} \theta_x + \dfrac{\partial w_0}{\partial x} \\ \theta_y + \dfrac{\partial w_0}{\partial y} - \dfrac{v_0}{r} \end{Bmatrix}, \quad \boldsymbol{\varepsilon}_p^{NL} = \begin{Bmatrix} \dfrac{1}{2}\left(\dfrac{\partial w_0}{\partial x}\right)^2 \\ \dfrac{1}{2}\left(\dfrac{\partial w_0}{\partial y} - \dfrac{v_0}{r}\right)^2 \\ \dfrac{\partial w_0}{\partial x}\left(\dfrac{\partial w_0}{\partial y} - \dfrac{v_0}{r}\right) \end{Bmatrix},$$

are respectively the linear membrane, bending, transverse shear, and nonlinear membrane strain vectors, with r the radius of curvature of the oval cylindrical shell, expressed as

$$r = \frac{r_0}{1 + \zeta \cos(2y/r_0)}. \tag{4}$$

The membrane stress resultant $\tilde{\boldsymbol{N}} = \{N_{xx} \;\; N_{yy} \;\; N_{xy}\}^T$, moment resultant $\tilde{\boldsymbol{M}} = \{M_{xx} \;\; M_{yy} \;\; M_{xy}\}^T$ and transverse shear stress resultant $\tilde{Q} = \{Q_{xz} \;\; Q_{yz}\}^T$ vectors are related to the membrane $\boldsymbol{\varepsilon}_p = \boldsymbol{\varepsilon}_p^L + \boldsymbol{\varepsilon}_p^{NL}$, bending $\boldsymbol{\varepsilon}_b$ and transverse shear $\boldsymbol{\varepsilon}_s$ strain vectors through the constitutive relation as

$$\begin{Bmatrix} \tilde{\boldsymbol{N}} \\ \tilde{\boldsymbol{M}} \end{Bmatrix} = \begin{bmatrix} \boldsymbol{A} & \boldsymbol{B} \\ \boldsymbol{B} & \boldsymbol{D} \end{bmatrix} \begin{Bmatrix} \boldsymbol{\varepsilon}_p \\ \boldsymbol{\varepsilon}_b \end{Bmatrix}, \qquad \tilde{\boldsymbol{Q}} = \boldsymbol{E}\boldsymbol{\varepsilon}_s, \tag{5}$$

where $B_{ij} = 0$ and the nonzero elements of A_{ij}, $D_{ij}(i, j = 1, 2, 6)$ and $E_{ij}(i, j = 4, 5)$ for an isotropic shell are:

$$A_{11} = A_{22} = \frac{Eh}{1 - \nu^2}, \quad A_{21} = A_{12} = \frac{\nu Eh}{1 - \nu^2}, \quad A_{66} = \frac{Eh}{2(1 + \nu)},$$
$$D_{11} = D_{22} = \frac{Eh^3}{12(1 - \nu^2)}, \quad D_{21} = D_{12} = \frac{\nu Eh^3}{12(1 - \nu^2)}, \quad D_{66} = \frac{Eh^3}{24(1 + \nu)},$$
$$E_{44} = E_{55} = \frac{Eh}{2(1 + \nu)}$$

The potential energy functional U is given by

$$U = \frac{1}{2}\left[\int_A \boldsymbol{\varepsilon}_p^T \boldsymbol{A}\boldsymbol{\varepsilon}_p + \boldsymbol{\varepsilon}_p^T \boldsymbol{B}\boldsymbol{\varepsilon}_b + \boldsymbol{\varepsilon}_b^T \boldsymbol{B}\boldsymbol{\varepsilon}_p + \boldsymbol{\varepsilon}_b^T \boldsymbol{D}\boldsymbol{\varepsilon}_b + \boldsymbol{\varepsilon}_s^T \boldsymbol{E}\boldsymbol{\varepsilon}_s\right] \mathrm{d}A - w_0(L/2, y^*, t)F \tag{6}$$

Based on the approach of [Rajasekaran and Murray 1973], this can be expressed as

$$U(\boldsymbol{\delta}) = \boldsymbol{\delta}^T\big(\tfrac{1}{2}\boldsymbol{K} + \tfrac{1}{6}\boldsymbol{K}_1(\boldsymbol{\delta}) + \tfrac{1}{12}\boldsymbol{K}_2(\boldsymbol{\delta})\big)\boldsymbol{\delta} - \boldsymbol{\delta}^T\boldsymbol{F}. \tag{7}$$

The kinetic energy of the shell is given by

$$\tilde{T}(\boldsymbol{\delta}) = \frac{1}{2}\int_A \big(\gamma(\dot{u}_0^2 + \dot{v}_0^2 + \dot{w}_0^2) + I(\dot{\theta}_x^2 + \dot{\theta}_y^2)\big)\,\mathrm{d}A \tag{8}$$

where $\gamma = \rho h$ and $I = \rho h^3/12$. The dot over the variables denotes derivative with respect to time.

Substituting (7) and (8) in the Lagrange's equation of motion and considering dissipative forces, the governing equation of the shell is written as

$$\boldsymbol{M}\ddot{\boldsymbol{\delta}} + (\alpha\boldsymbol{M} + \beta\boldsymbol{K})\dot{\boldsymbol{\delta}} + \big(\boldsymbol{K} + \tfrac{1}{2}\boldsymbol{K}_1(\boldsymbol{\delta}) + \tfrac{1}{3}\boldsymbol{K}_2(\boldsymbol{\delta})\big)\boldsymbol{\delta} = \boldsymbol{F}. \tag{9}$$

3. Element description

The field variables in the circumferential direction (y) are approximated using a C^0 continuous three-noded quadratic element and are expressed in terms of their nodal values as

$$(u_0^i, v_0^i, w_0^i, \theta_x^i, \theta_y^i) = \sum_{k=1}^{3} \bar{N}_k^0 (u_{0k}^i, v_{0k}^i, w_{0k}^i, \theta_{xk}^i, \theta_{yk}^i), \tag{10}$$

where $\bar{N}_1^0 = (\xi^2 - \xi)/2$, $\bar{N}_2^0 = (1 - \xi^2)$, $\bar{N}_3^0 = (\xi^2 + \xi)/2$; here ξ is the local natural circumferential coordinate of the element and the $\bar{N}_k^0$ are the original shape functions.

In order to avoid membrane and shear locking, the field redistributed substitute shape functions are used to interpolate the constrained strain fields. These substitute shape functions, obtained using the method of least squares, are

$$\bar{N}_1^1 = \tfrac{1}{2}\big(\tfrac{1}{3} - \xi\big), \quad \bar{N}_2^1 = \tfrac{2}{3}, \quad \bar{N}_3^1 = \tfrac{1}{2}\big(\tfrac{1}{3} + \xi\big), \tag{11}$$

where the $\bar{N}_i^1$ are consistent with $d\bar{N}_i^0/d\xi$.

Using smoothed interpolation functions, the constrained membrane and transverse shear strain components are expressed as

$$\begin{aligned}
\frac{\partial v_0}{\partial y} + \frac{w_0}{r} &= \sum_{i=1}^{M}\sum_{k=1}^{3}\left(\frac{\partial \bar{N}_k^0}{\partial y} V_i(x) v_{0k}^i + \bar{N}_k^1 W_i(x)\frac{w_{0k}^i}{r}\right),\\
\frac{\partial u_0}{\partial y} + \frac{\partial v_0}{\partial x} &= \sum_{i=1}^{M}\sum_{k=1}^{3}\left(\frac{\partial \bar{N}_k^0}{\partial y} U_i(x) u_{0k}^i + \bar{N}_k^1 \frac{\partial V_i}{\partial x} v_{0k}^i\right),\\
\theta_y + \frac{\partial w_0}{\partial y} - \frac{v_0}{r} &= \sum_{i=1}^{M}\sum_{k=1}^{3}\left(\bar{N}_k^1 \Theta_{yi}(x)\theta_{yk}^i + \frac{\partial \bar{N}_k^0}{\partial y} W_i(x) w_{0k}^i - \bar{N}_k^1 V_i(x)\frac{v_{0k}^i}{r}\right).
\end{aligned} \tag{12}$$

The other strain components are expressed in terms of the original shape functions ($\bar{N}_i^0$) and their derivatives. The element behaves very well for both thick and thin situations. It has good convergence characteristics and has no spurious rigid body modes [Babu and Prathap 1986].

Integration with respect to the meridional coordinate x is carried out explicitly using Mathematica 5.1. Based on the convergence study for the evaluation of various energy terms, a five-point Gauss-quadrature numerical integration scheme is used with respect to the circumferential coordinate y. Since the element is derived from the field consistency approach, exact integration is performed to evaluate all the energy terms.

4. Solution method

We briefly describe the method used to find periodic solutions to (9). The $2N$-component state vector $\{\boldsymbol{\delta}(t)\ \dot{\boldsymbol{\delta}}(t)\}^T$ evolves according to (9) from an initial state to be determined. The condition that a solution is periodic with period T is expressed by the equation

$$\begin{Bmatrix} \boldsymbol{\delta}(T) \\ \dot{\boldsymbol{\delta}}(T) \end{Bmatrix} = \begin{Bmatrix} \boldsymbol{\delta}(0) \\ \dot{\boldsymbol{\delta}}(0) \end{Bmatrix} \overset{\text{def}}{=} \boldsymbol{\eta}. \tag{13}$$

To find such solutions we use the shooting method. This involves taking a guess for the initial state, integrating the differential equation to the target time T, and then playing with the initial state so as to enforce the periodicity condition (13). To integrate (9) we use Newmark's direct time integration scheme. To find a satisfactory initial state we use the Newton–Raphson method.

To elaborate, we rewrite (13) stressing the dependence of $\boldsymbol{\delta}$ on the initial state vector, and also on the frequency of the forcing term $\boldsymbol{F}$:

$$\begin{Bmatrix} \boldsymbol{\delta}(T, \boldsymbol{\eta}, \omega_F) \\ \dot{\boldsymbol{\delta}}(T, \boldsymbol{\eta}, \omega_F) \end{Bmatrix} - \boldsymbol{\eta} = \boldsymbol{0}. \tag{14}$$

Given a first guess $\boldsymbol{\eta}_0$ for the initial state vector $\boldsymbol{\eta}$, Newton–Raphson tells us to solve the linear system

$$\begin{bmatrix} \left.\dfrac{\partial \boldsymbol{\delta}(T, \boldsymbol{\eta}, \omega_F)}{\partial \boldsymbol{\eta}}\right|_{\boldsymbol{\eta}=\boldsymbol{\eta}_0} \\ \left.\dfrac{\partial \dot{\boldsymbol{\delta}}(T, \boldsymbol{\eta}, \omega_F)}{\partial \boldsymbol{\eta}}\right|_{\boldsymbol{\eta}=\boldsymbol{\eta}_0} \end{bmatrix} - \boldsymbol{I} \Bigg] \Delta\boldsymbol{\eta}_0 = \boldsymbol{\eta}_0 - \begin{Bmatrix} \boldsymbol{\delta}(T, \boldsymbol{\eta}_0, \omega_F) \\ \dot{\boldsymbol{\delta}}(T, \boldsymbol{\eta}_0, \omega_F) \end{Bmatrix} \tag{15}$$

to find the correction $\Delta\boldsymbol{\eta}_0$ to the initial guess. We then repeat the process with $\eta_0 + \Delta\boldsymbol{\eta}_0$ in place of $\boldsymbol{\eta}_0$, and so on, until the equality (14) is satisfied within the desired tolerance limit, which we set at 0.001%. In (15), $\boldsymbol{I}$ is the $2N \times 2N$ identity matrix and the derivatives $\partial\boldsymbol{\delta}/\partial\boldsymbol{\eta}$ and $\partial\dot{\boldsymbol{\delta}}/\partial\boldsymbol{\eta}$ are $N \times 2N$ matrices. These derivatives are obtained for $t = T$ by applying Newmark's direct time integration scheme to the differential equation

$$\boldsymbol{M}\left(\frac{\partial \boldsymbol{\delta}}{\partial \boldsymbol{\eta}}\right)^{\cdot\cdot} + (\alpha\boldsymbol{M} + \beta\boldsymbol{K})\left(\frac{\partial \boldsymbol{\delta}}{\partial \boldsymbol{\eta}}\right)^{\cdot} + \big(\boldsymbol{K} + \boldsymbol{K}_1(\boldsymbol{\delta}) + \boldsymbol{K}_2(\boldsymbol{\delta})\big)\frac{\partial \boldsymbol{\delta}}{\partial \boldsymbol{\eta}} = \boldsymbol{0}, \tag{16}$$

which is simply the first variation of (9) with respect to $\boldsymbol{\eta}$ (recall that $K_1(\boldsymbol{\delta})$ is linear in $\boldsymbol{\delta}$ and $K_2(\boldsymbol{\delta})$ is quadratic). The initial condition for (16), following from the definition of $\boldsymbol{\eta}$ in (13), is

$$\begin{bmatrix} \partial\boldsymbol{\delta}/\partial\boldsymbol{\eta} \\ \partial\dot{\boldsymbol{\delta}}/\partial\boldsymbol{\eta} \end{bmatrix}_{t=0} = \boldsymbol{I}. \tag{17}$$

We also calculate the eigenvalues of the monodromy matrix $\begin{bmatrix} \partial\boldsymbol{\delta}/\partial\boldsymbol{\eta} \\ \partial\dot{\boldsymbol{\delta}}/\partial\boldsymbol{\eta} \end{bmatrix}$ using the QR algorithm, in order to study the stability of the periodic response.

We further desire T to be the minimal period. We take T as $2\pi/\omega_F$ for systems with harmonic excitation with angular frequency ω_F, for a response with fundamental and higher harmonics. To obtain the branches of the periodic response curve with subharmonic participation, the response time period T is taken as an integer multiple of fundamental period. For autonomous systems, T is treated as an unknown and an additional equation such as a phase condition/amplitude is required.

For obtaining the complete frequency response, the analysis is carried out in two phases: first, starting far away from resonance, the forcing frequency is incremented and the periodic solutions are obtained; then, when bifurcation points are encountered, the solution is continued via the arc length continuation method. For the second phase, the forcing frequency is treated as an unknown and an incremental arc length is specified.

5. Results and discussion

Validation of the present approach is carried out considering a movable simply supported ($v_0 = w_0 = \theta_y = 0$ at $x = 0, L$) circular cylindrical shell studied by [Amabili 2003]. Dimensions and material properties are: $L = 0.2\,\text{m}$, $r_0 = 0.1\,\text{m}$, $\zeta = 0.0$, $h = 0.247\,\text{mm}$, $E = 71.02\,\text{GPa}$, $\rho = 2796\,\text{kg/m}^3$, $\nu = 0.31$. Rayleigh proportional damping parameters α and β are determined such that damping factors $\xi_{1,6} = 0.0005$ (corresponding to asymmetric mode with $n = 6$) and $\xi_{1,0} = 0$ (corresponding to axisymmetric mode). The shell is subjected to a point harmonic force at midlength ($x = L/2$, $y^* = 0$): $F = F_0 \cos(\omega_F t)$, where $F_0 = 0.0785\,\text{N}$. The first four natural frequencies (ω_{mn}) of the shell corresponding to modes with axial half wave number $m = 1$ and number of circumferential waves $n = 7, 8, 9$ and 6 are found to be 484.38, 489.85, 546.11 and 553.33 Hz, respectively. The forcing frequency (ω_F) is varied in the neighbourhood of the mode with $(m, n) = (1, 6)$ ($\omega_{mn} = 553.33\,\text{Hz}$). In the approximate solution [Amabili 2003] for transverse displacement w_0, axisymmetric and asymmetric modes with kn ($k = 1, 2$; $n = 6$ for this case) circumferential waves were considered. The present results are obtained using a half-wave model of the shell along the circumference, with symmetry conditions at $y = 0, \pi r_0/n$, and the full model. In the half wave model, the participation of axisymmetric and asymmetric modes with kn circumferential waves can

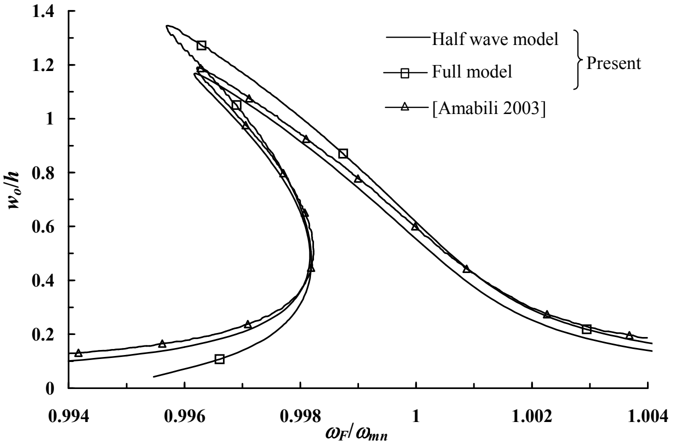

Figure 2. Comparison of steady state response for movable simply supported circular cylindrical shell.

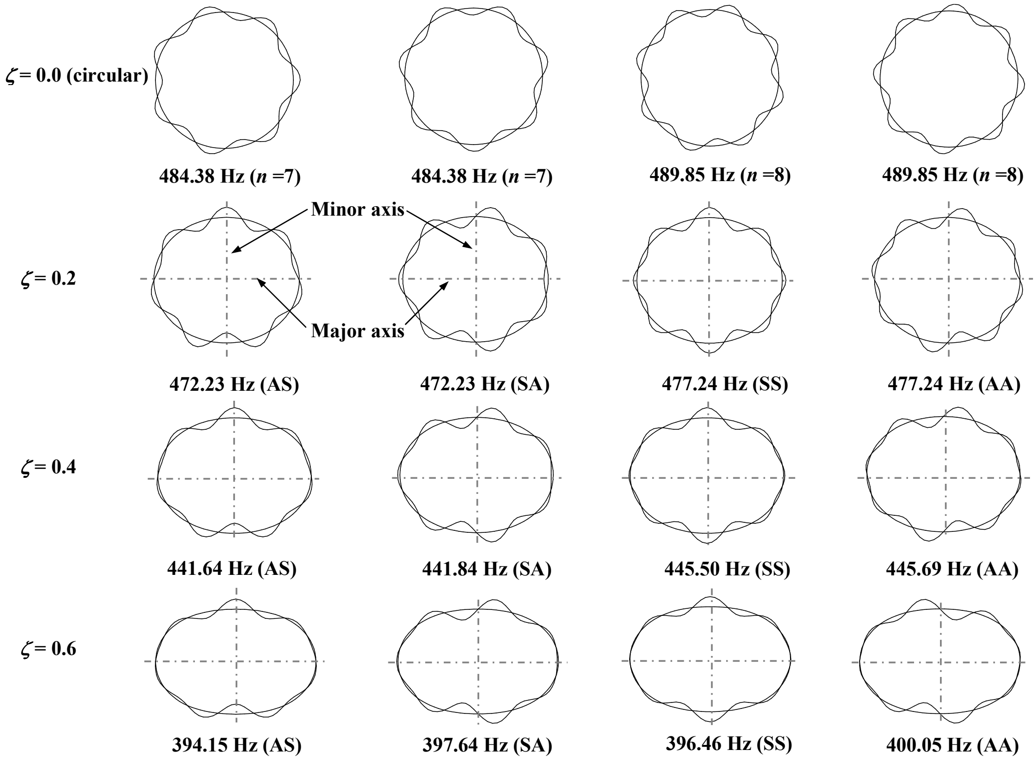

Figure 3. First four free vibration modes and corresponding frequencies of oval cylindrical shells.

be simulated. In the full model, the complete circumferential length of the shell is modelled and it can simulate the participation of all modes with appropriate discretization. The comparison of the results is given in Figure 2. The present results based on the half-wave model are found to be in good agreement with those of [Amabili 2003]. Those based on the full model are slightly different due to the additional participation of the mode with $n = 9$, which is excluded by Amabili and in the present half-wave model.

Next, a detailed study is carried out for different values of the ovality parameter, keeping the other shell parameters the same as in the validation example. The damping parameter α is taken as zero and β is determined such that $\xi_{1,n} = 0.004$. The shell is subjected to a discrete harmonic force ($F = F_0 \cos \omega_F t$) at $y^* = C/4$ for symmetric excitation about the minor axis and at $y^* = 3C/16$, $C/8$, $C/16$ for nonsymmetric excitation. The forcing frequency ω_F is varied in the neighbourhood of linear free vibration frequencies corresponding to first SS, SA, AS, AA modes (S = symmetric, A = antisymmetric; major axis symmetry listed first). The free vibration modes and corresponding frequencies of oval cylindrical shells considered in the present study are given in Figure 3. Note that the asymmetric free vibration modes of circular ($\zeta = 0$) cylindrical shells are not spatially fixed due to axisymmetric geometry and there are two modes corresponding to each frequency. Noncircular shells with doubly symmetric cross-section have spatially fixed free vibration modes.

The modal participation factors $\eta_j(t)$ are obtained from $w(x, y, t) = \sum_{j=1}^{\infty} \eta_j(t)\phi_j(x, y)$; where $\phi_j(x, y)$ is the j-th free vibration mode of the oval cylindrical shell. The total response at any location can be expressed as a Fourier series: $w(x, y, t) = A_0 + \sum_{i=1}^{\infty} A_i \cos(\omega_i t + \psi_i)$, where A_i is the harmonic amplitude, ω_i is a multiple of forcing frequency ω_F, and ψ_i is the phase difference.

A convergence study reveals that $\Delta t = \pi/(100\omega_F)$, $M = 3$, and 48-element discretization in the circumferential direction (total number of degrees of freedom, $N = 960$), are sufficient to yield results of the desired accuracy.

For symmetric loading of circular and oval shells, the travelling wave direction will depend upon the initial conditions. The solutions in the present work are obtained using the shooting technique with initial state vector as the solution of previous frequency step. This has resulted in the traveling wave directions indicated.

The stable regions of loading point response (w_0/h) versus forcing frequency (ω_F/ω_{mn}) characteristics are shown by continuous curves and unstable ones are shown by dashed curves. The bifurcation points marked in the response curves are identified as period doubling (PD) if at least one eigenvalue of the monodromy matrix crosses the unit circle along the negative real axis, as symmetry breaking (SB) / turning point (TP) if it leaves the unit circle along the positive real axis, and as secondary Hopf (SH) bifurcation if a pair of complex conjugate eigenvalues crosses the unit circle.

5.1. ***Response of symmetrically excited cylindrical shells (load at y* = C/4).*** The frequency response curves of movable simply supported oval cylindrical shells ($F_0 = 0.4$ N, $y^* = C/4$) are shown in Figure 4 for different ovality parameters ($\zeta = 0.0$, 0.2, 0.4 and 0.6). We see that with the increase in the ovality parameter, the nonlinear dynamic response changes significantly due to increased modal interactions and the frequency range corresponding to greater response amplitudes increases. For circular shells ($\zeta = 0.0$), no unstable regions are observed, whereas response of noncircular shells reveals the presence of bifurcation points and unstable regions. The forcing frequency parameter ω_F/ω_{mn} corresponding to

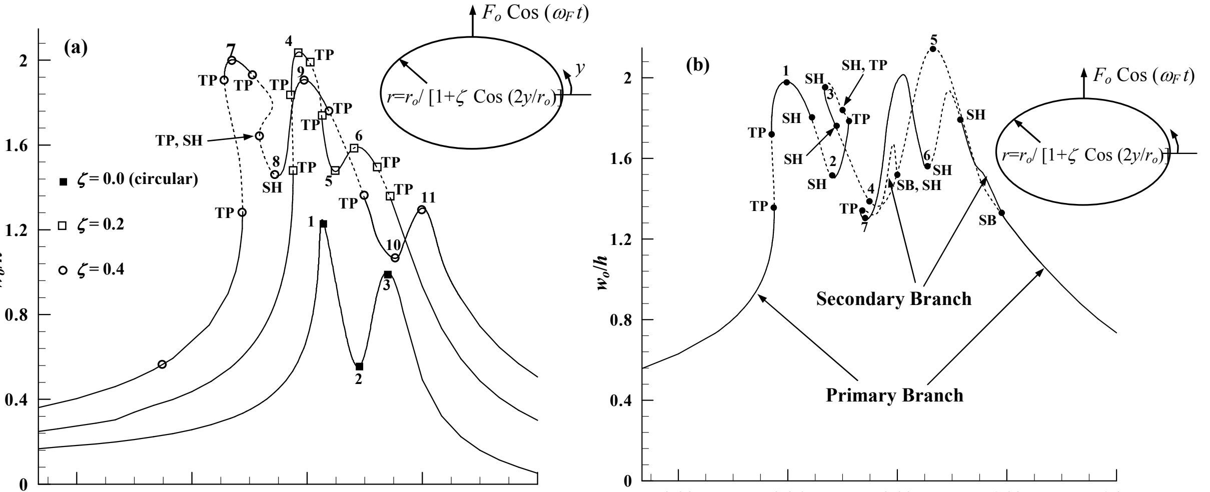

Figure 4. Nonlinear steady state response amplitude versus forcing frequency curves for movable simply supported cylindrical shells subjected to excitation in the neighbourhood of first mode: (a) $\zeta = 0.0$ (circular, $\omega_{mn} = 484.38$ Hz), $\zeta = 0.2$ ($\omega_{mn} = 472.23$ Hz), and $\zeta = 0.4$ ($\omega_{mn} = 441.64$ Hz); (b) $\zeta = 0.6$ ($\omega_{mn} = 394.15$ Hz).

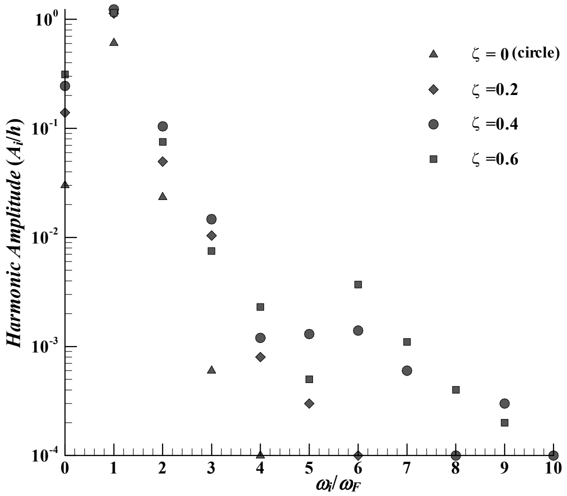

Figure 5. Frequency spectra of oval cylindrical shells with different ovality parameters corresponding to the first peaks of response curves (Figure 4).

first peak response decreases as the ovality parameter increases. The frequency response spectra plotted in Figure 5 corresponding to first peaks of the response curves (Figure 4) reveal that with an increase in the ovality parameter, the number of significant higher harmonics present in the response increases. In particular, the number of higher harmonics is three for $\zeta = 0.0$, five for $\zeta = 0.2$, and up to nine harmonics for $\zeta = 0.4, 0.6$.

The modal participation factors of the first four predominant modes are shown in Figure 6, corresponding to the points marked in Figure 4 for $\zeta = 0.0$. It can be noted from Figure 6 that the participation of the

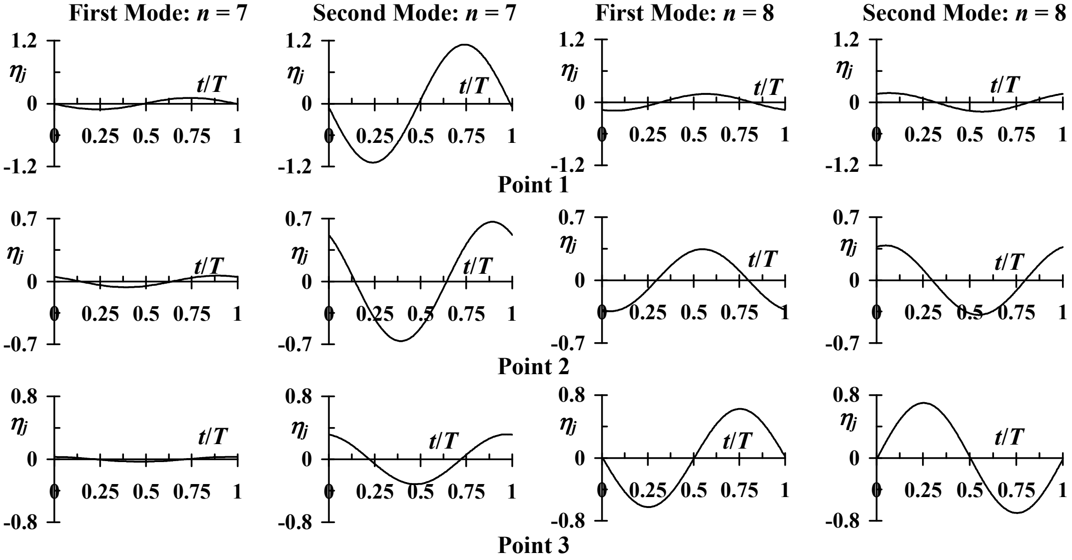

Figure 6. Modal participation factors of the first four modes corresponding to typical points marked (Figure 4a) on the response curves of circular shells ($\zeta = 0.0$).

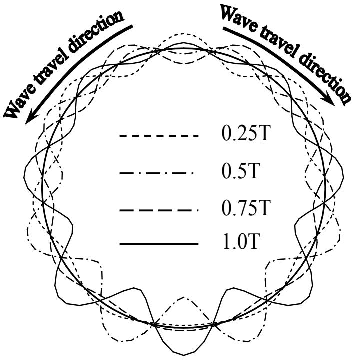

Figure 7. Transverse displacement variations along the circumference at different time instants of one cycle corresponding to point 2 (Figure 4a) on the response curve of circular cylindrical shell ($\zeta = 0.0$).

mode with $n = 7$ is predominant at the first response peak ($w_0/h = 1.24$, $\omega_F/\omega_{mn} = 0.994$) and decreases as the forcing frequency increases further. The participation of the mode with $n = 8$ increases with the forcing frequency and is predominant at point 3 ($w_0/h = 1.00$, $\omega_F/\omega_{mn} = 1.011$). These two modes ($n = 7$ and 8), whose linear free vibration frequencies are very close, are excited due to the concentrated harmonic excitation force.

The deformed shape of the shell cross-section at $x = L/2$ at different moments of one cycle corresponding to point 2 ($w_0/h = 0.55$, $\omega_F/\omega_{mn} = 1.003$) is plotted in Figure 7, revealing waves travelling in two opposite directions from the loading point. This phenomenon is observed for the narrow frequency range between points 1 and 3 due to the participation of modes with $n = 7$ and 8.

A detailed analysis of the modal participation factors for oval shells reveals that only AS and SS modes participate in the response corresponding to the primary branch of symmetrically excited shells

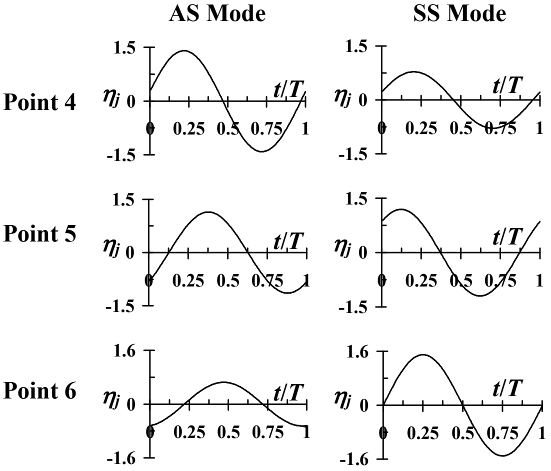

Figure 8. Modal participation factors of the first AS and SS modes for typical points marked (Figure 4a) on the response curve of oval cylindrical shell ($\zeta = 0.2$).

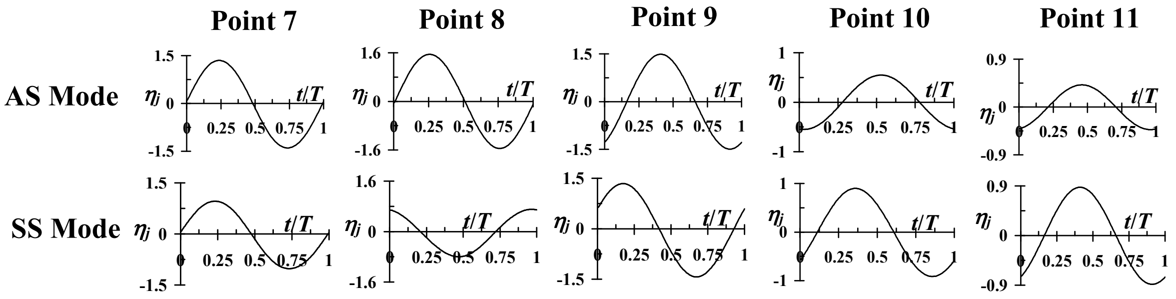

Figure 9. Modal participation factors of the first AS and SS modes corresponding to typical points marked on the response curve of oval cylindrical shell ($\zeta = 0.4$, Figure 4a).

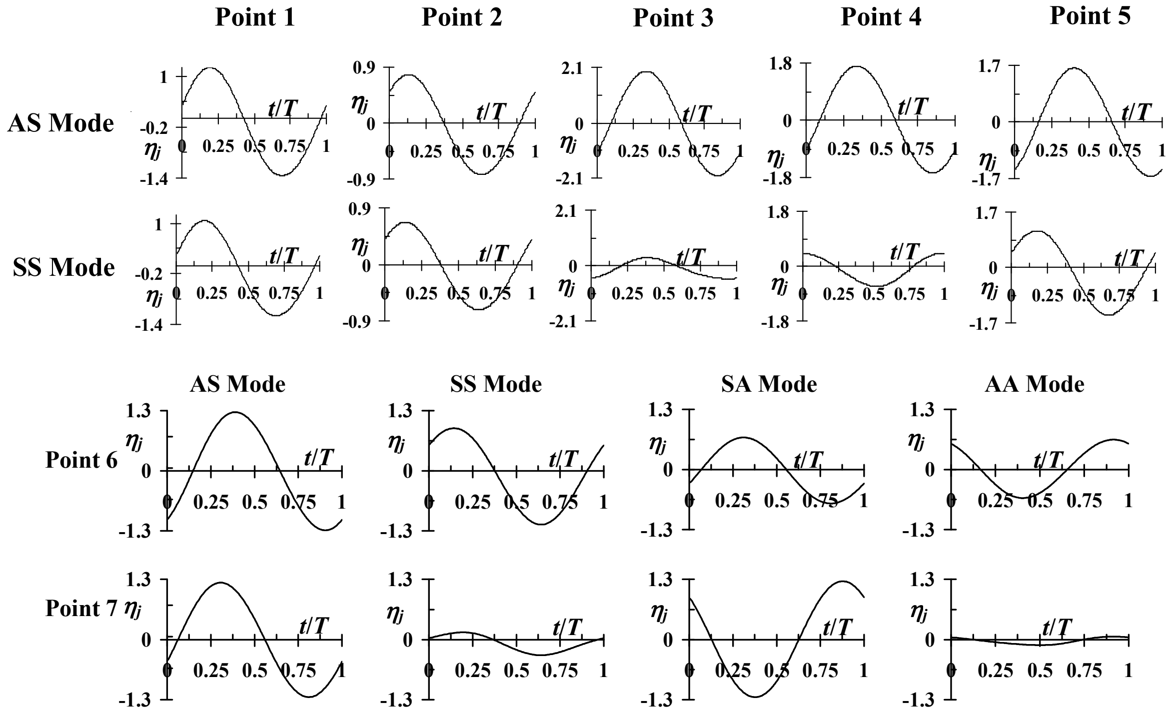

Figure 10. Modal participation factors of the first four modes corresponding to typical points marked on the response curve of oval cylindrical shell ($\zeta = 0.6$, Figure 4b).

($y^* = C/4$). The modal participation of the first AS and SS modes is shown in Figure 8 and 9 for oval shells with $\zeta = 0.2$ and 0.4, respectively, corresponding to the points marked in Figure 4. It can be seen from Figure 8 that at the first peak (point 4: $w_0/h = 2.04$, $\omega_F/\omega_{mn} = 0.988$) for $\zeta = 0.2$, the participation of the first AS mode is significantly greater than that of the first SS mode, whereas at the second peak (point 6: $w_0/h = 1.59$, $\omega_F/\omega_{mn} = 1.004$) the opposite trend is observed. At point 5 ($w_0/h = 1.48$, $\omega_F/\omega_{mn} = 0.997$), the participation of both the modes is of comparable amplitude. It can be seen from Figure 9 for $\zeta = 0.4$ that the participation of AS and SS modes at the first (point 7: $w_0/h = 2.00$,

$\omega_F/\omega_{mn} = 0.971$) and last (point 11: $w_0/h = 1.30$, $\omega_F/\omega_{mn} = 1.020$) peaks is qualitatively similar to that for $\zeta = 0.2$. At point 9 ($w_0/h = 1.91$, $\omega_F/\omega_{mn} = 0.989$), the participation of both the modes is comparable. The participation of AS mode is dominant at point 8 ($w_0/h = 1.45$, $\omega_F/\omega_{mn} = 0.982$) and that of SS mode at point 10 ($w_0/h = 1.07$, $\omega_F/\omega_{mn} = 1.013$). In general, it can be concluded that the relative participation of AS mode decreases and that of SS mode increases with the increase in the forcing frequency.

The steady state response amplitude versus forcing frequency curve plotted in Figure 4b for the shell with $\zeta = 0.6$ shows that different response peaks appear at almost equal response amplitudes unlike for $\zeta = 0.4$. The modal participation of the first AS and SS modes is shown in Figure 10 corresponding to the points marked in Figure 4b. It is seen from Figure 10 that at the first peak (point 1: $w_0/h = 1.98$, $\omega_F/\omega_{mn} = 0.960$), the contribution of both AS and SS modes is comparable. From point 1 to 2 (point 2: $w_0/h = 1.50$, $\omega_F/\omega_{mn} = 0.972$), the response amplitude decreases but the relative participation of the AS and SS modes remains the same. From point 2 to 3 (point 3: $w_0/h = 1.97$, $\omega_F/\omega_{mn} = 0.971$), the participation of AS mode increases significantly. The relative participation of the SS mode is very less from point 3 to 4 (point 4: $w_0/h = 1.36$, $\omega_F/\omega_{mn} = 0.985$). After point 4, the response amplitude increases and the curve loses stability through a symmetry breaking bifurcation and the main branch forms peak at point 5 ($w_0/h = 2.15$, $\omega_F/\omega_{mn} = 1.0$), where the contribution of both AS and SS modes is dominant.

The secondary branch emanating from the primary one at the symmetry breaking bifurcation corresponds to a significant participation of the SA and AA modes in addition to the AS and SS modes, as evident from the modal participation factors corresponding to points 6 ($w_0/h = 1.56$, $\omega_F/\omega_{mn} = 0.998$) and 7 ($w_0/h = 1.29$, $\omega_F/\omega_{mn} = 0.981$) shown in Figure 10. This is due to 1:1 internal resonance between AS/SS and SA/AA modes: the ratios of their linear free vibration frequencies are almost equal to one. The multiple peaks depicted in the secondary branch are due to increases/decreases in the relative participation of AS, SA, SS and AA modes. The deformed shape of the shell cross-section at $x = L/2$ at different moments in one cycle corresponding to the point 7 is plotted in Figure 11, showing waves travelling in one direction only.

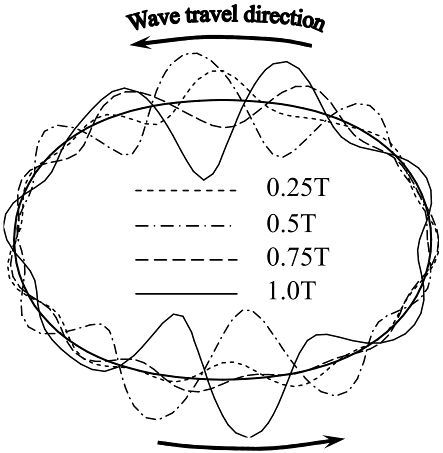

Figure 11. Transverse displacement variations along the circumference at different time instants of one cycle corresponding to point 7 (Figure 4b) on the response curve of oval shell ($\zeta = 0.6$).

To demonstrate the participation of all the modes corresponding to first peak for $\zeta = 0.6$ (point 1 marked in Figure 4b), the modal displacement variations along the circumference and corresponding modal participation factors with time are shown in Figures 12 and 13. It can be seen from Figure 13 that

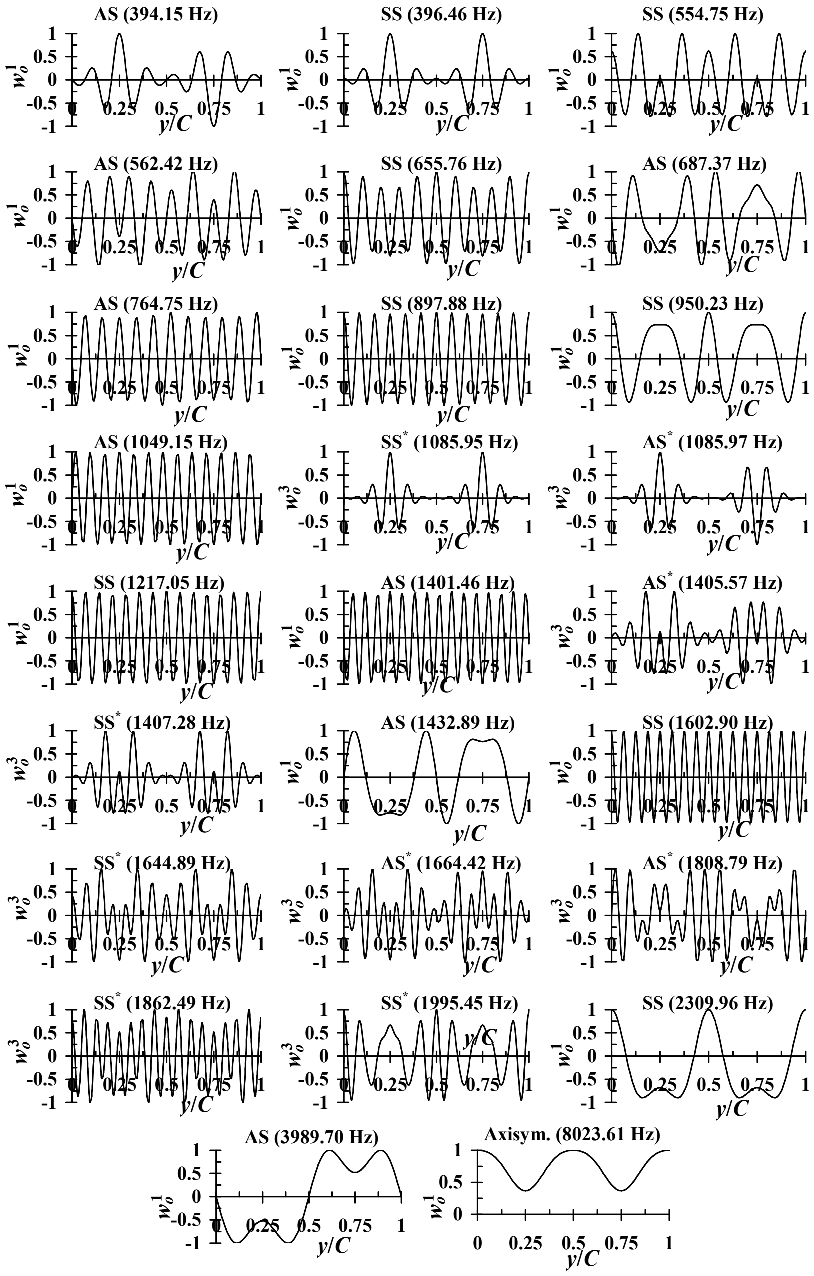

Figure 12. Modal displacement variation along the circumference of the modes participating in the response corresponding to point 1 (Figure 4b) on the response curve of oval cylindrical shell ($\zeta = 0.6$).

in addition to the first AS and SS modes, the other modes participate in the response with fundamental and higher harmonics. Further, due to the harmonic excitation at $(x, y^*) = (L/2, C/4)$, only AS/SS modes, not AA/SA modes, participate in the response corresponding to the primary branch.

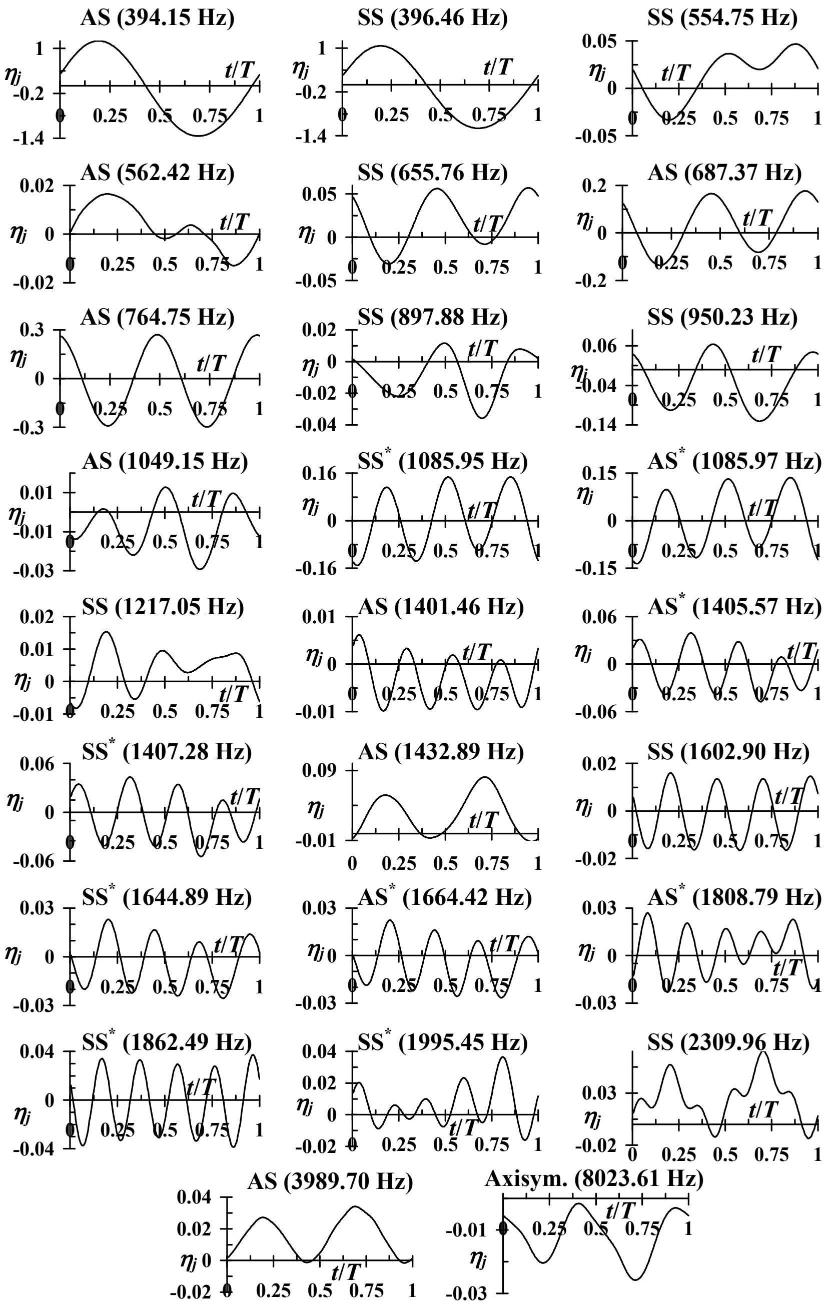

Figure 13. Modal participation factors in the response corresponding to point 1 marked (Figure 4b) on the response curve of oval cylindrical shell ($\zeta = 0.6$).

5.2. ***Response of nonsymmetrically excited cylindrical shells.*** The frequency response characteristics of oval shells are investigated by varying the location of the concentrated harmonic excitation force along the circumference. The steady state response amplitude of the loading location versus forcing frequency curves are shown in Figure 14 for oval cylindrical shells with $\zeta = 0.2$ subjected to a concentrated harmonic loading at $y^* = C/4$, $3C/16$, $C/8$ and $C/16$ with the forcing frequency in the neighbourhood of the first AS, SS, SA, and AA modes. The maximum response for the loading locations $y^* = 3C/16$, $C/8$ and $C/16$ is smaller than that corresponding to the loading at the minor axis ($y^* = C/4$). The modal participation factors of the first four participating modes corresponding to the typical points, marked in Figure 14 on the nonlinear steady state response amplitude versus forcing frequency curves, are shown in Figure 15.

In the response of nonsymmetrically excited oval shells, all types of modes (AS, SS, SA, AA) participate, unlike the primary branch of symmetrically excited shells. The frequency response curve for the shell with $\zeta = 0.2$ (load at $y^* = 3C/16$) shows an unstable region between turning points and a maximum response amplitude of $w_0/h = 1.72$ at $\omega_F/\omega_{mn} = 0.989$ (point 1). The modal participation factors obtained at the peak reveal that the contribution of the AS mode is around 70% of the total response amplitude. The contributions of the SA, SS and AA modes are around 64%, 40% and 40% of the AS mode contribution, respectively. It is also seen that the AS, SS and AA modes are almost in same phase, whereas the SA mode participates with opposite phase. With a further increase in the forcing frequency, the response amplitude decreases, as does the participation of the AS, SS and AA modes. However, the participation of the SA mode increases and at point 2 ($w_0/h = 1.41$, $\omega_F/\omega_{mn} = 0.994$) it becomes around 95% of the AS mode participation. Beyond point 2, another turning point bifurcation is encountered and at point 3 ($w_0/h = 1.40$, $\omega_F/\omega_{mn} = 0.994$), the contribution of AS mode is predominant. After point 3, the relative contribution of the SS mode increases and is maximum at point 4 ($w_0/h = 1.18$, $\omega_F/\omega_{mn} = 0.998$). At the local peak formed at point 5 ($w_0/h = 1.31$, $\omega_F/\omega_{mn} = 1.004$), the contribution

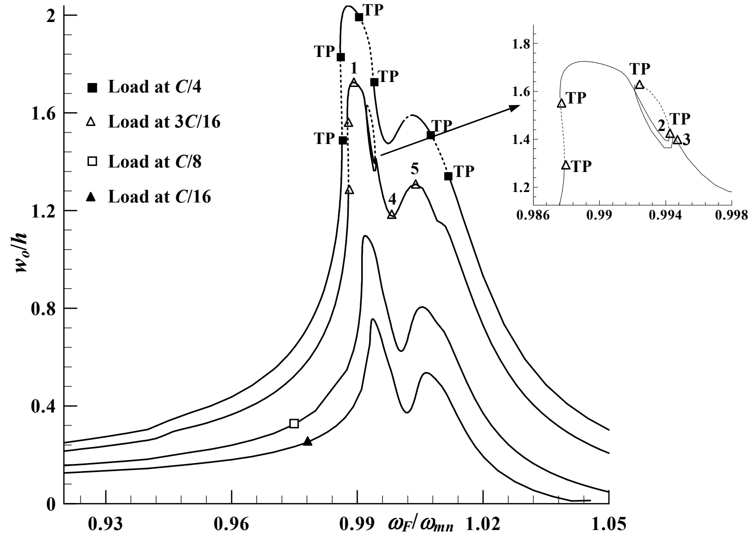

Figure 14. Nonlinear steady state response amplitude versus forcing frequency curves of movable simply supported oval shells subjected to excitation at different circumferential locations in the neighbourhood of the first mode ($\zeta = 0.2$: $\omega_{mn} = 472.23\,\text{Hz}$).

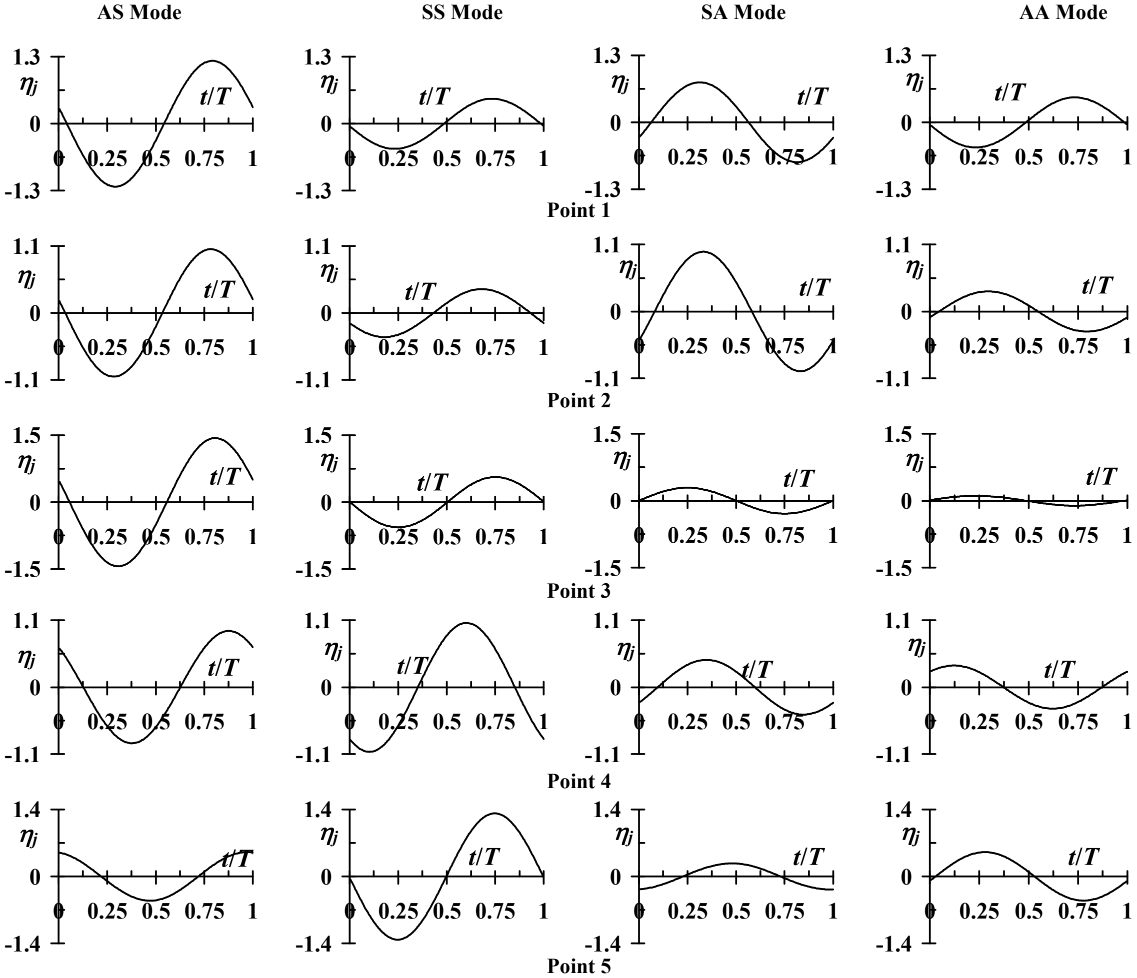

Figure 15. Modal participation factors of the first AS, SS, SA and AA modes corresponding to typical points marked (Figure 14) on the response curve of oval cylindrical shell ($\zeta = 0.2$).

of the SS mode is almost three times the AS mode participation. Further, with the shifting of the loading location towards the major axis, the response amplitude and number of peaks decrease.

The effect of the loading location on the nonlinear steady state response amplitude versus forcing frequency for the shell with $\zeta = 0.6$ is shown in Figure 16. Starting from a low frequency excitation ($\omega_F/\omega_{mn} = 0.925$), the response curve for the loading at $y^* = 3C/16$ loses its stability through a turning point and forms a peak in the unstable region at point 1 ($w_0/h = 1.18$, $\omega_F/\omega_{mn} = 0.979$). This region corresponds to the vibration of the shell predominantly in the AS mode, as seen from the modal participation factors plotted in Figure 17. The relative participations of the SA, SS and AA modes are around 35%, 35% and 15% of the AS mode, respectively.

After point 1, the response amplitude decreases and encounters a secondary Hopf bifurcation, then it increases, becomes stable and forms another peak at point 2 ($w_0/h = 1.43$, $\omega_F/\omega_{mn} = 0.991$). The

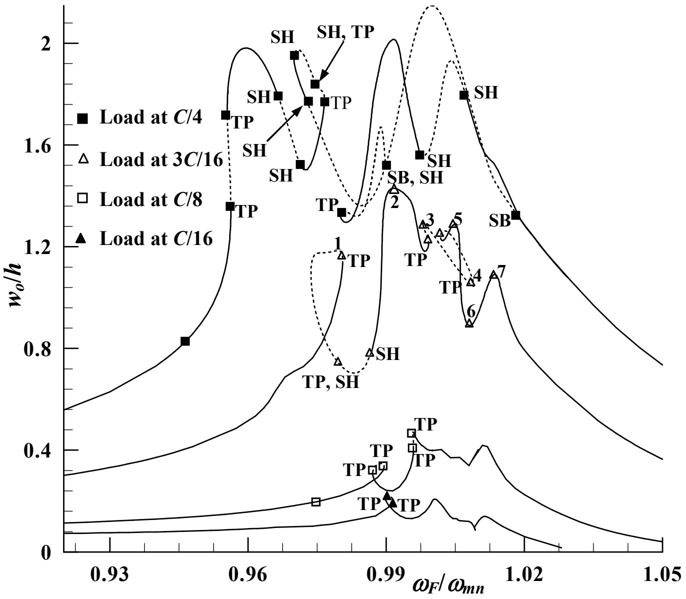

Figure 16. Nonlinear steady state response amplitude versus forcing frequency curves of movable simply supported oval shells subjected to excitation at different circumferential locations in the neighbourhood of the first mode ($\zeta = 0.6$: $\omega_{mn} = 394.15\,\text{Hz}$).

participation of the first AS, SA, SS and AA modes is significant at this point, with the AS mode having highest participation.

With a further increase in the forcing frequency after point 2, both the relative and the absolute participation of the AS mode decrease and at point 3 ($w_0/h = 1.29$, $\omega_F/\omega_{mn} = 0.998$), its contribution becomes even smaller than that of the SA and SS modes. The participation of the AS and AA modes is around 65% of the SA mode. In the narrow frequency range of $\omega_F/\omega_{mn} = 0.999$ to 1.009, both the absolute and the relative contribution of AA mode first increase and it reaches a peak at point 4 ($w_0/h = 1.05$, $\omega_F/\omega_{mn} = 1.009$), where the next significant mode is SS.

After point 4, the contribution of the AA mode decreases and that of the SS and SA modes increases significantly. At point 5 ($w_0/h = 1.29$, $\omega_F/\omega_{mn} = 1.006$), the relative contribution of the SA mode is greatest, with the participation of the SS, AS and AA modes around 86%, 38% and 30% of SA mode participation.

After point 5, the participation of the AS mode increases and forms a peak at point 6 ($w_0/h = 0.89$, $\omega_F/\omega_{mn} = 1.008$). Subsequently, its relative participation decreases and is least at point 7 ($w_0/h = 1.09$, $\omega_F/\omega_{mn} = 1.014$). From points 6 to 7, the absolute contribution of the SA and SS modes remain almost constant, whereas the contribution of the AA mode increases significantly.

The transverse displacement variations along the circumference at different time instants of one cycle of response corresponding to points 1 and 3 on the response curve are plotted in Figure 18. At point 1, a travelling wave with the significantly greater amplitudes in the upper half of the shell is predicted. At point 3, the travelling waves originating near major axis (y = 0) move in opposite directions in the top and bottom halves of the shell with greater amplitude near the minor axis.

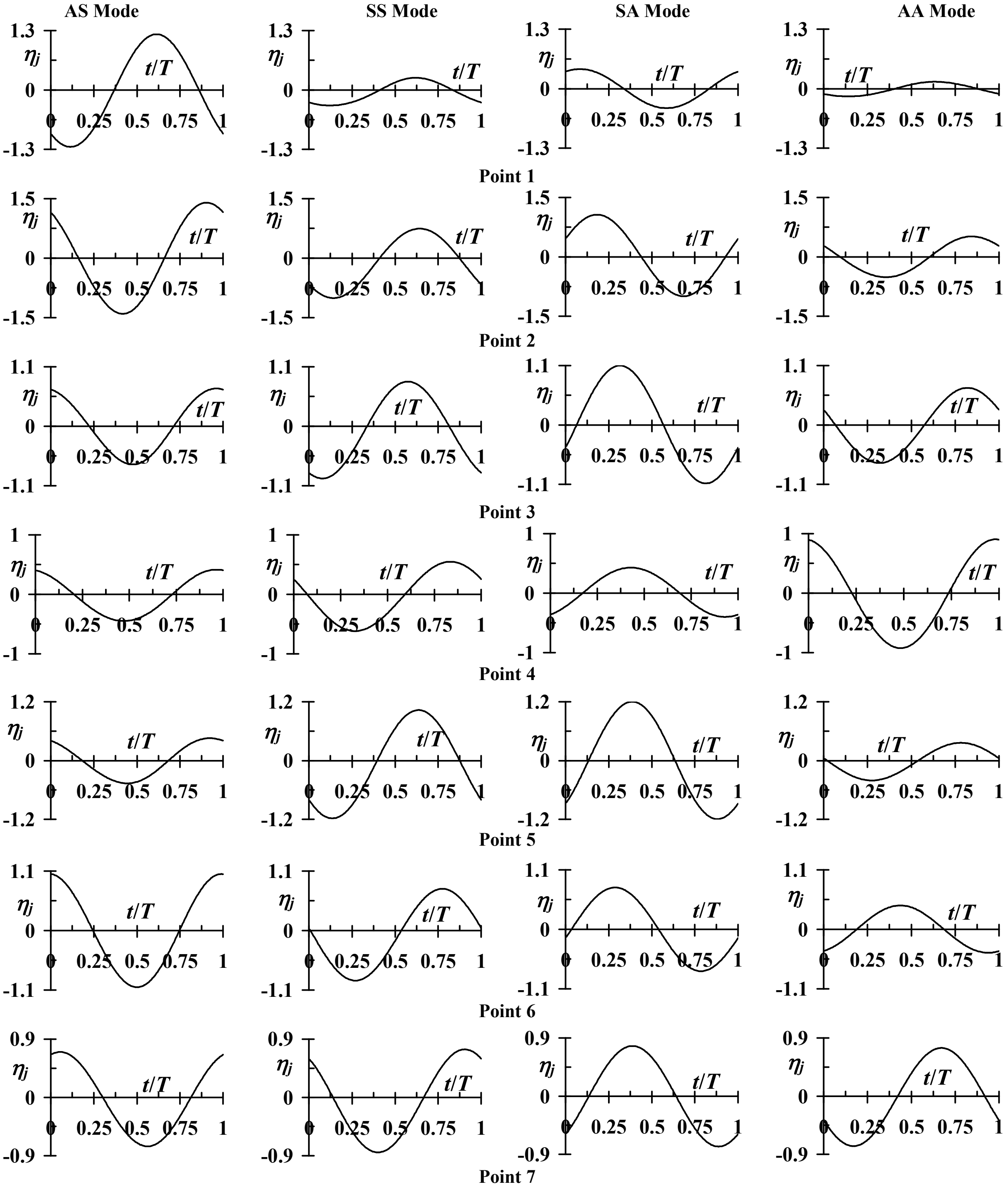

Figure 17. Modal participation factors of the first AS, SS, SA and AA modes corresponding to typical points marked (Figure 16) on the response curve of oval cylindrical shell ($\zeta = 0.6$).

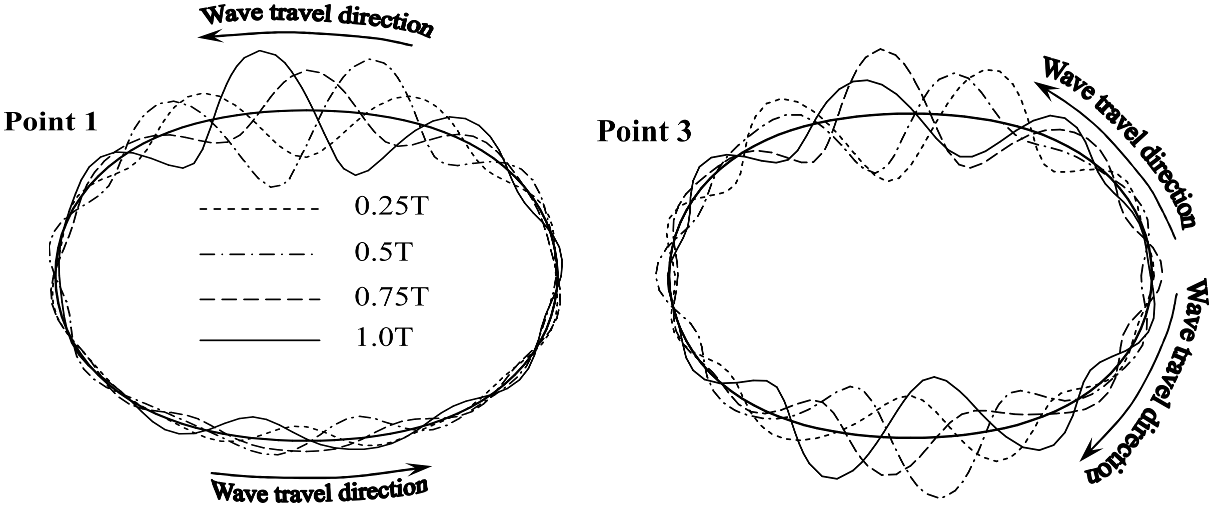

Figure 18. Transverse displacement variations along the circumference at different time instants of one cycle corresponding to points 1 and 3 (Figure 16) on the response curve of oval shell ($\zeta = 0.6$).

6. Conclusions

The nonlinear periodic response characteristics of oval cylindrical shells are investigated using the finite strip method. The governing equations are solved by the shooting technique, coupled with the Newmark time marching scheme and the arc length continuation algorithm.

The influence of ovality parameter and loading location on the periodic response is studied in detail. It is found that for the circular shells, all modes with close linear free vibration frequencies are excited due to the concentrated harmonic excitation force.

With an increase in ovality parameter, the nonlinear dynamic response changes significantly, due to increased modal interactions and participation of higher harmonics. The AS and SS modes participate in the response corresponding to primary branch of symmetrically excited noncircular shells.

For nonsymmetrically excited shells and in the secondary branch of symmetrically excited shells, all the modes participate in the nonlinear response. Due to 1:1 internal resonance between AS/SS and SA/AA modes, a secondary branch emanating from primary one through the symmetry breaking bifurcation is predicted for symmetrically excited oval shell with $\zeta = 0.6$.

For symmetrically excited oval shells, waves travelling in one direction from loading point in secondary branch of the response curve are predicted.

For nonsymmetrically excited oval shells ($\zeta = 0.6$), either waves moving in anticlockwise direction from the loading point ($y* = 3C/16$) or those originating near major axis ($y = 0$) moving in opposite directions in the top and bottom halves of the shell are observed in certain forcing frequency range.

The traveling waves in earlier work are due to driven and companion modes with a specific circumferential wave number, whereas the contribution of several modes is responsible for the traveling wave behavior predicted in the present work.

List of symbols

$\cdot_0$	Middle surface/magnitude
α, β	Rayleigh damping parameters
$\boldsymbol{A}, \boldsymbol{B}$	Stiffness coefficient matrices
$\cdot_b$	Bending component
C	Circumference
$\boldsymbol{D}, \boldsymbol{E}$	Stiffness coefficient matrices
$\ddot{\boldsymbol{\delta}}, \dot{\boldsymbol{\delta}}, \boldsymbol{\delta}$	Acceleration, velocity and displacement vectors
E	Young's modulus
$\boldsymbol{\varepsilon}$	Strain vector
$\boldsymbol{\eta}$	State vector
F	Discrete force
$\boldsymbol{F}$	Force vector
h	Thickness
I	Rotary inertia
$\boldsymbol{K}$	Constant stiffness matrix
$\boldsymbol{K}_1, \boldsymbol{K}_2$	Stiffness matrices linearly and quadratically dependent on field variables
L	Meridional length
$\cdot^L$	Linear
$\cdot_m$	Number of half sine waves in meridional direction
M	Number of terms in the displacement fields in the meridional direction
$\boldsymbol{M}$	Consistent mass matrix
$\tilde{\boldsymbol{M}}$	Moment resultant vector
N	Number of degrees of freedom
$\cdot_n$	Circumferential wave number
$\tilde{\boldsymbol{N}}$	Stress resultant vector
$\cdot^{NL}$	Nonlinear
$\bar{N}_k^0$	Original shape function
$\bar{N}_k^1$	Smoothed shape function
ν	Poisson's ratio
ω_{mn}	Linear free vibration frequency
ω_F	Forcing frequency
ω_i	Frequency of the i-th harmonic
$\cdot_p$	Extensional/stretching component
$\tilde{\boldsymbol{Q}}$	Transverse shear stress resultant vector
r	Radius of curvature
r_0	Average radius of curvature ($= C/2\pi$)
ρ	Density
t	Time
T	Time period
$\tilde{T}$	Kinetic energy
θ_x, θ_y	Rotation of meridional and circumferential sections
U	Total potential energy
u, v, w	Displacements in meridional, circumferential and thickness directions
x, y, z	Coordinate directions
ξ	Damping parameter
y^*	Circumferential location of discrete harmonic load
ζ	Ovality parameter

References

[Amabili 2003] M. Amabili, "A comparison of shell theories for large-amplitude vibrations of circular cylindrical shells: Lagrangian approach", *J. Sound Vib.* **264**:5 (2003), 1091–1125.

[Amabili 2008] M. Amabili, *Nonlinear vibrations and stability of shells and plates*, Cambridge University Press, New York, 2008.

[Amabili and Païdoussis 2003] M. Amabili and M. P. Païdoussis, "Review of studies on geometrically nonlinear vibrations and dynamics of circular cylindrical shells and panels, with and without fluid-structure interaction", *Appl. Mech. Rev.* (*ASME*) **56**:4 (2003), 349–381.

[Babu and Prathap 1986] C. R. Babu and G. Prathap, "A linear thick curved beam element", *Int. J. Numer. Methods Eng.* **23**:7 (1986), 1313–1328.

[Ibrahim et al. 2008a] S. M. Ibrahim, B. P. Patel, and Y. Nath, "Large amplitude vibrations of noncircular cylindrical shells", pp. 173–188 in *Vibration problems ICOVP-2007* (Shibpur, India, 2007), edited by E. Inan et al., Springer Proceedings in Physics **126**, 2008.

[Ibrahim et al. 2008b] S. M. Ibrahim, B. P. Patel, and Y. Nath, “On the nonlinear vibrations of clamped oval shells”, pp. 645–652 in *Proceedings of Ninth Biennial ASME Conference on Engineering Systems Design and Analysis*, vol. 1 (or CD-ROM), 2008.

[Ibrahim et al. 2009] S. M. Ibrahim, B. P. Patel, and Y. Nath, “Modified shooting approach to the non-linear periodic forced response of isotropic/composite curved beams”, *Int. J. Non-Linear Mech.* **44**:10 (2009), 1073–1084.

[Ibrahim et al. 2010] S. M. Ibrahim, B. P. Patel, and Y. Nath, “Nonlinear periodic response of composite curved beam subjected to symmetric and antisymmetric mode excitation”, *J. Comput. Nonlinear Dynam.* (*ASME*) **5**:2 (2010), #021009.

[Kozarov and Mladenov 1979] M. Kozarov and K. Mladenov, “Nonlinear vibrations of elliptic cylindrical shells”, *Akad. Nauk SSSR Izv. Mekh. Tverd. Tela* **5** (1979), 144–151. In Russian.

[Moussaoui and Benamar 2002] F. Moussaoui and R. Benamar, “Non-linear vibrations of shell-type structures: a review with bibliography”, *J. Sound Vib.* **255**:1 (2002), 161–184.

[Nayfeh and Balachandran 1994] A. H. Nayfeh and B. Balachandran, *Applied nonlinear dynamics: analytical, computational, and experimental methods*, Wiley, New York, 1994.

[Padmanabhan and Singh 1995] C. Padmanabhan and R. Singh, “Analysis of periodically excited non-linear systems by a parametric continuation technique”, *J. Sound Vib.* **184**:1 (1995), 35–58.

[Pandalai and Sathyamoorthy 1970] K. A. V. Pandalai and M. Sathyamoorthy, “Nonlinear flexural vibrations of orthotropic oval cylindrical shells”, pp. 47–74 in *Studies in structural mechanics: to honour N. J. Hoff*, edited by K. A. V. Pandalai, 1970.

[Patel et al. 2002] B. P. Patel, M. Ganapathi, D. P. Makhecha, and S. S. Gupta, “On the nonlinear free flexural vibrations problem for thin elastic rings”, *J. Aeronaut. Soc. India* **54** (2002), 298–309.

[Patel et al. 2003] B. P. Patel, M. Ganapathi, D. P. Makhecha, and P. Shah, “Large amplitude free flexural vibration of rings using finite element approach”, *Int. J. Non-Linear Mech.* **38**:6 (2003), 911–921.

[Patel et al. 2009] B. P. Patel, S. M. Ibrahim, and Y. Nath, “Periodic response of nonlinear dynamical system with large number of degrees of freedom”, *Sadhana* **34**:6 (2009), 1033–1037.

[Rajasekaran and Murray 1973] S. Rajasekaran and D. W. Murray, “Incremental finite element matrices”, *J. Struct. Div.* (*ASCE*) **99**:12 (1973), 2423–2338.

[Ribeiro 2004] P. Ribeiro, “Non-linear forced vibrations of thin/thick beams and plates by the finite element and shooting methods”, *Comput. Struct.* **82**:17-19 (2004), 1413–1423.

[Ribeiro 2008] P. Ribeiro, “Forced large amplitude periodic vibrations of cylindrical shallow shells”, *Finite Elem. Anal. Des.* **44**:11 (2008), 657–674.

[Soedel 1993] W. Soedel, *Vibrations of shells and plates*, 2nd ed., Dekker, New York, 1993.

[Soldatos 1999] K. P. Soldatos, “Mechanics of cylindrical shells with non-circular cross-section: a survey”, *Appl. Mech. Rev.* (*ASME*) **52**:8 (1999), 237–274.

[Sundararajan and Noah 1997] P. Sundararajan and S. T. Noah, “Dynamics of forced nonlinear systems using shooting/arc-length continuation method: application to rotor systems”, *J. Vib. Acoust.* (*ASME*) **119**:1 (1997), 9–20.

Received 28 Jan 2010. Revised 29 Apr 2010. Accepted 8 May 2010.

SYED MUHAMMAD IBRAHIM: `ibrahimmail@rediffmail.com`
Department of Applied Mechanics, Indian Institute of Technology Delhi, Hauz Khas, New Delhi 110016, India

BADRI PRASAD PATEL: `badripatel@hotmail.com`
Department of Applied Mechanics, Indian Institute of Technology Delhi, Hauz Khas, New Delhi 110016, India

YOGENDRA NATH: `nathyogendra@hotmail.com`
Department of Applied Mechanics, Indian Institute of Technology Delhi, Hauz Khas, New Delhi 110016, India

JOURNAL OF MECHANICS OF MATERIALS AND STRUCTURES
Vol. 5, No. 6, 2010

TIME-HARMONIC ELASTODYNAMIC GREEN'S FUNCTION FOR THE HALF-PLANE MODELED BY A RESTRICTED INHOMOGENEITY OF QUADRATIC TYPE

TSVIATKO V. RANGELOV AND GEORGE D. MANOLIS

We derive closed-form solutions for point-force generated motions in a continuously inhomogeneous half-plane, which represent the complete elastic wave-train in the interior domain obeying traction-free boundary conditions at the horizontal surface. More specifically, a special type of material inhomogeneity is studied, where the shear modulus varies quadratically with respect to the depth coordinate. Furthermore, the material density profile varies proportionally to the aforementioned profile, while Poisson's ratio remains fixed at one-quarter. Limit forms for the Green's functions are derived for both zero frequency and for the equivalent homogeneous medium. Next, a series of numerical results serve to validate this mechanical model, and to show the differences in the wave motion patterns developing in media that are inhomogeneous as compared to a reference homogeneous background. These singular solutions are useful within the context of boundary element formulations for the numerical solution of problems involving nonhomogeneous continua, which find applications in fields as diverse as composite materials, geophysical prospecting, petroleum exploration and earthquake engineering.

1. Introduction and problem statement

Detailed knowledge of wave motions produced by point forces in the elastic half-plane [Achenbach 1973] are of paramount importance in mechanics, since they form the backbone of any integral equation formulation whose numerical treatment yields boundary element method solutions to a wide range of boundary-value problems in elastodynamics [Kausel and Manolis 2000].

We examine here a restricted class of inhomogeneous media, where the elastic parameters and the density all vary proportionally with depth, which makes possible a decoupling of the equations of motion for the boundless continuum into pseudopressure and shear wave components in a transformed domain. Although somewhat unlikely, there are situations where this type of inhomogeneity has actually been observed. As an example, we mention the geological profile of the Sofia region in Bulgaria [Bonchev et al. 1982], which was measured from in-situ data. This profile seems to imply both a proportional variation of the shear modulus and of the density, plus a constant Poisson's ratio value of one-quarter, for a nearly thirty kilometer thickness of the local deposits as measured from the surface.

Let (x_1, x_2) be Cartesian coordinates in $\mathbb{R}^2$ and denote the lower half-plane by $\mathbb{R}^2_- = \{(x_1, x_2) : x_2 < 0\}$; see Figure 1. Consider the following boundary-value problem defined in the frequency domain, where

---

Keywords: inhomogeneous media, elastic waves, Fourier transforms, singular solutions.
The authors wish to acknowledge financial support provided through NATO Collaborative Linkage Grant No. 984136.

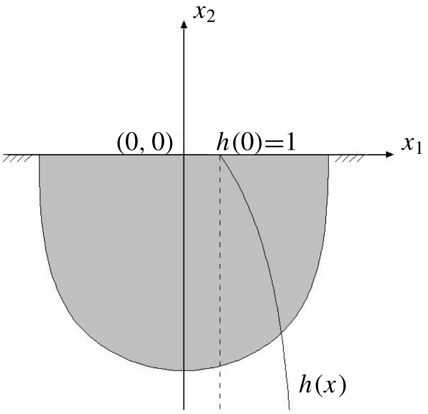

Figure 1. Elastic half-plane with quadratically varying material properties in the depth coordinate as described by the profile function $h(x)$.

all dependent variables have an $e^{i\omega t}$ type dependence on time:

$$L^a(G) \equiv (C_{ikpq}G_{ip,q})_{,j} - \rho\omega^2 G_{ik} = -\delta(x-\xi)\varepsilon_{ik}, \quad \text{where } x,\xi \in \mathbb{R}^2_-, \tag{1}$$

$$T^a(G) \equiv C_{j2pq}G_{ip,q} = 0 \quad \text{on } x_2 = 0, \tag{2}$$

$$G \to 0 \quad \text{for } x_2 \to -\infty. \tag{3}$$

Here Green's tensor G satisfies the Sommerfeld radiation condition along lines parallel to $\{x_2 = 0\}$, i.e., $\{(x_1, x_2), x_1 \to \pm\infty\}$. Furthermore, $x = (x_1, x_2)$ and $\xi = (\xi_1, \xi_2)$ are source/receiver points in the continuum; $C_{jkpq} = h(x_2)C^0_{jkpq}$ is the elasticity tensor; $\rho = h(x_2)\rho_0$, with $\rho_0 > 0$, is the material density; and $h(x_2) = (ax_2 + 1)^2$, with $a \le 0$, is the material profile, implying a quadratic variation with depth. In terms of the quantities defined for the corresponding homogeneous background, we have $C^0_{jkpq} = \mu_0(\delta_{jk}\delta_{pq} + \delta_{jp}\delta_{kq} + \delta_{jq}\delta_{kp})$, where $\mu_0 > 0$ is the shear modulus, δ_{jk} is Kronecker's delta, and $\omega > 0$ is the frequency. Finally, δ is Dirac's delta function, $\varepsilon = \varepsilon_{ik}$ is the unit tensor, commas denote partial differentiation with respect to the spatial coordinates and summation is implied over repeated indices.

In elastodynamics, the problem defined by (1)–(3) is a model of an isotropic elastic medium in $\mathbb{R}^2_-$ with a point force at ξ and traction-free boundary conditions. Poisson's ratio is fixed at a value of $\nu = 0.25$, while the shear modulus μ and the density ρ depend in the same manner on depth coordinate x_2. A fundamental solution to (1) of this problem in $\mathbb{R}^2_-$ was derived in [Manolis and Shaw 1996] for $a \neq 0$, while a solution of (1)–(3) defining a Green's function for the homogeneous half-plane, i.e., for $a = 0$, has been obtained in M. Kinoshita's M.Sc. thesis, quoted in [Kobayashi 1983]. A corresponding Green's function in the Laplace domain for a homogeneous half-plane can be found in [Guan et al. 1998], while an approximate such function using an image source across the free surface was derived earlier in [Kontoni et al. 1987]. Finally, the transient Green's function due to a suddenly applied load in the homogeneous half-plane, namely Lamb's problem, can be found in [Kausel 2006], a compilation of fundamental solutions in elastodynamics.

2. Solution outline

By following the procedure as outlined in references given above, we will now derive the unique solution to the problem (1)–(3), which corresponds to a Green's function G for the inhomogeneous half-plane with a quadratic variation of the material parameters. Let the matrix-valued function u be a fundamental solution to equation (1):

$$L^a(u) = -\delta(x-\xi)\varepsilon, \quad \text{where } \; x, \xi \in \mathbb{R}^2_-, \tag{4}$$

while w is a smooth matrix-valued function such that

$$L^a(w) = 0, \qquad \text{where } x, \xi \in \mathbb{R}^2_-, \tag{5}$$

$$T^a(w) = -T^a(u) \quad \text{on } x_2 = 0, \tag{6}$$

where superscript a in the operators corresponds to the degree of inhomogeneity. Then, by using superposition, the complete Green's function is simply $G = u + w$.

The fundamental solution u can be expressed as in [Manolis and Shaw 1996] in the form

$$u(x, \xi, \omega) = h^{-1/2}(\xi_2)U(x, \xi, \omega)h^{-1/2}(x_2), \tag{7}$$

where U is a fundamental solution for the corresponding homogeneous case, i.e.,

$$L^0(U) = -\delta(x-\xi)\varepsilon, \quad \text{with } \; x, \xi \in \mathbb{R}^2_-. \tag{8}$$

Finally, the traction matrix corresponding to displacements u on free surface $x_2 = 0$ is

$$\begin{aligned} T^a_{1k}(u) &= \mu_0 h^{-1/2}(\xi_2)(-aU_{1k} + U_{1k,2} + U_{2k,1}), \\ T^a_{2k}(u) &= \mu_0 h^{-1/2}(\xi_2)(-3aU_{2k} + U_{1k,1} + 3U_{2k,1}). \end{aligned} \tag{9}$$

The homogeneous matrix-valued function U in $\mathbb{R}^2$ can be found in [Eringen and Şuhubi 1974] as

$$U_{jk} = \frac{i}{4\mu_0}\left[\delta_{jk} H_0^{(1)}(k_2 r) + \frac{1}{k_2^2}\partial^2_{jk}\big(H_0^{(1)}(k_2 r) - H_0^{(1)}(k_1 r)\big)\right]. \tag{10}$$

Here the wave numbers corresponding to pressure and shear body waves are respectively $k_1 = \sqrt{\rho_0/3\mu_0}\,\omega$ and $k_2 = \sqrt{\rho_0/\mu_0}\,\omega$, while the radial distance between source and receiver is $r = \sqrt{(x_1-\xi_1)^2 + (x_2-\xi_2)^2}$ and $H_0^{(1)}(z)$ is the Bessel function of third kind (or Hankel function) and zero order.

In order to simplify the calculations, we fix the source point along the vertical axis as $\xi = (0, \xi_2)$, $\xi_2 < 0$. As will be shown later on, Green's function G actually depends on $x_1 - \xi_1$ and separately on x_2 and ξ_2 because the corresponding profile function h is independent of x_1; thus the assumption $\xi_1 = 0$ is not restrictive.

3. Solution methodology

The first step is to recover a general solution w to (5), in the form

$$w(x, \xi, \omega) = h^{-1/2}(x_2)W(x, \xi, \omega). \tag{11}$$

Then, the two corresponding differential operators for the homogeneous and inhomogeneous cases are related as

$$L^a(w) = h^{1/2}(x_2)L^0(W), \tag{12}$$

where

$$\begin{aligned} L^a(w) &= h^{-1/2}C^a_{jkpq}\big(W_{ip,qk} + h^{-1}(h^{1/2}_{,j}W_{ip,q} - h^{1/2}_{,q}W_{ik,j} - h^{1/2}_{,qk}W_{ip})\big) + \rho\omega^2 h^{-1/2}W_{ij} \\ &= h^{1/2}(C_{jkpq}W_{ip,qk} + \rho_0\omega^2 W_{ij}) = h^{1/2}L^0(W). \end{aligned}$$

Thus, if W solves (5) with $a = 0$, then w also solves (5) for $a < 0$ and we seek a solution $W = \{W_{jk}\}$ in the general Rayleigh form [Achenbach 1973; Rajapakse and Wang 1991] as a transformation between distance x_1 and wave number η:

$$W_{jk} = \frac{1}{2\pi}\int_R S_{jk}e^{i\eta x_1}\,d\eta, \tag{13}$$

where the kernel function S_{jk} depends on $e^{\beta x_2}$, η, ω, a, and the parameter β is found as solution of an algebraic system of equations to be developed.

Remark 1. It is not possible to proceed for the inhomogeneous case as in [Kinoshita 1983] for a homogeneous material. The algebraic transformation produces a function

$$\tilde{u}(x, \xi, \omega) = h^{-1/2}(-\xi_2)U(x, \xi, \omega)h^{-1/2}(x_2)$$

that is not well defined for all $\xi_2 < 0$ and is infinite if $h(-\xi_2) = 0$, corresponding to a value $\xi_2 = 1/a$, $a < 0$. Thus, we cannot use superposition as $u(x, \xi, \omega) + \tilde{u}(x, \xi, \omega)$, for which $T_{1k} = 0$, $T_{2k} = 0$ on $x_2 = 0$, but can only use $u(x, \xi, \omega)$ and then add a Rayleigh form to satisfy the boundary conditions.

Thus, in order to find $S = S_{jk}$ we use the Fourier transform $\Im$ with respect to the x_1 coordinate, defined, together with its inverse, by

$$\begin{aligned} \tilde{f}(\eta, x_2) &= \Im_{x_1\to\eta} f = \int_R f(x_1, x_2)e^{-i\eta x_1}\,dx_1, \\ f(x_1, x_2) &= \Im^{-1}_{\eta\to x_1}\tilde{f} = \frac{1}{2\pi}\int_R \tilde{f}(\eta, x_2)e^{i\eta x_1}\,d\eta, \end{aligned} \tag{14}$$

where η is the transform parameter. By applying the Fourier transform to W, we turn (1) with $a = 0$ into

$$L^0(\Im_{x_1\to\eta}(W)) = 0, \tag{15}$$

which in matrix form reads as

$$(M(\eta, \beta) + \rho_0\omega^2 I_2)S = 0, \tag{16}$$

where I_2 is the 2×2 unit matrix and

$$M(\eta, \beta) = \begin{pmatrix} -3\mu_0\eta^2 + \mu_0\beta^2 + \rho_0\omega^2 & 2i\mu_0\eta\beta \\ 2i\mu_0\eta\beta & -\mu_0\eta^2 + 3\mu_0\beta^2 + \rho_0\omega^2 \end{pmatrix}. \tag{17}$$

For every fixed value of η, a nonzero solution to (16) exists if $\det M(\eta, \beta) = 0$, which gives the following biquadratic equation for β:

$$3\mu_0^2\beta^4 - 2\mu_0(3\mu_0\eta^2 - 2\rho_0\omega^2)\beta^2 + \rho_0^2\omega^4 + 3\mu_0\omega^4 - 4\mu_0\eta^2\rho_0\omega^2 = 0. \tag{18}$$

If we set $\gamma_j^2 = \eta^2 - k_j^2$, equation (18) simplifies to

$$\beta^4 - (\gamma_1^2 + \gamma_2^2)\beta^2 + \gamma_1^2\gamma_2^2 = 0, \tag{19}$$

and the solutions are $\beta_j^2 = \pm\gamma_j^2$. In order to satisfy the radiation condition of (3), only the positive root is retained:

$$\beta_j = \gamma_j = \sqrt{\eta^2 - k_j^2}. \tag{20}$$

Since the matrix $M(\eta, \beta_j)$, for $j = 1, 2$, has rank 1, there are two eigenvectors, namely

$$\nu^1 = \begin{pmatrix} \eta \\ -i\beta_1 \end{pmatrix}, \quad \nu^2 = \begin{pmatrix} i\beta_2 \\ \eta \end{pmatrix}, \tag{21}$$

and every solution of (16) has the standard form

$$S = S_{jk} = \sum_{m=1}^{2} C_k^k \nu_j^m e^{\beta_m x_2}. \tag{22}$$

Recapitulating, the matrix form of (11) using indicial notation is

$$w_{jk}(x, \xi, \omega) = h^{-1/2}(x_2) W_{jk}(x, \xi, \omega), \tag{23}$$

and the remaining step is to determine functions $C_m^k(\eta, \xi_2, a)$ such that the boundary condition for zero tractions in (6) is satisfied. The traction field corresponding to displacement field w on $x_2 = 0$ is

$$\begin{aligned} T_{1k}^a &= \frac{1}{2\pi} \int_R \mu_0 \big[\eta(-a + 2\beta_1) C_1^k + i(-a\beta_2 + 2\eta^2 - k_2^2) C_2^k\big] e^{i\eta x_1} dx_1, \\ T_{2k}^a &= \frac{1}{2\pi} \int_R \mu_0 \big[i(3a\beta_1 - 2\eta^2 + k_2^2) C_1^k + \eta(-3a + 2\beta_2) C_2^k\big] e^{i\eta x_1} dx_1. \end{aligned} \tag{24}$$

To determine the traction field corresponding to displacement field u on $x_2 = 0$, we use the representation of $H_0^{(1)}$ based on a Fourier transform with respect to x_1 (see [Gradshteyn and Ryzhik 1980, formulas $6.677_{3,4}$ and Section 8.42]):

$$H_0^{(1)}(rk_j) = \frac{i}{2\pi} \int_R \frac{1}{\beta_j} e^{(\xi_2 - x_2)\beta_j} e^{i\eta x_1} d\eta. \tag{25}$$

Employing (7) and (10) for u and for U, respectively, we obtain

$$T_{jk}^a(u) = \frac{i}{2\pi} \int_R D_{jk} e^{i\eta x_1} d\eta. \tag{26}$$

where the matrix components D_{jk} are

$$
\begin{aligned}
D_{11} &= \frac{h^{-1/2}(\xi_2)}{2k_2^2}\left[(-a\beta_2 - 2\eta^2 + k_2^2)e^{\xi_2\beta_2} + \eta^2(a/\beta_1 + 2)e^{\xi_2\beta_1}\right],\\
D_{21} &= \frac{i\eta h^{-1/2}(\xi_2)}{2k_2^2\beta_1}\left[\beta_1(-3a - 2\beta_2)e^{\xi_2\beta_2} + \eta^2(3a\beta_1 + 2\eta^2 - k_2^2)e^{\xi_2\beta_1}\right],\\
D_{12} &= \frac{i\eta h^{-1/2}(\xi_2)}{2k_2^2\beta_2}\left[(-a\beta_2 - 2\eta^2 + k_2^2)e^{\xi_2\beta_2} + \beta_2(a + 2\beta_1)e^{\xi_2\beta_1}\right],\\
D_{22} &= \frac{i\eta h^{-1/2}(\xi_2)}{2k_2^2}\left[\eta^2(3a/\beta_2 + 2)e^{\xi_2\beta_2} + (-3a\beta_1 - 2\eta^2 + k_2^2)e^{\xi_2\beta_1}\right].
\end{aligned}
\tag{27}
$$

Combining equations (24) and (26), we obtain a system of two linear equations in C_m^1, C_m^2, which appear as kernels of integral equations when substituted in the boundary condition of (6). The determinant of this system is

$$
\Delta^a = \frac{\mu_0^2}{4\pi^2}\begin{vmatrix} \eta(-a + 2\beta_1) & i(-a\beta_2 + 2\eta^2 - k_2^2) \\ i(3a\beta_1 - 2\eta^2 + k_2^2) & \eta(-3a + 2\beta_2) \end{vmatrix}, \tag{28}
$$

which evaluates to

$$
\Delta^a = \frac{\mu_0^2}{4\pi^2}\left[3(\eta^2 - \beta_1\beta_2)a^2 - \left((\beta_1 + \beta_2)k_2^2 + \eta^2\beta_1\right)a - \Delta^0\right], \tag{29}
$$

where $\Delta^0 = 4\eta^2\beta_1\beta_2 - (2\eta^2 - k_2^2)^2$ is a Rayleigh function [Kobayashi 1983].

The functions C_m^1, C_m^2 are unique solutions of (6), since for every $\eta \in R$, $a < 0$, $\omega > 0$, $\rho_0 > 0$, $\mu_0 > 0$ the condition $\Delta^a \neq 0$ holds true. Possible combinations of values of parameter $|\eta|$ as compared to the two wave numbers k_1, k_2 yield the following cases:

(i) If $|\eta| < k_1$, then $\operatorname{Im}\Delta^a = -\left((|\beta_1| + |\beta_2|)k_2^2 + \eta^2|\beta_1|\right)a > 0$.

(ii) If $|\eta| = k_1$, then $\operatorname{Im}\Delta^a = -\left(|\beta_2|k_2^2 a + (2\eta^2 - k_2^2)^2\right) > 0$.

(iii) If $k_1 < |\eta| \le k_2$, then $\operatorname{Re}\Delta^a = 3\eta^2a^2 - \beta_1(k_2^2 + \eta^2)a + (2\eta^2 - k_2^2) > 0$.

(iv) If $k_2 < |\eta|$, then $\Delta^a > \Delta^0 > 0$.

An application of Cramer's rule yields the matrix functions

$$
C_m^k = \Delta_{mk}^a / \Delta^a, \tag{30}
$$

where the subdeterminants Δ_{mk}^a are given by

$$
\begin{aligned}
\Delta_{11}^a &= \begin{vmatrix} -D_{11} & i\mu_0(-a\beta_2 + 2\eta^2 - k_2^2) \\ -D_{21} & \mu_0\eta(-3a + 2\beta_2) \end{vmatrix}, &
\Delta_{21}^a &= \begin{vmatrix} \mu_0\eta(-a + 2\beta_1) & -D_{11} \\ i\mu_0(3a\beta_1 - 2\eta^2 + k_2^2) & -D_{21} \end{vmatrix}\\
\Delta_{12}^a &= \begin{vmatrix} \mu_0\eta(-a + 2\beta_1) & -D_{12} \\ i\mu_0(3a\beta_1 - 2\eta^2 + k_2^2) & -D_{22} \end{vmatrix}, &
\Delta_{22}^a &= \begin{vmatrix} -D_{12} & i\mu_0(-a\beta_2 + 2\eta^2 - k_2^2) \\ -D_{22} & \mu_0\eta(-3a + 2\beta_2) \end{vmatrix}.
\end{aligned}
\tag{31}
$$

Finally, the radiation boundary condition in (3) holds true because of the presence of the multiplier $h^{-1/2}(x_2)$ for u and $h^{-1/2}(x_2)e^{x_2\beta}$ under the integral sign on η for w in (13).

Remark 2. This method can be applied for complex wave numbers ($k_j = k_{jR} + ik_{jI}$ with $k_{jR} > 0$, $k_{jI} > 0$) and the structure of Green's function remains the same. This is because the representations for the fundamental solution of (10) and for the Bessel function (25) are valid for complex numbers as well. However, the proof that $\Delta^a \neq 0$ in this case is quite complicated.

Remark 3. The same method can be applied to obtain a transient Green's function in the inhomogeneous half-plane for the equations of motion defined in the time domain as

$$L^a(G) \equiv (C_{jkpq}G_{ip,q})_{,j} - \rho G_{ik,tt} = -f(t)\delta(x-\xi)\varepsilon_{ik}, \tag{32}$$

where $f(t) \in L^1_{\text{loc}}(\mathbb{R}^1)$ and $f = 0$ for $t < 0$. More specifically, $f(t) = H(t)F(t)$, with $H(t)$ the Heaviside function and $|F(t)| \leq Ae^{ct}$ for $t \to \infty$. The transient Green's function is obtained by applying Laplace's transformation to (32) and using a Kelvin function representation of the type $K_0(z) = (i\pi/2)H_0^{(1)}(iz)$. Formally, the Green's function in the Laplace domain is obtained by replacing frequency ω with the Laplace transform parameter written as a purely imaginary number is and then applying the inverse Laplace transform. This path was followed for the homogeneous case, i.e., $a = 0$ and with $F(t) = 1$, in [Guan et al. 1998].

Remark 4. Green's function $G(x, \xi, \omega, a)$ converges in the weak sense to $G(x, \xi, \omega, 0)$ for $a \to 0$, i.e., for every $\varphi(\xi) \in C_0^\infty(\mathbb{R}^2_-)$ we have

$$\int_{\mathbb{R}^2} G(x, \xi, \omega, a)\varphi(\xi)\,d\xi \;\to \int_{\mathbb{R}^2} G(x, \xi, \omega, 0)\varphi(\xi)\,d\xi \quad \text{for } a \to 0.$$

Also, Green's function $G(x, \xi, \omega, a)$ converges in the weak sense to $G(x, \xi, 0, a)$ for $\omega \to 0$, i.e., for every $\varphi(\xi) \in C_0^\infty(\mathbb{R}^2_-)$ we have

$$\int_{\mathbb{R}^2} G(x, \xi, \omega, a)\varphi(\xi)\,d\xi \;\to \int_{\mathbb{R}^2} G(x, \xi, 0, a)\varphi(\xi)\,d\xi \quad \text{for } \omega \to 0.$$

More details for this elastostatic case can be found in the Appendix.

4. Recovery of the homogeneous case

In order to check that it is possible to recover the homogeneous half-plane solution by setting the inhomogeneity parameter a to zero (and, correspondingly, $h(x_2) = h(\xi_2) = 1$ for the profile function) in the solution derived above, we start with the results presented in [Kobayashi 1983]. In that case, (24) reads as

$$\begin{aligned} T^0_{1k} &= \frac{1}{2\pi}\int_R \mu_0[2\eta\beta_1 C_1^k + i(2\eta^2 - k_2^2)C_2^k]e^{i\eta x_1}dx_1, \\ T^a_{2k} &= \frac{1}{2\pi}\int_R \mu_0[i(-2\eta^2 + k_2^2)C_1^k + 2\eta\beta_2 C_2^k]e^{i\eta x_1}dx_1. \end{aligned} \tag{33}$$

Also, in place of $u(x_1, x_2 - \xi_2)$ we use $u(x_1, x_2 - \xi_2) + \tilde{u}(x_1, x_2 + \xi_2)$, where $\tilde{u}(x_1, x_2 + \xi_2)$ is a smooth matrix-valued function defined in reference to (10) as

$$\tilde{u}_{jk}(x_1, x_2 + \xi_2) = \frac{i}{4\mu_0}\left[\delta_{jk}H_0^{(1)}(k_2\tilde{r}) + \frac{1}{k_2^2}\partial^2_{jk}\big(H_0^{(1)}(k_2\tilde{r}) - H_0^{(1)}(k_1\tilde{r})\big)\right], \tag{34}$$

with $\tilde{r}=\sqrt{x_1^2+(x_2+\xi_2)^2}$ the distance between source and receiver. Furthermore, the integral representation for the Hankel function corresponding to (25) is

$$H_0^{(1)}(\tilde{r}k_j)=\frac{i}{2\pi}\int_R \frac{1}{\beta_j}e^{(\xi_2+x_2)\beta_j}e^{i\eta x_1}d\eta. \tag{35}$$

Thus, the traction vector on the free surface $x_2=0$ for the complete displacement field $u+\tilde{u}$ that replaces (26) is

$$T_{jk}^0(u+\tilde{u})=\frac{i}{2\pi}\int_R \hat{D}_{jk}e^{i\eta x_1}d\eta. \tag{36}$$

with the new definitions

$$\begin{aligned}\hat{D}_{11}=0,\quad \hat{D}_{21}&=\frac{i\eta}{2k_2^2\beta_1}\left[-2\beta_1\beta_2e^{\xi_2\beta_2}+(2\eta^2-k_2^2)e^{\xi_2\beta_1}\right],\\ D_{12}=\frac{i\eta}{2k_2^2\beta_2}&\left[-(2\eta^2-k_2^2)e^{\xi_2\beta_2}+2\beta_1\beta_2e^{\xi_2\beta_1}\right],\quad \hat{D}_{22}=0.\end{aligned} \tag{37}$$

The new subdeterminants $\bar{\Delta}_{mk}^0$ are now

$$\begin{aligned}\hat{\Delta}_{11}^0&=\begin{vmatrix}0 & i\mu_0(2\eta^2-k_2^2)\\ -\hat{D}_{21} & 2\mu_0\beta_2\end{vmatrix}, & \hat{\Delta}_{21}^0&=\begin{vmatrix}2\mu_0\beta_1 & 0\\ -i\mu_0(2\eta^2-k_2^2) & -\hat{D}_{21}\end{vmatrix},\\ \hat{\Delta}_{12}^0&=\begin{vmatrix}-\hat{D}_{12} & i\mu_0(2\eta^2-k_2^2)\\ 0 & 2\mu_0\beta_2\end{vmatrix}, & \hat{\Delta}_{22}^0&=\begin{vmatrix}2\mu_0\beta_1 & -\hat{D}_{12}\\ -i\mu_0(2\eta^2-k_2^2) & 0\end{vmatrix},\end{aligned} \tag{38}$$

and the solution for the matrix functions is

$$\hat{C}_m^k=\hat{\Delta}_{mk}^0/\Delta^0. \tag{39}$$

Finally, the reconstruction of the complete Green's function that replaces (22) is

$$\hat{S}=\hat{S}_{jk}=\sum_{m=1}^{2}\hat{C}_m^k\nu_j^m e^{\beta_m x_2}, \tag{40}$$

whose components can be explicitly written as

$$\begin{aligned}\hat{S}_{11}&=\frac{i\eta\mu_0}{\Delta_0}\left[(2\eta^2-k_2^2)e^{x_2\beta_2}-2\beta_1\beta_2e^{x_2\beta_1}\right]\hat{D}_{21}, & \hat{S}_{21}&=\frac{\beta_1\mu_0}{\Delta_0}\left[(2\eta^2-k_2^2)e^{x_2\beta_2}-2\eta^2e^{x_2\beta_1}\right]\hat{D}_{21},\\ \hat{S}_{12}&=\frac{\beta_2\mu_0}{\Delta_0}\left[-2\eta^2e^{x_2\beta_2}+(2\eta^2-k_2^2)e^{x_2\beta_1}\right]\hat{D}_{12}, & \hat{S}_{22}&=\frac{i\eta\mu_0}{\Delta_0}\left[-2\beta_1\beta_2e^{x_2\beta_2}+(2\eta^2-k_2^2)e^{x_2\beta_1}\right]\hat{D}_{21}.\end{aligned} \tag{41}$$

Remark 5. The half-plane Green's function derived above can be used for solving general types of boundary-value problems in the half-plane enclosing singularities such as cracks, holes, cavities, etc. This can be done using boundary element method formulations [Manolis and Beskos 1988], and the advantage here is that a free surface ($x_2=0$) discretization is unnecessary.

5. Numerical example

As an example, we consider the lower part of an original full plane, keeping in mind that in the upper half-plane the material function h has a line of degeneracy (see Figure 1). A numerical study will be run for this inhomogeneous half-plane and its equivalent homogeneous limit form ($a = 0 \to h(x_2) = 1.0$) using the Green's functions derived herein. We start with the following source/receiver configuration:

$$(\xi_1, \xi_2) = (0.0, -30.0\,\text{m}), \quad (x_1, x_2) = (30.0\,\text{m}, 0.0). \tag{42}$$

The background homogeneous material corresponds to firm soil and has the following values for the pressure (P) and shear (S) wave speeds and for the density:

$$c_1 = 621.0\,\text{m/sec}, \quad c_2 = 359.0\,\text{m/sec}, \quad \rho = 2100.0\,\text{kg}. \tag{43}$$

The inhomogeneity parameter is assigned a value of $a = -0.001\,\text{m}^{-1}$, which implies that the inhomogeneous profile at the level of the source is stiffer by a factor of 1.07 (i.e., about 7%) compared to the reference value $\mu_0 = 270.0 \times 10^6\,\text{N/m}^2$ at the free surface level. The travel times for the P and S waves to reach the receiver starting from the source are $t_1 = r/c_1 = 42.4/621 = 0.07\,\text{sec}$, $t_2 = 42.4/359 = 0.12\,\text{sec}$, respectively, in the reference homogeneous background material. Choosing a total time $T = 2.0\,\text{sec}$ for the dynamic phenomenon to develop fully yields a frequency value $f = 1.0/T = 0.50\,\text{Hz}$, which is rounded-off to 0.64 Hz so it corresponds to $\Omega = 4.0\,\text{rad/sec}$. This interval is swept in 40 increments of $\Delta\omega = 0.1\,\text{rad/sec}$ starting from zero, where the static solution $G(x, \xi, 0, a)$ is used (see Remark 4).

In reference to the one-sided Fourier transform of (14), this is performed numerically using the fast Fourier transform. More specifically, we use the positive side of the horizontal axis going up to four times the distance of the receiver from the epicenter, i.e., for $X = 120.0\,\text{m}$. For better accuracy, we develop a two-sided transform by projecting symmetric values of the functions to be inverted along the negative X-axis. More specifically, for $N = 1024$ data points, the wave number spectrum $-H \le \eta \le +H$ is set up according to the following formulas:

$$\Delta x = 2X/N = 0.23437\,\text{m}, \quad \Delta\eta = 2\pi/N\Delta x = 0.02618\,\text{m}^{-1}, \quad H = \pi/\Delta x = 13.404\,\text{m}^{-1}. \tag{44}$$

We note in passing that it is possible to introduce viscoelastic material behavior using the Kelvin model with complex values for the material parameters [Flugge 1967], which is compatible with the static solution at zero frequency.

Figures 2 and 3 plot both amplitude and phase angle of the Green's functions $G^{\text{inhom}}(x, \xi, \omega)$ and $G^{\text{hom}}(x, \xi, \omega)$, respectively. The general structure of the Green's functions is

$$G_{IJ}(x, \xi, \omega) = U_{IJ}(x, \xi, \omega) + W_{IJ}(x, \xi, \omega), \quad I, J = 1, 2, \tag{45}$$

where $U_{IJ}(x, \xi, \omega)$ is the full space solution and $W_{IJ}(x, \xi, \omega)$ the Rayleigh-type correction. We note again that in the approach used in [Kinoshita 1983], the component $W_{IJ}(x, \xi, \omega)$ restores traction-free conditions at the free horizontal surface through addition to the full-plane solution $U_{IJ}(x, \xi, \omega)$ plus its image $U_{IJ}(x, -\xi, \omega)$. This latter operation results in a zeroing of the off-diagonal components and a doubling of the diagonal ones for the full-space solution.

We first observe in Figures 2 and 3 that the introduction of inhomogeneity results in a small decrease of a few percentage points in the amplitude of the full-space components $U_{I,J}(x, \xi, \omega)$, since the elastic

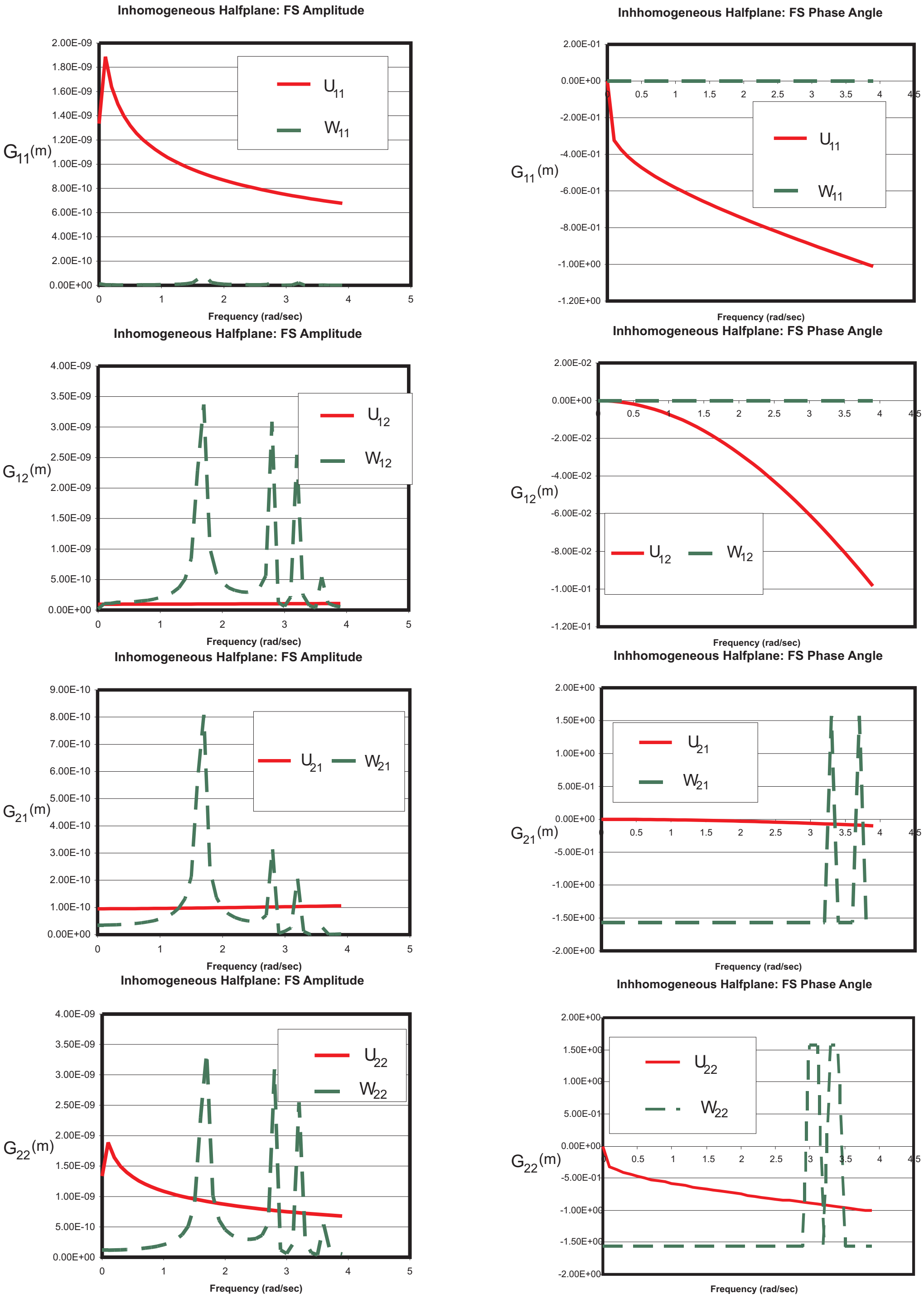

Figure 2. Inhomogenous half-plane ($a = -0.0010$) fundamental solution components: amplitude (left column) and phase angle (right column) versus frequency. From top to bottom, the graphs show G_{11}, G_{12}, G_{21} and G_{22}.

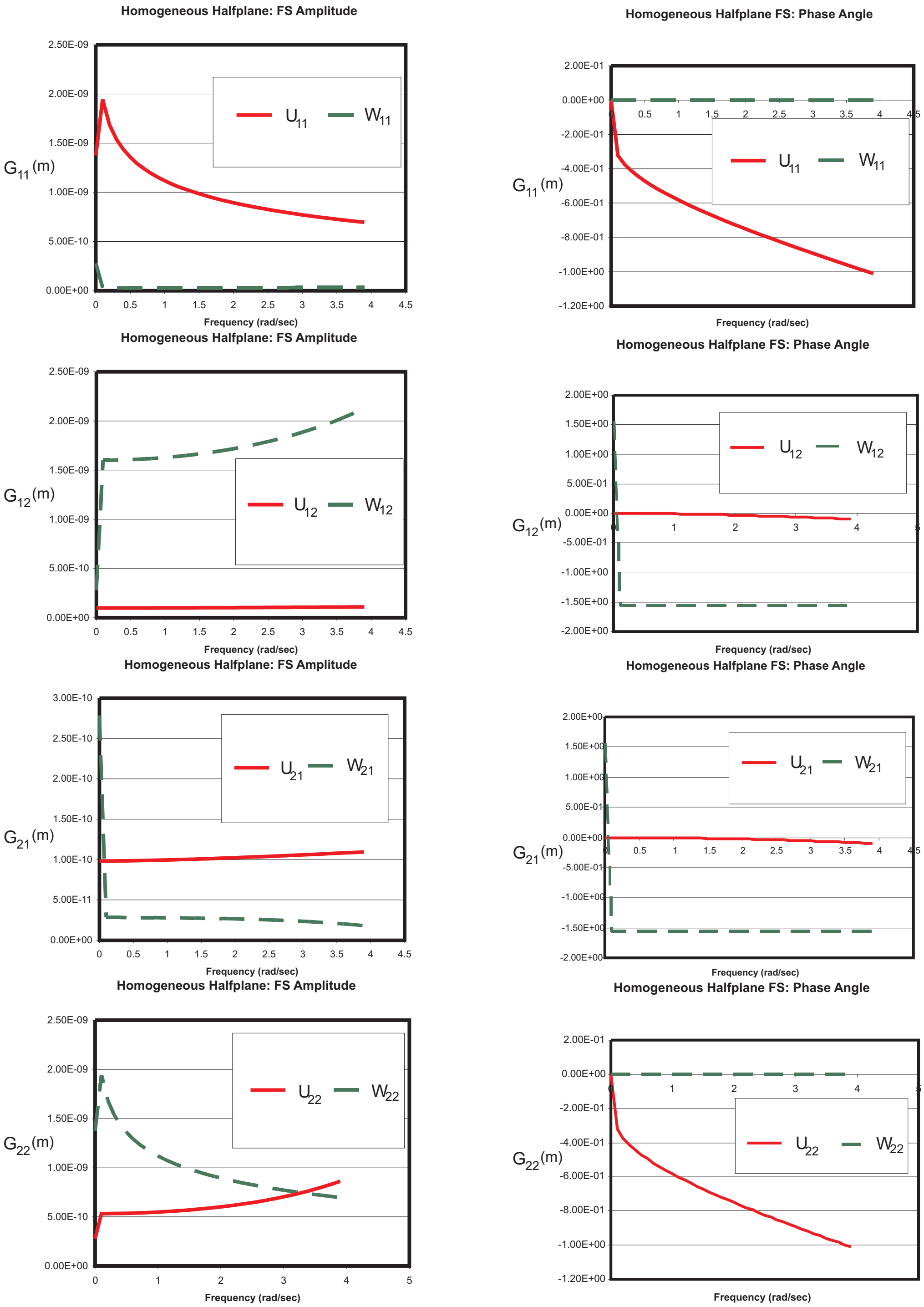

Figure 3. Homogenous half-plane fundamental solution components at surface source S: amplitude (left column) and phase angle (right column) versus frequency. From top to bottom, the graphs show G_{11}, G_{12}, G_{21} and G_{22}.

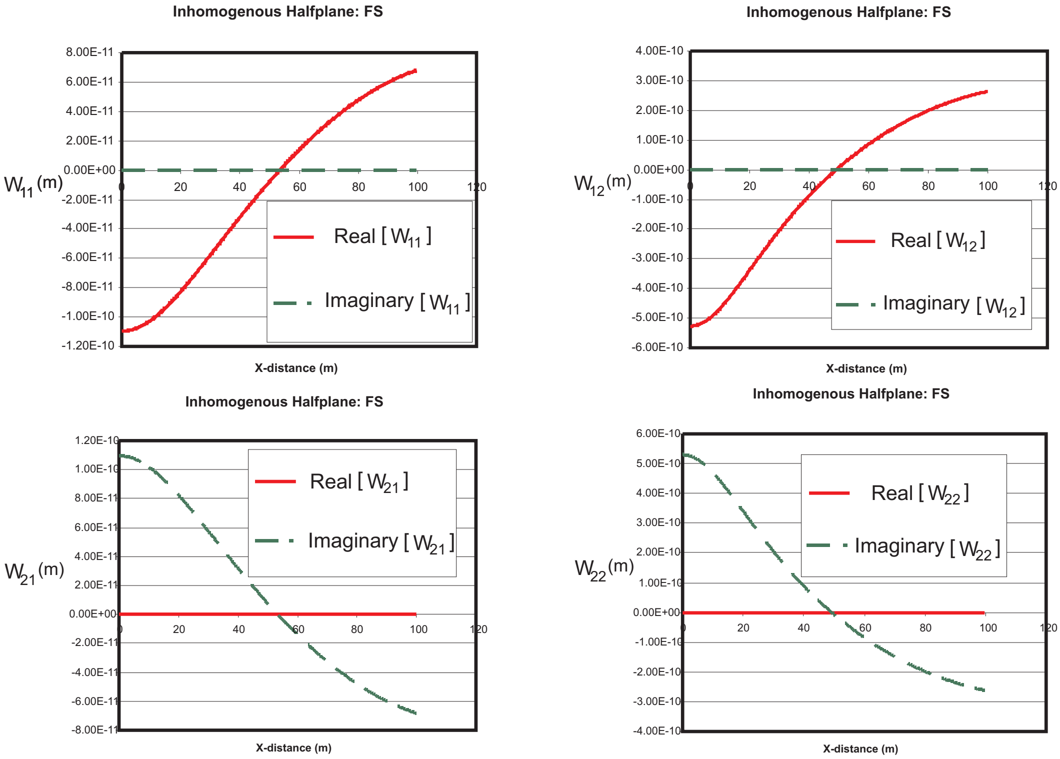

Figure 4. Inhomogeneous half-plane ($a = -0.0010$) Rayleigh-type fundamental solution components W_{11}, W_{12}, W_{21}, and W_{22}, at a frequency $\omega = 1.0$ rad/sec: real and imaginary parts versus distance along the surface.

waves are moving upwards in a medium with decreasing stiffness that is still larger than that of the equivalent homogeneous medium (but becomes equal to it at the surface). The same behavior holds true regarding the phase angle, i.e., there are some small differences between the two cases.. The situation is somewhat different regarding the Rayleigh-type correction. Starting with the homogeneous medium, this correction is substantial for the (1, 2) and (2, 2) components, and less so for the other two. The same trend holds for the inhomogeneous medium, but the correction is not a smoothly decreasing function of frequency as before. Instead, there are peaks at discrete frequency values such as $\omega = 1.5, 2.5, 3.5$ rad/sec. These local peaks are also manifested in the phase angle, with the exception when values that are nearly zero, as is the case with the (1, 1) and (1, 2) components.

In order to further investigate the behavior of the $W_{I,J}(x, \xi, \omega)$ components, Figures 4 and 5 show the variation of the Rayleigh-type solutions (both real and imaginary parts) along the free surface at a fixed value of the external frequency equal to $\omega = 1.0$ rad/sec for both inhomogeneous and equivalent homogeneous media. At first we note that in these solutions, either the real part (for the off-diagonal components) or the imaginary part (for the diagonal components) is zero. Next, these solutions decay slowly with increasing distance from the epicenter and show a sinusoidal type variation. The role of inhomogeneity is primarily seen in the magnitude of the nonzero components, in that they are quite more pronounced compared to the homogeneous medium case.

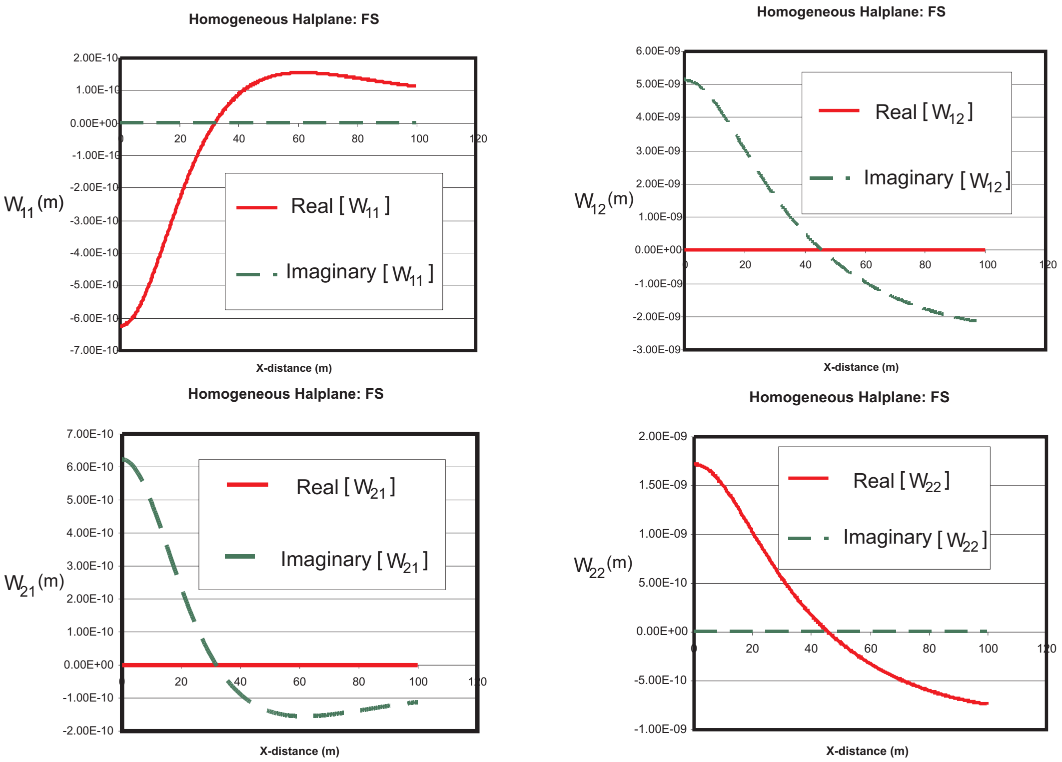

Figure 5. Homogenous half-plane Rayleigh-type fundamental solution components W_{11}, W_{12}, W_{21}, and W_{22}, at a frequency $\omega = 1.0$ rad/sec: real and imaginary parts versus distance along the surface.

We note in closing that approximate solutions using just one positive image source [Kontoni et al. 1987] lead to a doubling of the diagonal components of the displacement field and a zeroing of the off-diagonal ones in order to erase their corresponding traction contributions from the free surface. The use of a negative image source accomplishes the reverse. Thus, it is not possible to reproduce the correct traction conditions at the surface for all four components simultaneously, unless additional sources such as dipoles are added in the form of the Rayleigh integral [Kinoshita 1983].

6. Conclusions

In this work, we derived a new point-force solution in the continuously inhomogeneous half-plane with quadratic-type variation of all material parameters in terms of the depth coordinate. The solution comprises a complete elastic wave-train propagating outwards from the loaded area that satisfies traction-free boundary conditions along the horizontal surface. As such, solutions of this type are useful as kernel functions in boundary element method formulations of problems of engineering importance in elastodynamics and related fields of mechanics, with the added advantage that no free surface discretization is necessary.

Appendix: Elastostatic Green's functions for the half-plane

We derive here the Green's functions for the inhomogeneous half-plane as the external frequency of vibration tends to zero, i.e., the equivalent elastostatic forms. More specifically, based on the continuity of the Fourier transform as $\Im_{\eta\to x_1}(\lim_{\omega\to 0} g(\eta,\omega)) = \lim_{\omega\to 0}\Im_{\eta\to x_1}(g(\eta,\omega))$, it is sufficient to find the limit for $\omega \to 0$ of (22), (30) for the case $a < 0$ and of (39), (40) for $a = 0$.

To this purpose, we employ L'Hospital rule and re-define the wave numbers $k_j = q_j\omega$ in terms of the two wave slowness $q_1 = \sqrt{\rho_0/3\mu_0}$, $q_2 = \sqrt{\rho_0/\mu_0}$. Next, we define the following limit forms:

$$\begin{aligned}(\beta_j)'_\omega &= -\frac{q_j^2}{\sqrt{\eta^2 - q_j^2\omega^2}}\omega, \quad \text{with } \lim_{\omega\to 0}\frac{(\beta_j)'_\omega}{\omega} = -\frac{q_j^2}{|\eta|},\\ (\beta_1\beta_2)'_\omega &= -\frac{(q_1^2+q_2^2)\eta^2 - q_1^2q_2^2\omega^2}{\sqrt{(\eta^2 - q_1^2\omega^2)(\eta^2 - q_2^2\omega^2)}}\omega, \quad \text{with } \lim_{\omega\to 0}\frac{(\beta_1\beta_2)'_\omega}{\omega} = -(q_1^2+q_2^2),\end{aligned} \tag{A1}$$

$$\begin{aligned}(e^{\xi_2\beta_j})'_\omega &= -\frac{\xi_2 q_j^2 e^{\xi_2\beta_j}}{\sqrt{\eta^2 - q_j^2\omega^2}}\omega, \quad \text{with } \lim_{\omega\to 0}\frac{(e^{\xi_2\beta_j})'_\omega}{\omega} = -\frac{\xi_2 q_j^2 e^{\xi_2|\eta|}}{|\eta|},\\ (e^{x_2\beta_j})'_\omega &= -\frac{x_2 q_j^2 e^{x_2\beta_j}}{\sqrt{\eta^2 - q_j^2\omega^2}}\omega, \quad \text{with } \lim_{\omega\to 0}\frac{(e^{x_2\beta_j})'_\omega}{\omega} = -\frac{x_2 q_j^2 e^{x_2|\eta|}}{|\eta|},\end{aligned} \tag{A2}$$

where primes denote derivatives with respect to ω. For the limit of the determinant in (29) we have

$$\Delta^{a,0} = \lim_{\omega\to 0}\Delta^a = -\frac{\eta^2|\eta|\mu_0^2 a}{4\pi^2}, \tag{A3}$$

since

$$\lim_{\omega\to 0}\Delta^0 = 0.$$

For the coefficients appearing in (30), we set $D^{a,0}_{jm} = \lim_{\omega\to 0}\Delta^a_{jm}$, and by using (A1), (A2) and (27) we obtain the expressions

$$\begin{aligned}D^{a,0}_{11} &= \frac{h^{-1/2}(\xi_2)}{4q_2^2}\left[a\left(\frac{q_1^2+q_2^2}{|\eta|} + \xi_2(q_2^2-q_1^2)\right) + 2q_2^2 + 2\xi_2|\eta|(q_2^2-q_1^2)\right]e^{\xi_2|\eta|},\\ D^{a,0}_{21} &= \frac{i\eta h^{-1/2}(\xi_2)}{4q_2^2|\eta|}\left[3a\xi_2(q_1^2-q_2^2) + 2q_1^2 + 2\xi_2|\eta|(q_1^2-q_2^2)\right]e^{\xi_2|\eta|},\\ D^{a,0}_{12} &= -\frac{i\eta h^{-1/2}(\xi_2)}{4q_2^2|\eta|}\left[a\xi_2(q_1^2-q_2^2) + 2q_1^2 + 2\xi_2|\eta|(q_1^2-q_2^2)\right]e^{\xi_2|\eta|},\\ D^{a,0}_{22} &= \frac{h^{-1/2}(\xi_2)}{4q_2^2}\left[3a\left(\frac{q_1^2+q_2^2}{|\eta|} + \xi_2(q_1^2-q_2^2)\right) + 2q_2^2 + 2\xi_2|\eta|(q_1^2-q_2^2)\right]e^{\xi_2|\eta|}.\end{aligned} \tag{A4}$$

Also, by using (A3) , (A4) and (31) we recover

$$\begin{aligned}
\Delta_{11}^{a,0} &= \begin{vmatrix} -D_{11}^{a,0} & i\mu_0(-a|\eta|+2\eta^2) \\ -D_{21}^{a,0} & \mu_0\eta(-3a+2|\eta|) \end{vmatrix}, \quad \Delta_{21}^{a,0} = \begin{vmatrix} \mu_0\eta(-a+2|\eta|) & -D_{11}^{a,0} \\ i\mu_0(3a|\eta|-2\eta^2) & -D_{21}^{a,0} \end{vmatrix} \\
\Delta_{12}^{a,0} &= \begin{vmatrix} \mu_0\eta(-a+2|\eta|) & -D_{12}^{a,0} \\ i\mu_0(3a|\eta|-2\eta^2) & -D_{22}^{a,0} \end{vmatrix}, \quad \Delta_{22}^{a,0} = \begin{vmatrix} -D_{12}^{a,0} & i\mu_0(-a|\eta|+2\eta^2) \\ -D_{22}^{a,0} & \mu_0\eta(-3a+2|\eta|) \end{vmatrix}.
\end{aligned} \tag{A5}$$

Finally, the coefficients for the inhomogeneous case in (30) become

$$C_m^{k,a,0} = \lim_{\omega\to 0} C_m^k = \frac{\Delta_{mk}^{a,0}}{\Delta^{a,0}}. \tag{A6}$$

For completeness, we focus now on the homogeneous half-plane solution. First,

$$(\Delta_0)'_\omega = 4\eta^2(\beta_1\beta_2)'_\omega - 4(2\eta^2 - q_2^2\omega^2)q_2^2\omega, \quad \text{with } \lim_{\omega\to 0}\frac{(\Delta_0)'_\omega}{\omega} = 4\eta^2(q_1^2+3q_2^2). \tag{A7}$$

Next we set $\hat{D}_{jm}^0 = \lim_{\omega\to 0}\hat{D}_{jm}$, $\hat{\Delta}_{jm}^0 = \lim_{\omega\to 0}\hat{\Delta}_{jm}$, and by employing (A1), (A2) and (36) we obtain the following limits for the coefficients:

$$\begin{aligned}
&\hat{D}_{11}^0 = 0, \quad \hat{D}_{12}^0 = -\frac{i\eta}{4q_2^2|\eta|}\big[2q_1^2 + 2|\eta|\xi_2(q_1^2-q_2^2)\big]e^{\xi_2|\eta|}, \\
&\hat{D}_{21}^0 = \frac{i\eta}{4q_2^2|\eta|}\big[2q_1^2 + 2|\eta|\xi_2(q_1^2-q_2^2)\big]e^{\xi_2|\eta|}, \qquad \hat{D}_{22}^0 = 0.
\end{aligned} \tag{A8}$$

Because of (A7), the limit of (38) does not exist as $\omega\to 0$, but the limit of the coefficients $\hat{S}_{jm}$ does. By setting

$$\begin{aligned}
\bar{S}_{11} &= \frac{i\eta\mu_0}{\Delta^0}\left[(2\eta^2-k_2^2)e^{x_2\beta_2} - 2\beta_1\beta_2 e^{x_2\beta_1}\right], \quad \bar{S}_{21} = \frac{\beta_1\mu_0}{\Delta^0}\left[(2\eta^2-k_2^2)e^{x_2\beta_2} - 2\eta^2 e^{x_2\beta_1}\right], \\
\bar{S}_{12} &= \frac{\beta_2\mu_0}{\Delta^0}\left[-2\eta^2 e^{x_2\beta_2} + (2\eta^2-k_2^2)e^{x_2\beta_1}\right], \quad \bar{S}_{22} = \frac{i\eta\mu_0}{\Delta^0}\left[-2\beta_1\beta_2 e^{x_2\beta_2} + (2\eta^2-k_2^2)e^{x_2\beta_1}\right].
\end{aligned} \tag{A9}$$

we obtain

$$\begin{aligned}
\lim_{\omega\to 0}\hat{S}_{11} &= (\lim_{\omega\to 0}\bar{S}_{11})\hat{D}_{21}^0, \quad \lim_{\omega\to 0}\hat{S}_{21} = (\lim_{\omega\to 0}\bar{S}_{21})\hat{D}_{12}^0, \\
\lim_{\omega\to 0}\hat{S}_{12} &= (\lim_{\omega\to 0}\bar{S}_{12})\hat{D}_{12}^0, \quad \lim_{\omega\to 0}\hat{S}_{22} = (\lim_{\omega\to 0}\bar{S}_{22})\hat{D}_{21}^0.
\end{aligned}$$

Thus, the final expressions completing the elastostatic homogeneous case are

$$\begin{aligned}
\lim_{\omega\to 0}\bar{S}_{11} &= \frac{i\mu_0[x_2|\eta|(q_1^2-q_2^2)+q_1^2]}{\eta(q_1^2+3q_2^2)}e^{x_2|\eta|}, \quad \lim_{\omega\to 0}\bar{S}_{21} = \frac{\mu_0[x_2|\eta|(q_1^2-q_2^2)-q_2^2]}{\eta(q_1^2+3q_2^2)}e^{x_2|\eta|}, \\
\lim_{\omega\to 0}\bar{S}_{12} &= \frac{i\mu_0[x_2|\eta|(q_2^2-q_1^2)-q_1^2]}{\eta(q_1^2+3q_2^2)}e^{x_2|\eta|}, \quad \lim_{\omega\to 0}\bar{S}_{22} = \frac{i\mu_0[x_2|\eta|(q_2^2-q_1^2)+q_1^2]}{\eta(q_1^2+3q_2^2)}e^{x_2|\eta|}.
\end{aligned} \tag{A10}$$

References

[Achenbach 1973] J. D. Achenbach, *Wave propagation in elastic solids*, North Holland, Amsterdam, 1973.

[Bonchev et al. 1982] E. Bonchev, V. Bune, L. Christoskov, J. Karagyuleva, V. Kostadinov, G. Reisner, S. Rizikova, N. Shebalin, V. Sholpo, and D. Sokerova, "A method for compilation of seismic zoning prognostic maps for the territory of Bulgaria", *Geol. Balkanica* **12**:2 (1982), 3–48.

[Eringen and Şuhubi 1974] A. C. Eringen and E. S. Şuhubi, *Elastodynamics* (2 vol.), Academic Press, New York, 1974.

[Flugge 1967] W. Flugge, *Theory of viscoelasticity*, Blaisdell, Waltham, MA, 1967.

[Gradshteyn and Ryzhik 1980] I. S. Gradshteyn and I. M. Ryzhik, *Table of integrals, series, and products*, corrected and enlarged ed., Academic Press, New York, 1980.

[Guan et al. 1998] F. Guan, I. D. Moore, and C. C. Spyrakos, "Two dimensional transient fundamental solution due to suddenly applied load in a half-space", *Soil Dyn. Earthquake Eng.* **17** (1998), 269–277.

[Kausel 2006] E. Kausel, *Fundamental solutions in elastodynamics: a compendium*, Cambridge University Press, Cambridge, 2006.

[Kausel and Manolis 2000] E. Kausel and G. D. Manolis (editors), *Wave motion problems in earthquake engineering*, WIT Press, Southampton, 2000.

[Kinoshita 1983] M. Kinoshita, M.Sc. thesis, Department of Civil Engineering, Kyoto University, 1983. in Japanese; quoted in [Kobayashi 1983].

[Kobayashi 1983] S. Kobayashi, "Some problems of the boundary integral equation method in elastodynamics", pp. 775–784 in *Boundary elements V*, edited by C. A. Brebbia et al., Springer, Berlin, 1983.

[Kontoni et al. 1987] D. P. N. Kontoni, D. E. Beskos, and G. D. Manolis, "Uniform half-plane elastodynamic problems by an approximate boundary element method", *Soil Dyn. Earthquake Eng.* **6** (1987), 227–238.

[Manolis and Beskos 1988] G. D. Manolis and D. E. Beskos, *Boundary element methods in elastodynamics*, Unwin and Allen, London, 1988.

[Manolis and Shaw 1996] G. D. Manolis and R. P. Shaw, "Green's function for the vector wave equation in a mildly heterogeneous continuum", *Wave Motion* **24**:1 (1996), 59–83.

[Rajapakse and Wang 1991] R. K. N. D. Rajapakse and Y. Wang, "Elastodynamic Green's functions of orthotropic half plane", *J. Eng. Mech.* (*ASCE*) **117**:3 (1991), 588–604.

Received 4 Feb 2010. Revised 15 Sep 2010. Accepted 29 Sep 2010.

TSVIATKO V. RANGELOV: rangelov@math.bas.bg
Department of Mathematical Physics, Institute of Mathematics and Informatics, Bulgarian Academy of Sciences,,
acad. G. Bonchev str. bl. 8, 1113 Sofia, Bulgaria

GEORGE D. MANOLIS: gdm@civil.auth.gr
Department of Civil Engineering, Aristotle University, 54124 Thessaloniki, Greece

JOURNAL OF MECHANICS OF MATERIALS AND STRUCTURES
Vol. 5, No. 6, 2010

AN ENHANCED ASYMPTOTIC EXPANSION FOR THE STABILITY OF NONLINEAR ELASTIC STRUCTURES

CLAUS DENCKER CHRISTENSEN AND ESBEN BYSKOV

A new, enhanced asymptotic expansion applicable to stability of structures made of nonlinear elastic materials is established. The method utilizes "hyperbolic" terms instead of the conventional polynomial terms, covers full kinematic nonlinearity and is applied to nonlinear elastic Euler columns with two different types of cross-section. Comparison with numerical results show that our expansion provides more accurate predictions of the behavior than usual expansions.

The method is based on an extended version of the principle of virtual displacements that covers cases with auxiliary conditions, such as inextensibility. Membrane locking and similar problems are also handled by the method.

Part I. Theory

1. Introduction

The asymptotic expansions for elastic postbuckling and imperfection sensitivity originally introduced in [Koiter 1945] may be applied to any linearly elastic structure that experiences bifurcation instability in its geometrically perfect realization. There is, however, an inherent problem with these expansions, in that they employ polynomial terms, which means that the predictions of carrying capacities are inaccurate because the term of highest order approaches plus or minus infinity depending on its sign. This is, of course, not a desirable situation; it may be mended by exploiting some of the ideas introduced in [Christensen and Byskov 2008]. In particular, the concept of enhancing asymptotic expansions by using hyperbolic instead of polynomial terms is central here.

A set of explicit expressions for the coefficients of asymptotic elastic postbuckling and imperfection sensitivity analysis, applicable to linearly elastic structures with moderately large strains, linear loads and linear prebuckling was first proposed in [Budiansky and Hutchinson 1964]. Soon afterward, Fitch [1968] modified this to include nonlinear prebuckling. Later Byskov et al. [1996] extended the previous expansions to include loads which are nonlinear to fourth order in the displacements, and introduced Lagrange multiplier terms to fourth order in the displacements. The Lagrange multiplier terms provide a way to impose constraints on the structure, such as inextensibility, and a way of handling numerical phenomena such as membrane locking.

Here, we concentrate on two main subjects. The first is the development of a general asymptotic method akin to the one in [Byskov et al. 1996], but with strains, constraints and loads that may be arbitrarily nonlinear in the displacements. The constitutive relation is taken to be nonlinear elastic. Our second focus is the application of the enhanced asymptotic expansion developed in [Christensen and

Keywords: elastic stability, full nonlinearity, asymptotic expansion.

Byskov 2008], where we utilized the expansion to study postbuckling and imperfection sensitivity of the so-called Shanley–Hutchinson model column; see, e.g., [Hutchinson 1974]. In the present study this expansion is applied to the more realistic case of a nonlinear elastic Euler column.

2. Principle of virtual displacements

Consider a structure which, when it is geometrically perfect, experiences bifurcation at a certain critical load level λ_c. In order to investigate the behavior of the perfect structure and the influence of small geometric imperfections for situations in the vicinity of the critical load, we follow ideas from [Koiter 1945] and [Budiansky 1974], and use the perfect structure as a basis for the group of structures that only differ from the perfect one by an initial geometric imperfection. Regard the initial geometric imperfection as a small stress-free displacement $\hat{\boldsymbol{u}}$, which is not necessarily forced to obey the kinematic boundary conditions and does not depend on the actual stress and deformation state in the structure. A full nonlinear *modified principle of virtual displacements* including *Lagrange multiplier* terms, as previous used in [Byskov et al. 1996], for example, and nonlinear elasticity, may in general be written

$$\boldsymbol{P}(\boldsymbol{u},\lambda,\hat{\boldsymbol{u}})=\boldsymbol{\sigma}(\Delta\boldsymbol{\varepsilon})\cdot\delta\Delta\boldsymbol{\varepsilon}(\boldsymbol{u},\hat{\boldsymbol{u}})-\delta\left[\boldsymbol{\eta}\cdot\boldsymbol{C}(\boldsymbol{u},\hat{\boldsymbol{u}})\right]-\lambda\delta\Delta\boldsymbol{B}(\boldsymbol{u},\hat{\boldsymbol{u}})=0, \tag{1}$$

where $\boldsymbol{u}$ is defined as an extended field of additional displacements that may include both derivatives of the basic displacements with respect to position and Lagrange multipliers, $\boldsymbol{\varepsilon}$ is the strain measured on the perfect structure, $\boldsymbol{\sigma}$ the nonlinear elastic stress, λ is a scalar load parameter, $\boldsymbol{B}$ is a nonlinear loading functional based on the perfect structure, $\boldsymbol{C}$ contains the appropriate constraints with associated Lagrange multiplier fields $\boldsymbol{\eta}$, and Δ indicates the difference between nondeformed and deformed states. Finally, following the notation in [Budiansky and Hutchinson 1964], a dot ($\cdot$) signifies a generalized inner product over the entire structure.

For later purposes, let $\boldsymbol{u}$ include n components u and define

$$\boldsymbol{u}=\{u^1,u^2,\dots,u^n\}=u^i. \tag{2}$$

According to these definitions,

$$\Delta\boldsymbol{\varepsilon}=\boldsymbol{\varepsilon}(\boldsymbol{u}+\hat{\boldsymbol{u}})-\boldsymbol{\varepsilon}(0+\hat{\boldsymbol{u}}),\quad \Delta\boldsymbol{B}=\boldsymbol{B}(\boldsymbol{u}+\hat{\boldsymbol{u}})-\boldsymbol{B}(0+\hat{\boldsymbol{u}}). \tag{3}$$

The principle of virtual displacements depends linearly on the virtual displacements $\delta\boldsymbol{u}$ and may be written as

$$\boldsymbol{P}=\delta u^l\cdot\boldsymbol{p}_l=0, \tag{4}$$

where

$$\boldsymbol{p}_l=\boldsymbol{\sigma}\,(\Delta\boldsymbol{\varepsilon})\cdot\frac{\partial\boldsymbol{\varepsilon}(\boldsymbol{u}+\hat{\boldsymbol{u}})}{\partial u^l}-\frac{\partial\,[\boldsymbol{\eta}\cdot\boldsymbol{C}]}{\partial u^l}-\lambda\frac{\partial\boldsymbol{B}(\boldsymbol{u}+\hat{\boldsymbol{u}})}{\partial u^l}. \tag{5}$$

Note that $\boldsymbol{p}_l$ does not depend on $\delta\boldsymbol{u}$.

3. Perturbation expansion

Let the load be controlled by the scalar load parameter λ. When λ is close to its classical critical value λ_c, the displacement field $\boldsymbol{u}$, the scalar load parameter λ, and the principle of virtual displacements $\boldsymbol{P}(u^i,\lambda,\hat{u}^i)$ may be expanded in perturbation series around the prebuckling solution in the spirit of, for instance, [Budiansky and Hutchinson 1964; Budiansky 1974; Byskov et al. 1996]. Let us choose a characteristic buckling amplitude ξ, which vanishes at the critical point, as our perturbation parameter. Further, let $\bar{\xi}$ denote a characteristic amplitude of the imperfection shape $\tilde{\boldsymbol{u}}$:

$$\hat{\boldsymbol{u}} = \bar{\xi}\tilde{\boldsymbol{u}}. \tag{6}$$

It is our purpose to establish a formula for the maximum value of λ for a given value $\bar{\xi}$ of the imperfection amplitude.

Following [Budiansky 1974] we may imagine that in the space $(\bar{\xi}, \xi, \lambda)$ the values of λ form a surface and assume that the following relation is valid for small values of ξ, $\bar{\xi}$ and $|\lambda - \lambda_c|$:

$$\bar{\xi} = \alpha\xi^{\gamma} \tag{7}$$

where the coefficient α and the exponent γ both are scalars, and the value $\alpha = 0$ implies the traditional postbuckling path.

By choosing values of α and γ appropriately we may reach any point in the $(\bar{\xi}, \xi)$-plane, in particular the point associated with $\lambda_{\max}$, as indicated in Figure 1. In our search for the above mentioned maximum value of λ we select the value $\gamma = 2$ and determine the value of α by inserting (7) into the equations for the boundary value problem for the geometrically imperfect structure after having made an asymptotic expansion in terms of the characteristic buckling amplitude ξ. We shall assume that a perturbation expansion for the equilibria on which (7) holds may be written

$$\frac{\lambda}{\lambda_c} = 1 + \frac{\Delta\lambda}{\lambda_c} = 1 + \bar{a}_1\xi + \bar{a}_2\xi^2 + \bar{a}_3\xi^3 + O(\xi^4). \tag{8}$$

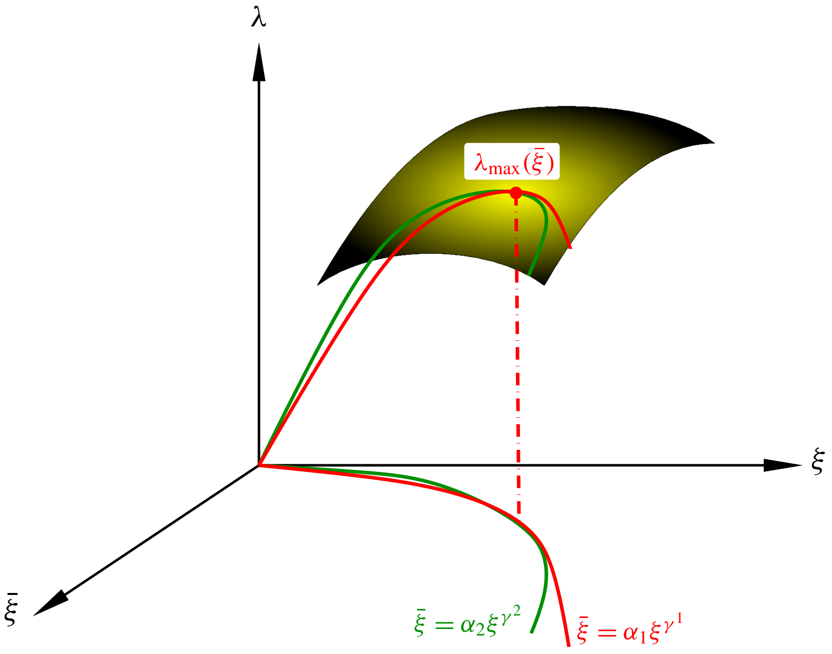

Figure 1. Prebuckling and equilibrium paths on which $\bar{\xi} = \alpha\xi^{\gamma}$ close to bifurcation.

Any such solution to the principle of virtual work includes parts of the prebuckling displacements $\boldsymbol{u}_0$, where subscript $_0$ indicates the prebuckling path. In anticipation of this we write the solution close to prebuckling as

$$\boldsymbol{u} = \boldsymbol{u}_0(\lambda) + \Delta\boldsymbol{u} = \bar{\boldsymbol{u}}_0(\lambda) + \xi\bar{\boldsymbol{u}}_1 + \xi^2\bar{\boldsymbol{u}}_2 + \xi^3\bar{\boldsymbol{u}}_3 + O(\xi^4). \tag{9}$$

The perturbation coefficients $\bar{a}_i$ and $\bar{\boldsymbol{u}}_i$ may be split into a part independent of α and a part which depends on α and vanishes when $\alpha = 0$:

$$\bar{a}_i = a_i + a_i^{\alpha}, \quad \bar{\boldsymbol{u}}_i = \boldsymbol{u}_i + \boldsymbol{u}_i^{\alpha}. \tag{10}$$

Now $\boldsymbol{P}$ may be expanded in terms of ξ through its dependence on λ and $\boldsymbol{u}$:

$$\boldsymbol{P} = \boldsymbol{P}_0(\lambda) + \Delta\boldsymbol{P} = \boldsymbol{P}_0(\lambda) + \xi\boldsymbol{P}_1 + \xi^2\boldsymbol{P}_2 + \xi^3\boldsymbol{P}_3 + O(\xi^4) = 0. \tag{11}$$

4. Asymptotic problems

Since the prebuckling path is a solution to the principle of virtual displacements (1), the prebuckling term of (11) is identically zero, i.e., $\boldsymbol{P}_0(\lambda) \equiv 0$. Therefore the matched asymptotic expansion (11) may be rewritten as

$$\Delta\boldsymbol{P} = \boldsymbol{P}(\boldsymbol{u}_0 + \Delta\boldsymbol{u}, \lambda) - \boldsymbol{P}(\boldsymbol{u}_0, \lambda) = \xi\boldsymbol{P}_1 + \xi^2\boldsymbol{P}_2 + \xi^3\boldsymbol{P}_3 + O(\xi^4) = 0, \tag{12}$$

where we demand that (12) is fulfilled exactly for all values of the expansion parameter ξ and obtain the higher-order asymptotic stability problems according to the order in ξ:

first-order problem $\boldsymbol{P}_1 = 0$ (13)

second-order problem $\boldsymbol{P}_2 = 0$ (14)

third-order problem $\boldsymbol{P}_3 = 0$ (15)

4.1. *First-, second- and third-order problems.*

In order to solve the asymptotic problems (13)–(15), the three high-order operators $\boldsymbol{P}_i$ $(i = 1, 2, 3)$ must be expressed in terms of the expansion coefficients of the basic variables, i.e., $\bar{\boldsymbol{u}}_i$ and $\bar{a}_i$. Prebuckling fields may be considered known at bifurcation and derivatives with respect to the scalar load parameter λ are defined:

$$(\;)' \equiv \frac{d(\;)}{d\lambda}. \tag{16}$$

In the following, subscript $_c$ or superscript ^{c} designates prebuckling values taken at bifurcation. From (12) it is evident that $\boldsymbol{P}_i$ are the coefficient fields of an expansion in ξ of the prebuckling solution given in Appendix B subtracted from the full postbuckling solution. In Appendix A this approach has been utilized to provide the higher-order problems $\boldsymbol{P}_i$ provided that $\boldsymbol{P}$ has continuous derivatives at least up til fourth order with respect to $\bar{u}^i$. This ensures that the indices (i, j, k) in the below expressions for $\boldsymbol{P}_1$, $\boldsymbol{P}_2$ and $\boldsymbol{P}_3$ may be swapped freely:

$$\boldsymbol{P}_1 = \boldsymbol{P}^c_{,i} \cdot \bar{u}^i_1, \tag{17}$$

$$\boldsymbol{P}_2 = \boldsymbol{P}^c_{,i} \cdot \bar{u}^i_2 + \tfrac{1}{2}\boldsymbol{P}^c_{,ij} \cdot [\bar{u}^i_1 \bar{u}^j_1] + \bar{a}_1 \lambda_c (\delta \boldsymbol{B}^c_{,i} + \boldsymbol{P}^c_{,ij} u^{j'}_c) \cdot \bar{u}^i_1 + \alpha \tilde{\boldsymbol{u}}(\boldsymbol{P}^c_{,\hat{\boldsymbol{u}}}), \tag{18}$$

$$\begin{aligned} \boldsymbol{P}_3 = {} & \boldsymbol{P}^c_{,i} \cdot \bar{u}^i_3 + \boldsymbol{P}^c_{,ij} \cdot [\bar{u}^i_2 \bar{u}^j_1] + \tfrac{1}{6}\boldsymbol{P}^c_{,ijk} \cdot [\bar{u}^i_1 \bar{u}^j_1 \bar{u}^k_1] + \bar{a}_2 \lambda_c (\delta \boldsymbol{B}^c_{,i} + \boldsymbol{P}^c_{,ij} u^{j'}_c) \cdot \bar{u}^i_1 \\ & + \bar{a}_1 \lambda_c \big[(\delta \boldsymbol{B}^c_{,i} + \boldsymbol{P}^c_{,ij} u^{j'}_c) \cdot \bar{u}^i_2 + \tfrac{1}{2} (\delta \boldsymbol{B}^c_{,ij} + \boldsymbol{P}^c_{,ijk} u^{k'}_c) \cdot [\bar{u}^i_1 \bar{u}^j_1] \big] \\ & + (\bar{a}_1 \lambda_c)^2 \big(\delta \boldsymbol{B}^c_{,ij} u^{j'}_c + \tfrac{1}{2} \boldsymbol{P}^c_{,ijk} [u^{j'}_c u^{k'}_c] + \tfrac{1}{2} \boldsymbol{P}^c_{,ij} u^{j''}_c \big) \cdot \bar{u}^i_1 \\ & + \alpha \tilde{\boldsymbol{u}} \cdot \big[\bar{a}_1 \lambda_c (\delta \Delta \boldsymbol{B}^c_{,\hat{\boldsymbol{u}}} + \boldsymbol{P}^c_{,i\hat{\boldsymbol{u}}} u^{i'}_c) + \boldsymbol{P}^c_{,i\hat{\boldsymbol{u}}} \bar{u}^i_1 \big], \end{aligned} \tag{19}$$

where, according to (4),

$$\boldsymbol{P}_{,i\ldots k} = \delta u^l \cdot \boldsymbol{p}_{l,i\ldots k} = \frac{\partial^n \boldsymbol{P}}{\partial u^i \ldots \partial u^k} \quad \text{and} \quad \boldsymbol{P}_{,\hat{\boldsymbol{u}}} = \delta u^l \cdot \boldsymbol{p}_{l,\hat{\boldsymbol{u}}} = \frac{\partial \boldsymbol{P}}{\partial \hat{u}^i} \tag{20}$$

and it is utilized that

$$\boldsymbol{P}_{,\lambda i\ldots k} = \delta \boldsymbol{B}_{i\ldots k} = \delta u^l \cdot \boldsymbol{B}_{,li\ldots k}. \tag{21}$$

4.2. ***Stability operators.*** In the first- to third-order problems, (17)–(19), a number of scalar operators may be identified, which we call the *stability operators*. These operators are given directly by the loading conditions, the strain measure, the stress-strain relation, the constraints, and the imperfection shape. In the following, the subscript of the operators indicates their degree.

Operators not acting on the imperfection shape. The following stability operators always enter the stability problems. Below the displacement fields, $\boldsymbol{u}_\alpha$, $\boldsymbol{u}_\beta$, $\boldsymbol{u}_\gamma$ and $\boldsymbol{u}_\delta$ may be any displacement field:

$$\begin{aligned} \mathcal{P}^c_1(\boldsymbol{u}_\alpha) &= \boldsymbol{p}^c_l \cdot [u^l_\alpha], \\ \mathcal{P}^c_2(\boldsymbol{u}_\alpha, \boldsymbol{u}_\beta) &= \boldsymbol{p}^c_{l,i} \cdot [u^l_\alpha u^i_\beta], \\ \mathcal{P}^c_3(\boldsymbol{u}_\alpha, \boldsymbol{u}_\beta, \boldsymbol{u}_\gamma) &= \boldsymbol{p}^c_{l,ij} \cdot [u^l_\alpha u^i_\beta u^j_\gamma], \\ \mathcal{P}^c_4(\boldsymbol{u}_\alpha, \boldsymbol{u}_\beta, \boldsymbol{u}_\gamma, \boldsymbol{u}_\delta) &= \boldsymbol{p}^c_{l,ijk} \cdot [u^l_\alpha u^i_\beta u^j_\gamma u^k_\delta], \end{aligned} \tag{22}$$

$$\begin{aligned} \mathcal{B}^c_1(\boldsymbol{u}_\alpha) &= \boldsymbol{B}^c_{,l} \cdot [u^l_\alpha], \\ \mathcal{B}^c_2(\boldsymbol{u}_\alpha, \boldsymbol{u}_\beta) &= \boldsymbol{B}^c_{,li} \cdot [u^l_\alpha u^i_\beta], \\ \mathcal{B}^c_3(\boldsymbol{u}_\alpha, \boldsymbol{u}_\beta, \boldsymbol{u}_\gamma) &= \boldsymbol{B}^c_{,lij} \cdot [u^l_\alpha u^i_\beta u^j_\gamma], \\ \mathcal{B}^c_4(\boldsymbol{u}_\alpha, \boldsymbol{u}_\beta, \boldsymbol{u}_\gamma, \boldsymbol{u}_\delta) &= \boldsymbol{B}^c_{,lijk} \cdot [u^l_\alpha u^i_\beta u^j_\gamma u^k_\delta]. \end{aligned} \tag{23}$$

It is easily shown that $\boldsymbol{p}^c_{l,i\ldots k}$ is not influenced by the imperfection since $\hat{\boldsymbol{u}} = \bar{\xi}\tilde{\boldsymbol{u}} = \alpha\xi^2\tilde{\boldsymbol{u}}$ vanishes at the critical load. Thus $\mathcal{P}^c_i$ and $\mathcal{B}^c_i$ only depend indirectly on the geometric imperfection through the displacements they operate on.

Operators acting on the imperfection shape. These operators enter only when imperfections are present ($\alpha \neq 0$) and operate directly on the imperfection shape, $\tilde{\boldsymbol{u}}$:

$$\bar{\mathcal{P}}^c_2(\boldsymbol{u}_\alpha, \tilde{\boldsymbol{u}}) = \boldsymbol{p}^c_{l,\hat{\boldsymbol{u}}} \cdot [u^l_\alpha \tilde{\boldsymbol{u}}] \quad \text{and} \quad \bar{\mathcal{P}}^c_3(\boldsymbol{u}_\alpha, \boldsymbol{u}_\beta, \tilde{\boldsymbol{u}}) = \boldsymbol{p}^c_{l,i\hat{\boldsymbol{u}}} \cdot [u^l_\alpha u^i_\beta \tilde{\boldsymbol{u}}], \tag{24}$$

$$\bar{\mathcal{B}}^c_2(\boldsymbol{u}_\alpha, \tilde{\boldsymbol{u}}) = \Delta \boldsymbol{B}^c_{,l\hat{\boldsymbol{u}}} \cdot [u^l_\alpha \tilde{\boldsymbol{u}}] = \boldsymbol{B}^c_{,li} \cdot [u^l_\alpha \tilde{u}^i] \tag{25}$$

5. Bifurcation

The first-order problem (13) is referred to as the eigenvalue problem at bifurcation as it is used to determine the critical load λ_c and its associated bifurcation mode $\bar{\boldsymbol{u}}_1$, which is not necessarily identical to the traditional buckling mode $\boldsymbol{u}_1$ because imperfections may interact. Insert $\boldsymbol{P}_1$ as given by (17) in the first-order problem (13) to furnish

$$0 = \mathcal{P}_2^c(\bar{\boldsymbol{u}}_1, \delta\boldsymbol{u}), \tag{26}$$

where the first postcritical constant $\bar{a}_1$ does not enter. Thus, $\bar{\boldsymbol{u}}_1$ is simply determined as an eigenfield of (26) at the critical load, fixed by the characteristic amplitude ξ. As (26) is independent of the imperfection because the characteristic amplitude is only an expansion parameter, the first postcritical displacement field does not depend on the imperfection, and (10) yields

$$\bar{\boldsymbol{u}}_1 = \boldsymbol{u}_1 \text{ and } \boldsymbol{u}_1^\alpha = 0. \tag{27}$$

6. Higher-order problems

The main purpose of the higher-order problems (14) and (15) which are sometimes called the *postcritical problems*, is to provide a relation between the expansion parameter ξ, which usually is identified as some characteristic buckling mode amplitude, and the load level characterized by the value of the load parameter λ. In order to do this, we need the values of the constants $\bar{a}_1, \bar{a}_2, \dots$, which determine the initial displacement-load relation after the classical critical load has been reached. Therefore, the higher-order displacement fields $\bar{\boldsymbol{u}}_2, \dots$, must be found. Interest is, however, usually focused on determining the first nonvanishing postcritical constant. In the case of an unsymmetric structure, or a symmetric structure loaded unsymmetrically, the first postbuckling constant $a_1 = 0$ does not vanish, and we shall not need more than the buckling field $\boldsymbol{u}_1$. On the other hand, when the structure as well as the load is symmetric $\bar{a}_1$ becomes zero, and we need to determine the higher order displacement field $\boldsymbol{u}_2$ and the higher-order postbuckling constant $\bar{a}_2$. When $\bar{a}_1 = 0$ computation of $\hat{a}_2$ is simplified because in this case certain terms vanish from the higher order problems.

6.1. ***First postcritical problem.*** The first postcritical problem (14) determines the second order displacements $\bar{\boldsymbol{u}}_2$ and the first-order postcritical constant, $\bar{a}_1$, when the first-order displacement field has been determined by the buckling problem. Introduce $\boldsymbol{P}_2$ in (14) to obtain

$$0 = \mathcal{P}_2^c(\bar{\boldsymbol{u}}_2, \delta\boldsymbol{u}) + \tfrac{1}{2}\mathcal{P}_3^c(\boldsymbol{u}_1, \boldsymbol{u}_1, \delta\boldsymbol{u}) + \bar{a}_1\lambda_c\big(\mathcal{B}_2^c(\boldsymbol{u}_1, \delta\boldsymbol{u}) + \mathcal{P}_3^c(\boldsymbol{u}_c', \boldsymbol{u}_1, \delta\boldsymbol{u})\big) + \alpha\bar{\mathcal{P}}_2^c(\tilde{\boldsymbol{u}}, \delta\boldsymbol{u}). \tag{28}$$

First postcritical constant. To determine the first postcritical constant $\bar{a}_1$ introduce $\delta u^l = \bar{u}_2^l$ in the buckling problem (26) and subtract it from the first postcritical problem (28) with $\delta u^l = u_1^l$ and exploit that, as shown in Appendix C, $\boldsymbol{p}_{l,i}^c = \boldsymbol{p}_{i,l}^c$ and eliminate the unknown postcritical displacement field $\bar{u}_2^i$ from the problem. The solution takes the form

$$\bar{a}_1 = a_1 + a_1^\alpha = a_1 + \alpha\rho_1, \tag{29}$$

where we for later use define a_1 and ρ_1 by

$$a_1 = \frac{a_1^N}{a_1^D}\frac{1}{\lambda_c} \quad \text{and} \quad \rho_1 = \frac{\rho_1^N}{a_1^D}\frac{1}{\lambda_c}, \tag{30}$$

with

$$a_1^N = -\tfrac{1}{2}\mathcal{P}_3^c(\boldsymbol{u}_1, \boldsymbol{u}_1, \boldsymbol{u}_1), \quad \rho_1^N = -\bar{\mathcal{P}}_2^c(\tilde{\boldsymbol{u}}, \boldsymbol{u}_1), \tag{31}$$

and

$$a_1^D = \mathcal{B}_2^c(\boldsymbol{u}_1, \boldsymbol{u}_1) + \mathcal{P}_3^c(\boldsymbol{u}_c', \boldsymbol{u}_1, \boldsymbol{u}_1). \tag{32}$$

Postcritical displacement field. When $\bar{a}_1$ has been determined $\bar{\boldsymbol{u}}_2$ is found as a particular solution of the first postcritical problem (28) where $\bar{\boldsymbol{u}}_2$ only enters linearly. It appears from (28) that the complete solution for this problem takes the form

$$\bar{\boldsymbol{u}}_2 = c_1\boldsymbol{u}_1 + \bar{\boldsymbol{u}}_2^{\text{partic}}. \tag{33}$$

In principle the arbitrary constant c_1 may be chosen freely. Each specific choice will only lead to a different interpretation of the expansion parameter ξ. Conversely, c_1 is fixed when ξ has been chosen. Often some orthogonality condition between the buckling displacement $\boldsymbol{u}_1$ and the postcritical displacement $\bar{\boldsymbol{u}}_2$ is enforced in order to exclude domination of the buckling field on the postcritical field in (33); see, e.g., [Fitch 1968; Budiansky 1974; Byskov et al. 1996]. Since $\bar{\boldsymbol{u}}_1$ does not depend on the imperfection, and because $\bar{a}_1$ depends linearly on α, $\boldsymbol{u}_2$ and $\boldsymbol{u}_2^\alpha$ may be found separately from (28), where we note that $\boldsymbol{u}_2^\alpha$ depends linearly on α. The variational equation for $\boldsymbol{u}_2$ is

$$0 = \mathcal{P}_2^c(\boldsymbol{u}_2, \delta\boldsymbol{u}) + \tfrac{1}{2}\mathcal{P}_3^c(\boldsymbol{u}_1, \boldsymbol{u}_1, \delta\boldsymbol{u}) + a_1\lambda_c\left(\mathcal{B}_2^c(\boldsymbol{u}_1, \delta\boldsymbol{u}) + \mathcal{P}_3^c(\boldsymbol{u}_c', \boldsymbol{u}_1, \delta\boldsymbol{u})\right) \tag{34}$$

and the equation for $\boldsymbol{u}_2^\alpha = \alpha\boldsymbol{v}_2$ becomes

$$0 = \mathcal{P}_2^c(\boldsymbol{v}_2, \delta\boldsymbol{u}) + \bar{\mathcal{P}}_2^c(\tilde{\boldsymbol{u}}, \delta\boldsymbol{u}) + \rho_1\lambda_c\left(\mathcal{B}_2^c(\boldsymbol{u}_1, \delta\boldsymbol{u}) + \mathcal{P}_3^c(\boldsymbol{u}_c', \boldsymbol{u}_1, \delta\boldsymbol{u})\right). \tag{35}$$

Note that α does not enter (35), and therefore $\boldsymbol{v}_2$ does not depend on α.

6.2. *Second postcritical problem.*

The sole purpose of the second postcritical problem (15) is to determine the second postcritical constant $\bar{a}_2$. Utilize $\boldsymbol{P}_3$ in (15) to provide a problem depending on $\bar{a}_2$, $\bar{\boldsymbol{u}}_3$ and lower-order fields alone:

$$\begin{aligned}0 = \mathcal{P}_2^c(\bar{\boldsymbol{u}}_3, \delta\boldsymbol{u}) &+ \mathcal{P}_3^c(\bar{\boldsymbol{u}}_2, \boldsymbol{u}_1, \delta\boldsymbol{u}) + \tfrac{1}{6}\mathcal{P}_4^c(\boldsymbol{u}_1, \boldsymbol{u}_1, \boldsymbol{u}_1, \delta\boldsymbol{u}) + \bar{a}_2\lambda_c\left(\mathcal{B}_2^c(\boldsymbol{u}_1, \delta\boldsymbol{u}) + \mathcal{P}_3^c(\boldsymbol{u}_c', \boldsymbol{u}_1, \delta\boldsymbol{u})\right)\\ &+ \bar{a}_1\lambda_c\left(\mathcal{B}_2^c(\bar{\boldsymbol{u}}_2, \delta\boldsymbol{u}) + \mathcal{P}_3^c(\boldsymbol{u}_c', \bar{\boldsymbol{u}}_2, \delta\boldsymbol{u}) + \tfrac{1}{2}\mathcal{B}_3^c(\boldsymbol{u}_1, \boldsymbol{u}_1, \delta\boldsymbol{u}) + \tfrac{1}{2}\mathcal{P}_4^c(\boldsymbol{u}_c', \boldsymbol{u}_1, \boldsymbol{u}_1, \delta\boldsymbol{u})\right)\\ &+ (\bar{a}_1\lambda_c)^2\left(\mathcal{B}_3^c(\boldsymbol{u}_c', \boldsymbol{u}_1, \delta\boldsymbol{u}) + \tfrac{1}{2}\mathcal{P}_4^c(\boldsymbol{u}_c', \boldsymbol{u}_c', \boldsymbol{u}_1, \delta\boldsymbol{u}) + \tfrac{1}{2}\mathcal{P}_3^c(\boldsymbol{u}_c'', \boldsymbol{u}_1, \delta\boldsymbol{u})\right)\\ &+ \alpha\left(\bar{\mathcal{P}}_3^c(\boldsymbol{u}_1, \tilde{\boldsymbol{u}}, \delta\boldsymbol{u}) + \bar{a}_1\lambda_c(\bar{\mathcal{B}}_2^c(\tilde{\boldsymbol{u}}, \delta\boldsymbol{u}) + \bar{\mathcal{P}}_3^c(\boldsymbol{u}_c', \tilde{\boldsymbol{u}}, \delta\boldsymbol{u}))\right).\end{aligned} \tag{36}$$

Second postcritical constant. The second postcritical constant $\bar{a}_2$ is determined by a procedure similar to the one used to calculate the first postcritical constant $\bar{a}_1$. Let $\delta u^l = \bar{u}_3^l$ in the buckling problem (26) and subtract it from the second postcritical problem (36) with $\delta u^l = u_1^l$ to eliminate the unknown postcritical displacement field $\bar{u}_3^i$ from the problem:

$$\bar{a}_2\lambda_c = (a_2 + a_2^\alpha)\lambda_c = (a_2 + \rho_2\alpha + \rho_3\alpha^2)\lambda_c = \frac{(a_2^N + \rho_2^N\alpha + \rho_3^N\alpha^2)}{a_1^D}. \tag{37}$$

Here, a_1^D is determined earlier by (32) and a_2^N, a_2, ρ_i^N and ρ_i are parameters that do not depend on α:

$$\begin{aligned}
a_2^N =& -\mathcal{P}_3^c(\boldsymbol{u}_2,\boldsymbol{u}_1,\boldsymbol{u}_1)-\tfrac{1}{6}\mathcal{P}_4^c(\boldsymbol{u}_1,\boldsymbol{u}_1,\boldsymbol{u}_1,\boldsymbol{u}_1)\\
&-a_1\lambda_c\left(\mathcal{B}_2^c(\boldsymbol{u}_2,\boldsymbol{u}_1)+\mathcal{P}_3^c(\boldsymbol{u}_c',\boldsymbol{u}_2,\boldsymbol{u}_1)+\tfrac{1}{2}\mathcal{B}_3^c(\boldsymbol{u}_1,\boldsymbol{u}_1,\boldsymbol{u}_1)+\tfrac{1}{2}\mathcal{P}_4^c(\boldsymbol{u}_c',\boldsymbol{u}_1,\boldsymbol{u}_1,\boldsymbol{u}_1)\right)\\
&-(a_1\lambda_c)^2\left(\mathcal{B}_3^c(\boldsymbol{u}_c',\boldsymbol{u}_1,\boldsymbol{u}_1)+\tfrac{1}{2}\mathcal{P}_4^c(\boldsymbol{u}_c',\boldsymbol{u}_c',\boldsymbol{u}_1,\boldsymbol{u}_1)+\tfrac{1}{2}\mathcal{P}_3^c(\boldsymbol{u}_c'',\boldsymbol{u}_1,\boldsymbol{u}_1)\right),
\end{aligned}\tag{38}$$

$$\begin{aligned}
\rho_2^N =& -\mathcal{P}_3^c(\boldsymbol{v}_2,\boldsymbol{u}_1,\boldsymbol{u}_1)\\
&-a_1\lambda_c\left(\mathcal{B}_2^c(\boldsymbol{v}_2,\boldsymbol{u}_1)+\mathcal{P}_3^c(\boldsymbol{u}_c',\boldsymbol{v}_2,\boldsymbol{u}_1)\right)\\
&-\rho_1\lambda_c\left(\mathcal{B}_2^c(\boldsymbol{u}_2,\boldsymbol{u}_1)+\mathcal{P}_3^c(\boldsymbol{u}_c',\boldsymbol{u}_2,\boldsymbol{u}_1)+\tfrac{1}{2}\mathcal{B}_3^c(\boldsymbol{u}_1,\boldsymbol{u}_1,\boldsymbol{u}_1)+\tfrac{1}{2}\mathcal{P}_4^c(\boldsymbol{u}_c',\boldsymbol{u}_1,\boldsymbol{u}_1,\boldsymbol{u}_1)\right)\\
&-2\rho_1 a_1\lambda_c^2\left(\mathcal{B}_3^c(\boldsymbol{u}_c',\boldsymbol{u}_1,\boldsymbol{u}_1)+\tfrac{1}{2}\mathcal{P}_4^c(\boldsymbol{u}_c',\boldsymbol{u}_c',\boldsymbol{u}_1,\boldsymbol{u}_1)+\tfrac{1}{2}\mathcal{P}_3^c(\boldsymbol{u}_c'',\boldsymbol{u}_1,\boldsymbol{u}_1)\right)\\
&-\left(\bar{\mathcal{P}}_3^c(\boldsymbol{u}_1,\boldsymbol{u}_1,\tilde{\boldsymbol{u}})+a_1\lambda_c(\bar{\mathcal{B}}_2^c(\boldsymbol{u}_1,\tilde{\boldsymbol{u}})+\bar{\mathcal{P}}_3^c(\boldsymbol{u}_c',\boldsymbol{u}_1,\tilde{\boldsymbol{u}}))\right),
\end{aligned}\tag{39}$$

$$\begin{aligned}
\rho_3^N =& -\rho_1\lambda_c\left(\mathcal{B}_2^c(\boldsymbol{v}_2,\boldsymbol{u}_1)+\mathcal{P}_3^c(\boldsymbol{u}_c',\boldsymbol{v}_2,\boldsymbol{u}_1)\right)\\
&-(\rho_1\lambda_c)^2\left(\mathcal{B}_3^c(\boldsymbol{u}_c',\boldsymbol{u}_1,\boldsymbol{u}_1)+\tfrac{1}{2}\mathcal{P}_4^c(\boldsymbol{u}_c',\boldsymbol{u}_c',\boldsymbol{u}_1,\boldsymbol{u}_1)+\tfrac{1}{2}\mathcal{P}_3^c(\boldsymbol{u}_c'',\boldsymbol{u}_1,\boldsymbol{u}_1)\right)\\
&-\rho_1\lambda_c(\bar{\mathcal{B}}_2^c(\boldsymbol{u}_1,\tilde{\boldsymbol{u}})+\bar{\mathcal{P}}_3^c(\boldsymbol{u}_c',\boldsymbol{u}_1,\tilde{\boldsymbol{u}})).
\end{aligned}\tag{40}$$

In the actual computation of a_2, ρ_2 and ρ_3 it may be exploited that several patterns of stability operators appear more than once.

7. Asymptotic problems to lowest order

As mentioned earlier, we are often only interested in determining the lowest-order postcritical effects with the implication that solving the asymptotic problems is simplified a great deal.

7.1. ***Postbuckling of a symmetric structure.*** Here, a_1 equals zero. In order to predict the initial postbuckling behavior for these structures, the second postbuckling constant a_2 must be found. However, when $a_1=0$ the formulas (28) and (37) for determining $\boldsymbol{u}_2$ and a_2 simplify considerably, becoming

$$0=\mathcal{P}_2^c(\boldsymbol{u}_2,\delta\boldsymbol{u})+\tfrac{1}{2}\mathcal{P}_3^c(\boldsymbol{u}_1,\boldsymbol{u}_1,\delta\boldsymbol{u})\tag{41}$$

and

$$a_2\lambda_c=\frac{-\mathcal{P}_3^c(\boldsymbol{u}_2,\boldsymbol{u}_1,\boldsymbol{u}_1)-\tfrac{1}{6}\mathcal{P}_4^c(\boldsymbol{u}_1,\boldsymbol{u}_1,\boldsymbol{u}_1,\boldsymbol{u}_1)}{\mathcal{B}_2^c(\boldsymbol{u}_1,\boldsymbol{u}_1)+\mathcal{P}_3^c(\boldsymbol{u}_c',\boldsymbol{u}_1,\boldsymbol{u}_1)}.\tag{42}$$

8. Determination of stability operators

The stress field $\boldsymbol{\sigma}$ may be given by the displacements u^i and $\tilde{u}^i$. However, for simplicity the stress field $\boldsymbol{\sigma}$ is often given as a function of the additional strain field $\Delta\boldsymbol{\varepsilon}$ of (3), which itself is a function of u^i and $\tilde{u}^i$.

The scalar stability operators given in (22) which determine the asymptotic coefficients $\bar{a}_i$ and $\bar{\boldsymbol{u}}_i$ depend on strain terms, Lagrange multiplier terms and load terms through the principle of virtual displacements.

8.1. ***Operators of the principle of virtual displacements.*** Together with the load operators $\mathcal{B}_i^c$ given in (23) the general operators below are used both for calculating the postbuckling equilibrium and the asymptotic effects of initial imperfections. As was the case for the stability operators, $\boldsymbol{u}_\alpha$, $\boldsymbol{u}_\beta$, $\boldsymbol{u}_\gamma$ and $\boldsymbol{u}_\delta$

may be any relevant displacement field:

$$
\begin{aligned}
\mathcal{E}_1^c(\boldsymbol{u}_\alpha) &= \boldsymbol{\varepsilon}^c_{,l} u^l_\alpha, \\
\mathcal{E}_2^c(\boldsymbol{u}_\alpha, \boldsymbol{u}_\beta) &= \boldsymbol{\varepsilon}^c_{,li} u^l_\alpha u^i_\beta, \\
\mathcal{E}_3^c(\boldsymbol{u}_\alpha, \boldsymbol{u}_\beta, \boldsymbol{u}_\gamma) &= \boldsymbol{\varepsilon}^c_{,lij} u^l_\alpha u^i_\beta u^j_\gamma, \\
\mathcal{E}_4^c(\boldsymbol{u}_\alpha, \boldsymbol{u}_\beta, \boldsymbol{u}_\gamma, \boldsymbol{u}_\delta) &= \boldsymbol{\varepsilon}^c_{,lijk} u^l_\alpha u^i_\beta u^j_\gamma u^k_\delta,
\end{aligned}
\tag{43}
$$

$$
\begin{aligned}
\mathcal{C}_1^c(\boldsymbol{u}_\alpha) &= (\boldsymbol{\eta} \cdot \boldsymbol{C})^c_{,l} u^l_\alpha, \\
\mathcal{C}_2^c(\boldsymbol{u}_\alpha, \boldsymbol{u}_\beta) &= (\boldsymbol{\eta} \cdot \boldsymbol{C})^c_{,li} u^l_\alpha u^i_\beta, \\
\mathcal{C}_3^c(\boldsymbol{u}_\alpha, \boldsymbol{u}_\beta, \boldsymbol{u}_\gamma) &= (\boldsymbol{\eta} \cdot \boldsymbol{C})^c_{,lij} u^l_\alpha u^i_\beta u^j_\gamma, \\
\mathcal{C}_4^c(\boldsymbol{u}_\alpha, \boldsymbol{u}_\beta, \boldsymbol{u}_\gamma, \boldsymbol{u}_\delta) &= (\boldsymbol{\eta} \cdot \boldsymbol{C})^c_{,lijk} u^l_\alpha u^i_\beta u^j_\gamma u^k_\delta.
\end{aligned}
\tag{44}
$$

The derivatives of the stress field with respect to the strain field are

$$
\boldsymbol{\sigma} = \sigma_i, \quad \boldsymbol{D} = \boldsymbol{\sigma}_{,\boldsymbol{\varepsilon}} = D_{ij}, \quad \boldsymbol{D}' = \boldsymbol{\sigma}_{,\boldsymbol{\varepsilon\varepsilon}} = D'_{ijk} \quad \text{and} \quad \boldsymbol{D}'' = \boldsymbol{\sigma}_{,\boldsymbol{\varepsilon\varepsilon\varepsilon}} = D''_{ijkl}, \tag{45}
$$

where i, j, k and l may take on any natural number between 1 and the number of stress components. The operators D_{ij}, D'_{ijk} and D''_{ijkl} are symmetric in their indices for nonlinear elastic materials; thus the indices may be swapped freely. Now use the fact that the initial imperfection $\hat{\boldsymbol{u}}$ does not depend on any displacement component and that $\hat{\boldsymbol{u}} = 0$ at the classical critical load to evaluate the stability operators given in (22). Finally, introduce the operators from (43) to provide the *scalar* stability operators.

Note that in the following the fields in brackets have the same number of dimensions as the corresponding field of stiffnesses, which is one for each $\mathcal{E}^c$. When evaluating the bracket each $\mathcal{E}^c$ is treated as a tensor with a separate index. The order of the $\mathcal{E}^c$-fields in the bracket is unimportant, since the corresponding field of stiffnesses is symmetric.

$$
\begin{aligned}
\mathcal{P}_1^c(\boldsymbol{u}_\alpha) &= \boldsymbol{\sigma}_c \cdot \mathcal{E}_1^c(\boldsymbol{u}_\alpha) - \mathcal{C}_1^c(\boldsymbol{u}_\alpha) - \lambda_c \mathcal{B}_1^c(\boldsymbol{u}_\alpha), \\
\mathcal{P}_2^c(\boldsymbol{u}_\alpha, \boldsymbol{u}_\beta) &= \boldsymbol{D}_c \cdot [\mathcal{E}_1^c(\boldsymbol{u}_\beta)\mathcal{E}_1^c(\boldsymbol{u}_\alpha)] + \boldsymbol{\sigma}_c \cdot \mathcal{E}_2^c(\boldsymbol{u}_\alpha, \boldsymbol{u}_\beta) - \mathcal{C}_2^c(\boldsymbol{u}_\alpha, \boldsymbol{u}_\beta) - \lambda_c \mathcal{B}_2^c(\boldsymbol{u}_\alpha, \boldsymbol{u}_\beta), \\
\mathcal{P}_3^c(\boldsymbol{u}_\alpha, \boldsymbol{u}_\beta, \boldsymbol{u}_\gamma) &= \boldsymbol{D}'_c \cdot [\mathcal{E}_1^c(\boldsymbol{u}_\gamma)\mathcal{E}_1^c(\boldsymbol{u}_\beta)\mathcal{E}_1^c(\boldsymbol{u}_\alpha)] \\
&\qquad + \boldsymbol{D}_c \cdot \big(\mathcal{E}_2^c(\boldsymbol{u}_\beta, \boldsymbol{u}_\gamma)\mathcal{E}_1^c(\boldsymbol{u}_\alpha) + \mathcal{E}_1^c(\boldsymbol{u}_\beta)\mathcal{E}_2^c(\boldsymbol{u}_\alpha, \boldsymbol{u}_\gamma) + \mathcal{E}_1^c(\boldsymbol{u}_\gamma)\mathcal{E}_2^c(\boldsymbol{u}_\alpha, \boldsymbol{u}_\beta)\big) \\
&\qquad + \boldsymbol{\sigma}_c \cdot \mathcal{E}_3^c(\boldsymbol{u}_\alpha, \boldsymbol{u}_\beta, \boldsymbol{u}_\gamma) - \mathcal{C}_3^c(\boldsymbol{u}_\alpha, \boldsymbol{u}_\beta, \boldsymbol{u}_\gamma) - \lambda_c \mathcal{B}_3^c(\boldsymbol{u}_\alpha, \boldsymbol{u}_\beta, \boldsymbol{u}_\gamma).
\end{aligned}
\tag{46}
$$

In the stability problems, the fourth stability operator $\mathcal{P}_4$ operates at least twice on the buckling displacement field, $\boldsymbol{u}_1$. Exploit this to show that

$$
\begin{aligned}
\mathcal{P}_4^c(\boldsymbol{u}_1, \boldsymbol{u}_1, \boldsymbol{u}_\alpha, \boldsymbol{u}_\beta) =& \boldsymbol{D}''_c \cdot [\mathcal{E}_1^c(\boldsymbol{u}_1)^2 \mathcal{E}_1^c(\boldsymbol{u}_\alpha)\mathcal{E}_1^c(\boldsymbol{u}_\beta)] \\
&+ \boldsymbol{D}'_c \cdot \big(\mathcal{E}_2^c(\boldsymbol{u}_1, \boldsymbol{u}_1)\mathcal{E}_1^c(\boldsymbol{u}_\alpha)\mathcal{E}_1^c(\boldsymbol{u}_\beta) + \mathcal{E}_2^c(\boldsymbol{u}_\alpha, \boldsymbol{u}_\beta)\mathcal{E}_1^c(\boldsymbol{u}_1)^2 \\
&\qquad + 2\mathcal{E}_1^c(\boldsymbol{u}_1)\mathcal{E}_1^c(\boldsymbol{u}_\alpha)\mathcal{E}_2^c(\boldsymbol{u}_1, \boldsymbol{u}_\beta) + 2\mathcal{E}_1^c(\boldsymbol{u}_1)\mathcal{E}_1^c(\boldsymbol{u}_\beta)\mathcal{E}_2^c(\boldsymbol{u}_1, \boldsymbol{u}_\alpha)\big) \\
&+ \boldsymbol{D}_c \cdot \big(\mathcal{E}_2^c(\boldsymbol{u}_1, \boldsymbol{u}_1)\mathcal{E}_2^c(\boldsymbol{u}_\alpha, \boldsymbol{u}_\beta) + 2\mathcal{E}_2^c(\boldsymbol{u}_1, \boldsymbol{u}_\alpha)\mathcal{E}_2^c(\boldsymbol{u}_1, \boldsymbol{u}_\beta) + \mathcal{E}_3^c(\boldsymbol{u}_1, \boldsymbol{u}_1, \boldsymbol{u}_\alpha)\mathcal{E}_1^c(\boldsymbol{u}_\beta) \\
&\qquad + \mathcal{E}_3^c(\boldsymbol{u}_1, \boldsymbol{u}_1, \boldsymbol{u}_\beta)\mathcal{E}_1^c(\boldsymbol{u}_\alpha) + 2\mathcal{E}_3^c(\boldsymbol{u}_1, \boldsymbol{u}_\alpha, \boldsymbol{u}_\beta)\mathcal{E}_1^c(\boldsymbol{u}_1)\big) \\
&+ \boldsymbol{\sigma}_c \cdot \mathcal{E}_4^c(\boldsymbol{u}_1, \boldsymbol{u}_1, \boldsymbol{u}_\alpha, \boldsymbol{u}_\beta) - \mathcal{C}_4^c(\boldsymbol{u}_1, \boldsymbol{u}_1, \boldsymbol{u}_\alpha, \boldsymbol{u}_\beta) - \lambda_c \mathcal{B}_4^c(\boldsymbol{u}_1, \boldsymbol{u}_1, \boldsymbol{u}_\alpha, \boldsymbol{u}_\beta).
\end{aligned}
\tag{47}
$$

8.2. ***Scalar operators associated with imperfections.*** Let operators evaluated at the *initially* perfect reference before loading be indicated by superscript ^{I}. Then, operators associated with imperfections may be written

$$\mathcal{E}_1^I(\tilde{\boldsymbol{u}}) = \boldsymbol{\varepsilon}^I_{,l}\tilde{u}^l \quad \text{and} \quad \mathcal{D}_2^I(\boldsymbol{u}_\alpha, \tilde{\boldsymbol{u}}) = \boldsymbol{\eta}_\alpha \boldsymbol{C}^I_{,i}\tilde{u}^i; \tag{48}$$

thus, the stability operators introducing imperfection given by (24) become

$$\begin{aligned} \bar{\mathcal{P}}_2^c(\boldsymbol{u}_\alpha, \tilde{\boldsymbol{u}}) &= \mathcal{P}_2^c(\boldsymbol{u}_\alpha, \tilde{\boldsymbol{u}}) - \boldsymbol{D}_c \cdot [\mathcal{E}_1^I(\tilde{\boldsymbol{u}})\mathcal{E}_1^c(\boldsymbol{u}_\alpha)] + \mathcal{D}_2^I(\boldsymbol{u}_\alpha, \tilde{\boldsymbol{u}}), \\ \bar{\mathcal{P}}_3^c(\boldsymbol{u}_\alpha, \boldsymbol{u}_\beta, \tilde{\boldsymbol{u}}) &= \mathcal{P}_3^c(\boldsymbol{u}_\alpha, \boldsymbol{u}_\beta, \tilde{\boldsymbol{u}}) - \boldsymbol{D}_c' \cdot [\mathcal{E}_1^I(\tilde{\boldsymbol{u}})\mathcal{E}_1^c(\boldsymbol{u}_\alpha)\mathcal{E}_1^c(\boldsymbol{u}_\beta)] - \boldsymbol{D}_c \cdot [\mathcal{E}_1^I(\tilde{\boldsymbol{u}})\mathcal{E}_2^c(\boldsymbol{u}_\alpha, \boldsymbol{u}_\beta)], \end{aligned} \tag{49}$$

and

$$\bar{\mathcal{B}}_2^c(\boldsymbol{u}_\alpha, \tilde{\boldsymbol{u}}) \ = \mathcal{B}_2^c(\boldsymbol{u}_\alpha, \tilde{\boldsymbol{u}}). \tag{50}$$

The asymptotic coefficients given earlier by the buckling, the first postcritical and the second postcritical problem are simple to compute when the above given stability operators have been computed for the specific structure.

9. Load-carrying capacity of imperfect structures

The asymptotic equilibrium path of both perfect and imperfect structures where $\bar{\xi} = \alpha\xi^2$ may be written

$$\frac{\lambda}{\lambda_c} = 1 + (a_1 + \rho_1\alpha)\xi + (a_2 + \rho_2\alpha + \rho_3\alpha^2)\xi^2 + O(\xi^3). \tag{51}$$

In reality the imperfection amplitude $\bar{\xi}$ is constant for each load case and introduction of $\alpha = \bar{\xi}/\xi^2$ provides an expression which links the load parameter λ to the characteristic buckling amplitude ξ for given $\bar{\xi}$:

$$\frac{\lambda}{\lambda_c} = \big(1 + a_1\xi + a_2\xi^2 + O(\xi^3)\big) + \frac{\bar{\xi}}{\xi}\big(\rho_1 + \rho_2\xi + O(\xi^2)\big) + \left(\frac{\bar{\xi}}{\xi}\right)^2(\rho_3 + O(\xi)) + O((\bar{\xi}/\xi)^3). \tag{52}$$

9.1. ***Enhanced asymptotic expansion through the origin.*** Structures for which ξ is a characteristic buckling amplitude are subject to the simple boundary condition $\lambda(\xi = 0) = 0$. The asymptotic expansion (52) does not fulfill this condition. An expression which does fulfill $\lambda(\xi = 0) = 0$ *and* matches (52) asymptotically may be constructed as

$$\begin{aligned} \frac{\lambda}{\lambda_c} = \big(1 + a_1\xi + a_2\xi^2 + O(\xi^3)\big) &+ \left(\frac{\bar{\xi}/\xi}{1 + m_1\bar{\xi}/\xi}\right)\big(\psi_1 + \psi_2\xi + O(\xi^2)\big) \\ &+ \left(\frac{\bar{\xi}/\xi}{1 + m_1\bar{\xi}/\xi}\right)^2(\psi_3 + O(\xi)) + O\left(\left(\frac{\bar{\xi}/\xi}{1 + m_1\bar{\xi}/\xi}\right)^3\right). \end{aligned} \tag{53}$$

An asymptotic match of (53) with (52) provides the constants ψ_i as

$$\psi_1 = \rho_1, \quad \psi_2 = \rho_2 \quad \text{and} \quad \psi_3 = \rho_3 + m_1\rho_1, \tag{54}$$

while the condition $\lambda(\xi = 0) = 0$ furnishes for m_1 the expression

$$m_1^2 + 2\rho_1 m_1 + \rho_3 = 0. \tag{55}$$

Remark. Our enhancement is not the only possible one. For instance, Koiter [1945] establishes one in a more physically intuitive way than ours, which is of a more mathematical origin and nature. Koiter's method, which results in modifying the load term in the expression for the potential energy or principle of virtual work by multiplication by the load parameter, has been applied elsewhere, as in [Byskov and Hutchinson 1977] and [Koiter 2009]. After a simple rearrangement of terms, Koiter's expression, valid for linear elasticity and linear prebuckling, is

$$\frac{\lambda}{\lambda_c} = \frac{\xi + b_1\xi + b_2\xi^2}{\xi + \bar{\xi}} \tag{56}$$

which at first appears to be different from our expression. An expansion in terms of $\bar{\xi}$ reveals, however, that the structure of the two formulas is the same for small values of $\bar{\xi}$. At the same time, our choice seems justified by the remarkably accurate results for large values of the rotation θ_0 shown in Figure 11.

9.2. ***Asymptotic maximum load of imperfect structures.*** The maximum load-carrying capacity of the imperfect structure may be determined asymptotically from either the traditional asymptotic expansion (52) or from the enhanced asymptotic expansion (53) with the same *asymptotic* accuracy. The asymptotic procedure for determining maximum load is, however, simpler for the traditional asymptotic expansion (52) and we shall later tie our enhanced expansion to it, but for larger imperfections abandon it in favor of the enhanced expansion.

The asymptotic maximum load of the imperfect structure is found where the derivative of λ/λ_c, given by (51), with respect to the buckling amplitude ξ becomes zero:

$$\frac{d(\lambda/\lambda_c)}{d\xi} = (a_1 - \rho_1\alpha_m) + 2(a_2 - \rho_3\alpha_m^2)\xi_m + O(\xi_m^2) = 0, \tag{57}$$

where subscript $_m$ indicates quantities related to the asymptotic maximum load and where we have used

$$\frac{d\alpha}{d\xi} = -2\frac{\alpha}{\xi}, \tag{58}$$

a consequence of (7).

An asymptotic match in (57) reveals that

$$\alpha_m = c_1 + c_2\xi_m + O(\xi_m^2) \quad \text{or} \quad \bar{\xi} = c_1\xi_m^2 + c_2\xi_m^3 + O(\xi_m^4), \tag{59}$$

where the constants are readily found to be

$$c_1 = \frac{a_1}{\rho_1} \quad \text{and} \quad c_2 = 2\frac{a_2\rho_1 - a_1\rho_3}{\rho_1^2}. \tag{60}$$

Insert the asymptotic expansion (59) for α_m in (51) to obtain a relation between the maximum load, λ_m, and the buckling amplitude at maximum load, ξ_m:

$$\frac{\lambda_m}{\lambda_c} = 1 + 2a_1\xi_m + \big(a_2 + \rho_1c_2 + \rho_2c_1 + \rho_3c_1^2\big)\xi_m^2 + O(\xi_m^3). \tag{61}$$

In order to determine the maximum load for imperfect structures from (61), an asymptotic expression for ξ at maximum load must be found from (59). Since $a_1 = 0$ implies $c_1 = 0$, the asymptotic investigation is split into two cases, one for unsymmetric ($a_1 \neq 0$) and one for symmetric ($a_1 = 0$) structures.

Maximum load of unsymmetric structures. The asymptotic expression for the buckling amplitude ξ_m at maximum load becomes

$$\xi_m = l_1 \bar{\xi}^{\frac{1}{2}} + l_2 \bar{\xi} + O(\bar{\xi}^{\frac{3}{2}}) \quad \text{with} \quad l_1 = \sqrt{\frac{\rho_1}{a_1}} \quad \text{and} \quad l_2 = \frac{a_1\rho_3 - a_2\rho_1}{a_1^2}. \tag{62}$$

The asymptotic expansion for ξ_m, given by (62), may be inserted in (61) to provide the exact initial asymptotic dependency of the maximum load on the imperfection amplitude and shape when $a_1 \neq 0$:

$$\frac{\lambda_m}{\lambda_c} = 1 + c^m_{\frac{1}{2}} \bar{\xi}^{\frac{1}{2}} + c^m_{\frac{2}{2}} \bar{\xi} + O(\bar{\xi}^{\frac{3}{2}}) = 1 - 2\sqrt{a_1\rho_1}\, \bar{\xi}^{\frac{1}{2}} + \left(\frac{a_2\rho_1}{a_1} + \rho_2 + \frac{\rho_3 a_1}{\rho_1} \right) \bar{\xi} + O(\bar{\xi}^{\frac{3}{2}}) \,, \tag{63}$$

with

$$c^m_{\frac{1}{2}} = -2\sqrt{a_1\rho_1} \quad \text{and} \quad c^m_{\frac{2}{2}} = \left(\frac{a_2\rho_1}{a_1} + \rho_2 + \frac{\rho_3 a_1}{\rho_1} \right), \tag{64}$$

where we note that the maximum only exists when $a_1\rho_1 > 0$.

Maximum load of symmetric structures. At maximum load the asymptotic expression for the buckling amplitude ξ_m becomes

$$\xi_m = q_1 \bar{\xi}^{\frac{1}{3}} + O(\bar{\xi}^{\frac{2}{3}}) \quad \text{with} \quad q_1 = \left(\frac{\rho_1}{2a_2} \right)^{\frac{1}{3}}. \tag{65}$$

Insert the asymptotic expansion for ξ_m, given by the imperfection amplitude $\bar{\xi}$ (65) in (61) to provide the exact asymptotic dependency of the maximum load on the imperfection amplitude and shape when $a_1 = 0$ and get

$$\frac{\lambda_m}{\lambda_c} = 1 + c^m_{\frac{2}{3}} \bar{\xi}^{\frac{2}{3}} + O(\bar{\xi}) \quad \text{with} \quad c^m_{\frac{2}{3}} = 3a_2^{\frac{1}{3}} \left(\frac{\rho_1}{2} \right)^{\frac{2}{3}}. \tag{66}$$

Note that the maximum only exists when $a_2 < 0$.

For a symmetric structure the third postbuckling constant a_3 will also vanish and one more term may be added to the asymptotic expansion (66) of the maximum load when $a_1 = 0$ without further expansion of the stability problems.

It is easily shown that the third degree term, t_3, of (51) takes the form

$$t_3 = k_i \alpha^i \xi^3, \quad \text{summed over } \ i \geq 1. \tag{67}$$

Thus, the expression for the maximum load associated with ξ_m simplifies to the exact asymptotic expansion

$$\frac{\lambda_m}{\lambda_c} = 1 + 3a_2\xi_m^2 + \frac{2a_2\rho_2}{\rho_1}\xi_m^3 + O(\xi_m^4), \tag{68}$$

where it has been exploited that both a_1 and a_3 vanish.

Use ξ_m as given in (65) to obtain the asymptotic expression for the maximum load as a function of the imperfection shape and amplitude:

$$\frac{\lambda_m}{\lambda_c} = 1 + c^m_{\frac{2}{3}} \bar{\xi}^{\frac{2}{3}} + c^m_{\frac{3}{3}} \bar{\xi} + O(\bar{\xi}^{\frac{4}{3}}) \ \text{ with } \ c^m_{\frac{3}{3}} = \rho_2, \tag{69}$$

where $c^m_{\frac{2}{3}}$ follows from (66)b.

Enhanced maximum load prediction. Because the above asymptotic expansion of the maximum load eventually approaches plus or minus infinity, it often deviates considerably from the real maximum load, even for relatively small imperfection amplitudes; this is the basic reason for our enhanced expansion (53). Due to the fact that the load parameter is zero before loading is applied, the maximum load of any imperfect structure must be greater than or equal to zero. Since we concentrate on structures whose maximum load decreases with the imperfection amplitude $\bar{\xi}$, but is always greater than zero, an enhanced maximum load prediction of the asymptotic method may be obtained by matching the asymptotic maximum load prediction given above with an expression that approaches zero with $\bar{\xi}$.

The traditional polynomial asymptotic expression for maximum load is determined by (63) for $a \neq 0$ and by (66) or (69) when $a = 0$. In the enhanced approach each asymptotic term is chosen to be a hyperbolic function approaching a constant at infinity. Often only the first asymptotic term is determined and therefore the enhanced asymptotic expansion is required to approach zero even if only one asymptotic term is used. The second term in the enhanced asymptotic expansion is required to match the second traditional asymptotic term, if present. A third enhancing term is included to force the expansion to approach zero at infinity. Its presence does, however, not interfere with the asymptotic correctness of the expansion because its dependence on the expansion parameters is beyond the limit of the original expansion. We establish the enhanced asymptotic expansion for the two separate cases:

Enhanced expansion, $a \neq 0$:

$$\frac{\lambda_m}{\lambda_c} = 1 + c^m_{\frac{1}{2}} \left(\frac{\bar{\xi}}{1 + (c^m_{\frac{1}{2}})^2 \bar{\xi}} \right)^{\frac{1}{2}} + c^m_{\frac{2}{2}} \left(\frac{\bar{\xi}}{1 + (c^m_{\frac{1}{2}})^2 \bar{\xi}} \right) + c^m_{\frac{2}{2}} c^m_{\frac{1}{2}} \left(\frac{\bar{\xi}}{1 + (c^m_{\frac{1}{2}})^2 \bar{\xi}} \right)^{\frac{3}{2}} + O(\bar{\xi}^{\frac{3}{2}}) \tag{70}$$

Enhanced expansion, $a = 0$:

$$\frac{\lambda_m}{\lambda_c} = 1 + c^m_{\frac{2}{3}} \left(\frac{\bar{\xi}}{1 + (-c^m_{\frac{2}{3}})^{\frac{3}{2}} \bar{\xi}} \right)^{\frac{2}{3}} + c^m_{\frac{3}{3}} \left(\frac{\bar{\xi}}{1 + (-c^m_{\frac{2}{3}})^{\frac{3}{2}} \bar{\xi}} \right) - c^m_{\frac{3}{3}} (-c^m_{\frac{2}{3}})^{\frac{1}{2}} \left(\frac{\bar{\xi}}{1 + (-c^m_{\frac{2}{3}})^{\frac{3}{2}} \bar{\xi}} \right)^{\frac{4}{3}} + O(\bar{\xi}^{\frac{3}{2}}) \tag{71}$$

Part II. Application: the Euler column

10. Introduction to the Euler column

A vast number of analytical asymptotic and numerical studies have been performed on the postbuckling and imperfection sensitivity of the linear elastic Euler column (see [Kuznetsov and Levyakov 2002], for example), while the effects of nonlinear elasticity on the behavior of Euler columns have been studied less frequently; but see, for instance, [Tvergaard and Needleman 1982].

In the following, the formulas derived above are applied to the pin-ended Euler column (see Figure 2 on the next page), taking into account the effect of nonlinear elasticity as well as full nonlinear kinematics. Two different cross-sections, one symmetric and one asymmetric, of the column are investigated in order to show the ability of our method to handle both kinds of structures. Furthermore, the influence and possible simplifications caused by introduction of inextensibility is examined. In Appendix D the problem of stability of the geometrically perfect column is solved for nonlinear elasticity, considering extensibility as well as inextensibility. It turns out that the extensible and inextensible case yield the same

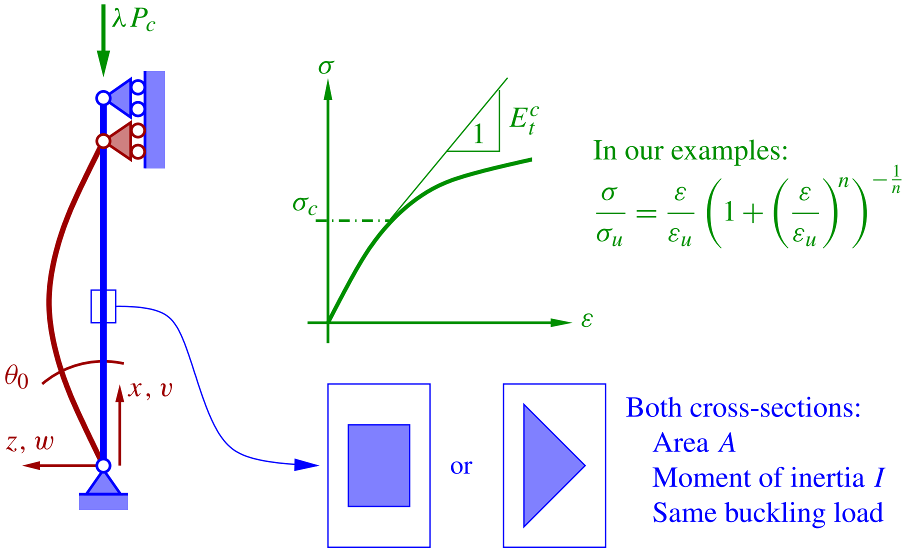

Figure 2. The nonlinear elastic Euler column.

critical load, while the first and second postbuckling constants are only identical or close to identical when the material model is linear. Thus, to solve stability problems for nonlinear elastic structures it is imperative to model extensibility.

11. Geometry and constitutive relation of the Euler column

In solving the stability problems we shall employ *fully nonlinear strain measures* and a *fully nonlinear elastic stress-strain relation*. The column is *not* regarded as inextensible but the usual Bernoulli–Euler beam theory simplifications are implemented, with the following nondimensional cross-sectional constants:

$$\begin{aligned} &A_0 \equiv \int_{A_0} dA, && Z_0 \equiv \int_{A_0} z\,dA = 0 \\ &I_j \equiv \int_{A_0} z^{j+1} dA, && i_j \equiv \left(\frac{\pi}{L}\right)^{j+1} \frac{I_j}{A_0} \ll 1 \qquad (i = 1, 2, 3), \end{aligned} \tag{72}$$

where A_0 is the initial area of the columns cross-section and it important to note that all i_j vanish compared to unity according to the Bernoulli–Euler beam theory.

For convenience we introduce the nondimensional material stiffnesses

$$e_c' = i_1 E_{t,\varepsilon}^c / E_t^c \quad \text{and} \quad e_c'' = i_3 E_{t,\varepsilon\varepsilon}^c / E_t^c, \tag{73}$$

where we note that $E_{t,\varepsilon}^c / E_t^c$ and $E_{t,\varepsilon\varepsilon}^c / E_t^c$ may be very large. Thus, the constants e_c' and e_c'' are not necessarily small compared to unity.

11.1. ***Cross-sections.*** In order to demonstrate the capability of our method to predict the postbuckling behavior of geometrically perfect columns as well as describing the load-displacement relation of geometrically imperfect columns, either with symmetric or asymmetric cross-sections consider the two types of cross-sections shown in Figure 2. In both cases, which were studied in [Tvergaard and Needleman 1982], we let the area A and the moment of inertia I_1 of the cross-sections be identical for the two columns. In order to obtain the same critical load, given by the value of i_1 and material expense of the two types of column, the height and width of the triangular cross-section must be

$$h_T = \sqrt{\tfrac{3}{2}}h, \quad b_T = \sqrt{\tfrac{2}{3}}b, \tag{74}$$

where h and b are the height and width of the rectangular cross-section, respectively, h_T and b_T denote the equivalent quantities of the triangular cross-section, and

$$i_1 = \frac{1}{12}\left(\frac{h\pi}{L}\right)^2. \tag{75}$$

The higher-order nondimensional moments i_2 and i_3 are, of course, not the same for the nonsymmetric and symmetric cross-sections.

Triangular cross-section. Only the second dimensionless moment of inertia i_2 is needed since $a_1 \neq 0$ when the material is nonlinear:

$$i_2 = \frac{\sqrt{\frac{3}{2}}}{90}\left(\frac{h\pi}{L}\right)^3. \tag{76}$$

Rectangular cross-section. Here, both i_2 and i_3 are necessary because $a_1 = 0$:

$$i_2 = 0, \quad i_3 = \frac{1}{80}\left(\frac{h\pi}{L}\right)^4. \tag{77}$$

11.2. ***Strain-displacement relation.*** According to Bernoulli–Euler beam theory the only nonvanishing strains are in the axis direction and may be given as

$$\varepsilon(x) = \epsilon(x) + z\kappa(x), \tag{78}$$

where ε is the fiber strain, ϵ the strain of the neutral axis, and κ denotes the curvature strain. In the following we consider full kinematic nonlinearity, and thus

$$\epsilon = \sqrt{(1+\dot{v})^2 + \dot{w}^2} - 1, \quad \kappa = \dot{\theta} = \frac{\ddot{w}(1+\dot{v}) - \ddot{v}\dot{w}}{(1+\dot{v})^2 + \dot{w}^2}, \tag{79}$$

where a dot over a quantity denotes differentiation with respect to x, and the coordinates x and z and the displacements v and w are defined in Figure 2.

11.3. ***Stress-strain relation.*** Obviously, the choice of stress-strain relation influences the postbifurcation constants through the nondimensional derivatives with respect to strain at critical load defined in (73), i.e., through e'_c and e''_c, which both equal zero in linear elasticity. Provided that buckling takes place under decreasing stiffness in compression, e'_c may be any positive value and e''_c any value at all, independently of each other and of i_1 and i_3 respectively:

$$e'_c \in]0; \infty[, \quad e''_c \in]-\infty; \infty[. \tag{80}$$

To investigate the stability behavior of a structure for realistic cases, we shall assume that the column obeys the nonlinear elastic constitutive relation

$$\frac{\sigma}{\sigma_u} = \frac{\varepsilon}{\varepsilon_u}\left(1+\left(\frac{\varepsilon}{\varepsilon_u}\right)^n\right)^{-1/n}, \tag{81}$$

where E is Young's modulus, $\sigma_u < 0$ is the ultimate stress in compression, $\varepsilon_u = \sigma_u/E < 0$ is the strain corresponding to σ_u assuming linear elasticity, and n is a hardening parameter. High values of n imply nearly linear elastic behavior up till σ_u, while low values of n induce nonlinear elastic behavior even at small stresses compared to σ_u.

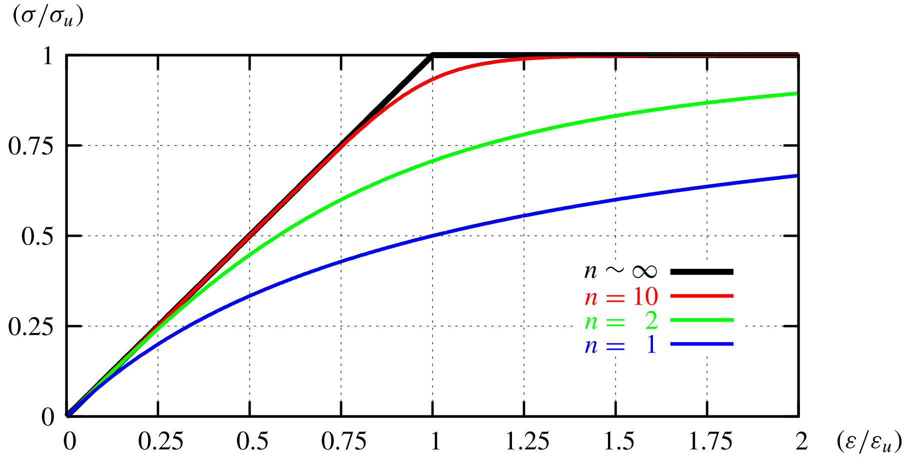

Figure 3. Stress-strain relation for different levels of the strain hardening parameter n. For $n \to \infty$ the constitutive model approaches linear elasticity-perfect plasticity.

11.4. ***Expansion parameter.*** Let the expansion parameter ξ be identified as the rotation of the column at $x = 0$:

$$\xi \equiv \theta(0). \tag{82}$$

12. Geometrically perfect Euler column

Appendix D contains the detailed calculations and derivations which lead to the determination of the asymptotic coefficient fields and critical load. In particular, we note that

$$\lambda_c = 1, \quad \sigma_c = i_1 E_t^c. \tag{83}$$

12.1. ***Unsymmetric elastic triangular cross-section.*** When the cross-section of the column is nonsymmetric *and* the material model is nonlinear elastic at the same time, the first postbuckling constant a_1 does not vanish. Under these conditions it is only necessary to determine the buckling displacement field $\boldsymbol{u}_1$ and a_1. The asymptotic displacement field is

$$\begin{aligned} w &= w_1\xi + O(\xi^2) = (L/\pi)\sin(\pi x/L)\xi + O(\xi^2),\\ v &= v_1\xi + O(\xi^2) = 0 + O(\xi^2), \end{aligned} \tag{84}$$

and the asymptotic load parameter is

$$\frac{\lambda}{\lambda_c} = 1 + a_1\xi + O(\xi^2) = 1 - \frac{4e'_c i_2}{3\pi i_1^2(1+e'_c)}\,\xi + O(\xi^2), \tag{85}$$

which is in exact agreement with the result obtained in [Tvergaard and Needleman 1982] for the nonsymmetric cross-section.

12.2. ***Symmetric as well as linear elastic unsymmetric cross-sections.*** When the cross-section of the column is symmetric or when the material is linear elastic, the first postbuckling constant a_1 vanishes. Then, it is necessary to determine the second postbuckling constant a_2 to investigate postbuckling behavior. To the lowest order the asymptotic loads and displacements are

$$\begin{aligned} w &= w_1\xi + w_2\xi^2 + O(\xi^3) = (L/\pi)\sin(\pi x/L)\xi + O(\xi^3), \\ v &= v_1\xi + v_2\xi^2 + O(\xi^3) = -\frac{1}{4}\left((1+e'_c)x + (1-e'_c)\frac{L}{2\pi}\sin(2\pi x/L)\right)\xi^2 + O(\xi^3), \end{aligned} \tag{86}$$

and the asymptotic load parameter is

$$\frac{\lambda}{\lambda_c} = 1 + a_2\xi^2 + O(\xi^3) = 1 + \frac{i_1 - 3(e'_c)^2 + e''_c}{8i_1(1+e'_c)}\,\xi^2 + O(\xi^3). \tag{87}$$

12.3. ***Comparison with known results: the elastica.*** The load-carrying capacity in initial and advanced postbuckling of the linear elastic pin-ended Euler column has received much attention since the original study in [Euler 1744] of the so-called *elastica* and has been investigated in [Britvec 1973; Kuznetsov and Levyakov 2002], among other works, for a full nonlinear strain measure.

Excluding material nonlinearity from our initial postbuckling loads (87) provides the linear elastic postbuckling constants $a_1 = 0$ and $a_2 = \frac{1}{8}$, which agree exactly with the elastica solution in [Britvec 1973]. It may be worth noticing that, according to the kinematically moderately linear theory, a_2 as well as a_1 vanishes which underlines the importance of applying a general full nonlinear stability theory to obtain accurate postbuckling constants. On the other hand, the fact that the results for the second postbuckling constant differ between the two theories should not, in general, discredit the moderately nonlinear theory. The relative difference in predicted load is, after all, only $\xi/8$ (around 9.8% at the very large end rotation 45°).

12.4. ***Postbuckling behavior assuming nonlinear elasticity.*** As is evident from the expressions (85) and (87), introduction of nonlinear elasticity requires, apart from more constitutive parameters, i.e., e'_c and e''_c, a detailed knowledge of the cross-section geometry through i_2 and i_3. Because the expressions are only valid for small i_1 compared to unity the ratio between h and L must be limited. Since the absolute value of ε_u usually is less than one tenth of a per cent, the order of i_1 lies in the same range. In Figures 4–7 results for the Euler column are shown for the constitutive relation given by (81). The critical load, the first and second postbuckling constants are plotted as functions of the ratio between i_1 and the absolute value of ε_u in the range [0; 2] (where $\varepsilon_c/\varepsilon_u \in [0; 1]$ as indicated at the top of Figures 4–6).

Bifurcation load. In Figure 4 the nondimensional critical load, σ_c/σ_u, of the column is plotted for both nonlinear and initially linear elastic behavior. It is not surprising that the difference in critical load between nonlinear and linear elasticity increases with increasing cross-section, given by i_1, relative to the "ultimate" strain ε_u.

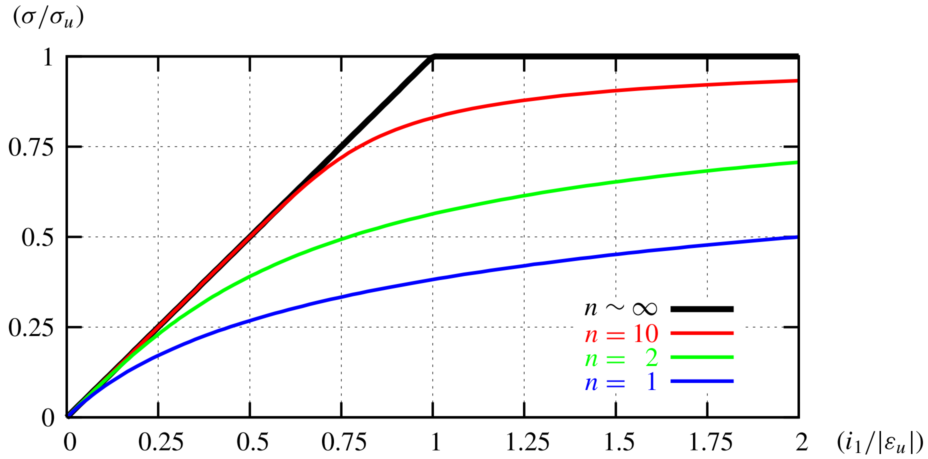

Figure 4. Bifurcation load of nonlinear elastic Euler columns with an ultimate stress.

Triangular cross-section. Figure 5 shows the first postbuckling constant a_1 of the triangular cross-section for nonlinear elasticity. Only at extremely small values of $i_1/|\varepsilon_u|$, i.e., for very slender columns, or extremely high values of n with relatively low values of $i_1/|\varepsilon_u|$ is a_1 according to the nonlinear elastic theory close to vanishing as it does according to linear elastic theory. The fact that nonlinear stress-strain relations deviate faster from initial linearity for lower values of n reflects in that a_1 initially deviates more rapidly from zero with increasing values of $\varepsilon_c/\varepsilon_u$ (and thus $i_1/|\varepsilon_u|$) the lower the value of n. When $\varepsilon_c/\varepsilon_u$ approaches unity ($i_1/|\varepsilon_u|$ approaches 2) high n yields the largest absolute values of a_1 because of the sudden large drop in tangent modulus near ε_u.

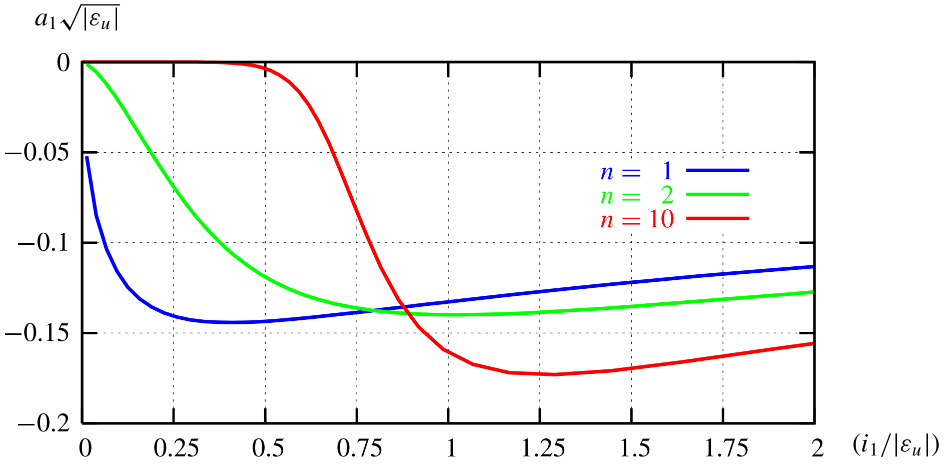

Figure 5. First postbuckling constant a_1 for triangular cross-section.

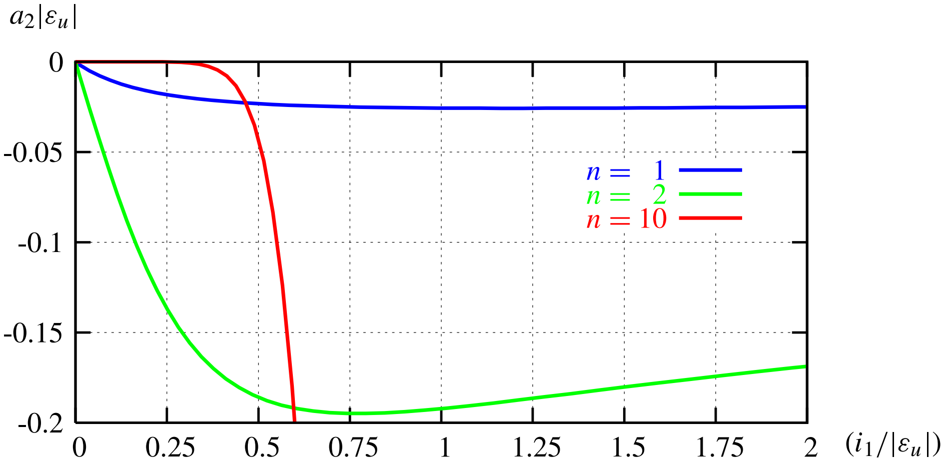

Figure 6. Second postbuckling constant a_2 for rectangular cross-section.

Rectangular cross-section. Results for the second postbuckling constant a_2 of the rectangular cross-section in nonlinear elastic postbuckling are shown in Figure 6. When $i_1/|\varepsilon_u| \to 0$, i.e., for extremely slender columns, the buckling stress is very low, and therefore the second postbuckling constant a_2 of nonlinear elasticity approaches that of linear elasticity. In linear elasticity $a_2|\varepsilon_u|$ is usually of the order 10^{-4}. However, as $i_1/|\varepsilon_u|$ is increased a_2 rapidly grows negative and reaches a global minimum. The higher the value of n the lower the minimum (the minimum for $n = 10$ falls outside the bounds of this plot), and as $n \to \infty$ the minimum value of a_2 becomes $-\infty$ and is reached for $i_1/|\varepsilon_u| = 2$ where $\varepsilon_c = \varepsilon_u$). Thus, assuming material linearity only furnishes reliable values of a_2 for extremely slender columns.

The large deviation of $a_2|\varepsilon_u|$ in Figure 6 from its linear elastic counterpart helps to demonstrate that the linear elastic value of a_2, assuming full nonlinear kinematics differs *very* little from the value obtained under the assumption of moderately nonlinear kinematics compared to the effects of nonlinearity of the stress-strain curve. Therefore, as discussed earlier, the simplifications of moderately nonlinear geometry should not necessarily be discarded.

12.5. ***Comparison with numerical results.*** An immediate and important consequence of including nonlinear elastic effects is that both symmetric (except for *extremely* slender columns) and nonsymmetric cross-sections may become imperfection sensitive in contrast to the predictions of linear elasticity. It follows that nonlinear material effects may not be handled safely by assuming that the correct nonlinear elastic bifurcation load shown in Figure 4 predicts the real load-carrying capacity.

The two cross-section types, triangular and rectangular are, as mentioned earlier, constructed to occupy the same amount of material for the same critical load. However, as is clear from Figure 7, the postbuckling paths of the cross-sections are not identical as the column with triangular cross-section experiences asymmetric buckling (in contrast to its linear elastic counterpart), while the column with rectangular cross-section buckles symmetrically. This agrees with the findings in [Tvergaard and Needleman 1982].

Figure 7 shows an example of the load parameter, λ, plotted against the end rotation of the column for both the triangular and the rectangular cross-sections where $|\varepsilon_u| = 0.002$, $n = 2$, $i_1/|\varepsilon_u| = 0.2$ $(h/L = 0.022)$ which yields $a_1\sqrt{|\varepsilon_u|} = -0.0538$ for the triangle and $a_2|\varepsilon_u| = -0.117$ for the rectangle.

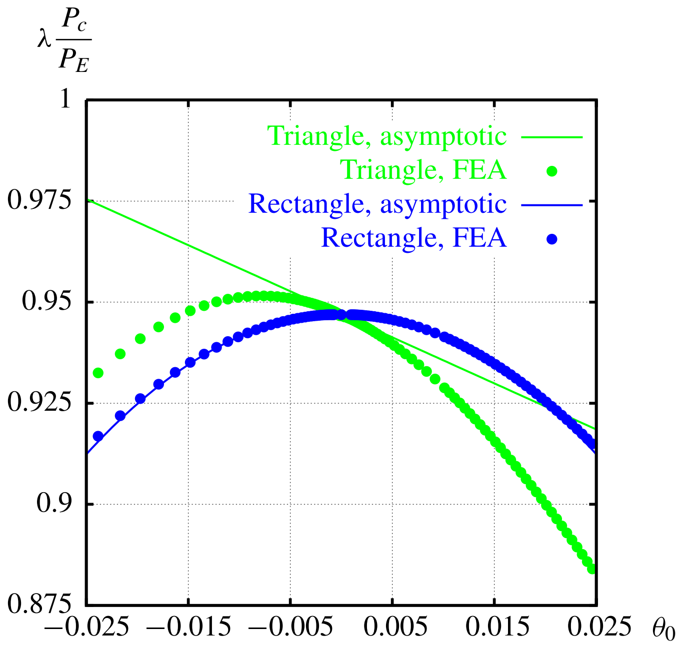

Figure 7. Initial postbuckling behavior for rectangular and triangular cross-sections, $|\varepsilon_u| = 0.002$, $n = 2$, $i_1/|\varepsilon_u| = 0.2$. The classic Euler load of linear elasticity is denoted P_E.

The asymptotic results for initial postbuckling are verified by a finite element analysis. While the symmetric asymptotic analysis including both the postbuckling constants a_1 ($= 0$) and a_2 matches the finite element analysis results nicely in the range $\theta_0 \in [-0.025; 0.025]$ the precision of the nonsymmetric analysis which is only carried out to the first postbuckling constant a_1 rapidly deteriorates mainly because of the heavy nonlinearities introduced through the material law.

The column with rectangular cross-section always exhibits imperfection sensitivity although not as distinct as with the triangular cross-section because it experiences symmetric postbuckling.

According to the asymptotic analysis the triangular cross-section column is initially stable in postbuckling when forced to bifurcate in the opposite direction of the w-axis (see Figure 2), in the direction of the cross-section axis z while it is imperfection sensitive when buckling in the direction of the w-axis. On the other hand, the finite element analysis shows that the initial postbuckling stability is soon negated by a decrease in load-carrying capacity which is not detected by the asymptotic analysis. Therefore and because the accuracy of the asymptotic approach decreases soon after bifurcation it may be an obvious idea to include the next asymptotic term a_2 for nonsymmetric structures as well as for symmetric ones.

13. Imperfect Euler column

In principle the geometric imperfection may be of any shape. Here, in the spirit of Koiter, we restrict ourselves to columns subject to an initial imperfection in the shape of the buckling displacement field $\boldsymbol{u}_1$ and characterized by the imperfection amplitude $\bar{\xi}$:

$$\widehat{w} = \bar{\xi} w_1, \quad \widehat{v} = \bar{\xi} v_1 = 0. \tag{88}$$

The asymptotic equilibrium path of the imperfect column close to bifurcation may be examined through the stability problems derived earlier by calculating the imperfection shape parameters ρ_1, ρ_2 and ρ_3. However, since the second postbuckling constant a_2 was not determined for the nonsymmetric perfect column, ρ_2 and ρ_3 may not be determined exactly and are therefore excluded for nonsymmetric perfect columns.

13.1. ***Asymptotic imperfection shape parameters.*** In Appendix E the asymptotic stability problems for imperfect structures are solved in details. For small values of i_1 The asymptotic imperfection parameters are given as

$$\rho_1\lambda_c = \frac{-1}{1+e'_c} \tag{89}$$

for all columns, while ρ_2 and ρ_3 are only determined for symmetric columns:

$$\rho_2\lambda_c = 0, \qquad \rho_3\lambda_c = (\rho_1\lambda_c)^2 - \frac{{e'_c}^2 - \frac{5}{9}e''_c}{2(1+e'_c)^3}. \tag{90}$$

For various values of the hardening parameters n the dependence on the slenderness $i_1/|\varepsilon_u|$ of the two nonvanishing imperfection shape parameters ρ_1 and ρ_3 are shown in Figure 8. For infinitely slender columns, i.e., for $i_1/|\varepsilon_u| \to 0$, the imperfection parameters ρ_1 and ρ_3 approach their linear elastic counterparts $\rho_1 = -1$ and $\rho_3 = -1$, respectively. When $i_1/|\varepsilon_u|$ increases the absolute values of ρ_1 and ρ_3 decrease towards zero, though for ρ_3 the sign changes for large n. The larger the value of the hardening parameter, the faster decrease of $|\rho_1|$ and $|\rho_3|$. In general, this means that the equilibrium of a geometrically imperfect nonlinear elastic column is closer to the equilibrium of its perfect realization

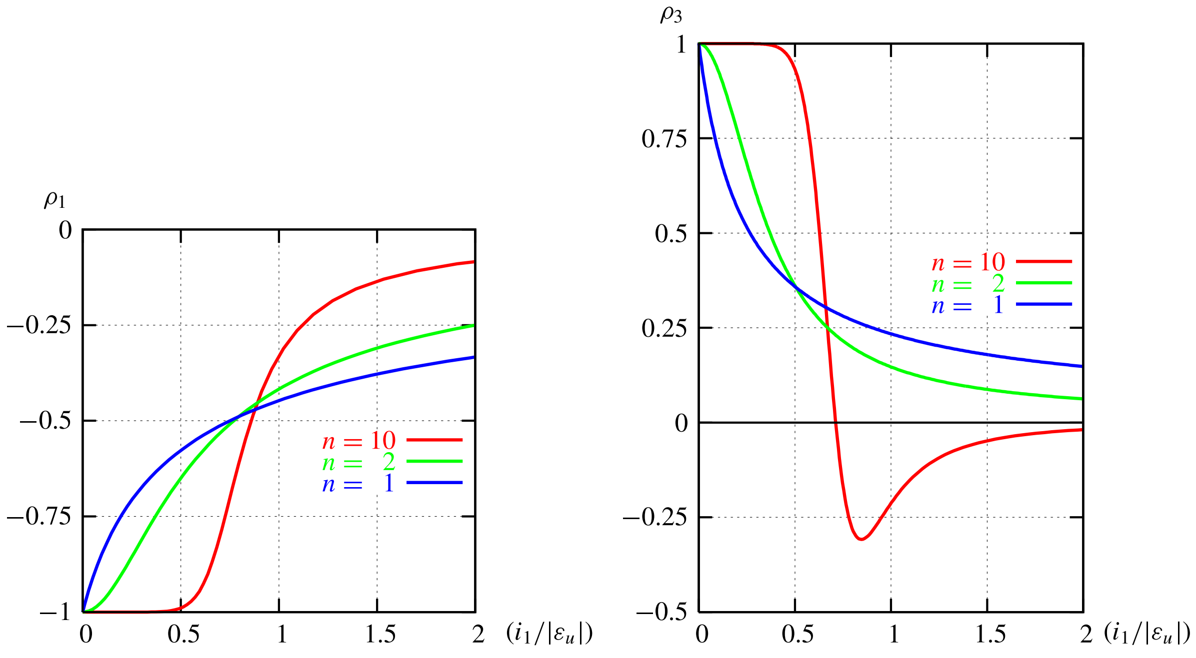

Figure 8. Left: The first imperfection shape parameter ρ_1. Right: The third imperfection shape parameter ρ_3 for symmetric columns.

than it is for a linear elastic column. The initial imperfection sensitivity, described by the maximum load, depends both on the initial postbuckling path and the three imperfection shape parameters. The nonlinear elastic effect of smaller imperfection parameters partly neutralizes the more rapid decrease in postbuckling load capacity shown for the perfect Euler column.

13.2. ***Asymptotic maximum load.*** As mentioned above, the expression for the asymptotic maximum load depends on whether the perfect structure is symmetric or not.

Nonsymmetric column. The asymptotic maximum load of the nonsymmetric column may be computed from (63):

$$\frac{\lambda_m}{\lambda_c} = 1 + c^m_{\frac{1}{2}} \bar{\xi}^{\frac{1}{2}} + O(\bar{\xi}^1) \tag{91}$$

where the constant $c^m_{\frac{1}{2}}$, shown in Figure 9, is given by

$$c^m_{\frac{1}{2}} = -\frac{4}{1+e'_c}\sqrt{\frac{i_2}{3\pi i_1^2}e'_c}, \tag{92}$$

where λ_c and a_1 are determined for the perfect column and ρ_1 is given by (89).

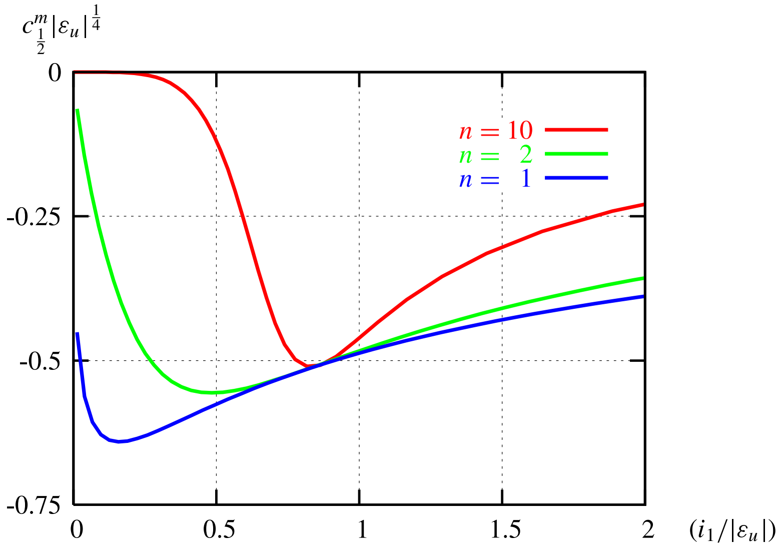

Figure 9. The maximum load constant, $c^m_{\frac{1}{2}}$, for nonsymmetric columns.

Symmetric column. The asymptotic maximum load of the symmetric column is determined from (69):

$$\frac{\lambda_m}{\lambda_c} = 1 + c^m_{\frac{2}{3}} \bar{\xi}^{\frac{2}{3}} + O(\bar{\xi}^{\frac{4}{3}}), \tag{93}$$

where the constant $c^m_{\frac{2}{3}}$, shown in Figure 10, is given by

$$c^m_{\frac{2}{3}} = \frac{3}{2(1+e'_c)}\left(\frac{i_1 - 3(e'_c)^2 + e''_c}{4i_1}\right)^{\frac{1}{3}}. \tag{94}$$

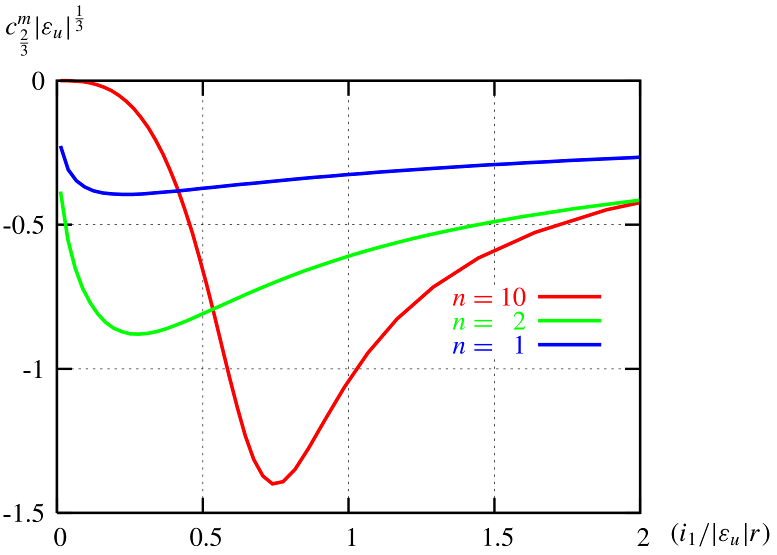

Figure 10. The maximum load constant $c^m_{\frac{2}{3}}$ for symmetric columns.

While λ_c and a_2 are associated with the perfect column, ρ_1 is given by (89). Note that even though ρ_2 and ρ_3 do not affect the maximum load directly in this case, then the fact that ρ_2 vanishes enables us to show that the remainder $O(\bar{\xi}^{\gamma})$ is of order $\bar{\xi}^{\frac{4}{3}}$ and not of order $\bar{\xi}^{1}$.

13.3. ***Comparison with numerical results.*** Here, results of the usual asymptotic and the enhanced asymptotic expansion, both taking imperfections into account, are compared with numerical results obtained by a full nonlinear finite element analysis for the same symmetric column that was used for comparison of perfect column results. Equilibria for the imperfection levels $\bar{\xi} = 0.0025, 0.01, 0.04$ are plotted in Figure 11 for a regular expansion with one and two terms, as well as the enhanced asymptotic expansion of (53), which is forced to obey the condition $\lambda(\xi = 0) = 0$. The one-term asymptotic expansion is the traditional lowest order asymptotic method developed in [Koiter 1945] which only depends on ρ_1 in (52), while ρ_2 is ignored. The two-term asymptotic expansion takes also ρ_2 into account by (52). For the structure in question the relevant constants are

$$\rho_1 = -0.90, \quad \rho_3 = 0.57, \quad m_1 = 1.39, \quad \psi_3 = -0.681. \tag{95}$$

It appears from Figure 11 that, as expected, independent of the imperfection amplitude the enhanced solution through (0, 0) yields the best approximation to the numerical solution, especially for small values of the characteristic buckling amplitude, θ_0. Though both the one- and the two-term solutions diverge close to zero, the two-term solution provides accurate results for much smaller buckling amplitudes than the one-term solution. While the one-term solution provides reliable estimates of the equilibrium path only for very small imperfection levels, the two-term solution approximates loads around the maximum well even for moderate imperfection amplitudes, although the shape of the equilibrium path is badly approximated for smaller amplitudes of the buckling mode (small values of ξ). As seen from the plot, the estimates of the equilibrium paths given by the enhanced asymptotic expansion lie very close to the numerical results for any limited buckling amplitude and even for relatively large imperfection amplitudes.

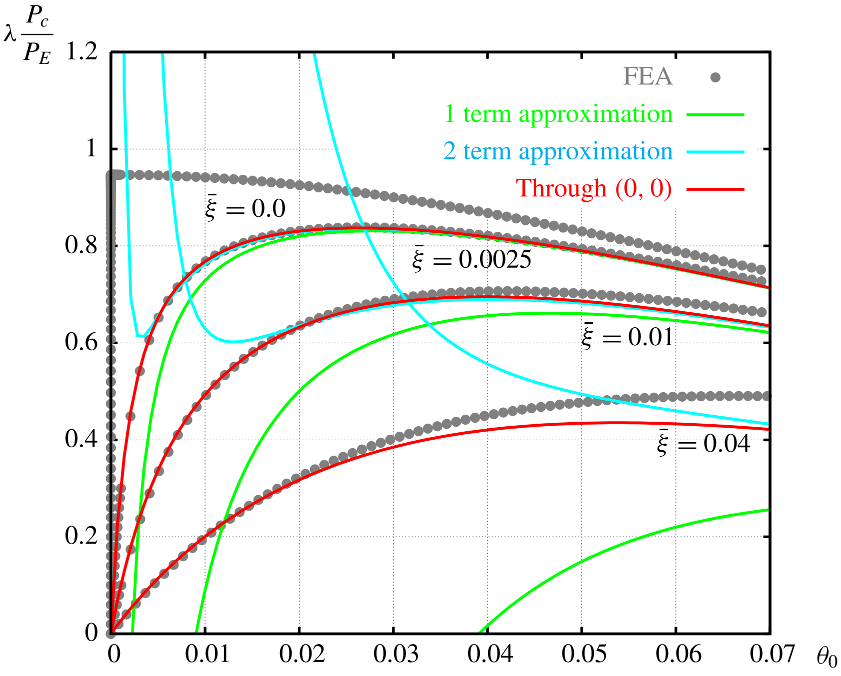

Figure 11. Comparison of equilibrium paths for geometrically imperfect column with rectangular cross-section, $|\varepsilon_u| = 0.002$, $n = 2$, $i_1/|\varepsilon_u| = 0.2$. The classic Euler load of linear elasticity is denoted P_E.

In Figure 12 the dependence of the maximum load on the imperfection amplitude $\bar{\xi}$ is illustrated for the traditional polynomial 1-term asymptotic expansion given by (93), for the enhanced hyperbolic

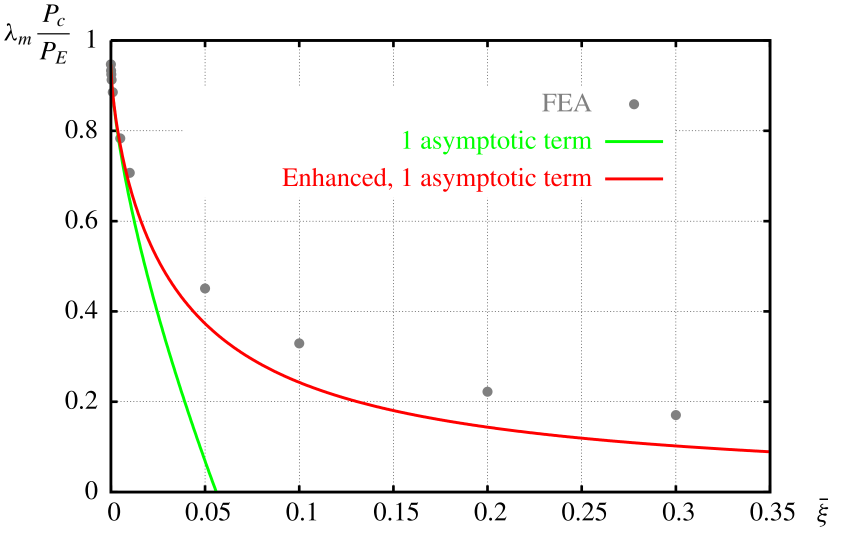

Figure 12. Comparison of maximum load prediction for rectangular cross-section, $|\varepsilon_u| = 0.002$, $n = 2$, $i_1/|\varepsilon_u| = 0.2$. The classic Euler load of linear elasticity is denoted P_E.

asymptotic expansion suggested in (71) and for numerical finite element calculations. For the actual column the relevant constants are

$$c^{m}_{\frac{2}{3}} = -6.83, \qquad c^{m}_{\frac{3}{3}} = 0. \tag{96}$$

and thus only one nonvanishing asymptotic term exists for both the enhanced and the traditional asymptotic method. Comparison between numerical results and the traditional 1-term polynomial asymptotic expansion shows good agreement only for very small values of $\bar{\xi}$. The enhanced expansion provides relatively accurate approximations of the maximum load even at large values of the imperfection amplitude $\bar{\xi}$. In part, this is due to the fact that the enhanced method utilizes that the maximum load does not drop below zero by letting the maximum load approach zero for large values of $\bar{\xi}$. For this column numerical studies show that the maximum load has a lower limit which is higher than zero, yet the enhanced method provides excellent results.

14. Conclusion

In the body of the text a generally applicable asymptotic expansion valid for determination of postbifurcation behavior and imperfection sensitivity of structures under the assumption of full kinematic and elastic nonlinearity has been established. The asymptotic prediction of equilibria for imperfect structures has been enhanced such that the boundary condition that the buckling amplitude vanishes with the load for any imperfection is fulfilled.

The above comparisons with numerical results indicate that exploitation of additional boundary conditions and limit states imposed on the asymptotic expansion may lead to modified, but still asymptotically correct, expressions for imperfect structures which provide stable and relatively accurate results even for larger values of the imperfection amplitude.

Appendix A. Asymptotic coefficient fields $\boldsymbol{P}_i$

Consider the function $\boldsymbol{P}(u^i, \lambda)$ of a field of n variables, $\boldsymbol{u}(\xi)$:

$$\boldsymbol{u}(\xi) = \{u^1(\xi), u^2(\xi), \ldots, u^n(\xi)\} = u^i(\xi), \tag{A-1}$$

where $\boldsymbol{P}(u^i, \lambda)$ depends linearly on the scalar load parameter $\lambda(\xi)$, and where we shall assume that the partial derivatives of $\boldsymbol{P}$ with respect to u^i are continuous at least to third order to ensure that the order of differentiation is unimportant.

A.1. ***Expansion of P at bifurcation.*** Suppose $\xi = 0$ at the bifurcation and expand in series in ξ around the singular point:

$$\begin{aligned} \lambda/\lambda_c &= 1 + \bar{a}_1\xi + \bar{a}_2\xi^2 + \bar{a}_3\xi^3 + O(\xi^4), \\ \boldsymbol{u}(\xi) &= \boldsymbol{u}_c + \xi\bar{\boldsymbol{u}}_1^T + \xi^2\bar{\boldsymbol{u}}_2^T + \xi^3\bar{\boldsymbol{u}}_3^T + O(\xi^4), \\ \boldsymbol{P}\,(\boldsymbol{u}(\xi), \lambda(\xi)) &= \boldsymbol{P}_c + \xi\,\boldsymbol{P}_1^T + \xi^2\boldsymbol{P}_2^T + \xi^3\boldsymbol{P}_3^T + O(\xi^4), \end{aligned} \tag{A-2}$$

where $_c$ designates prebifurcation values taken at the critical point. In the following we exploit that $\boldsymbol{P}$ depends linearly on λ to eliminate higher-order derivatives with respect to λ when the derivatives of $\boldsymbol{P}$ with respect to ξ are obtained.

We define a generalized displacement field consisting of $\boldsymbol{u}$ and the imperfection $\hat{\boldsymbol{u}}$:

$$\boldsymbol{U} \in \{\boldsymbol{u}, \hat{\boldsymbol{u}}\} = \{\boldsymbol{u}, \alpha\tilde{\boldsymbol{u}}\xi^2\}, \tag{A-3}$$

where (6) and (7) are introduced. Then,

$$\begin{aligned}
\frac{\partial \boldsymbol{P}}{\partial \xi} &= \frac{\partial \boldsymbol{P}}{\partial U^i}\frac{\partial U^i}{\partial \xi} + \frac{\partial \boldsymbol{P}}{\partial \lambda}\frac{\partial \lambda}{\partial \xi},\\
\frac{\partial^2 \boldsymbol{P}}{\partial \xi^2} &= \frac{\partial \boldsymbol{P}}{\partial U^i}\frac{\partial^2 U^i}{\partial \xi^2} + \frac{\partial^2 \boldsymbol{P}}{\partial U^i \partial U^j}\frac{\partial U^i}{\partial \xi}\frac{\partial U^j}{\partial \xi} + \frac{\partial \boldsymbol{P}}{\partial \lambda}\frac{\partial^2 \lambda}{\partial \xi^2} + 2\frac{\partial^2 \boldsymbol{P}}{\partial \lambda \partial U^i}\frac{\partial \lambda}{\partial \xi}\frac{\partial U^i}{\partial \xi},\\
\frac{\partial^3 \boldsymbol{P}}{\partial \xi^3} &= \frac{\partial \boldsymbol{P}}{\partial U^i}\frac{\partial^3 U^i}{\partial \xi^3} + 3\frac{\partial^2 \boldsymbol{P}}{\partial U^i \partial U^j}\frac{\partial^2 U^i}{\partial \xi^2}\frac{\partial U^j}{\partial \xi} + \frac{\partial^3 \boldsymbol{P}}{\partial U^i \partial U^j \partial U^k}\frac{\partial U^i}{\partial \xi}\frac{\partial U^j}{\partial \xi}\frac{\partial U^k}{\partial \xi}\\
&\quad + \frac{\partial \boldsymbol{P}}{\partial \lambda}\frac{\partial^3 \lambda}{\partial \xi^3} + \frac{\partial^2 \boldsymbol{P}}{\partial \lambda \partial U^i}\left(\frac{\partial^2 \lambda}{\partial \xi^2}\frac{\partial U^i}{\partial \xi} + \frac{\partial \lambda}{\partial \xi}\frac{\partial^2 U^i}{\partial \xi^2}\right) + 3\frac{\partial^3 \boldsymbol{P}}{\partial \lambda \partial U^i \partial U^j}\frac{\partial \lambda}{\partial \xi}\frac{\partial U^i}{\partial \xi}\frac{\partial U^j}{\partial \xi}.
\end{aligned} \tag{A-4}$$

Now the coefficient fields $\boldsymbol{P}_i^T$ are expressible in terms of $\bar{\boldsymbol{u}}_i^T$ and $\bar{a}_i$ and the imperfection shape $\tilde{\boldsymbol{u}}$ as

$$\begin{aligned}
\boldsymbol{P}_1^T &= \left.\frac{\partial \boldsymbol{P}}{\partial \xi}\right|_c = \boldsymbol{P}^c_{,i}\bar{u}_1^{Ti} + \bar{a}_1\lambda_c\boldsymbol{P}^c_{,\lambda},\\
\boldsymbol{P}_2^T &= \frac{1}{2}\left.\frac{\partial^2 \boldsymbol{P}}{\partial \xi^2}\right|_c = \boldsymbol{P}^c_{,i}\bar{u}_2^{Ti} + \bar{a}_2\lambda_c\boldsymbol{P}^c_{,\lambda} + \bar{a}_1\lambda_c\boldsymbol{P}^c_{,\lambda i}\bar{u}_1^{Ti} + \tfrac{1}{2}\boldsymbol{P}^c_{,ij}\bar{u}_1^{Ti}\bar{u}_1^{Tj} + \alpha\tilde{\boldsymbol{u}}(\boldsymbol{P}^c_{,\hat{\boldsymbol{u}}}),\\
\boldsymbol{P}_3^T &= \frac{1}{6}\left.\frac{\partial^3 \boldsymbol{P}}{\partial \xi^3}\right|_c = \boldsymbol{P}^c_{,i}\bar{u}_3^{Ti} + \bar{a}_3\lambda_c\boldsymbol{P}^c_{,\lambda} + \bar{a}_2\lambda_c\boldsymbol{P}^c_{,\lambda i}\bar{u}_1^{Ti} + \bar{a}_1\lambda_c(\boldsymbol{P}^c_{,\lambda i}\bar{u}_2^{Ti} + \tfrac{1}{2}\boldsymbol{P}^c_{,\lambda ij}\bar{u}_1^{Ti}\bar{u}_1^{Tj})\\
&\qquad + \boldsymbol{P}^c_{,ij}\bar{u}_2^{Ti}\bar{u}_1^{Tj} + \tfrac{1}{6}\boldsymbol{P}_{,ijk}\bar{u}_1^{Ti}\bar{u}_1^{Tj}\bar{u}_1^{Tk} + \alpha\tilde{\boldsymbol{u}}(\bar{a}_1\lambda_c\boldsymbol{P}^c_{,\lambda\hat{\boldsymbol{u}}} + \boldsymbol{P}^c_{,i\hat{\boldsymbol{u}}}\bar{u}_1^{Ti}),
\end{aligned} \tag{A-5}$$

where

$$(\ )_{,i,\dots,k} = \frac{\partial^n(\ )}{\partial u^i, \dots, \partial u^k}. \tag{A-6}$$

A.2. ***Perturbation expansion close to the precritical path.*** Let a perturbation expansion of the function $\boldsymbol{P}$ around the precritical path, indicated by subscript $_0$, be given:

$$\begin{aligned}
\boldsymbol{u}(\xi) &= \boldsymbol{u}_0(\xi) + \xi\bar{\boldsymbol{u}}_1 + \xi^2\bar{\boldsymbol{u}}_2 + \xi^3\bar{\boldsymbol{u}}_3 + O(\xi^4),\\
\boldsymbol{P}(\boldsymbol{u}(\xi)) &= \boldsymbol{P}_0(\xi) + \xi\boldsymbol{P}_1 + \xi^2\boldsymbol{P}_2 + \xi^3\boldsymbol{P}_3 + O(\xi^4),
\end{aligned} \tag{A-7}$$

and an expansion of the precritical path in ξ:

$$\begin{aligned}
\boldsymbol{u}_0(\xi) &= \boldsymbol{u}_c + \xi\boldsymbol{u}_1^0 + \xi^2\boldsymbol{u}_2^0 + \xi^3\boldsymbol{u}_3^0 + O(\xi^4),\\
\boldsymbol{P}_0(\boldsymbol{u}(\xi)) &= \boldsymbol{P}_c + \xi\boldsymbol{P}_1^0 + \xi^2\boldsymbol{P}_2^0 + \xi^3\boldsymbol{P}_3^0 + O(\xi^4).
\end{aligned} \tag{A-8}$$

It is now possible to determine the asymptotic coefficient fields $\boldsymbol{P}_i$ when the precritical path is established. Insert the precritical path (A-8) in the perturbation expansion (A-7) and match it with the expansion of $\boldsymbol{P}$ (A-2) to provide

$$\bar{\boldsymbol{u}}_i = \bar{\boldsymbol{u}}_i^T - \boldsymbol{u}_i^0, \tag{A-9}$$

which yields

$$\begin{aligned} \boldsymbol{P}_1 &= \boldsymbol{P}_1^T - \boldsymbol{P}_1^0 = \boldsymbol{P}^c_{,i}\bar{u}^i_1, \\ \boldsymbol{P}_2 &= \boldsymbol{P}_2^T - \boldsymbol{P}_2^0 = \boldsymbol{P}^c_{,i}\bar{u}^i_2 + \bar{a}_1\lambda_c\boldsymbol{P}^c_{,\lambda i}\bar{u}^i_1 + \tfrac{1}{2}\boldsymbol{P}^c_{,ij}(\bar{u}^i_1\bar{u}^j_1 + 2\bar{u}^i_1 u^{0j}_1) + \alpha\tilde{\boldsymbol{u}}(\boldsymbol{P}^c_{,\hat{\boldsymbol{u}}}), \\ \boldsymbol{P}_3 &= \boldsymbol{P}_3^T - \boldsymbol{P}_3^0 = \boldsymbol{P}^c_{,i}\bar{u}^i_3 + \bar{a}_2\lambda_c\boldsymbol{P}^c_{,\lambda i}\bar{u}^i_1 + \bar{a}_1\lambda_c(\boldsymbol{P}^c_{,\lambda i}\bar{u}^i_2 + \tfrac{1}{2}\boldsymbol{P}^c_{,\lambda ij}(\bar{u}^i_1\bar{u}^j_1 + 2\bar{u}^i_1 u^{0j}_1)) \\ &\qquad + \boldsymbol{P}^c_{,ij}(\bar{u}^i_2\bar{u}^j_1 + \bar{u}^i_2 u^{0j}_1 + u^{0j}_2\bar{u}^i_1) \\ &\qquad + \tfrac{1}{6}\boldsymbol{P}_{,ijk}(\bar{u}^i_1\bar{u}^j_1\bar{u}^k_1 + 3\bar{u}^i_1 u^{0j}_1 u^{0k}_1 + 3\bar{u}^i_1\bar{u}^j_1 u^{0k}_1) \\ &\qquad + \alpha\tilde{\boldsymbol{u}}(\bar{a}_1\lambda_c\boldsymbol{P}^c_{,\lambda\hat{\boldsymbol{u}}} + \boldsymbol{P}^c_{,i\hat{\boldsymbol{u}}}(\bar{u}^i_1 + u^{0i}_1)), \end{aligned} \tag{A-10}$$

The prebuckling fields established in Appendix B are introduced to provide the specific expressions for $\boldsymbol{P}_i$ in (17)–(19).

Appendix B. Expansion of $\boldsymbol{u}_0$ in ξ

A traditional expansion of $\boldsymbol{u}_0$ around Bifurcation in λ yields

$$\boldsymbol{u}_0 = \boldsymbol{u}_c + (\lambda - \lambda_c)\boldsymbol{u}'_c + \tfrac{1}{2}(\lambda - \lambda_c)^2\boldsymbol{u}''_c + O((\lambda - \lambda_c)^3). \tag{B-1}$$

Insertion of λ given by (8) in (B-1) provides the desired expansion in ξ as

$$\boldsymbol{u}_0 = \boldsymbol{u}_c + \xi\boldsymbol{u}^0_1 + \xi^2\boldsymbol{u}^0_2 + O(\xi^3), \tag{B-2}$$

where

$$\boldsymbol{u}^0_1 = a_1\lambda_c\boldsymbol{u}'_c \quad \boldsymbol{u}^0_2 = a_2\lambda_c\boldsymbol{u}'_c + \tfrac{1}{2}(a_1\lambda_c)^2\boldsymbol{u}''_c. \tag{B-3}$$

Appendix C. Symmetry of $\boldsymbol{p}_{l,i}$

Differentiation of $\boldsymbol{p}_l$ given by (5) provides

$$\boldsymbol{p}_{l,i} = \boldsymbol{\sigma}\cdot\boldsymbol{\varepsilon}_{,li} + \boldsymbol{\sigma}_{,i}\cdot\boldsymbol{\varepsilon}_{,l} - (\boldsymbol{\eta}\cdot\boldsymbol{C})_{,li} - \lambda\boldsymbol{B}_{,li}. \tag{C-1}$$

The stress field is a function of the strain field alone, i.e., $\boldsymbol{\sigma}(\boldsymbol{\varepsilon})$, so differentiation of the stress field with respect to the displacement field yields

$$\boldsymbol{\sigma}_{,i} = \frac{\partial\boldsymbol{\sigma}}{\partial\boldsymbol{\varepsilon}}\boldsymbol{\varepsilon}_{,i} = \boldsymbol{D}\boldsymbol{\varepsilon}_{,i}, \tag{C-2}$$

where $\boldsymbol{D}$ is the field of tangent stiffnesses.

Because $\boldsymbol{P}$ and therefore also $\boldsymbol{p}_l$ has continuous derivatives of at least to fourth order with respect to $\boldsymbol{u}$, the constituent functions of $\boldsymbol{p}_l$ must be equally differentiable. This ensures that the order of differentiation may be switched without altering the result. Thus

$$\begin{aligned} \boldsymbol{p}_{l,i} &= \boldsymbol{\sigma}\cdot\boldsymbol{\varepsilon}_{,li} + \boldsymbol{D}\boldsymbol{\varepsilon}_{,i}\cdot\boldsymbol{\varepsilon}_{,l} - (\boldsymbol{\eta}\cdot\boldsymbol{C})_{,li} - \lambda\boldsymbol{B}_{,li} \\ &= \boldsymbol{\sigma}\cdot\boldsymbol{\varepsilon}_{,il} + \boldsymbol{D}\boldsymbol{\varepsilon}_{,l}\cdot\boldsymbol{\varepsilon}_{,i} - (\boldsymbol{\eta}\cdot\boldsymbol{C})_{,il} - \lambda\boldsymbol{B}_{,il} = \boldsymbol{p}_{i,l}, \end{aligned} \tag{C-3}$$

which proves that $\boldsymbol{p}_{l,i}$ is symmetric and that the indices may be interchanged freely, i.e., $\boldsymbol{p}_{l,i} = \boldsymbol{p}_{i,l}$.

Appendix D. Perfect Euler column: asymptotic coefficients

D.1. ***Prebuckling.*** The straightforward prebuckling solution for the Euler column is

$$w_0(x) = 0, \qquad \ddot{v}_0(x) = 0, \tag{D-1}$$

where dots over a quantity denote differentiation with respect to x.

D.2. ***Principle of virtual displacements and operators.*** The principle of virtual displacements as given in (1) depends on strains, stresses, constraints and load.

The Bernoulli–Euler beam theory assumes the only influential strains to be the strains in the direction of the x-axis, here denoted ε:

$$\varepsilon = \epsilon + z\kappa, \tag{D-2}$$

where

$$\epsilon = \sqrt{(1+\dot{v})^2 + \dot{w}^2} - 1, \quad \kappa = \dot{\theta} = \frac{\ddot{w}(1+\dot{v}) - \ddot{v}\dot{w}}{(1+\dot{v})^2 + \dot{w}^2}, \tag{D-3}$$

and the corresponding stresses $\sigma(\varepsilon)$ may depend on the strains to any degree of nonlinearity.

The load operator $\boldsymbol{B}$ is taken to be linear in the displacements:

$$\boldsymbol{B}(\boldsymbol{u}) = -\boldsymbol{P}_c v(L). \tag{D-4}$$

In the present application no Lagrange constraints are enforced.

The operators $\mathcal{C}_i^c$, $\mathcal{B}_i^c$ *and* $\boldsymbol{\mathcal{E}}_i^c$. Use (23), (43) and (44) to show that for this column the operators associated with the principle of virtual displacements are as follows:

Constraints:

$$\mathcal{C}_i^c \equiv 0 \tag{D-5}$$

Loads:

$$\mathcal{B}_1^c(\boldsymbol{u}_\alpha) = -\boldsymbol{P}_c v_\alpha(L), \quad \mathcal{B}_i^c = 0, \; i \neq 1 \tag{D-6}$$

Strains: The strain operator may be split up in parts that are independent of the cross-sectional variable z:

$$\boldsymbol{\mathcal{E}}_i^c = \boldsymbol{\mathcal{E}}_i^{c\epsilon} + z\boldsymbol{\mathcal{E}}_i^{c\kappa}. \tag{D-7}$$

The stretch ratio at critical load s_c is

$$\frac{1}{s_c} = \frac{1}{1+\dot{v}_c} = 1 - \dot{v}_c + O(\dot{v}_c^2) = 1 + i_1(1-n_c) + O(i_1^2), \tag{D-8}$$

where $0 \le n_c \le 1$ and $n_c = 0$ for linear elasticity. Thus the strain operators are

$$\boldsymbol{\mathcal{E}}_1^{c\epsilon}(\boldsymbol{u}_\alpha) = \dot{v}_\alpha, \quad \boldsymbol{\mathcal{E}}_2^{c\epsilon}(\boldsymbol{u}_\alpha, \boldsymbol{u}_\beta) = \dot{w}_\alpha \dot{w}_\beta \frac{1}{s_c} \tag{D-9}$$

and

$$\boldsymbol{\mathcal{E}}_1^{c\kappa}(\boldsymbol{u}_\alpha) = \ddot{w}_\alpha \frac{1}{s_c}, \quad \boldsymbol{\mathcal{E}}_2^{c\kappa}(\boldsymbol{u}_\alpha, \boldsymbol{u}_\beta) = -\big((\dot{w}_\alpha \dot{v}_\beta)^{\cdot} + (\dot{w}_\beta \dot{v}_\alpha)^{\cdot}\big)\frac{1}{s_c^2}. \tag{D-10}$$

Provided that we only determine the second postbuckling constant a_2 when the column is symmetric $\boldsymbol{\mathcal{E}}_3^c$ enters solely as $\boldsymbol{\mathcal{E}}_3^c(\boldsymbol{u}_\alpha, \boldsymbol{u}_1, \boldsymbol{u}_1)$ and $\boldsymbol{\mathcal{E}}_4^c$ as $\boldsymbol{\mathcal{E}}_4^c(\boldsymbol{u}_1, \boldsymbol{u}_1, \boldsymbol{u}_1, \boldsymbol{u}_1)$ after $\boldsymbol{u}_1$ has been determined. It is later shown that $v_1 \equiv 0$, and thus we get

$$\begin{aligned} \boldsymbol{\mathcal{E}}_3^{c\epsilon}(\boldsymbol{u}_\alpha, \boldsymbol{u}_1, \boldsymbol{u}_1) &= -(\dot{v}_\alpha \dot{w}_1 \dot{w}_1)\frac{1}{s_c^2}, \\ \boldsymbol{\mathcal{E}}_4^{c\epsilon}(\boldsymbol{u}_1, \boldsymbol{u}_1, \boldsymbol{u}_1, \boldsymbol{u}_1) &= -3(\dot{w}_1 \dot{w}_1 \dot{w}_1 \dot{w}_1)\frac{1}{s_c^3}, \end{aligned} \tag{D-11}$$

and

$$\boldsymbol{\mathcal{E}}_3^{c\kappa}(\boldsymbol{u}_\alpha, \boldsymbol{u}_1, \boldsymbol{u}_1) = -2(\dot{w}_\alpha \dot{w}_1 \dot{w}_1)^{\cdot}\frac{1}{s_c^3}, \quad \boldsymbol{\mathcal{E}}_4^{c\kappa}(\boldsymbol{u}_1, \boldsymbol{u}_1, \boldsymbol{u}_1, \boldsymbol{u}_1) = 0. \tag{D-12}$$

Stability operators $\mathcal{P}_i^c$*.* The relevant stability operators $\mathcal{P}_1^c$–$\boldsymbol{\mathcal{P}}_4^c$ are provided by (46) and (47):

$$\begin{aligned} \mathcal{P}_1^c(\boldsymbol{u}_\alpha) &= \int_0^L (-\lambda_c \boldsymbol{P}_c \dot{v}_\alpha)\, dx + \lambda_c \boldsymbol{P}_c v_\alpha(L), \\ \mathcal{P}_2^c(\boldsymbol{u}_\alpha, \boldsymbol{u}_\beta) &= \int_0^L \left(E_t^c A \dot{v}_\alpha \dot{v}_\beta + \frac{E_t^c I_1}{s_c^2} \ddot{w}_\alpha \ddot{w}_\beta - \frac{\sigma_c A}{s_c} \dot{w}_\alpha \dot{w}_\beta \right) dx. \end{aligned} \tag{D-13}$$

Again, we only determine the second postbuckling constant a_2 when the column is symmetric. Thus $\mathcal{P}_3^c$ enters solely as $\mathcal{P}_3^c(\boldsymbol{u}_\alpha, \boldsymbol{u}_1, \boldsymbol{u}_1)$ and $\boldsymbol{\mathcal{P}}_4^c$ as $\mathcal{P}_4^c(\boldsymbol{u}_1, \boldsymbol{u}_1, \boldsymbol{u}_1, \boldsymbol{u}_1)$ after $\boldsymbol{u}_1$ has been determined. Utilize $v_1 \equiv 0$ in (D-9) and (D-11) to provide

$$\begin{aligned} \mathcal{P}_3^c(\boldsymbol{u}_\alpha, \boldsymbol{u}_1, \boldsymbol{u}_1) &= \int_0^L \left(\left(\frac{E_{t,\varepsilon}^c}{s_c^2} - \frac{2E_t^c}{s_c^3} \right) I_1 \dot{v}_\alpha \ddot{w}_1^2 + \left(\frac{E_t^c}{s_c} + \frac{\sigma_c}{s_c^2} \right) A \dot{v}_\alpha \dot{w}_1^2 - \frac{2E_t^c}{s_c^3} I_1 \dot{w}_1 \ddot{v}_\alpha \ddot{w}_1 + \frac{E_{t,\varepsilon}^c}{s_c^3} I_2 \ddot{w}_\alpha \ddot{w}_1^2 \right) dx, \\ \mathcal{P}_4^c(\boldsymbol{u}_1, \boldsymbol{u}_1, \boldsymbol{u}_1, \boldsymbol{u}_1) &= \int_0^L \left(\frac{E_{t,\varepsilon\varepsilon}^c}{s_c^4} I_3 \ddot{w}_1^4 + \left(\frac{6E_{t,\varepsilon}^c}{s_c^3} - \frac{24E_t^c}{s_c^4} \right) I_1 \dot{w}_1^2 \ddot{w}_1^2 + 3\left(\frac{E_t^c}{s_c^2} + \frac{\sigma_c}{s_c^3} \right) A \dot{w}_1^4 \right) dx. \end{aligned} \tag{D-14}$$

D.3. ***Expansion parameter and boundary conditions.*** Let the expansion parameter ξ be the rotation of the column end, i.e.,

$$\xi = \theta(0), \quad \tan\theta(0) = \frac{\dot{w}(0)}{1 + \dot{v}(0)}. \tag{D-15}$$

The solution to the boundary value problem of the geometrically perfect column must fulfill (D-15)b. Insert (D-15)a in the asymptotic expansion (9) of $\boldsymbol{u}$ and match the right-hand side of (D-15)b with the left-hand side to reveal the rather obvious boundary conditions

$$\dot{w}_1(0) = 1, \quad \dot{w}_2(0) = \dot{v}_1(0). \tag{D-16}$$

D.4. ***Buckling.*** The buckling equation (26) using the stability operator (D-13) with the operators of (D-9) inserted provides

$$0 = \int_0^L \left(E_t^c A \dot{v}_1 \delta\dot{v} + \frac{E_t^c I_1}{s_c^2} \ddot{w}_1 \delta\ddot{w} - \frac{\lambda_c P_c}{s_c} \dot{w}_1 \delta\dot{w} \right) dx. \tag{D-17}$$

Fulfill (D-17) for all admissible δv and δw to get

$$E_t^c A \ddot{v}_1 = 0, \quad \ddddot{w}_1 + \frac{s_c \lambda_c \boldsymbol{P}_c}{E_t^c I_1} \ddot{w}_1 = 0, \tag{D-18}$$

respectively. Apply the kinematic boundary conditions at the pinned ends to obtain the eigenmode solution of (D-18). The amplitude of the eigenmode is determined by condition (D-16)a:

$$v_1 = 0, \quad w_1 = \frac{L}{\pi}\sin(\pi x/L). \tag{D-19}$$

Normalize the applied force as follows to make $\lambda_c = 1$:

$$P_c/A = \sigma_c = E_t^c\big(i_1 + O(i_1^2)\big) \implies \lambda_c = 1. \tag{D-20}$$

D.5. *First postbuckling problem.*

First postbuckling constant. As mentioned earlier, in the case of a nonsymmetric structure, we shall limit ourselves to determining the first postbuckling constant a_1 and refrain form determining the second, a_2. From (29) with (D-14) inserted we get

$$a_1^N = -\int_0^L \frac{1}{2s_c^3} E_{t,\varepsilon}^c I_2 \ddot{w}_1^3 \, dx = E_t^c A L \frac{2e'_c i_2}{3\pi i_1 s_c^3}. \tag{D-21}$$

Utilize the necessary coefficient from the expansion of the prebuckling path, namely

$$\dot{v}'_c(x) = -\frac{\sigma_c}{E_t^c} = -i_1, \tag{D-22}$$

to determine

$$\begin{aligned} a_1^D &= -\frac{\sigma_c}{E_t^c}\int_0^L \left(\left(\frac{E_{t,\varepsilon}^c}{s_c^2} - \frac{2E_t^c}{s_c^3}\right) I_1 \ddot{w}_1^2 + \left(\frac{E_t^c}{s_c} + \frac{\sigma_c}{s_c^2}\right) A \dot{w}_1^2\right) dx \\ &= -\tfrac{1}{2} E_t^c A L i_1\big(1 + e'_c + O(i_1)\big). \end{aligned} \tag{D-23}$$

As $i_1 \ll 1$, introduction of the nondimensional quantities defined in (72) and (73) yields

$$a_1 = -\frac{4e'_c i_2}{3\pi i_1^2 (1 + e'_c)}. \tag{D-24}$$

From (D-24) it is clear that only when the cross-section is nonsymmetric ($i_2 \neq 0$) *and* the material model is nonlinear will the first postbuckling constant a_1 differ from zero.

Postbuckling displacement field. The postbuckling displacement field, which is only determined when $a_1 = 0$ (implying $e'_c i_2 = 0$), may be determined from the variational equation (41) together with the boundary conditions (D-16). Utilize the stability operators (D-13)–(D-14) and get

$$\begin{aligned} 0 = \int_0^L &\left(E_t^c A \dot{v}_2 \delta\dot{v} + \frac{1}{s_c^2} E_t^c I_1 \ddot{w}_2 \delta\ddot{w} - \frac{1}{s_c}\sigma_c A \dot{w}_2 \delta\dot{w}\right) dx \\ &+ \frac{1}{2}\int_0^L \left(\frac{1}{s_c^2} E_{t,\varepsilon}^c I_1 \ddot{w}_1^2 \delta\dot{v} + \left(\frac{1}{s_c} E_t^c + \frac{1}{s_c^2}\sigma_c\right) A \dot{w}_1^2 \delta\dot{v} + \frac{1}{s_c^3} 2E_t^c I_1 \dddot{w}_1 \dot{w}_1 \delta\dot{v}\right) dx. \end{aligned} \tag{D-25}$$

Gather terms in (D-25) and introduce $\boldsymbol{u}_1$ from (D-19) and s_c from (D-8) to reach the differential equations

$$\dot{v}_2 = -\tfrac{1}{2}\Big((1 - n_c i_1)\cos^2\frac{\pi x}{L} + e'_c\big(1 + 2(1 - n_c)i_1\big)\sin^2\frac{\pi x}{L}\Big) + O(i_1^2), \quad \dddot{w}_2 + \left(\frac{\pi}{L}\right)^2 \dot{w}_2 = 0, \tag{D-26}$$

and the static boundary conditions

$$\ddot{w}_2(0) = 0, \quad \ddot{w}_2(L) = 0. \tag{D-27}$$

Use the kinematic boundary conditions (D-27) at the pinned ends along with the conditions (D-16). When $i_1 \ll 1$ the second postbuckling displacement field becomes

$$v_2 = -\tfrac{1}{4}\Big((1+e_c')x + (1-e_c')\frac{L}{2\pi}\sin\frac{2\pi x}{L}\Big) + O(i_1), \quad w_2 = 0. \tag{D-28}$$

D.6. ***Second postbuckling constant.*** For symmetric cross-sections ($a_1 = 0$, $e_c' i_2 = 0$) the numerator of the second postbuckling constant a_2^N may be found from (42). Utilize the operator expressions (D-13)–(D-14) to obtain

$$\begin{aligned} a_2^N = -\int_0^L \bigg(\Big(\frac{1}{s_c^2}E^c_{t,\varepsilon} - \frac{2}{s_c^3}E^c_t\Big) I_1\dot{v}_2\ddot{w}_1^2 + \Big(\frac{1}{s_c}E^c_t + \frac{1}{s_c^2}\sigma_c\Big) A\dot{v}_2\dot{w}_1^2 - \frac{2}{s_c^3}E^c_t I_1\dot{w}_1\ddot{v}_2\ddot{w}_1\bigg)dx \\ -\frac{1}{6}\int_0^L \bigg(\frac{1}{s_c^4}E^c_{t,\varepsilon\varepsilon}I_3\ddot{w}_1^4 + 6\Big(\frac{1}{s_c^3}E^c_{t,\varepsilon} - \frac{4}{s_c^4}E^c_t\Big) I_1\ddot{w}_1^2\dot{w}_1^2 + 3\Big(\frac{1}{s_c^2}E^c_t + \frac{1}{s_c^3}\sigma_c\Big) A\dot{w}_1^4\bigg)dx. \end{aligned} \tag{D-29}$$

Since the terms proportional to $E^c_t A$ vanish, it is essential to include the first-order terms of i_1 in $\boldsymbol{u}_2$ (D-26) and $1/s_c$ (D-8). After some derivations (D-29) yields

$$a_2^N = -\tfrac{1}{16}E^c_t AL\big(i_1 - 3(e_c')^2 + e_c''\big) + O(i_1^2) + e_c' O(i_1) + e_c'' O(i_1). \tag{D-30}$$

The denominator of a_2 is identical to the denominator of a_1, which is given by (D-23). Utilize that $i_1 \ll 1$ to truncate terms of order 1, e_c' and e_c'' respectively to the lowest order of i_1. Then, the second postbuckling constant becomes

$$a_2 = \frac{i_1 - 3(e_c')^2 + e_c''}{8i_1(1+e_c')}. \tag{D-31}$$

Note that the term i_1 in the numerator of a_2 is not necessarily small compared to the other terms e_c' and e_c''. When the column exhibits linear or near linear material behavior at buckling, the absolute value of the nonlinear material constants e_c' and e_c'' decrease and the i_1-term becomes important.

D.7. ***Nonlinear elastic inextensible Euler column.*** When the Euler column is constrained to be inextensible, it is easily shown that

$$C^1 = \boldsymbol{\eta}^1 \cdot \big(\dot{v} + \tfrac{1}{2}\dot{v}^2 + \tfrac{1}{2}\dot{w}^2\big) = 0, \quad C^2 = \boldsymbol{\eta}^2 \cdot (\sin\theta - \dot{w}) = 0, \quad B = -\boldsymbol{P}_c v(L), \tag{D-32}$$

and

$$\epsilon = 0, \quad \kappa = \dot{\theta}. \tag{D-33}$$

Furthermore, when prebuckling is given by

$$v_0 = w_0 = \theta_0 = \boldsymbol{\eta}_0^2 = 0, \quad \boldsymbol{\eta}_0^1 = \lambda\boldsymbol{P}_c, \tag{D-34}$$

the operators associated with the principle of virtual displacements may be found from (23) and (43) and (44) together with (D-32)–(D-33).

Constraints: Inextensibility requires

$$\begin{aligned} \mathcal{C}_1^{1c}(\boldsymbol{u}_\alpha) &= \lambda_c \boldsymbol{P}_c \cdot \dot{v}_\alpha, \\ \mathcal{C}_2^{1c}(\boldsymbol{u}_\alpha, \boldsymbol{u}_\beta) &= \boldsymbol{\eta}_\beta^1 \cdot \dot{v}_\alpha + \boldsymbol{\eta}_\alpha^1 \cdot \dot{v}_\beta + \lambda_c \boldsymbol{P}_c \cdot (\dot{v}_\alpha \dot{v}_\beta + \dot{w}_\alpha \dot{w}_\beta), \\ \mathcal{C}_3^{1c}(\boldsymbol{u}_\alpha, \boldsymbol{u}_1, \boldsymbol{u}_1) &= \boldsymbol{\eta}_\alpha^1 \cdot \dot{w}_1^2, \\ \mathcal{C}_4^{1c}(\boldsymbol{u}_1, \boldsymbol{u}_1, \boldsymbol{u}_1, \boldsymbol{u}_1) &= 0 \end{aligned} \tag{D-35}$$

and

$$\begin{aligned} \mathcal{C}_1^{2c}(\boldsymbol{u}_\alpha) &= 0, \\ \mathcal{C}_2^{2c}(\boldsymbol{u}_\alpha, \boldsymbol{u}_\beta) &= \boldsymbol{\eta}_\beta^2 \cdot (\theta_\alpha - \dot{w}_\alpha) + \boldsymbol{\eta}_\alpha^2 \cdot (\theta_\beta - \dot{w}_\beta), \\ \mathcal{C}_3^{2c}(\boldsymbol{u}_\alpha, \boldsymbol{u}_1, \boldsymbol{u}_1) &= 0, \\ \mathcal{C}_4^{2c}(\boldsymbol{u}_1, \boldsymbol{u}_1, \boldsymbol{u}_1, \boldsymbol{u}_1) &= -4\boldsymbol{\eta}_1^2 \cdot \theta_1^3, \end{aligned} \tag{D-36}$$

where it is utilized that $v_1 = \boldsymbol{\eta}_1^1 \equiv 0$ has been established before $\mathcal{C}_3^i$ and $\mathcal{C}_4^i$ are used.

Loads: $$\mathcal{B}_1^c(\boldsymbol{u}_\alpha) = -\boldsymbol{P}_c v_\alpha(L), \quad \mathcal{B}_i^c = 0,\ i \neq 1. \tag{D-37}$$

Strains: $$\mathcal{E}_1^c(\boldsymbol{u}_\alpha) = z\dot{\theta}_\alpha, \quad \mathcal{E}_i^c = 0. \tag{D-38}$$

Stability operators: The stability operators defined in (46) and (47) become

$$\begin{aligned} \mathcal{P}_1^c(\boldsymbol{u}_\alpha) &= \int_0^L \big(-\lambda_c \boldsymbol{P}_c \dot{v}_\alpha\big) dx + \lambda_c \boldsymbol{P}_c v_\alpha(L), \\ \mathcal{P}_2^c(\boldsymbol{u}_\alpha, \boldsymbol{u}_\beta) &= \int_0^L \Big(E_t^c I_1 \dot{\theta}_\alpha \dot{\theta}_\beta - \big(\boldsymbol{\eta}_\beta^1 \dot{v}_\alpha + \boldsymbol{\eta}_\alpha^1 \dot{v}_\beta + \lambda_c \boldsymbol{P}_c (\dot{v}_\alpha \dot{v}_\beta + \dot{w}_\alpha \dot{w}_\beta)\big) \\ &\qquad\qquad - \big(\boldsymbol{\eta}_\beta^2 (\theta_\alpha - \dot{w}_\alpha) + \boldsymbol{\eta}_\alpha^2 (\theta_\beta - \dot{w}_\beta)\big)\Big) dx, \\ \mathcal{P}_3^c(\boldsymbol{u}_\alpha, \boldsymbol{u}_1, \boldsymbol{u}_1) &= \int_0^L \big(E_{t,\varepsilon}^c I_2 \dot{\theta}_\alpha \dot{\theta}_1^2 - \boldsymbol{\eta}_\alpha^1 \dot{w}_1^2 \big)\, dx, \\ \mathcal{P}_4^c(\boldsymbol{u}_1, \boldsymbol{u}_1, \boldsymbol{u}_1, \boldsymbol{u}_1) &= \int_0^L \big(E_{t,\varepsilon\varepsilon}^c I_3 \dot{\theta}_1^4 + 4\boldsymbol{\eta}_1^2 \theta_1^3 \big)\, dx. \end{aligned} \tag{D-39}$$

Buckling and postbuckling. Insert the stability operators in the stability problems (26) and (29) together with (41) and (42) to provide the buckling solution

$$\begin{aligned} &\lambda_c = 1, \quad P_c = \frac{\pi^2 E_t^c I_1}{L^2}, \quad \sigma_c = i_1 E_t^c, \\ &v_1 = 0, \quad w_1 = \frac{L}{\pi} \sin \frac{\pi x}{L}, \quad \theta_1 = \cos \frac{\pi x}{L}, \\ &\boldsymbol{\eta}_1^1 = 0, \quad \boldsymbol{\eta}_1^2 = P_c \cos \frac{\pi x}{L}, \end{aligned} \tag{D-40}$$

the first postbuckling constant a_1 for nonsymmetric cross-sections

$$a_1 = -\frac{4e_c' i_2}{3\pi i_1^2}, \tag{D-41}$$

the postbuckling solution

$$\begin{aligned} v_2 &= -\tfrac{1}{4}\Big(x + \frac{L}{2\pi}\sin\frac{2\pi x}{L}\Big), \quad && w_2 = 0, \quad \theta_2 = 0, \\ \boldsymbol{\eta}_2^1 &= \tfrac{1}{2} P_c \cos^2\frac{\pi x}{L}, && \boldsymbol{\eta}_2^2 = 0, \end{aligned} \tag{D-42}$$

and the second postbuckling constant a_2 for symmetric cross-sections

$$a_2 = \frac{i_1 + e_c''}{8 i_1}. \tag{D-43}$$

Appendix E. Imperfect Euler column: asymptotic coefficients

The prebuckling, buckling and postbuckling solution may be taken from Appendix D and the strain measure with respect to the perfect reference is given by (D-3).

E.1. ***Scalar stability operators connected with imperfection.*** The effects of initial imperfections are determined by the imperfection shape parameters, ρ_i. The scalar general stability operators $\mathcal{P}_i^c$ determined for the perfect column in (D-13) and (D-14), some of the additional general stability operators defined by (46) and (47) and the scalar operators associated with imperfections defined by (49) are needed in order to compute ρ_i.

Additional general stability operator. Most general stability operators needed to determine ρ_i were determined for the perfect structure in (D-13) and (D-14). Because the second postbuckling constant a_2 only is determined when $a_1 = 0$ some general stability operators enter only the imperfection sensitivity analysis. These stability operators are $\mathcal{P}_3^c(\boldsymbol{u}_\alpha, \boldsymbol{u}_1, \boldsymbol{u}_c')$ and $\boldsymbol{\mathcal{E}}_4^c(\boldsymbol{u}_1, \boldsymbol{u}_1, \boldsymbol{u}_1, \boldsymbol{u}_c')$. First we determine the additional operators associated with the principle of virtual displacements needed to compute $\mathcal{P}_3^c(\boldsymbol{u}_\alpha, \boldsymbol{u}_1, \boldsymbol{u}_c')$ and $\boldsymbol{\mathcal{E}}_4^c(\boldsymbol{u}_1, \boldsymbol{u}_1, \boldsymbol{u}_1, \boldsymbol{u}_c')$ from (43) when it is exploited that $v_1 = 0$ and $w_0 = 0$ and the strains are given by (D-3):

$$\begin{aligned} &\boldsymbol{\mathcal{E}}_3^{c\epsilon}(\boldsymbol{u}_\alpha, \boldsymbol{u}_1, \boldsymbol{u}_c') = -(\dot{w}_\alpha \dot{w}_1 \dot{v}_c') s_c^{-2}, \quad && \boldsymbol{\mathcal{E}}_4^{c\epsilon}(\boldsymbol{u}_1, \boldsymbol{u}_1, \boldsymbol{u}_1, \boldsymbol{u}_c') = 0, \\ &\boldsymbol{\mathcal{E}}_3^{c\kappa}(\boldsymbol{u}_\alpha, \boldsymbol{u}_1, \boldsymbol{u}_c') = 2(\dot{v}_\alpha \dot{w}_1 \dot{v}_c')^{\boldsymbol{\cdot}} s_c^{-3}, && \boldsymbol{\mathcal{E}}_4^{c\epsilon}(\boldsymbol{u}_1, \boldsymbol{u}_1, \boldsymbol{u}_c', \boldsymbol{u}_c') = 2\dot{w}_1^2 (\dot{v}_c')^2 s_c^{-3}. \end{aligned} \tag{E-1}$$

Thus, the additional general stability operators become

$$\begin{aligned} \mathcal{P}_3^c(\boldsymbol{u}_c', \boldsymbol{u}_1, \boldsymbol{u}_\alpha) &= -\int_0^L \frac{\sigma_c}{E_t^c}\bigg(\bigg(\frac{E_{t,\varepsilon}^c}{s_c^2} - 3\frac{E_t^c}{s_c^3}\bigg) I_1 \ddot{w}_1 \ddot{w}_\alpha + \frac{E_t^c A}{s_c}\dot{w}_1 \dot{w}_\alpha\bigg) dx, \\ \mathcal{P}_4^c(\boldsymbol{u}_c', \boldsymbol{u}_1, \boldsymbol{u}_1, \boldsymbol{u}_1) &= 0, \\ \mathcal{P}_4^c(\boldsymbol{u}_c', \boldsymbol{u}_c', \boldsymbol{u}_1, \boldsymbol{u}_1) &= \int_0^L \bigg(\frac{\sigma_c}{E_t^c}\bigg)^2 \bigg(\bigg(\frac{E_{t,\varepsilon\varepsilon}^c}{s_c^2} - 4\frac{E_{t,\varepsilon}^c}{s_c^3} + 6\frac{E_t^c}{s_c^4}\bigg) I_1 \ddot{w}_1^2 + \bigg(\frac{E_{t,\varepsilon}^c}{s_c} - 2\frac{E_t^c}{s_c^2} + 2\frac{\sigma_c}{s_c^3}\bigg) A \dot{w}_1^2\bigg) dx, \end{aligned} \tag{E-2}$$

where we have used that $\dot{v}_c' = -\sigma_c / E_t^c$ and $\ddot{v}_c' = 0$ according to (D-22) and the buckling problem has been utilized to eliminate terms.

Stability operators associated with imperfections. Use (48) to show that the operators associated with imperfections are

$$\boldsymbol{\mathcal{E}}_1^{I\epsilon}(\tilde{\boldsymbol{u}}) = \dot{\tilde{v}}, \quad \boldsymbol{\mathcal{E}}_1^{I\kappa}(\tilde{\boldsymbol{u}}) = \ddot{\tilde{w}}, \quad \mathcal{D}_2^I(\boldsymbol{u}_\alpha, \tilde{\boldsymbol{u}}) = 0, \tag{E-3}$$

when no constraints are enforced.

The only stability operators associated with imperfections needed to determine ρ_1 and when $a_1 = 0$, as well as ρ_2 and ρ_3 are $\bar{\mathcal{P}}_2^c(\boldsymbol{u}_\alpha, \tilde{\boldsymbol{u}})$, $\bar{\mathcal{P}}_3^c(\boldsymbol{u}_1, \boldsymbol{u}_1, \tilde{\boldsymbol{u}})$ and $\bar{\mathcal{P}}_3^c(\boldsymbol{u}_c', \boldsymbol{u}_1, \tilde{\boldsymbol{u}})$. The third degree operators are only determined for symmetric and/or linear elastic columns, thus I_2 and/or derivatives of E_t with respect to ε vanish. From (49) we have

$$\begin{aligned}
\bar{\mathcal{P}}_2^c(\boldsymbol{u}_\alpha, \tilde{\boldsymbol{u}}) &= \mathcal{P}_2^c(\boldsymbol{u}_\alpha, \tilde{\boldsymbol{u}}) - \int_0^L \left(E_t^c A \dot{v}_\alpha \dot{\tilde{v}} + \frac{E_t^c I_1}{s_c} \ddot{w}_\alpha \ddot{\tilde{w}} \right) dx, \\
\bar{\mathcal{P}}_3^c(\boldsymbol{u}_1, \boldsymbol{u}_1, \tilde{\boldsymbol{u}}) &= \mathcal{P}_3^c(\boldsymbol{u}_1, \boldsymbol{u}_1, \tilde{\boldsymbol{u}}) - \int_0^L \left(\frac{E_{t,\varepsilon} I_1}{s_c^2} \dot{\tilde{v}} \ddot{w}_1^2 + \frac{E_t^c A}{s_c} \dot{\tilde{v}} \dot{w}_1^2 \right) dx, \qquad \text{(E-4)} \\
\bar{\mathcal{P}}_3^c(\boldsymbol{u}_c', \boldsymbol{u}_1, \tilde{\boldsymbol{u}}) &= \mathcal{P}_3^c(\boldsymbol{u}_c', \boldsymbol{u}_1, \tilde{\boldsymbol{u}}) - \int_0^L \left(\left(\frac{E_{t,\varepsilon}}{s_c} - \frac{E_t^c}{s_c^2} \right) I_1 \ddot{\tilde{w}} \ddot{w}_1 \dot{v}_c' \right) dx.
\end{aligned}$$

E.2. ***Expansion parameter.*** Since the expansion parameter ξ is identified as the rotation of the column end even for the imperfect structure, the condition (D-15) must apply. Similar to the asymptotic match for the perfect structure (D-15) yields

$$\dot{\bar{w}}_1(0) = 1, \quad \dot{\bar{w}}_2(0) = \dot{w}_2(0) + \alpha \dot{\omega}_2(0) = \dot{\bar{v}}_1(0), \qquad \text{(E-5)}$$

where ω_2 is associated with the shape of the imperfection.

Because $\boldsymbol{u}_1$ is independent of the imperfection and $\dot{w}_2(0)$ already fulfills the condition $\dot{w}_2(0) = \dot{v}_1(0)$, the boundary condition on ω_2 becomes

$$\dot{\omega}_2(0) = 0. \qquad \text{(E-6)}$$

E.3. ***Imperfection in shape of the buckling displacements.*** When the shape of the imperfection is given, the imperfect stability operators (E-4) may be evaluated. For simplicity, let the shape of the imperfection be the buckling displacement field $\boldsymbol{u}_1$:

$$\widehat{w} = \bar{\xi} w_1 = \bar{\xi} \left(\frac{L}{\pi} \right) \sin \frac{\pi x}{L}, \quad \widehat{v} = \bar{\xi} v_1 = 0. \qquad \text{(E-7)}$$

Thus, from the buckling problem $\mathcal{P}_2^c(\boldsymbol{u}_\alpha, \boldsymbol{u}_1) = 0$, and the stability operators associated with imperfections become

$$\begin{aligned}
\bar{\mathcal{P}}_2^c(\boldsymbol{u}_\alpha, \boldsymbol{u}_1) &= -\int_0^L \frac{E_t^c I_1}{s_c} \ddot{w}_\alpha \ddot{w}_1 dx, \\
\bar{\mathcal{P}}_3^c(\boldsymbol{u}_1, \boldsymbol{u}_1, \boldsymbol{u}_1) &= \mathcal{P}_3^c(\boldsymbol{u}_1, \boldsymbol{u}_1, \boldsymbol{u}_1) = 0, \qquad \text{(E-8)} \\
\bar{\mathcal{P}}_3^c(\boldsymbol{u}_c', \boldsymbol{u}_1, \boldsymbol{u}_1) &= \mathcal{P}_3^c(\boldsymbol{u}_c', \boldsymbol{u}_1, \boldsymbol{u}_1) - \int_0^L \left(\left(\frac{E_{t,\varepsilon}}{s_c} - \frac{E_t^c}{s_c^2} \right) I_1 \ddot{w}_1^2 \dot{v}_c' \right) dx.
\end{aligned}$$

First imperfection parameter. The first imperfection shape parameter ρ_1 may be determined from (30) with $\tilde{\boldsymbol{u}} = \boldsymbol{u}_1$:

$$\rho_1 \lambda_c = \frac{\rho_1^N}{a_1^D}, \qquad \text{(E-9)}$$

where a_1^D has already been determined in (D-23) and

$$\rho_1^N = -\bar{\mathcal{P}}_2^c(\boldsymbol{u}_1, \boldsymbol{u}_1) = \int_0^L \frac{E_t^c I_1}{s_c} \ddot{w}_1^2 dx = \tfrac{1}{2} E_t^c A L i_1 \bigl(1 + O(i_1)\bigr). \tag{E-10}$$

Thus, as $i_1 \ll 1$,

$$\rho_1 \lambda_c \simeq \frac{-1}{1 + e_c'}. \tag{E-11}$$

Imperfection displacement field for symmetric columns. The lowest degree displacement field which depends on the imperfection is $\boldsymbol{v}_2$. The field $\boldsymbol{v}_2$ may be found as a linear solution of (35). Let $\boldsymbol{v}_2 = (v_2^v, w_2^v)$, where v_2^v is affine with v and w_2^v with w, and insert stability the operators (E-2), (E-8) and (D-13)–(D-14):

$$\begin{aligned} 0 = \int_0^L \left(E_t^c A \dot{v}_2^v \delta\dot{v} + \frac{1}{s_c^2} E_t^c I_1 \ddot{w}_2^v \delta\ddot{w} - \frac{1}{s_c} \sigma_c A \dot{w}_2^v \delta\dot{w} \right) dx - \int_0^L \frac{E_t^c I_1}{s_c} \ddot{w}_1 \delta\ddot{w} dx \\ - \int_0^L \rho_1 \lambda_c \frac{\sigma_c}{E_t^c} \left(\left(\frac{E_{t,\varepsilon}^c}{s_c^2} - 3\frac{E_t^c}{s_c^3} \right) I_1 \ddot{w}_1 \delta\ddot{w} + \frac{E_t^c A}{s_c} \dot{w}_1 \delta\dot{w} \right) dx. \end{aligned} \tag{E-12}$$

Gather terms of the same variational fields and introduce $\boldsymbol{u}_1$ to provide

$$E_t^c A \dot{v}_2^v = 0, \quad \left(\frac{L}{\pi}\right)^2 \dddot{w}_2^v + \dot{w}_2^v = k_1 \cos\frac{\pi x}{L}, \tag{E-13}$$

where the constant k_1 is

$$k_1 = -s_c - \rho_1 \lambda_c \left(\frac{e_c'}{s_c} - \frac{3 i_1}{s_c^2} + 1 \right) = O(i_1). \tag{E-14}$$

Introducing the geometric boundary conditions and the expansion parameter condition (E-6) yields

$$v_2^v = 0, \quad w_2^v = k_1 \left(\frac{L}{2\pi} \sin(\pi x/L) - \frac{L}{4}(1 - \cos(\pi x/L)) - \frac{1}{2} x \cos(\pi x/L) \right). \tag{E-15}$$

Second imperfection parameter for symmetric columns. The second imperfection parameter ρ_2 may in general be computed from (37). For symmetric columns, and when stability operators which equal zero for the column are excluded, (37) provides

$$\rho_2 \lambda_c = \frac{\rho_2^N}{a_1^D}, \tag{E-16}$$

where a_1^D is given by (D-23), and

$$\rho_2^N = -\mathcal{P}_3^c(\boldsymbol{v}_2, \boldsymbol{u}_1, \boldsymbol{u}_1) - \rho_1 \lambda_c \mathcal{P}_3^c(\boldsymbol{u}_c', \boldsymbol{u}_2, \boldsymbol{u}_1), \tag{E-17}$$

where the operators are given by (D-14) and (E-2), respectively. The first operator depends linearly on $\dot{v}_2^v = 0$ for symmetric postbuckling behavior and the second operator depends linearly on w_2 and derivatives which are all zero. Thus, (E-16) and (E-17) yields

$$\rho_2 \lambda_c = 0 \implies \rho_2 = 0. \tag{E-18}$$

Third imperfection parameter for symmetric columns. The third imperfection parameter ρ_3 may in general be calculated from (37). For symmetric columns, and when stability operators which equal zero for the column are excluded, (37) provides

$$\rho_3 \lambda_c = \frac{\rho_3^N}{a_1^D}, \tag{E-19}$$

where a_1^D is given by (D-23) and the only nonvanishing contributions to ρ_3^N are

$$\rho_3^N = -\rho_1 \lambda_c \left(\mathcal{P}_3^c(\boldsymbol{u}_c', \boldsymbol{v}_2, \boldsymbol{u}_1) + \bar{\mathcal{P}}_3^c(\boldsymbol{u}_c', \boldsymbol{u}_1, \tilde{\boldsymbol{u}}) \right) - \tfrac{1}{2}(\rho_1 \lambda_c)^2 \left(\mathcal{P}_4^c(\boldsymbol{u}_c', \boldsymbol{u}_c', \boldsymbol{u}_1, \boldsymbol{u}_1) + \mathcal{P}_3^c(\boldsymbol{u}_c'', \boldsymbol{u}_1, \boldsymbol{u}_1) \right). \tag{E-20}$$

When the relevant displacement fields are introduced in the four operators given by (D-14), (E-2) and (E-4), and $\boldsymbol{u}_c''$ given by

$$\dot{v}_c'' = -e_c' i_1, \tag{E-21}$$

the expression to lowest degree in i_1 for ρ_3^N is

$$\rho_3^N = -\tfrac{1}{2} E_t^c A L i_1 \left(-\rho_1 \lambda_c - \tfrac{1}{2}(\rho_1 \lambda_c)^2 \left({e_c'}^2 - \frac{i_1^2}{i_3} e_c'' \right) \right) (1 + O(i_1)). \tag{E-22}$$

Utilize the result of (E-22) with $\rho_1 \lambda_c$ given by (E-11) and a_1^D in (E-19) to provide

$$\rho_3 \lambda_c \simeq (\rho_1 \lambda_c)^2 - \frac{{e_c'}^2 - (i_1^2 / i_3) e_c''}{2(1 + e_c')^3} \tag{E-23}$$

when $i_1 \ll 1$. Since i_3 is generally of order i_1^2, both terms in the numerator may become important.

References

[Britvec 1973] S. J. Britvec, *The stability of elastic systems*, Pergamon Unified Engineering Series **12**, Pergamon Press, New York, 1973.

[Budiansky 1974] B. Budiansky, "Theory of buckling and post-buckling behavior of elastic structures", *Adv. Appl. Mech.* **14** (1974), 1–65.

[Budiansky and Hutchinson 1964] B. Budiansky and J. W. Hutchinson, "Dynamic buckling of imperfection-sensitive structures", pp. 636–651 in *Proceedings of the 11th International Congress on Applied Mechanics* (Munich, 1964), edited by H. Görtler, Springer, Berlin, 1964.

[Byskov and Hutchinson 1977] E. Byskov and J. W. Hutchinson, "Mode interaction in axially stiffened cylindrical shells", *AIAA J.* **15**:7 (1977), 941–948.

[Byskov et al. 1996] E. Byskov, C. D. Christensen, and K. Jørgensen, "Elastic postbuckling with nonlinear constraints", *Int. J. Solids Struct.* **33**:17 (1996), 2417–2436.

[Christensen and Byskov 2008] C. D. Christensen and E. Byskov, "Advanced postbuckling and imperfection sensitivity of the elastic-plastic Shanley–Hutchinson model column", *J. Mech. Mater. Struct.* **3**:3 (2008), 459–492.

[Euler 1744] L. Euler, *Methodus inveniendi lineas curvas maximi minimive proprietate gaudentes*, Bousquet, Lausanne, 1744.

[Fitch 1968] J. Fitch, "The buckling and post-buckling behavior of spherical caps under concentrated load", *Int. J. Solids Struct.* **4**:4 (1968), 421–466.

[Hutchinson 1974] J. W. Hutchinson, "Plastic buckling", *Adv. Appl. Mech.* **14** (1974), 67–144.

[Koiter 1945] W. T. Koiter, *Over de stabiliteit van het elastisch evenwicht*, Ph.D. thesis, Delft University of Technology, 1945, available at http://tinyurl.com/Koiter-WT-1945-Thesis. In Dutch; translated in *On the stability of elastic equilibrium*, NASA Technical Translation NASA-TT-F-10833 (1967) and *The stability of elastic equilibrium*, Air Force Flight Dynamics Laboratory report AFFDL TR 70-25 (1970), http://contrails.iit.edu/DigitalCollection/1970/AFFDLTR70-025.pdf.

[Koiter 2009] W. T. Koiter, *W. T. Koiter's elastic stability of solids and structures*, edited by A. M. A. van der Heijden, Cambridge University Press, Cambridge, 2009.

[Kuznetsov and Levyakov 2002] V. V. Kuznetsov and S. V. Levyakov, "Complete solution of the stability problem for elastica of Euler's column", *Int. J. Non-Linear Mech.* **37**:6 (2002), 1003–1009.

[Tvergaard and Needleman 1982] V. Tvergaard and A. Needleman, "On the foundations of plastic buckling", pp. 205–233 in *Developments in thin-walled structures*, edited by J. Rhodes and A. C. Walker, Applied Science Publishers, London, 1982.

Received 19 Mar 2010. Revised 24 Aug 2010. Accepted 30 Aug 2010.

CLAUS DENCKER CHRISTENSEN: `claus.dencker.christensen@nktflexibles.com`
NKT Flexibles I/S, Priorparken 510, DK-2605 Brøndby, Denmark

ESBEN BYSKOV: `eb@civil.aau.dk`
Department of Civil Engineering, Aalborg University, Sohngaardsholmsvej 57, DK-9000 Aalborg, Denmark

JOURNAL OF MECHANICS OF MATERIALS AND STRUCTURES
Vol. 5, No. 6, 2010

STRESS AND STRAIN RECOVERY FOR THE IN-PLANE DEFORMATION OF AN ISOTROPIC TAPERED STRIP-BEAM

DEWEY H. HODGES, ANURAG RAJAGOPAL, JIMMY C. HO AND WENBIN YU

The variational-asymptotic method was recently applied to create a beam theory for a thin strip-beam with a width that varies linearly with respect to the axial coordinate. For any arbitrary section, ratios of the cross-sectional stiffness coefficients to their customary values for a uniform beam depend on the rate of taper. This is because for a tapered beam the outward-directed normal to a lateral surface is not perpendicular to the longitudinal axis. This changes the lateral-surface boundary conditions for the cross-sectional analysis, in turn producing different formulae for the cross-sectional elastic constants as well as for recovery of stress, strain and displacement over a cross-section. The beam theory is specialized for the linear case and solutions are compared with those from plane-stress elasticity for stress, strain and displacement. The comparison demonstrates that for beam theory to yield such excellent agreement with elasticity theory, one must not only use cross-sectional elastic constants that are corrected for taper but also the corrected recovery formulae, which are in turn based on cross-sectional in- and out-of-plane warping corrected for taper.

A list of symbols can be found on page 975.

1. Introduction

It is typical in beam theory to assume that taper affects cross-sectional stiffness constants, stress and strain only from the change in section geometry along the beam axis. In other words, if for a homogeneous, isotropic beam, the bending stiffness is *EI*, then for a homogeneous, isotropic, tapered beam, the bending stiffness is simply written as $EI(x)$, where the area moment of inertia varies with the axial coordinate due to change in the sectional geometry arising from taper. A recent work, [Das et al. 2009], is one among a series of papers on tapered beams by the same authors that follows this methodology. In [Abdel-Jaber et al. 2008] and [de Rosa et al. 2010], the bending energy per unit length is simply written as $EI(x)\kappa^2/2$. Results in [Abdel-Jaber et al. 2008] were compared with those of an older work [Rao and Rao 1988], both of which clearly follow this methodology. These are only a few selected examples out of the many recent works on tapered beams based on cross-sectional stiffnesses that are not corrected for taper.

An asymptotic beam theory for an isotropic strip-beam with linearly tapered width was presented in [Hodges et al. 2008]. Section stiffnesses for this theory depend on taper in ways other than the simplistic approach noted above. The main reason for this is the tilting of the outward-directed normal so that it has a non-zero component along the beam longitudinal axis, and to be accurate the cross-sectional analysis must take this tilt into account. Because of the strip-like geometry, accuracy of the cross-sectional stiffnesses was evaluated using plane-stress elasticity solutions for extension, bending and flexure from [Timoshenko and Goodier 1970] and [Krahula 1975] and were shown to be in excellent agreement. The

---

Keywords: beam theory, elasticity, asymptotic methods.

plane stress problem of the in-plane deformation of an isotropic tapered strip was chosen because it is a simple example to illustrate the proposed theory. All results are closed-form expressions that can be validated from corresponding elasticity solutions available in the literature.

One purpose of this paper is to show that high-fidelity information is available in beam theories based on asymptotic methods, which are no more complicated than "engineering" theories. This paper focuses on the recovery of the stress, strain, and displacement fields for the linearly tapered isotropic strip-beam. This aspect was not addressed in [Hodges et al. 2008]. The recovery is performed by the variational-asymptotic method (VAM) and is consistent with the derivation of the stiffness constants in that paper. It will be shown that to capture the recovery relations accurately, one needs to evaluate the warping one order higher. The recovery relations are then compared with the corresponding elasticity solutions, a comparison that confirms that a VAM-based beam theory is able to satisfactorily predict all aspects of the behavior of beam-like structures.

Section 2 of this paper revisits the previous work of [Hodges et al. 2008] and reviews the importance of including taper in the stiffness constants. Section 3 provides details of the procedure to determine the recovery relations using the VAM and presents a comparison with the corresponding elasticity solutions. In Section 4, the range of the small parameters used in the VAM is determined for which the VAM solution is in close proximity with the elasticity solutions. Finally conclusions are drawn.

2. Corrected stiffness constants for a tapered beam

For better understanding of the results to be presented, a brief review of the variational-asymptotic method and a summary of the results from [Hodges et al. 2008] is presented here. The VAM is used to perform cross-sectional analysis of beams using the principle of minimum total potential energy, exploiting the presence of small parameters. The total potential energy is developed from a general displacement field subject to a restriction to small strain. The leading terms of the energy can be obtained asymptotically in terms of the small parameters of the analysis, which can be used to obtain the equations governing in- and out-of-plane warping. This procedure can be repeated for successively higher powers of the small parameters until the desired accuracy is achieved. As a result of this analysis, the warping is expressed in terms of one-dimensional (1D) strains and can then be used to calculate the strain energy per unit length. This 1D strain energy per unit length provides the cross-section constants, reducing the 2D plane stress problem to 1D, and formulae that allow for recovery of stress, strain and displacement over the cross-section.

We now proceed to outline a procedure to obtain the cross-sectional constants using the VAM for a tapered-strip beam as in Figure 1. For details, the reader is encouraged to consult [Hodges et al. 2008].

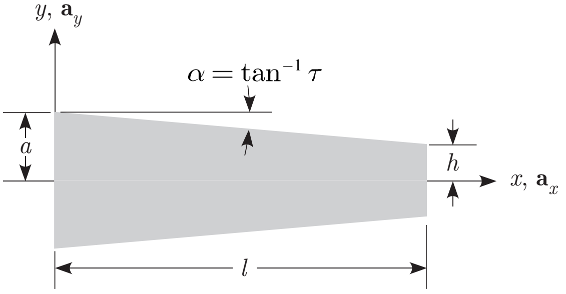

Figure 1. Schematic of the isotropic strip tapered beam.

The two small parameters of the system are a slenderness parameter $\delta = a/l$ and a taper parameter $\tau = -b'(x)$, which are assumed to be of the same asymptotic order. Considering the position vector of an arbitrary point in the undeformed and deformed configurations of the beam, the expressions for strain can be derived as

$$\Gamma_{xx} = \bar{\epsilon} - y\bar{\kappa} + w_{x,x}, \quad \Gamma_{xy} = w_{x,y} + w_{y,x}, \quad \Gamma_{yy} = w_{y,y}, \tag{1}$$

where $\bar{\epsilon}$ and $\bar{\kappa}$ are the classical 1D stretching and bending strain measures, respectively. The strain energy per unit length is then

$$U = \frac{Et}{2(1-\nu^2)} \left\langle \Gamma_{xx}^2 + \Gamma_{yy}^2 + 2\nu\Gamma_{xx}\Gamma_{yy} + \frac{1-\nu}{2}\Gamma_{xy}^2 \right\rangle, \tag{2}$$

where

$$\langle \bullet \rangle = \int_{-b(x)}^{b(x)} \bullet \, dy. \tag{3}$$

The first step is to solve for the zeroth-order warping. For this, we identify and remove all the terms that are first and higher order in the small parameters from the strain energy. The resulting equations obtained using the principle of minimum total potential energy can be used to evaluate the zeroth-order warping, which in turn gives the zeroth-order strain energy per unit length as

$$U_0 = \tfrac{1}{2}EA(x)\bar{\epsilon}^2 + \tfrac{1}{2}EI(x)\bar{\kappa}^2, \tag{4}$$

the expected expression for strain energy per unit length associated with classical Euler–Bernoulli beam theory.

To refine this result it is necessary to solve for the warping corrected to first order in δ and τ. To do so, the solution of warping previously obtained is perturbed to the next higher order. A similar procedure is preformed as described previously, the only difference being that all the terms in the energy correct through second order in the small parameters are retained. The first-order warping thus obtained is used to obtain the strain energy per unit length:

$$\begin{aligned} U_2 = {} & Etb(x)\big(1 - \tfrac{2}{3}(1+\nu)\tau^2\big)\bar{\epsilon}^2 + \tfrac{2}{3}Et\nu\tau b(x)^2\bar{\epsilon}\,\bar{\epsilon}' + \tfrac{1}{9}Etb(x)^3\big(3 + 2(14\nu+15)\tau^2\big)\bar{\kappa}^2 \\ & - \tfrac{4}{9}Et\tau(8\nu+9)b(x)^4\bar{\kappa}\,\bar{\kappa}' + \tfrac{4}{15}Et(1+\nu)b(x)^5\bar{\kappa}'^2 + \tfrac{2}{45}Et(11\nu+12)b(x)^5\bar{\kappa}\,\bar{\kappa}'', \end{aligned} \tag{5}$$

which is asymptotically correct through second order.

However, this strain energy per unit length is unsuitable for an engineering beam theory because it contains derivatives of the classical 1D strain measures. Hence, it is transformed into a generalized Timoshenko form as follows: First, the 1D classical strain measures are written in terms of 1D generalized Timoshenko strain measures using simple beam kinematics. A 1D shear strain measure enters into the picture through this transformation. Second, the derivatives of the 1D generalized Timoshenko strain measures are evaluated using equilibrium equations. The equilibrium equations can be simply obtained by the standard textbook approach of considering an element of the beam and writing the force and moment equilibrium.

Thus, the strain energy per unit length of a beam correct through second order, when transformed to the form of a generalized Timoshenko theory, is given by

$$U^* = \tfrac{1}{2} Z \epsilon^2 + \tfrac{1}{2} W \kappa^2 + \tfrac{1}{2} Y \gamma^2 + X \kappa \gamma, \tag{6}$$

where

$$\begin{aligned} Z &= EA(x)\left(1 - \frac{2\tau^2}{3}\right), & W &= EI(x)\left(1 + \frac{(\nu-48)\nu-45}{45(\nu+1)}\tau^2\right), \\ Y &= \tfrac{5}{6} GA(x), & X &= \frac{Et(5\nu+3)b(x)^2\tau}{9(1+\nu)}, \end{aligned} \tag{7}$$

where, for a linearly tapered beam, τ is the tangent of the taper angle α as shown in Figure 1. It should be noted that the stiffness associated with shear is what one obtains from the usual Timoshenko beam theory. There is no taper correction to this term because the shear strain is already one order higher in the small parameter δ than the strains associated with 1D bending and extension measures, so that the overall contribution of the term to the strain energy per unit length is correct through second order. This theory is said to be a generalized Timoshenko theory in that it contains contributions to the strain energy associated with extension, bending and shear. However, it is not subject to any of the usual restrictions on kinematics associated with the original Timoshenko theory. Moreover, it includes a bending-shear coupling term X, which is not found in the original theory.

Validation of these stiffness constants, presented in [Hodges et al. 2008], showed that the theory is only accurate when corrections associated with nonzero τ are included. Unfortunately, a review of the literature shows that there is hardly any awareness among researchers that beam stiffness constants depend on taper, as all references the authors have found to date would provide the above stiffness constants with τ set equal to zero.

An important aspect of the asymptotic theory is that bending and shear are coupled for a tapered beam; hence, the coefficient X is present in the energy. Therefore, if one takes the bending and shear stiffnesses as $EI(x)$ and $5GA(x)/6$ (i.e., only changing the sectional width in the stiffness formulae), the strain energy associated with bending-shear coupling will be missed. This can lead to significant errors in prediction of the beam deflection.

Figure 2 shows the percentage errors in extension and bending stiffnesses (Z and W from (7)) when one neglects the effect of taper and proceeds with the simplistic change in the sectional stiffnesses. It can be concluded that neglecting taper introduces an error in the beam sectional stiffnesses that can be significant, affecting deflections under load as well as natural frequencies.

To assess the importance of the bending-shear coupling term X relative to the pure bending and pure shear term, the coupling stiffness is normalized, such that

$$\overline{X} = \frac{X}{\sqrt{YW}} = \frac{(5\nu+3)\tau}{\sqrt{45(\nu+1) + \left(\nu^2 - 48\nu - 45\right)\tau^2}}. \tag{8}$$

This normalized value can be thought of as a measure of coupling strength to be compared with unity. For a taper (τ) of 0.2, it varies from 0.0215 to 0.1367 as Poisson's ratio varies from -0.5 to 0.5. Moreover, the plot shown in Figure 3 indicates that these values are by no means negligible compared to unity.

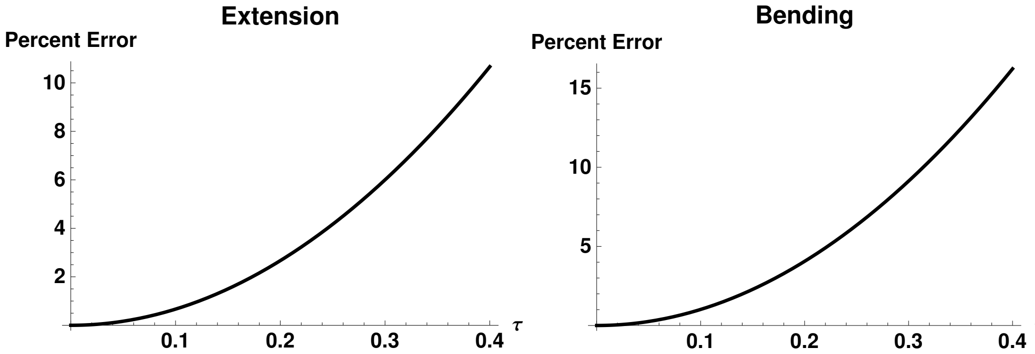

Figure 2. Percentage errors in the stiffnesses for $\nu = 0.3$.

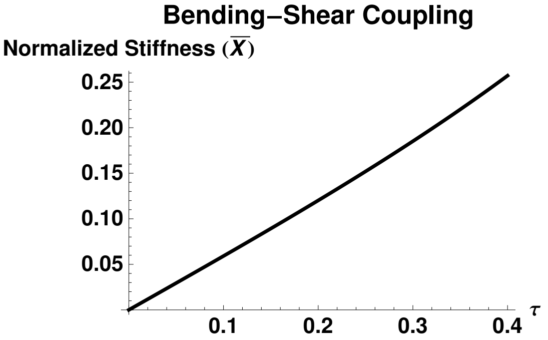

Figure 3. Normalized stiffness for bending-shear coupling, $\nu = 0.3$.

Therefore, its absence may cause significant errors, and it is thus important to include these corrections in the stiffnesses to account correctly for the effects of taper.

3. Recovery relations

This section presents strain, stress and displacement components obtained from the beam theory based on VAM and comparisons with elasticity solutions. Although the baseline elasticity solutions are not restricted to small values of the parameters δ and τ, they are compared to solutions from the beam theory, which are subject to small values of δ and τ. In particular, beam theory based on the VAM is used to analyze the problem of a tapered beam subjected to three different types of loading described as extension, bending and flexure shown in Figure 4. These three cases correspond to constant axial force, constant bending moment and constant shear force, respectively. As in [Hodges et al. 2008], the warping and strain energy are evaluated through first and second orders, respectively.

For greater accuracy than in the earlier paper, the warping is here evaluated to second order. For this, the same procedure outlined in Section 2 is followed. The first-order warping is perturbed and from the perturbed warping, strains are obtained that are, in turn, used to evaluate the strain energy as a function of the unknown warping perturbations. Minimization of the strain energy using calculus of variations

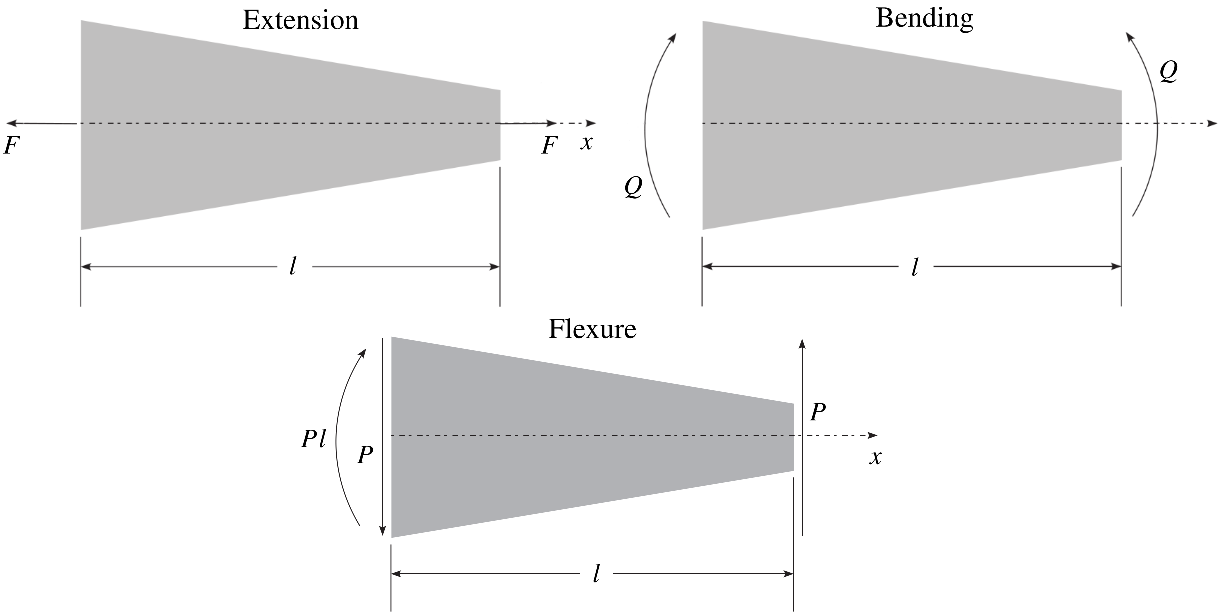

Figure 4. Schematic of beam loaded for extension, bending and flexure.

yields the expression for the second-order terms in warping as

$$w_x^{(2)} = 0, \quad w_y^{(2)} = A_0\bar{\epsilon} + A_1\bar{\epsilon}' + A_2\bar{\epsilon}'' + B_0\bar{\kappa} + B_1\bar{\kappa}' + B_2\bar{\kappa}'', \tag{9}$$

where

$$\begin{aligned}
A_0 &= \tfrac{1}{6}b^{-2}y(\nu+1)\tau^2\big(y^2(\nu+1) - b^2(\nu-3)\big),\\
A_1 &= \tfrac{1}{6}b^{-1}y\tau\big(y^2(\nu+1)^2 - b^2(\nu^2+2\nu+3)\big),\\
A_2 &= \tfrac{1}{6}y\nu^2(b^2-y^2),\\
B_0 &= -\tfrac{1}{18}(8\nu^2+6\nu-3)\tau^2(b^2-3y^2),\\
B_1 &= \tfrac{1}{9}b\nu(5\nu+6)\tau(b^2-3y^2),\\
B_2 &= \tfrac{1}{360}\big(-b^4(40\nu^2+54\nu+7) + 30b^2y^2(4\nu^2+6\nu+1) - 15y^4(2\nu+1)\big).
\end{aligned} \tag{10}$$

Thus, an expression for the warping through second order has been obtained. The derivatives of the 1D classical strain measures make it unsuitable for use in an engineering beam theory. The classical strain measures are transformed into generalized Timoshenko strain measures, whose derivatives are computed using the equilibrium equations. The required sectional stiffnesses for use in the equilibrium equations are given by (7).

Note that the second-order warping functions are not used for obtaining stiffnesses but only for recovery of stress, strain and displacement. The expressions for strain in (1) are restricted only by the assumption of small strain. The 1D strain measures may be used in their geometrically exact form. Herein, however, for the purpose of comparison with linear elasticity theory, we restrict them to small displacement and rotation. Care should be taken to distinguish between the 1D classical strain measures appearing in (1) and 1D generalized Timoshenko strain measures in (6). The relation between the two is detailed in [Hodges 2006] and specialized in [Hodges et al. 2008] and here as

$$\bar{\epsilon} = \epsilon, \qquad \bar{\kappa} = \kappa + \gamma'. \tag{11}$$

Since the problem under consideration is that of plane stress, the stresses are simply obtained from the constitutive law as

$$\begin{Bmatrix} \sigma_{xx} \\ \sigma_{yy} \\ \sigma_{xy} \end{Bmatrix} = \frac{E}{1-\nu^2} \begin{bmatrix} 1 & \nu & 0 \\ \nu & 1 & 0 \\ 0 & 0 & \frac{1}{2}(1-\nu) \end{bmatrix} \begin{Bmatrix} \Gamma_{xx} \\ \Gamma_{yy} \\ \Gamma_{xy} \end{Bmatrix}. \tag{12}$$

The 2D displacements from linear beam theory are computed from subtracting the position vector of an arbitrary point on the undeformed cross-sectional plane from the corresponding position vector in the deformed cross-sectional surface, such that

$$u_x = u - y v_{,x} + w_x \quad \text{and} \quad u_y = v + w_y, \tag{13}$$

where u and v are the 1D displacement variables of the beam theory, while u_x and u_y are the 2D displacements of an arbitrary point of the cross-section. These 1D displacement variables can be computed from the 1D strain measures by using the linear 1D strain-displacement equations

$$\epsilon = u', \quad \gamma = v' - \theta, \quad \kappa = \theta'. \tag{14}$$

To completely determine the 1D displacement and rotation variables, i.e., u, v and θ, the boundary condition specified at $x = 0$ sets u, v and θ to zero.

From this the stress, strain and displacement components were obtained from the beam analysis based on VAM. They are compared with the plane-stress elasticity solutions obtained from [Krahula 1975] and [Timoshenko and Goodier 1970]. Results are presented in Figures 5–7 for the three loading cases of extension, bending and flexure, respectively. The two results from the variational-asymptotic method, VAM (I) and VAM (II), correspond to the cases when warping is evaluated through first and second orders, respectively. The elasticity solutions also have been plotted for comparison purposes. For the three loading cases, the recovery relations are plotted at $x = l/2$, versus ζ, a dimensionless variable defined as $y/b(x)$.

It is clear that if the warping is accurate to second order, then the recovery relations of the beam theory agree very well with results from the elasticity solution. On the other hand, if warping is evaluated only to first order as in [Hodges et al. 2008], some results are not in good agreement with the elasticity solutions. Note that for presentation the recovery relations were normalized by certain standard quantities. In the case of strain the normalizing quantities were $F/(ELt)$, $Q/(EL^2t)$ and $P/(ELt)$ for extension, bending and flexure, respectively. For stresses and displacements, they were the strain normalizing factors multiplied by modulus of elasticity and length of the beam, respectively. The results were generated for $\nu = 0.3$, $\tau = 0.2$ and $\delta = 0.25$. It is essential to state here that the VAM solutions are compared with the total elasticity solutions, not with the elasticity solutions expanded to a certain order in small parameters.

Asymptotic expansions of the expressions for recovered strains were carried out, and it was seen that the results are in excellent agreement with the elasticity solutions expanded through the corresponding order. For the extension case, if the warping is correct through second order, i.e., $O(a\delta^2\epsilon)$, then the strains

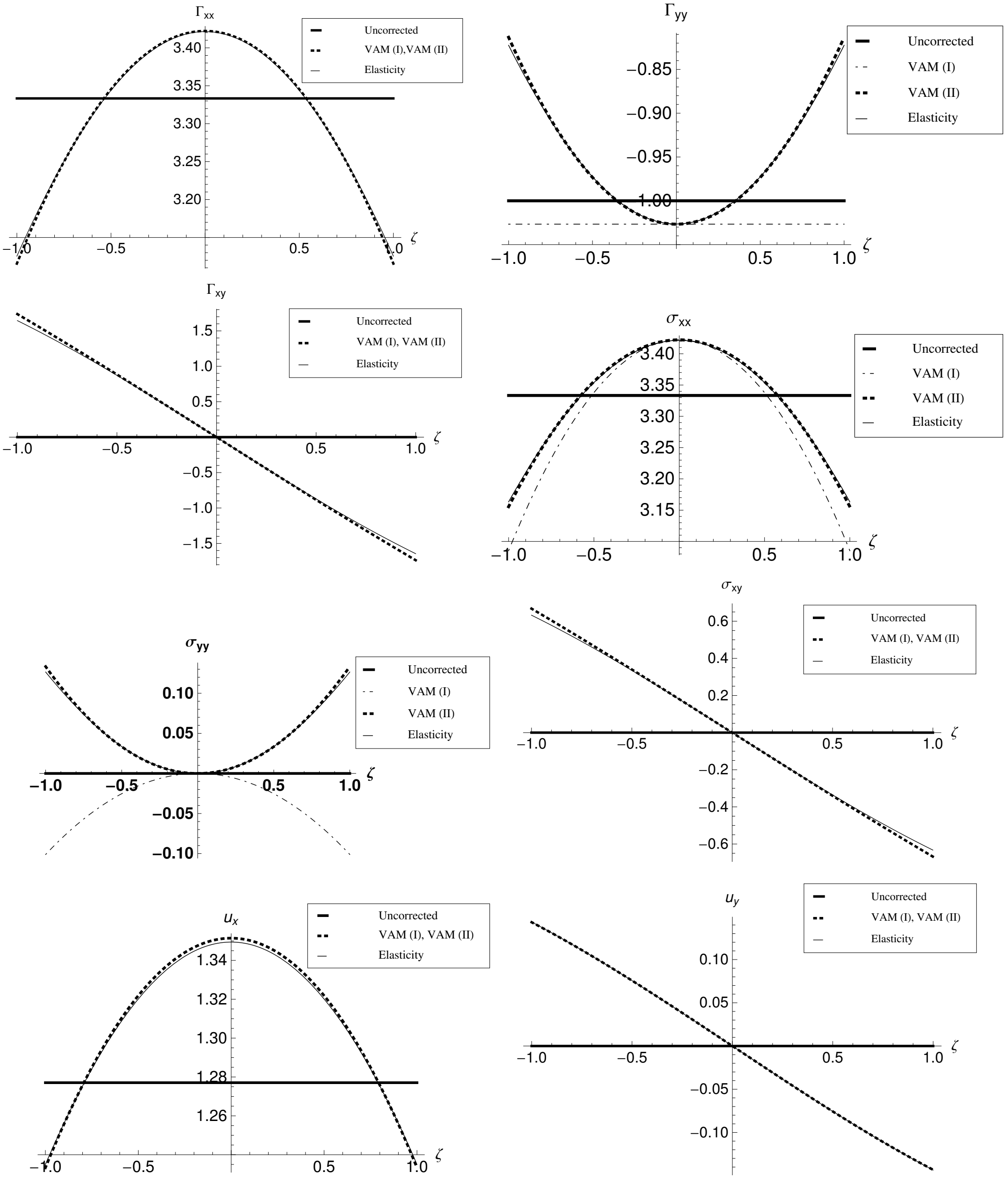

Figure 5. Comparison of the normalized VAM strains, stresses and displacements with the elasticity solutions for extension.

Γ_{xx}, Γ_{xy} and Γ_{yy} are expected to be correct through orders 3, 1 and 2, respectively. However, based on the trends in the evaluation of warping the third-order contribution to the warping, w_y is expected to be zero. Therefore, under these special circumstances, the strains listed in the same order as above are actually correct through orders 3, 2 and 3, respectively, relative to the leading term. Expansions of the

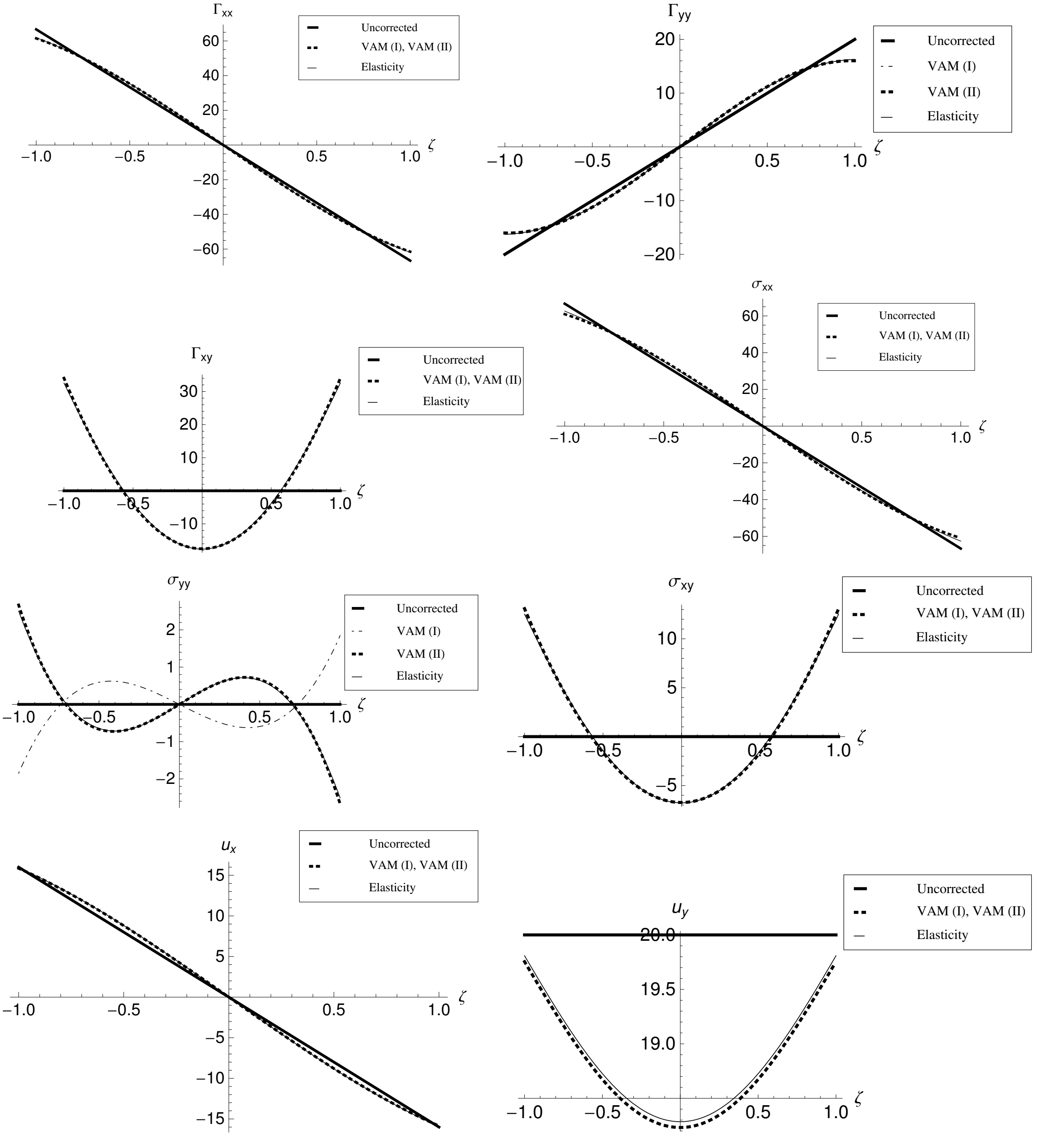

Figure 6. Comparison of the normalized VAM strains, stresses and displacements with the elasticity solutions for bending.

2D strain components for extension are presented in Table 1 on page 973. For brevity, the bending and flexure cases are not included. The third-order terms are zero for Γ_{xx} and Γ_{yy} and hence the expansions are correct through the third order. Also, the second-order terms are zero for Γ_{xy}, and hence it is correct through second order.

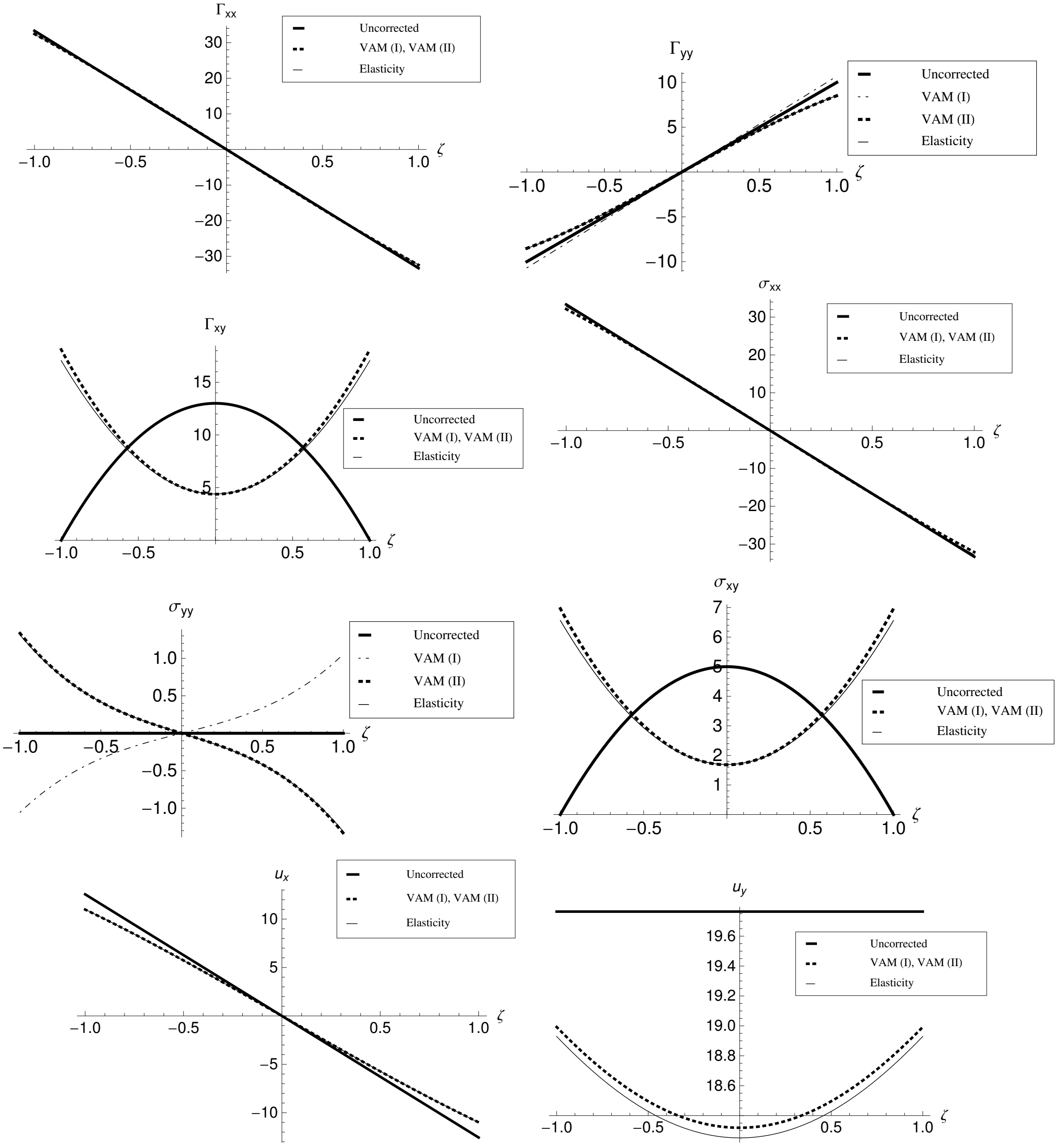

Figure 7. Comparison of the normalized VAM strains, stresses and displacements with the elasticity solutions for flexure.

Recovery relations without taper corrections. When the sectional formulae of an untapered beam are used for a tapered one, with the only effect of taper being a change in the width, it follows that taper does not enter into the expressions for strains and stresses. The stresses, strains and displacements from this type of analysis, which as mentioned in Section 2 is the starting point for most of the research

Strain	Expansion
Γ_{xx}	$\frac{F}{2Etb}\left(1+\frac{1}{3}\tau^2(-3\zeta^2\nu-6\zeta^2+2)\right)$
Γ_{xy}	$-\frac{\tau F\zeta(\nu+1)}{Etb}$
Γ_{yy}	$-\frac{F\nu}{2Etb}\left(\frac{\tau^2(-6\zeta^2\nu-3\zeta^2+2\nu)}{3\nu}+1\right)$

Table 1. Asymptotic expansions of the strains from VAM and elasticity for the extension case.

on tapered beams, has been plotted along with the VAM and elasticity solutions in Figures 5–7. The recovery relations are erroneous and certain trends are incorrect. The bending-shear coupling effect is not captured as expected, and it can be seen from the graphs of Γ_{xy} and σ_{xy} in Figure 6 that the case of bending does not result in any shear stress or strain. Another example is that of σ_{xy} for flexure, where the trend for a tapered beam is exactly opposite that of a prismatic beam, as shown in the graph for σ_{xy} in Figure 7. Using the change in sectional width in the stiffness formulae for prismatic beams leads to erroneous stress, strain and displacement. This implies that the problem is being posed in a fundamentally incorrect way. A prominent error of this type was identified in [Hodges et al. 2008], wherein it was shown that the lateral-surface boundary conditions in the typical tapered beam analysis are incorrect.

4. Validity of the recovery expressions

In the previous sections, the recovery relations obtained from the VAM were compared with the exact elasticity solutions. The VAM analysis was based on considering the parameters δ and τ to be small. This section addresses the definition of the "smallness" of these parameters. In other words, we increase the values of δ and τ till the point at which the VAM solution deviates from the exact elasticity solutions, thus determining the range of applicability of the VAM solution. It is important to note that from their definitions, the value of τ must always be less than or equal to the value of δ. If τ were equal to δ, this is a special case of a tapered beam, i.e., a wedge, for which a singularity exists in the case of flexure and extension, as the force applied at the end in both the cases, acts over a vanishing area. Hence, we will address the cases for which τ is strictly less than δ. The percentage errors for various values of δ at are plotted in Figure 8. By error here we mean the maximum of the percentage errors of the recovery relations for all the three loading cases. The error of a VAM solution is obtained by comparison with the corresponding elasticity solution. Results for those combinations of τ and δ for which the maximum error was below 5% was considered to be satisfactory. It is seen that at the extreme case of $\delta = 0.4$, the results are accurate up to $\tau = 0.26$. Investigations were terminated at $\delta = 0.4$ as for higher values, it is generally expected that an engineering analysis would be done considering the structure as a plate and not a beam.

5. Conclusions

A beam theory has been presented based on the VAM for tapered strip-beam. The strip-beam is sufficiently thin that it can be assumed to be in a state of plane stress. The novel feature of the beam theory is that the effect of the taper parameter τ on the lateral-surface boundary conditions is included. This

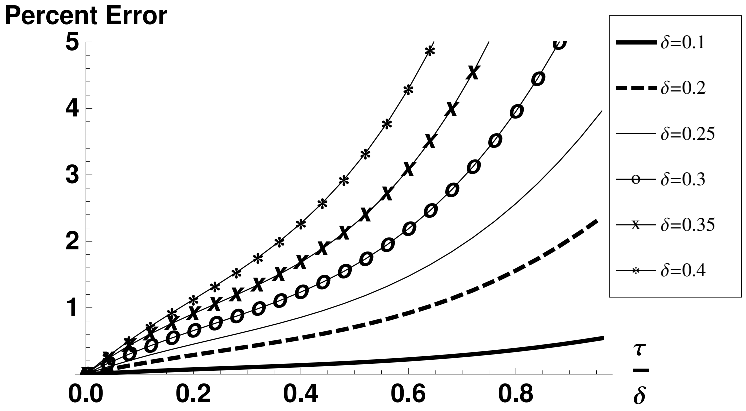

Figure 8. Percentage errors with respect to τ/δ at a given δ for the VAM recovery relations with respect to the elasticity solutions.

effect must be accounted for when performing a cross-sectional analysis, which gives the cross-sectional elastic constants necessary for solving the 1D beam equations, and the recovery relations necessary for accurately capturing stress, strain and displacement. To obtain accurate recovery relations, it is necessary to evaluate warping through second order in the small parameters, while only first-order warping is sufficient for obtaining accurate cross-sectional elastic constants.

When the VAM-based beam theory is linearized and applied to problems for which elasticity solutions exist, such as constant axial force, constant bending moment and constant transverse shear force, the results agree quite well for all values of τ for a beam with δ up to 0.25. Beyond this value of δ, the values of τ for which the solutions are good reduces; and, finally, for $\delta = 0.4$, the maximum value of τ is 0.26, which is satisfactory. Therefore, a VAM-based beam cross-sectional analysis can solve the problem of a tapered beam with sufficient accuracy.

References

[Abdel-Jaber et al. 2008] M. S. Abdel-Jaber, A. A. Al-Qaisia, M. Abdel-Jaber, and R. G. Beale, "Nonlinear natural frequencies of an elastically restrained tapered beam", *J. Sound Vib.* **313**:3–5 (2008), 772–783.

[Das et al. 2009] D. Das, P. Sahoo, and K. Saha, "Dynamic analysis of non-uniform taper bars in post-elastic regime under body force loading", *Appl. Math. Model.* **33**:11 (2009), 4163–4183.

[Hodges 2006] D. H. Hodges, *Nonlinear composite beam theory*, Progress in Astronautics and Aeronautics **213**, AIAA, Reston, VA, 2006.

[Hodges et al. 2008] D. H. Hodges, J. C. Ho, and W. Yu, "The effect of taper on section constants for in-plane deformation of an isotropic strip", *J. Mech. Mater. Struct.* **3**:3 (2008), 425–440.

[Krahula 1975] J. L. Krahula, "Shear formula for beams of variable cross section", *AIAA J.* **13**:10 (1975), 1390–1391.

[Rao and Rao 1988] B. N. Rao and G. V. Rao, "Large amplitude vibrations of a tapered cantilever beam", *J. Sound Vib.* **127**:1 (1988), 173–178.

[de Rosa et al. 2010] M. A. de Rosa, M. Lippiello, M. J. Maurizi, and H. D. Martin, "Free vibration of elastically restrained cantilever tapered beams with concentrated viscous damping and mass", *Mech. Res. Commun.* **37**:2 (2010), 261–264.

[Timoshenko and Goodier 1970] S. P. Timoshenko and J. N. Goodier, *Theory of elasticity*, 3rd ed., McGraw-Hill, New York, 1970.

List of symbols

$A(x)$	cross-sectional area of the strip-beam
E	Young's modulus
F	axial force
G	shear modulus
$I(x)$	area moment of inertia of the strip-beam about the z axis
P	shear force
Q	bending moment
U	strain energy per unit length
U_0	zeroth-order sectional strain energy
U_2	second-order sectional strain energy
U^*	second-order sectional strain energy transformed to generalized Timoshenko form
a	half-width of the strip-beam at $x = 0$, equal to $b(0)$
$b(x)$	half-width of the strip-beam
h	half-width of the strip-beam at $x = l$, equal to $b(l)$
l	length of the strip-beam
t	thickness of the strip-beam
u, v	1D displacements
u_x, u_y	2D displacements
w_x, w_y	warping of the strip-beam section, out-of-plane and in-plane, respectively
$w_x^{(2)}, w_y^{(2)}$	second-order warping of the strip-beam section
x	axial coordinate of the strip-beam
y, z	cross-sectional coordinates of the strip-beam, with z through the thickness
$\Gamma_{xx}, \Gamma_{yy}, \Gamma_{xy}$	2D strain components
α	taper angle of the strip-beam
δ	ratio of the maximum half-width of the strip-beam to its length
$\bar{\epsilon}$	1D classical generalized stretching strain
ϵ	1D generalized Timoshenko stretching strain
$\bar{\kappa}$	1D classical generalized bending strain
κ	1D generalized Timoshenko bending strain
γ	1D generalized Timoshenko shearing strain
ν	Poisson's ratio
$\sigma_{xx}, \sigma_{yy}, \sigma_{xy}$	2D stress components
θ	1D rotation
τ	taper of the strip-beam, equal to $\tan\alpha$
ζ	dimensionless cross-sectional coordinate $y/b(x)$, such that $-1 \le \zeta \le 1$

Received 1 May 2010. Revised 10 Jul 2010. Accepted 17 Aug 2010.

DEWEY H. HODGES: `dhodges@gatech.edu`
Daniel Guggenheim School of Aerospace Engineering, Georgia Institute of Technology, 270 Ferst Drive, Atlanta, GA 30332-0150, United States
http://www.ae.gatech.edu/~dhodges/

ANURAG RAJAGOPAL: `r_anurag87@gatech.edu`
Daniel Guggenheim School of Aerospace Engineering, Georgia Institute of Technology, 270 Ferst Drive, Atlanta, GA 30332-0150, United States

JIMMY C. HO: `jimmy.c.ho@us.army.mil`
Science and Technology Corporation, Ames Research Center, Moffett Field, CA 94035, United States

WENBIN YU: `wenbin@engineering.usu.edu`
Department of Mechanical and Aerospace Engineering, Utah State University, Logan, UT 84322-4130, United States

JOURNAL OF MECHANICS OF MATERIALS AND STRUCTURES
Vol. 5, No. 6, 2010

ASSESSMENT OF THE PERFORMANCE OF UNIFORM MONOLITHIC PLATES SUBJECTED TO IMPULSIVE LOADS

JONAS DAHL

The uniform monolithic metallic plate is the standard for assessing structural performance against blasts. For example, this has been the reference in recent work assessing the blast resistance of sandwich plates. Here, the performance of monolithic plates made from a hardening metal with high ductility is investigated by systematic optimization. The thickness distribution of clamped monolithic wide plates is optimized with respect to minimizing the permanent deflection at midspan under impulsive loads. The optimized plates are compared to a uniform plate of the same mass. Two load cases are considered: one with impulses acting uniformly along the plate, and one with impulses acting over a central patch. In both cases the reduction of permanent deflection of the optimized plate relative to the uniform plate is pronounced for small impulses but progressively smaller for larger impulses. For large impulses the optimal thickness distribution differs only slightly from that of a uniform plate. The study confirms the effectiveness of uniform thickness plates against large impulses.

1. Introduction

Plates subjected to blast loads have been extensively studied; especially so, in recent years, in the context of all-metal sandwich plates [Fleck and Deshpande 2004; Xue and Hutchinson 2004; Qiu et al. 2005; Dharmasena et al. 2008]. In all of these studies the performance of the sandwich plates is compared to the performance of uniform monolithic plates of the same mass. The aim of the present study is to optimize the thickness distribution of monolithic plates for impulsive loads. This has direct applications in its own right, and the results can also be used to asses the effectiveness of the uniform plate as the standard reference for blast load resistance.

An infinite depth clamped plate with length $2L$ and thickness H in Figure 1 is considered. The plate is loaded with a pressure given as an exponentially decaying function typical of blast loads:

$$P(x,t) = f(x)\exp\left(\frac{-t}{\tau}\right), \quad -L \le x \le L, \quad t \ge 0, \tag{1}$$

where τ is the characteristic time of loading, t is time, x is the distance from midspan (see Figure 1), and $f(x)$ describes the spatial distribution of the pressure, which is detailed below. The characteristic time τ is chosen such that it is much shorter than the response time of the plate T (defined as the time to reach the maximum midspan deflection), hence the loading is effectively impulsive[1]. Two situations are considered: uniform loading with $f(x) = p_0$, and loading over a central patch with $f(x) = p_0 \exp(-(x/a)^2)$, where

---

Keywords: impulsive loads, FE simulations, finite deflections, blast resistance, monolithic plates.

[1] Numerical studies show that for all practical purposes $T/\tau = 75$ is more than adequate for this purpose.

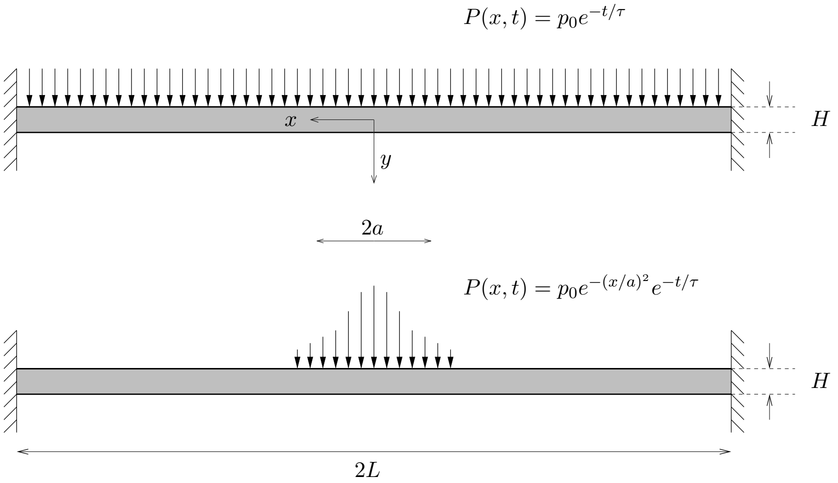

Figure 1. Clamped plate loaded with a pressure $P(x, t)$. Uniform loading (top) and loading over a central patch (bottom).

a is the characteristic spatial width of the pressure pulse. The impulse per unit depth of the plate is

$$I = 2\int_0^{\infty}\int_0^{L} P(x,t)\,dx\,dt = \begin{cases} 2Lp_0\tau & \text{for uniform loading,} \\ \sqrt{\pi}ap_0\tau & \text{for central patch loading } (a \ll L), \end{cases} \tag{2}$$

where the expression for central patch loading is an excellent approximation for localized pressure ($a \ll L$) as considered in this study, and the infinite upper limit on the integral over time is a good approximation when the simulation time is much larger than τ. The dimensionless impulse per unit depth of the plate $\hat{I} = I/(L^2\sqrt{\sigma_Y \rho})$ is used throughout this article, where σ_Y and ρ are defined below.

The plate material is assumed isotropic with power-law hardening stress-strain relationship

$$\sigma = \begin{cases} E\epsilon, & \epsilon \le \dfrac{\sigma_Y}{E}, \\ \sigma_Y\Big(\dfrac{E\epsilon}{\sigma_Y}\Big)^N, & \epsilon > \dfrac{\sigma_Y}{E}, \end{cases} \tag{3}$$

where σ is the true stress, ϵ the true strain, σ_Y the initial yield stress, E the Young's modulus, and N the hardening exponent.

The conventional J_2 flow rule is used. For a sufficiently ductile metal alloy such that necking occurs before any material failure, necking controls the maximum impulse the plate can withstand. This is due to the fact that if a plate is loaded with an impulse that is just large enough to produce necking at the boundary, then any larger impulse will almost certainly cause separation at the boundary because all the additional energy associated with the larger impulse will be absorbed only within the highly localized necking region. Necking and localization of plastic deformation is accurately captured by the finite strain finite element formulation used, which is detailed below. A material failure criterion that would predict details of the final fracture of the neck is not adopted. Failure by necking is evident in experiments on thin beams subject to a uniform impulsive load [Menkes and Opat 1973]. As detailed above, impulse levels above those required to produce the onset of necking caused the beams to fully separate at the clamped ends in a necking mode.

The material parameters used throughout the article are: $\sigma_Y = 260\,\text{MPa}$, $N = 0.2$, $E = 200\,\text{GPa}$, density $\rho = 7800\,\text{kg/m}^3$, and Poisson's ratio $\nu = 0.3$. Unless otherwise stated the following dimensions are used: $L = 100\,\text{mm}$, $H = 6\,\text{mm}$, and $a = 20\,\text{mm}$. For this choice of parameters numerical studies show that for $a/L < 0.15$ necking at midspan develops for the uniform plate at large impulses, while for $a/L > 0.15$ the plate fails by necking at the supports, which is also the case for uniform pressure. In this paper $a/L = 0.2$ is used, hence the failure modes for the central patch and uniform loading are identical. All computations are performed using the finite strain formulation available in the finite element code ABAQUS/Explicit version 6.6-1 [2006].

The clamped plate is modeled using four-node plane strain quadrilateral elements with reduced integration and hourglass control (CPE4R), with 5 elements through the thickness of the plate H and 125 elements along half of the plate length L. Symmetry is exploited; thus symmetry boundary conditions are used at the center and only half the plate is modeled. To evaluate the permanent deflection, an artificial viscous damping is introduced after a few elastic oscillations, which damps out the elastic vibrations (see Figure 2). This shows the time history of the vertical deflection (the y-axis of the coordinate system in Figure 1) of the midspan denoted δ. As only negligible plastic deformation takes place after the damping is activated it is assumed that this is a valid approach for finding the permanent deformation.

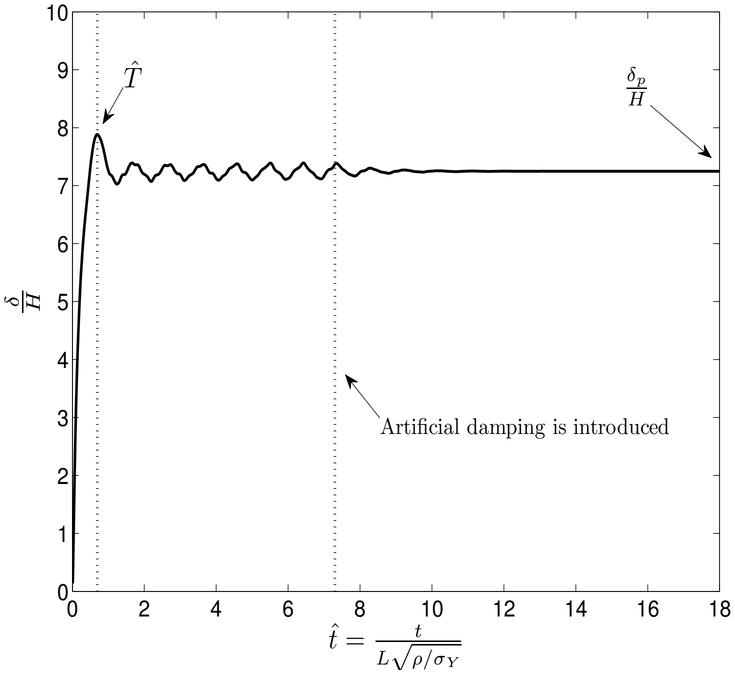

Figure 2. Normalized deflection at the midspan for central patch loading with $H/L = 6/100$, $\hat{I} = 0.0535$, and $a/L = 0.2$. The introduction of artificial viscous damping is indicated as is the dimensionless plate response time $\hat{T}$ and the normalized permanent deflection δ_p/H.

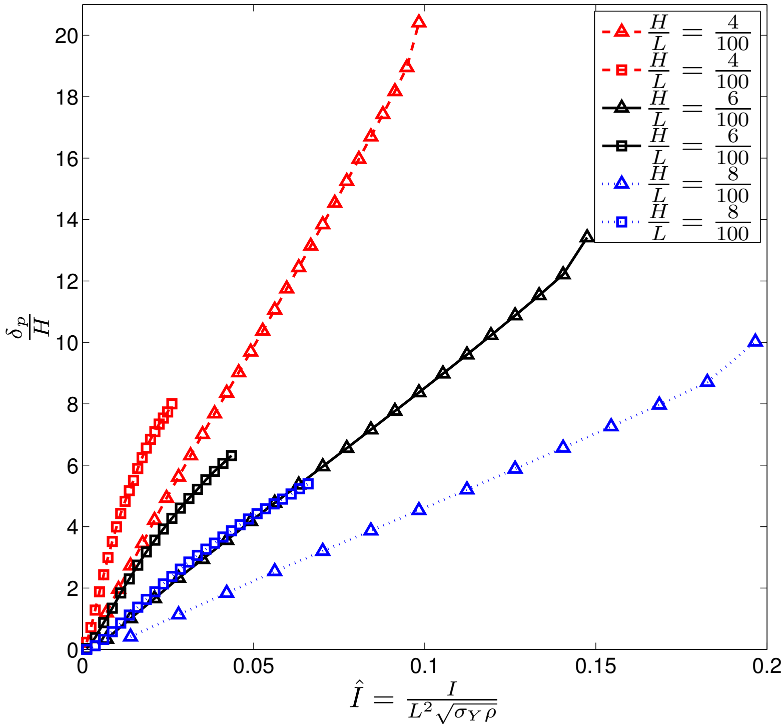

Figure 3. Permanent deflection at the midspan of uniform plates. Triangular markers indicate uniform pressure, and square markers indicate central patch pressure (with characteristic spatial width $a/L = 0.2$). The curves terminate at the impulse when substantial necking is observed.

Figure 3 gives an overview of the nondimensional permanent displacement of the midspan δ_p/H of uniform plates of different thicknesses. The curves are terminated at an impulse level within the small range of impulse levels where necking occurs. In Figure 3, a rapid upturn of the curves between the last two impulse levels is observed. For practical purposes this represents the limit of impulses that the plates can withstand.

2. Computational model and optimization scheme

In this study, the topology of the plate is not subject to change, that is, the top and bottom contours of the plate are parameterized and material is distributed throughout the thickness which these contours define, see Figure 4. Preliminary studies show that if both the top and bottom contours of the plate are allowed to change freely, the optimized structure will approach a V-shape such that the response is dominated by stretching from the initial application of the loading. In this study we are interested in plate-like structures, hence the contours must in some way be restrained. For example, restrictions could be put on the top or bottom contour, or on the midplane. We choose to restrict the top contour of the undeformed plate to be planar, as this ensures that the loading pressure does not change during optimization, see Figure 4. The gradient based code for constrained optimization SNOPT [Gill et al. 2005] is used to alter the design in an iterative fashion to minimize an object function, which is a measure of the performance of the

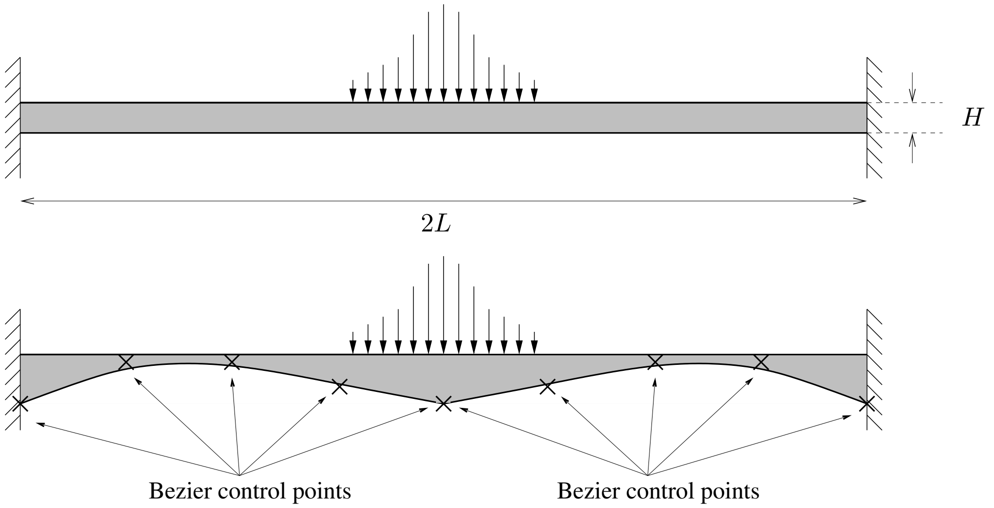

Figure 4. Plate loaded over a central patch. Uniform reference plate with thickness H (top) and optimized plate with average thickness H (bottom). The geometry of the lower contour of the plate is determined by equidistanced Bézier points, as indicated, which can move in the vertical direction. The top surface is restricted to be a plane. Symmetry is exploited, hence only the left half of the plate is modeled and parameterized.

structure. The gradients used in the optimization are obtained by finite differences with a perturbation of the control points equal to approximately $1/100$ of the element side length. The standard settings of SNOPT are used.

Object function. Several object functions could be used, such as minimization of average deflection, minimization of maximum deflection, minimization of maximum permanent deflection, et cetera. In this paper, minimization of the permanent deflection at midspan is used (specifically the bottom finite element node at the midspan symmetry line), which is denoted δ_{p}. The object function is normalized to cater for the performance of the optimization algorithm:

$$\psi = \frac{\delta_{\mathrm{p,ref}} - \delta_{\mathrm{p,opt}}}{\delta_{\mathrm{p,ref}}} \tag{4}$$

where $\delta_{\mathrm{p,ref}}$ is the permanent deflection of a uniform plate with the same mass acted upon by the same loading and $\delta_{\mathrm{p,opt}}$ is the permanent deflection of the optimized plate.

Parametrization and constraints. As mentioned earlier, to obtain plate-like geometries, the top surface of the plate is not allowed to change during the optimization process. The bottom surface of the plate is parameterized using a Bézier curve with control points at the left support and midspan and a number of equidistanced control points in between. This limits the design to relatively smooth designs, depending on the number of control points, and prevents infeasible designs with a large number of stiffers that depend on the spatial discretization, as observed for static elastic plate problems in [Cheng and Olhoff 1981]. The design variables of the problem are the vertical positions of the Bézier control points, see Figure 4. To establish an adequate number of control points, a plate has been optimized for a given load, with the number of Bézier control points ranging from 3 to 15. It was observed that the optimized designs were similar when using more than 4 control points, and that using a large number of control points made convergence to local minima more likely. Therefore, in this paper all optimizations are carried out using five Bézier control points, as this is the number of control points for which the object function seemed to plateau. The motion of the control points is constrained by enforcing a constant mass of the plate, that is, an average thickness equal to H. This is readily implemented using SNOPT, and the gradient of the mass constraint is evaluated in the same finite difference loop as the gradient of the object function. A feasibility constraint is employed to keep the optimization routine from requesting analysis of plates with very thin sections, which would cause numerical difficulties due to severely distorted elements during the finite element analysis. In this paper, the feasibility constraint demands that the thickness of the plate is everywhere more than $1/10$ of the uniform plate thickness. This limit is seldom reached during optimization, but it makes the optimization process more robust. Attention must be paid to two general problems arising in shape optimization: convergence to a local minimum, which is avoided in this paper by varying the initial guesses on the position of the control points, and the fact that the parametrization prevents the plate from reaching optimum, which is avoided by doing a convergence study in the number of parametrization variables, as mentioned above. For a general description of the shape optimization method the reader is referred to the review [Haftka and Grandhi 1986] and the more recent monograph [Haslinger and Mäkinen 2003].

3. Optimization results

The permanent midspan deflection of the optimized plates ($H/L = 0.06$) is compared to the permanent midspan deflection of a uniform plate with the same mass in Figure 5, left. To present the results more clearly, the relative improvement is plotted in Figure 5, right, against the dimensionless impulse, and in Figure 6 against the permanent deflection of the optimized plates (here several plate thicknesses are considered). As mentioned earlier, the curves have been terminated in the range where necking is observed. The figures show that the permanent deflection is significantly reduced in the range where the impulses are relatively small. Nevertheless the impulse levels in this range are still able to cause significant plastic deformation of the plate, giving rise to maximum permanent deflections less than about two times the plate thickness. The improvement relative to the uniform plate declines for larger impulses where the response transitions from being bending-dominated to stretching-dominated. The improvement over the uniform plate almost vanishes for impulses causing permanent midspan deflections greater than about 6 times the plate thickness. Nevertheless improvements of more than 10 percent can be achieved well into the stretching-dominated regime ($\delta_{\mathrm{p}}/H > 1$). The plates optimized for this range of impulses do not, however, perform as well as uniform plates when subjected to larger impulses.

Reduction of imparted kinetic energy. In general, greater performance improvement is achieved in the optimized plates for central patch loading than for uniform loading; see Figures 5–6. This can be understood by studying the kinetic energy imparted to the plates. The kinetic energy imparted to the plates must be dissipated through plastic straining (neglecting elastic vibrations). Hence reducing the imparted kinetic energy is a potential means for reducing the permanent deflection. When considering a mass m initially at rest subjected to an impulse $I = mv$, where v is the velocity of the mass, the imparted kinetic

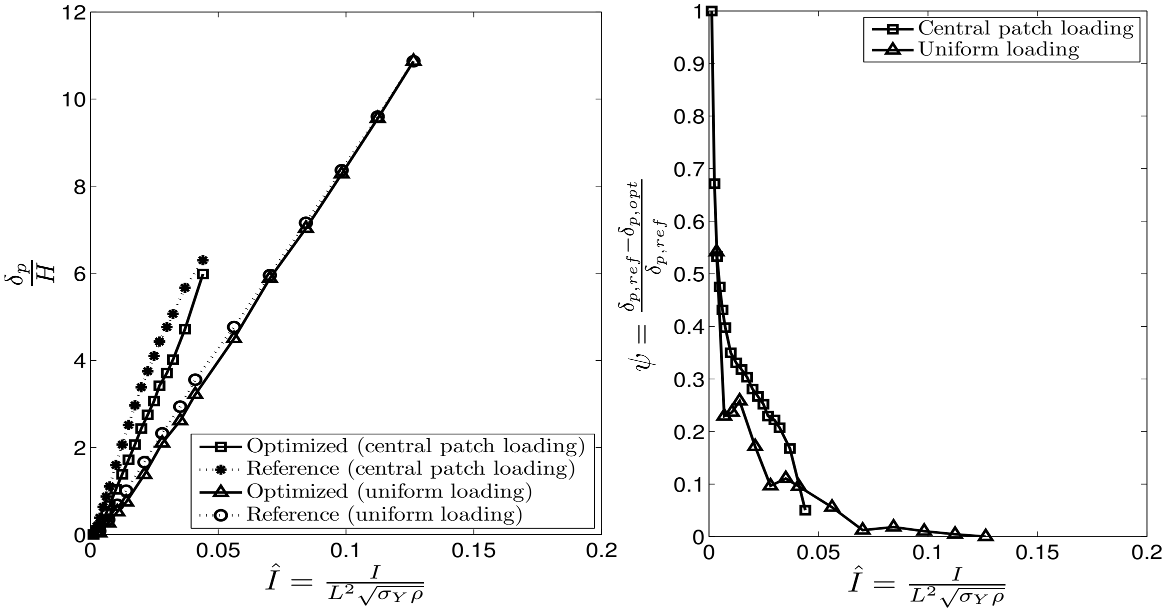

Figure 5. Left: permanent deflection at the midspan for a plate with dimensions $H/L = 0.06$. Right: relative improvement of the permanent deflection at the midspan for a plate with dimensions $H/L = 0.06$.

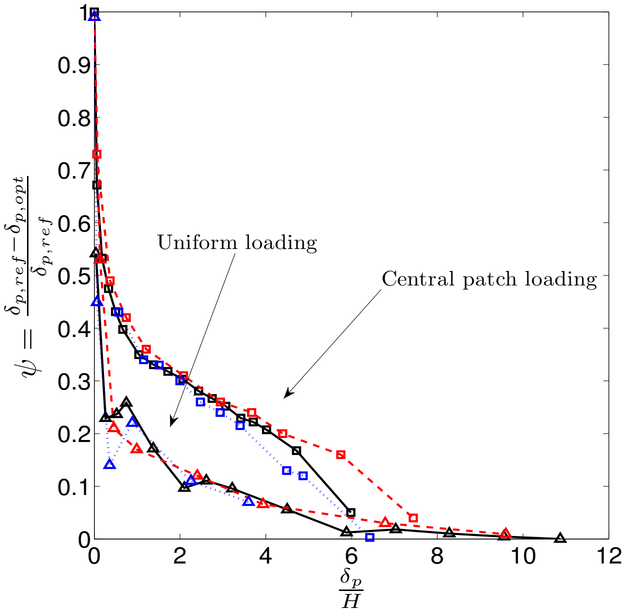

Figure 6. The relative reduction of permanent deflection plotted against the deflection of the optimized plates shows that the reduction depends but little on the height-length ratio of the plate, and that significant improvement can be obtained well into the stretching-dominated response range. The normalized plate thicknesses are $H/L = 0.04$ (dashed), 0.06 (continuous line), and 0.08 (dotted) for both uniform and central patch loading.

energy of this mass is

$$E_{\text{kin}} = \frac{mv^2}{2} = \frac{I^2}{2m}. \tag{5}$$

Hence, increasing the mass on which a given impulse is acting will decrease the kinetic energy imparted to the mass. The same is true for the plates considered here. In the case of central patch loading, mass can be redistributed to the midspan where the loading acts, effectively decreasing the kinetic energy imparted to the plate, which in turn must be dissipated through plastic strain. This is seen in Figure 7, where the kinetic energy imparted to the optimized plates is plotted relative to the kinetic energy imparted to a uniform thickness plate. This effect is observed also in the case of uniform loading, as regions near the supports contribute only slightly to the kinetic energy. Thus it can be beneficial to move some mass to the midspan, but the effect is much smaller than for central patch loading.

Optimized thickness distributions. The inserts in Figure 7 show the optimized thickness distributions (for the left symmetric half) for a number of impulse levels. The optimized thickness distributions are similar for central patch and uniform loading. For small impulses the optimized plates resemble what is found for optimization of static elastic plates [Cheng and Olhoff 1981], that is, the thickness distribution

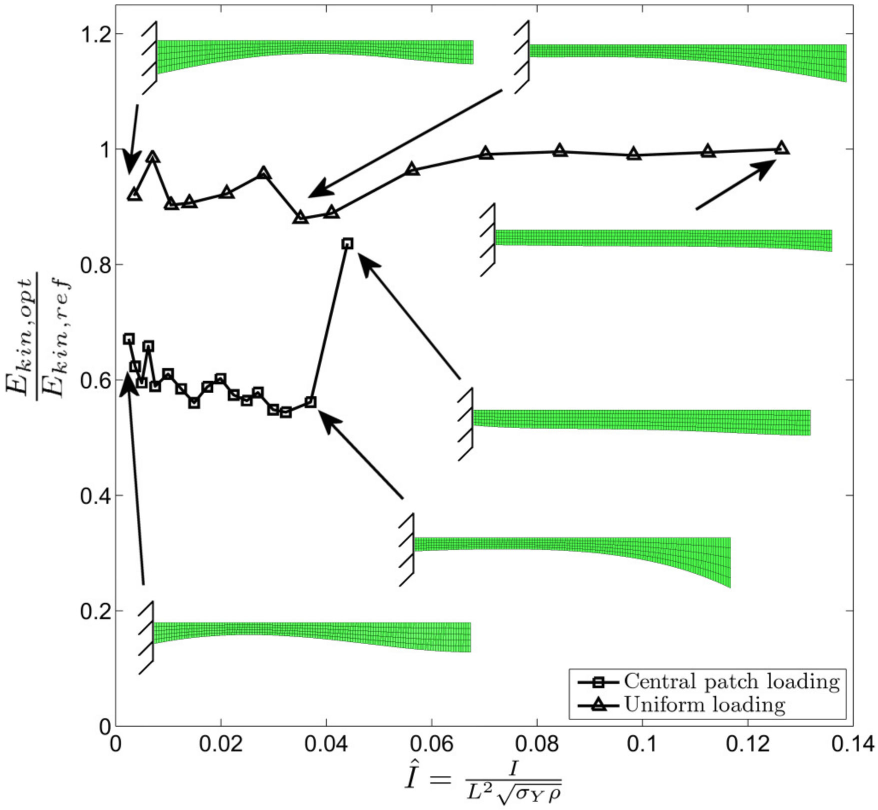

Figure 7. Kinetic energy imparted to the optimized plate relative to the kinetic energy imparted to the uniform plate. The inserts show the left symmetric half of the optimized plates.

varies with the bending moment distribution. For medium impulses, most of the redistributed mass is concentrated near the midspan of the plate which indicates that it is beneficial to reduce the kinetic energy imparted to the plate, compared to increasing the stiffness of the plate, as the discussion above suggests. For large impulses, causing permanent midspan deflections of more than about six times the plate thickness, the optimized plates are nearly uniform for both uniform and central patch loading. In this stretching-dominated range, uniform plates perform well, as changes in thickness variation promote necking in the thinnest regions.

4. Conclusions

In general, the reduction of permanent midspan deflection of the optimized plates compared to the uniform plates is significant for relatively small impulses, which give rise to permanent deflections that are less than two times the plate thickness. For larger impulses, which give rise to deflections greater than about six times the plate thickness, the payoff from optimization is less than five percent. Optimization of the thickness distribution shows more promise for plates subjected to central patch loading, as the kinetic energy imparted to the plates can be significantly reduced by relocating mass to areas below the loading. Three impulse domains have been identified:

- Small impulses (maximum permanent deflection less than the average plate thickness): The optimized plates resemble those found by shape optimization of linear elastic plates subjected to a static load at midspan [Cheng and Olhoff 1981]. This suggests that the response is primarily governed by the bending moment distribution. In this range of impulse levels the optimized plates perform significantly better than uniform plates.
- Medium impulses (maximum permanent deflection greater than the average plate thickness but less than about six times the average plate thickness): The optimized plates have a significant amount of material at the midspan, as to reduce the kinetic energy imparted to the plate. This effect is limited in the case of uniform loading, as pressure is applied everywhere on the top surface of the plate. Therefore, the impulse is transferred to the whole plate, hence moving mass from one region to another does not reduce the kinetic energy transferred to the plate, except near the supports. In this range of impulse levels the optimized plates perform 10–35% better than uniform plates in the case of central patch loading, and 5–15% better under uniform loading.
- Large impulses (maximum permanent deflection greater than about six times the average plate thickness): The plate response is dominated by stretching. Uniform plates perform very well, and only a slight reduction of permanent deflection can be obtained from optimization. In this range nonuniform thickness variations promote necking in regions where the thickness is minimum.

Finally, it can be emphasized again that the present study establishes that uniform plates perform well for large impulses, and that little is gained by varying the thickness distribution of the plate. This is an important observation for the monolithic plates studied here, and it establishes that the uniform monolithic plate is in fact a good reference for sandwich plates subjected to blast loads.

Acknowledgement

The author gratefully acknowledges discussions with John W. Hutchinson and Jens H. Andreasen.

References

[ABAQUS 2006] *ABAQUS/Explicit user's manual*, Version 6.6, ABAQUS Inc., Providence, RI, 2006.

[Cheng and Olhoff 1981] K. T. Cheng and N. Olhoff, "An investigation concerning optimal design of solid elastic plates", *Int. J. Solids Struct.* **17**:3 (1981), 305–323.

[Dharmasena et al. 2008] K. P. Dharmasena, H. M. G. Wadley, Z. Xue, and J. W. Hutchinson, "Mechanical response of metallic honeycomb sandwich panel structures to high-intensity dynamic loading", *Int. J. Impact Eng.* **35**:9 (2008), 1063–1074.

[Fleck and Deshpande 2004] N. A. Fleck and V. S. Deshpande, "The resistance of clamped sandwich beams to shock loading", *J. Appl. Mech.* **71** (2004), 386–401.

[Gill et al. 2005] P. E. Gill, W. Murray, and M. A. Saunders, "SNOPT: An SQP algorithm for large-scale constrained optimization", *SIAM Rev.* **47**:1 (2005), 99–131.

[Haftka and Grandhi 1986] R. T. Haftka and R. V. Grandhi, "Structural shape optimization: a survey", *Comput. Methods Appl. Mech. Engrg.* **57**:1 (1986), 91–106.

[Haslinger and Mäkinen 2003] J. Haslinger and R. A. E. Mäkinen, *Introduction to shape optimization: theory, approximation, and computation*, Advances in Design and Control **7**, Society for Industrial Mathematics, 2003.

[Menkes and Opat 1973] S. B. Menkes and H. J. Opat, "Broken beams: tearing and shear failures in explosively loaded clamped beams", *Exp. Mech.* **13**:11 (1973), 1283–1305.

[Qiu et al. 2005] X. Qiu, V. S. Deshpande, and N. A. Fleck, "Impulsive loading of clamped monolithic and sandwich beams over a central patch", *J. Mech. Phys. Solids* **53**:5 (2005), 1015–1046.

[Xue and Hutchinson 2004] Z. Xue and J. W. Hutchinson, "A comparative study of impulse-resistant metal sandwich plates", *Int. J. Impact Eng.* **30** (2004), 1283–1305.

Received 4 May 2010. Revised 13 Oct 2010. Accepted 4 Nov 2010.

JONAS DAHL: `jda@m-tech.aau.dk`
Department of Mechanical and Manufacturing Engineering, Aalborg University, Pontoppidanstræde 103, DK-9220 Aalborg, Denmark

JOURNAL OF MECHANICS OF MATERIALS AND STRUCTURES
Vol. 5, No. 6, 2010

STRESS SMOOTHING HOLES IN PLANAR ELASTIC DOMAINS

SHMUEL VIGDERGAUZ

The actual elastostatic problem of optimizing the stress state in a two-dimensional perforated domain by proper shaping of holes is considered with respect to minimization of the global variations of the boundary hoop stresses. This new criterion radically extends the rather restrictive equistress principle introduced by Cherepanov and results in a favorable response of the structure to an external load, with neither local stress concentrations nor underloading of other parts of the boundary. Mathematically, the variations provide an integral-type assessment of the local stresses which requires less computational effort than direct minimization of the stress concentration factor. The proposed criterion can thus be easily incorporated in the numerical optimization scheme previously developed by the author in the closely related context of energy optimization. It includes an efficient complex-valued direct solver and a standard evolutionary optimization algorithm enhanced with an economical shape parametrization tool. The effectiveness of the proposed scheme is illustrated through numerical simulations.

1. Introduction and motivation

Thin and flat construction elements with holes enjoy frequent application in engineering. The holes may cause significant stress concentration and crack initiation, which occur when the resultant maximum hoop stresses σ_h along the hole boundaries L exceeds the material-specific constant σ_0:

$$\mathcal{K}(L) \equiv \max|\sigma_h(t)| > \sigma_0, \quad t \in L. \tag{1-1}$$

This weakening effect of the holes can be efficiently reduced by their proper shaping to achieve a more favorable stress state of the construction under the same given loading. Such an approach is all the more promising as the hole area usually matters much more than its shape, which thus permits a certain design freedom.

With (1-1), the commonly used criterion for assessing the elastic structure optimality is the minimum of $\mathcal{K}(L)$ over the pool $\{L\}$ of all admissible shapes L_j of each hole:

$$\max|\sigma_h(t)| \equiv \mathcal{K} \xrightarrow[\{L\}]{\qquad} \min; \quad t \in L; \quad L = \bigcup_{j=0}^{N} L_j. \tag{1-2}$$

The stress-minimizing holes (1-2) maximize the undamaging level of the acting load. The direct problem of evaluating the factor $\mathcal{K}$ over given holes and the inverse problem of its possible minimization are

---

Keywords: plane elasticity problem, Kolosov–Muskhelishvili potentials, shape optimization, hoop stresses, extremal elastic structures, genetic algorithm.

Preliminary results in this paper were presented at the Fourth European Conference on Computational Mechanics (ECCM 2010), Paris, May 16–21, 2010.

amongst the main topics in elasticity. The related literature is abundant. In the next sections, some relevant papers are commented on for comparison purposes.

Much less attention, however, has been paid to another criterion, according to which the hoop stresses should have *minimal possible variation* along the holes:

$$V[\sigma_h(L)] \xrightarrow[\{L\}]{} \min . \tag{1-3}$$

In accordance with the general theory of real-valued functions [Natanson 1955], the variation of the stress function is defined as

$$V[\sigma_h(L)] = \sup \sum_j \sum_{i=0}^{n} \left|\sigma_h(t_{i+1}^{(j)}) - \sigma_h(t_i^{(j)})\right|, \tag{1-4}$$

where the supremum is taken over all possible partitions of L_j with an arbitrary system of points $t_0^{(j)}, t_1^{(j)}, \dots, t_n^{(j)}$ ordered by a chosen direction of traversing. For a closed contour we require $t_n^{(j)} = t_0^{(j)}$. Since the variation is always nonnegative and reaches its zero global minimum only at constant-valued functions, i.e.,

$$V[\sigma_h(L)] = 0 \Longleftrightarrow \sigma_h(L_j) = C_j \quad \forall j, \tag{1-5}$$

this is an integral measure of how the function is everywhere close to uniformity.

When the constants $\{C_j\}$ are reasonably small, the uniform stress distribution (1-5) presents an ideal response of the structure to an applied external load while avoiding both excessive local stress concentration and underloading of other parts of the boundary at an acceptable stress level.

Though the criteria (1-2) and (1-3) for $V[\sigma_h(L)] > 0$ are implicitly connected through the evident inequality

$$\max \sigma_h(L) - \min \sigma_h(L) \le V[\sigma_h(L)], \tag{1-6}$$

where the equality sign is attained at, for instance, *any* monotone function, it remains unclear whether they go to their minima together or at each other's expense.

The absolutely nontrivial and purely analytical example here consists of the equistress shapes (ESS) [Cherepanov 1974; Vigdergauz 1976; Banichuk 1977] along which the hoop stresses are simultaneously uniform [Cherepanov 1974] and globally minimal [Vigdergauz 1976]. In other words, an ESS is optimal with respect to *both* criteria, which, for brevity, will be referred to as $\mathcal{H}$ and V, respectively.

However, these shapes exist only under the following restrictive conditions:

(A_1) The elastic domain is infinite.

(A_2) The absolute value of the ratio of deviatoric stresses to dilatational stresses externally applied at infinity must be no greater than 1 or, equivalently, the principal remote stresses must have the same sign. Under this requirement, the resultant stress field in the domain remains rather isotropic, thus preserving the ellipticity of the optimization problem.

(A_3) All the contours must be optimized simultaneously: no fixed holes are allowed.

If all this takes place, the constants C_j are all equal, and are determined only by an external load independently of the number of holes and their relative arrangement. They are found analytically in parallel with the parametric representation of the ESS by solving the Dirichlet problem in a plane with rectilinear slits. See [Milton 2002] and references therein.

Whenever any of the conditions (A_1)–(A_3) is violated, an ESS most likely no longer exists.

A less restrictive *piecewise* constant distribution of the hoop stresses (M-equistressness) was proposed in [Vigdergauz and Cherkaev 1986] and more comprehensively in [Vigdergauz 2006], as an immediate extension of (1-5) to *any* loading at infinity. The M-equistress single hole under remote shear is semi-analytically identified in [Vigdergauz 2006]; two closely spaced holes are numerically found in [Waldman et al. 2003]. Physically, they contain four angular points $t_1, \dots, t_4$ across which the hoop stresses change sign:

$$\sigma_h(t) = \begin{cases} C', & t_1 < t < t_2, \quad t_3 < t < t_4, \\ C'', & t_4 < t < t_1, \quad t_2 < t < t_3, \qquad C', C'' \neq 0, \quad C'C'' < 0, \end{cases} \tag{1-7}$$

so that $V[\sigma_h(L)] = 2|C' - C''|$.

Less constrained optimal problems of this kind have received little or no attention in the literature. We study them here using only the V-criterion, with no additional prerequisites like, say, the piecewise constancy (1-7) of σ_h. The numerical results obtained (Section 5) show that this approach, among other things, reliably reproduces equi- and M-equistressness. In this connection, we note that, as mentioned above, any nonzero variation corresponds to at least an immense variety of monotone functions with the same extrema; thus, the fact that the V-criterion identifies just the independently found piecewise constant M-distributions (when they exist) strongly counts in its favor.

On the other hand, the equistressness (1-5) for a general geometry and the M-equistressness (1-7) for a single hole were first derived as a stationary point of the variation of the strain energy integral over the solid phase with moving boundaries [Cherepanov 1974]. In contrast, we formulate the V-criterion as an essential relaxation of equistressness rather than variationally. Nevertheless, the fact that the stress variation is bounded from below by zero allows one to formulate the V-related shaping of the holes as a global optimization problem (Section 3). A possible relation between energy minimization and the V-criterion deserves a separate study, which is currently beyond our scope.

In the general unrestricted case, the ESS serve as an absolute benchmark to measure the effectiveness of a shape optimization which may be performed now only *separately* for the concentration factor (1-2) and for the variation of the stresses (1-3).

Though both criteria have comparable practical implications, they generalize the ESS in diverging directions. More importantly in the current context, they substantially differ in computational complexity. Indeed, a typical numerical optimization strategy involves two main ingredients: the solution of a given direct problem which has to be repeated many times, and a minimization scheme. The direct solver assesses the fitness of each candidate for optimization by a chosen criterion. The stress concentration factor (1-2), due to its local nature, must be evaluated here with high accuracy to avoid spurious oscillations around the true value, which frequently occur in numerical stress analysis. By contrast, the integral-type criterion (1-3) may be assessed less accurately because the sums (1-4) permit, at least partially, the compensation of numerical errors in the stress computation. The results displayed in Section 5 illustrate that minimization of the variation of the stresses effectively smooths them also outside of limitations (A_1)–(A_3). It works as an oscillation filter within the numerical optimization scheme composed here as follows:

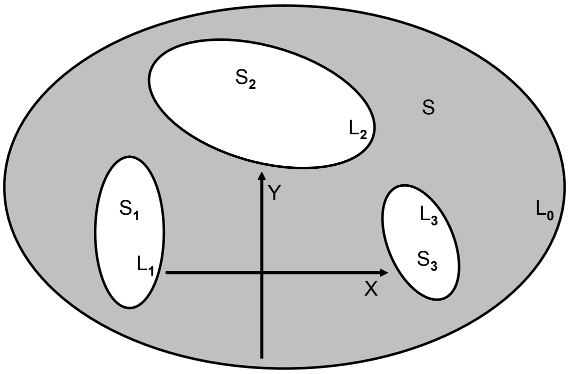

Figure 1. The problem schematic: a two-dimensional elastic region with holes. The outer boundary L_0 may recede to infinity.

- The *direct solver* employs complex-valued Kolosov–Muskhelishvili (KM) potentials [Muskhelishvili 1963], which result in a specially derived system of linear algebraic equations involving no singularities and, hence, providing a fast and accurate assessment of any admissible hole shape.
- The *minimization process* is based on a standardized configured genetic algorithm (GA) which includes the above-described solver for fitness evaluation in a gradientless search of the global optimum. Of importance here is the novel encoding scheme, where each optimized shape is presented *separately* by a sequence of the first N Laurent coefficients of the function mapping it conformally onto a unit circle. As a whole, the proposed scheme was validated previously [Vigdergauz 2008; 2010] in the closely related context of the minimization of the strain energy.

Our contribution, therefore, is twofold: the relaxation of the equistress principle and its efficient numerical implementation.

The paper is organized as follows. In Section 2, the two-dimensional boundary value elastostatic problem for a multiply connected region and the hoop stresses variations is formulated in complex-variable terms. On this basis, Section 3 poses the optimization problem and illustrates its peculiarities by the example of the equistress and the M-equistress shapes. Section 4 described the components of the numerical optimization scheme and how they are combined together. In Section 5, numerical results for a selection of benchmark problems are detailed and discussed to illustrate the validity of our approach and its limitations. Finally, some concluding remarks are made in Section 6.

2. Problem setup and governing equations

Consider, in the complex plane $E : z = x + iy \in E$, a linearly elastic, homogeneous, and isotropic solid S which contains a finite number N of nonintersecting holes S_j with boundaries L_j, $j = 1, \dots, N$, as shown in Figure 1. The infinite region outside the outer boundary L_0 is denoted by S_0, so $S + \bigcup_{j=0}^{N} S_j = E$. Each curve L_j, $j = 0, \dots, N$, is supposed to be closed and piecewise smooth, with area F_j. When it exists, the outer boundary L_0 is subject to given external stresses

$$\sigma_{nn}(t) \text{ and } \sigma_{n\tau}(t), \quad t \in L_0, \tag{2-1}$$

in a local system of curvilinear orthogonal coordinates (n, τ), while the boundaries of the holes are taken to be traction-free:

$$\sigma_{nn}(t) \equiv 0, \quad \sigma_{n\tau}(t) \equiv 0, \qquad t \in L_j,\ j = 1, \ldots, N. \tag{2-2}$$

The load-induced stress tensor $\{\sigma(z)\}$ at any point of the elastic domain is expressed by the complex-valued Kolosov–Muskhelishvili (KM) functions $\Phi(z)$, $\Psi(z)$ holomorphic in S (see [Muskhelishvili 1963] for these and other formulas in this section):

$$\sigma_{xx}(z) + \sigma_{yy}(z) = 4\,\mathrm{Re}\,\Phi(z), \quad z \in S, \tag{2-3a}$$

$$\sigma_{yy}(z) - \sigma_{xx}(z) + 2i\sigma_{xy}(z) = 2[\bar{z}\Phi'(z) + \Psi(z)]. \tag{2-3b}$$

In conformity with the loading conditions (2-1)–(2-2) the KM potentials are linearly linked along the boundary $L = \bigcup_{j=0}^{N} L_j$ of the solid S by

$$2\frac{\partial \bar{t}}{\partial t}\,\mathrm{Re}\,\Phi(t) + \bar{t}\Phi'(t) - \sigma_{nn}(t) - i\sigma_{n\tau}(t) = -\Psi(t), \quad t \in L_0; \tag{2-4a}$$

$$2\frac{\partial \bar{t}}{\partial t}\,\mathrm{Re}\,\Phi(t) + \bar{t}\Phi'(t) = -\Psi(t), \qquad t \in L_j,\ j = 1, \ldots, N. \tag{2-4b}$$

The second potential $\Psi(z)$ is isolated in the right-hand side of (2-4) for future use (see Section 4.1). When the elastic domain is infinite, the outer boundary L_0 does not exist and the nonzero conditions (2-4a) are replaced by the given far-field principal stresses $\sigma_{xx}^{\infty} = P$, $\sigma_{yy}^{\infty} = Q$, $\sigma_{xy}^{\infty} = 0$, which dictate the asymptotics

$$\Phi(z) = Bz + O(|z|^{-2}), \quad 4B = P + Q, \quad z \to \infty; \tag{2-5a}$$

$$\Psi(z) = \Gamma z + O(|z|^{-2}), \qquad 2\Gamma = Q - P. \tag{2-5b}$$

The identities (2-4a)+(2-4b) or (2-4a)+(2-5) form a boundary value problem to be solved for KM potentials, which in turn define the resultant stresses through (2-3). Using the traction-free condition (2-4b) and the coordinate invariance of the stress tensor trace in the left side of (2-3a) we obtain, along each inner hole,

$$\sigma_{\tau\tau}(t) = 4\,\mathrm{Re}\,\Phi(t), \quad t \in L_j,\ j = 1, \ldots, N, \tag{2-6}$$

and, in like manner, when the outer boundary is present,

$$\sigma_{\tau\tau}(t) = 4\,\mathrm{Re}\,\Phi(t) - \sigma_{nn}(t), \quad t \in L_0. \tag{2-7}$$

Here $\sigma_{\tau\tau}(t)$ denotes the hoop stresses abstractly written in Section 1 as σ_h. In view of (2-6), (2-7), their total variation is written as

$$V[\sigma_{\tau\tau}(L)] = \sum_{j=0}^{N} V[\sigma_{\tau\tau}(L_j)] = 4\sum_{j=0}^{N} V[\mathrm{Re}\,\Phi(L_j) - \delta_{j,0}\sigma_{nn}(L_j)] \tag{2-8}$$

where $\delta_{j,0}$ stands for the Kronecker delta.

At a fixed external load, the stresses and hence their boundary variations depend only on a number of the holes, their shape, size and mutual arrangement. As it will be shown later, the hole shapes admit an effective finite parametrization, which significantly facilitates the numerical shape optimization technique with respect to the V-criterion.

3. Problem formulation

We are now in a position to define more precisely the problem (1-3) of minimizing the variation of the hoop elastic stresses in complex-variable terms:

> *Given relative locations and areas of a number of traction-free holes in a two-dimensional thin elastic domain, find the hole shapes L_j that minimize the hoop stresses variation* (1-3)+(2-8) *under a load specified either along a fixed outer boundary by* (2-1)+(2-4a) *or at infinity by* (2-5).

Except for the novel criterion, this is a standard shape optimization problem in elasticity.

As already noted, the global minimum (1-5) of the variation criterion V is reached, for instance, at the equistress holes in an infinite plate; they are derived in the current terms as follows.

Substitution of (1-5) into (2-6) gives at the inner traction-free holes

$$\operatorname{Re}\Phi(t) = C_j, \quad j = 1, \ldots, N. \tag{3-1}$$

The identities (3-1) and the bulk-type asymptotics (2-5a) form the elementary Dirichlet problem in the holomorphic function $\Phi(z)$ with the unique solution

$$\Phi(z) = \text{constant} = B, \quad z \in S; \qquad C_j = B, \quad j = 1, \ldots, N; \tag{3-2}$$

which is valid for *any* hole shapes and locations. By (3-2), the traction-free condition (2-4a) then simplifies to the boundary-value problem in the second KM potential $\Psi(z)$

$$\Psi(t) = -2B\frac{\partial \bar{t}}{\partial t}, \quad t \in L_j,\ j = 1, \ldots, N, \tag{3-3}$$

with shear-type asymptotics (2-5b) at infinity. In contrast to (3-1), this problem may have a solution only for *specifically shaped* holes along which the right-hand side of (3-3) is the boundary value of a function holomorphic in S. The bulk-type asymptotics (2-5) provides a necessary condition for solvability of the problem. Indeed, taking the absolute values of both sides of (3-3) and using the evident fact that

$$\left|\frac{\partial \bar{t}}{\partial t}\right| \equiv 1, \quad t \in L, \tag{3-4}$$

for any arc L in the complex plane, we have

$$\left|\Psi(t)\right| = 2\left|B\frac{\partial \bar{t}}{\partial t}\right| = 2|B|. \tag{3-5}$$

Since the modulus of a holomorphic function is a real subharmonic function of z [Courant 1950], it obeys the maximum principle and hence achieves its maximum only at the domain boundary L. Particularly

$$\left|\Psi(z = \infty)\right| = |\Gamma| \leq 2|B| \tag{3-6}$$

or, in equivalent form, $\Delta \equiv \Gamma/(2B)$, which implies

$$|\Delta| = \left|\frac{\sigma_{yy}^{\infty} - \sigma_{xx}^{\infty}}{\sigma_{yy}^{\infty} + \sigma_{xx}^{\infty}}\right| \leq 1, \tag{3-7}$$

a quantitative expression of the solvability condition (A_2) discussed in Section 1.

In themselves, the equistress shapes are found parametrically by the conformal mapping of the optimized infinite domain into a plane with parallel slits [Cherepanov 1974] where the transformed boundary conditions (3-3) are met. For further references, we reproduce here the equations for the upper side of the right hole in the case of two identical ESS disposed symmetrically about the y-axis [Cherepanov 1974]:

$$\left.\begin{aligned} \frac{y(\xi)}{C} &= (1+\gamma)\Big(E\big(\theta,\sqrt{1-\xi_0^2}\big)+d_0F\big(\theta,\sqrt{1-\xi_0^2}\big)-R(\xi)\Big)\\ \frac{x(\xi)}{C} &= x_0+(1-\gamma)(\xi-\xi_0) \end{aligned}\right\}\quad \text{for } 0<\xi_0\le\xi\le 1, \tag{3-8}$$

where

$$\theta=\arcsin\frac{1}{\xi}\sqrt{\frac{\xi^2-\xi_0^2}{1-\xi_0^2}},\qquad x_0=(1-\gamma)\xi_0+(1+\gamma)\bigg(E\Big(\frac{\pi}{2},\xi_0\Big)-(1+d_0)F\Big(\frac{\pi}{2},\xi_0\Big)\bigg),$$

$$d_0=-\frac{E\Big(\dfrac{\pi}{2},\sqrt{1-\xi_0^2}\Big)}{F\Big(\dfrac{\pi}{2},\sqrt{1-\xi_0^2}\Big)},\qquad R(\xi)=\xi^{-1}\sqrt{(1-\xi^2)(\xi^2-\xi_0^2)}.$$

Here F and E are the elliptic integrals of the first and second kind, respectively, C denotes a nonessential scaling factor up to which the two-hole geometry is described by the single dimensionless parameter λ, the ratio of the half interdistance x_0 to the square rooted area $F_1=F_2$ of either of the holes:

$$\lambda=\frac{x_0}{\sqrt{F_{1,2}}},\qquad 0<\lambda<\infty. \tag{3-9}$$

With decreasing distance x_0, and, hence, increasing interaction between the holes, the resultant optimal shape (3-8) evolves from an ellipse to a kidney-like shape, as illustrated in [Cherepanov 1974].

The seeming ease of obtaining the globally optimal solution (3-8) is completely due to the conditions (A_1)–(A_3) listed in Section 1, which make it possible to preliminary find the first KM potential $\Phi(z)$ in the geometry-independent form (3-2). Other examples of the ESS such as a circular hole under uniform pressure are too trivial to be considered.

Now it becomes clear how the loading inequality (3-6) works. Indeed, consider a single traction-free hole under remote shear [Vigdergauz and Cherkaev 1986]: then $B=0$ and $\Gamma=1$. The nonzero equistress condition (3-1) then makes no sense in view of the mean value theorem for a harmonic function $\operatorname{Re}\Phi(z)$ [Courant 1950], by which

$$\widehat{\operatorname{Re}\Phi(t)}=C_1=\operatorname{Re}\Phi(\infty)=B\equiv 0,\qquad t\in L_1, \tag{3-10}$$

where the hat denotes the function's mean value along L_1. In contrast, the weakened M-equistress condition (1-7) is compatible with (3-10) provided that $C'=-C''$ and $\arg t_k=(2k-1)i\pi/4$ ($k=1,2,3,4$), as dictated by the problem's rotational symmetry. Again, as above, substitution of (1-7) into the boundary condition (2-4a) and conformal mapping help to find the shape and the stress constant C' [Vigdergauz and Cherkaev 1986], this time only numerically. The optimal shape looks like a slightly rounded square. A more efficient semianalytical approach [Vigdergauz 2006] is given in Section 5 for comparison.

The general case, however, does not lend itself to solution by this approach and the whole situation calls for a numerical treatment based on a novel analytical approach.

4. Numerical scheme

Particularly relevant to the present purposes, is the scheme previously developed in [Vigdergauz 2008; 2010], in the similar context of the energy-related shape optimization. For completeness and reader's convenience, its basic features are briefly outlined below.

4.1. ***Direct solver.*** It is shown in the previous section that the ESS allow one to find the KM potentials (a) sequentially rather than in parallel, and (b) in closed form.

Actually, however, $\Phi(z)$, $\Psi(z)$ can be separated for *any* set of hole shapes, though in a quite different manner and only numerically. As compared to the standard practice, this option halves the computational complexity of the direct problem. Crucial here is that, in contrast to $\Phi(z)$, the second potential $\Psi(z)$ enters the boundary conditions (2-4) with neither conjugates nor derivatives. This offers a way of solving (2-4) as a regular boundary-value problem in only $\Phi(z)$ and, when needed, to find $\Psi(z)$ by simple integration thereafter.

Indeed, since the Cauchy-type integral of the holomorphic function $\Psi(z)$, $z \in S$, over L vanishes identically in each complementary region S_j, $j = 0, \dots, N$ [Ahlfors 1978], we have from (2-4)

$$\int_L \frac{2\,\mathrm{Re}\,\Phi(t)\,d\bar{t} + \bar{t}\Phi'(t)\,dt}{t-z} = \int_{L_0} \frac{\sigma_{nn}(t) + i\sigma_{n\tau}(t)}{t-z}dt, \quad \forall z \in S_j,\ j = 0, \dots, n. \tag{4-1}$$

Here L is traversed in the positive direction with respect to the elastic domain S.

Evidently, a Taylor-like expansion of the Cauchy kernel $1/(t-z)$ around arbitrary finite points $a_j \in S_j$, $j = 1, \dots, n$, namely

$$\frac{1}{t-z} = \frac{1}{t-a_j} + \sum_{k=1}^{\infty} \frac{(z-a_j)^k}{(t-a_j)^{k+1}}, \quad |z-a_j| < \epsilon,\ j = 1, \dots, N, \tag{4-2}$$

is absolutely convergent at least for a sufficiently small ϵ. Similarly, at infinity,

$$\frac{1}{t-z} = -\frac{1}{z} - \sum_{k=1}^{\infty} \frac{t^k}{z^{k+1}}, \quad |z| > R, \tag{4-3}$$

for a sufficiently large R.

Next, substitution of (4-2) and (4-3) into (4-1) and equating like powers on both side yields the infinite set of identities ($k = 1, 2, \dots$)

$$\int_L \frac{2\,\mathrm{Re}\,\Phi(t)\,d\bar{t} + \bar{t}\Phi'(t)\,dt}{(t-a_j)^k} = \int_{L_0} \frac{\sigma_{nn}(t) + i\sigma_{n\tau}(t)}{(t-a_j)^k}dt; \quad j = 1, \dots, N, \tag{4-4a}$$

$$\int_L \big(2\,\mathrm{Re}\,\Phi(t)\,d\bar{t} + \bar{t}\Phi'(t)\big)t^{k-1}dt = \int_{L_0} \big(\sigma_{nn}(t) + i\sigma_{n\tau}(t)\big)t^{k-1}dt. \tag{4-4b}$$

By the principle of analytical continuation [Ahlfors 1978], these identities are valid not only near the points $\{a_j\}$ but everywhere outside S. Therefore, taken together, they are equivalent to the initial boundary conditions (2-4). Finally, the Laurent series of $\Phi(z)$ around the same points a_j and at infinity,

$$\Phi(z) = \sum_{j=1}^{n} \sum_{k=2}^{\infty} \frac{d_j^{(k)}}{(z-a_j)^k} + \sum_{k=2}^{\infty} \frac{d_0^{(k)}}{z^k}, \quad z \in S, \tag{4-5}$$

transforms (4-4) into an infinite set of linear algebraic equations

$$A\vec{x} = D, \quad A = \{A_{kl}\}, \quad D = \{D_k\}, \tag{4-6}$$

for the unknowns $\vec{x} = \{d_j^{(k)}\}$, with $j = 0, \dots, N$ and $k = 2, \dots$. The coefficients of the system involve *regular* rather then *singular* integrals and hence are computationally more advantageous than the conventional integral equation schemes [Muskhelishvili 1963]. For certain geometries, they are displayed in Section 5. When S is infinite, the integrals along the outer contour L_0 are discarded together with the coefficients $\{d_0^{(k)}\}$, while the right-hand side of the system is a linear combination of specific integrals over all holes with the loading coefficients B and Γ from (2-5) as detailed in [Vigdergauz 2008; 2010]. In both cases, the system involves only the first KM potential $\Phi(z)$ and hence has a halved size when truncated for numerical purposes to a finite number N_{syst}. The number of the unknowns may be further reduced for a problem with symmetry as shown for specific cases in Section 5.

4.2. ***Shape encoding algorithm.*** The key issue in numerical applications of the proposed solver is how to effectively parametrize hole shapes, both for evaluating the contour integrals (4-4) in the system coefficients and optimizing the shapes over the same parameters. A workable approach here is a conformal mapping of the domain D outside a unit circle $\rho = \exp i\theta$, $0 \le \theta \le 2\pi$, $|\rho| = 1$, onto the infinite domain $E_j \equiv E - S_j$ performed *separately* [Vigdergauz 2008; 2010] for each shape L_j, $j = 0, \dots, N$, by $N+1$ functions with a finite Laurent expansion in D:

$$\frac{\omega_j(\zeta)}{C} = \zeta + \sum_{m=1}^{M} \frac{b_m^{(j)}}{\zeta^m} \quad \text{with } |\zeta| \ge 1, \quad j = 0, \dots, N, \tag{4-7}$$

where C is the scaling coefficient at which

$$\omega_j(\rho) = t \in L_j, \quad j = 0, \dots, N. \tag{4-8}$$

Taken as design variables, the mapping coefficients $b_m^{(j)}$, with $m = 1, \dots, M$ and $j = 0, \dots, N$, offer a number of substantial advantages over the commonly used nodal point shape representation, as detailed in [Vigdergauz 2010]. First, the conformal mapping-based description (4-8) is *continuous* rather than discrete, and hence even a small number M of them gives a wide variety of smooth closed shapes as compared to tens and hundreds of nodal points required for the same purpose. This is all the more so because the $b_j^{(m)}$ are bounded by the successively narrowed intervals

$$-\frac{1}{\sqrt{m}} \le b_m^{(j)} \le \frac{1}{\sqrt{m}}, \quad j = 0, \dots, N, \quad m = 1, 2, \dots \tag{4-9}$$

(see [Ahlfors 1978]), which are the necessary condition for the nonnegativeness of the area F_j inside L_j:

$$F_j = \pi\left(1 - \sum_{m=1}^{M} m\left|b_m^{(j)}\right|^2\right), \quad j = 0, \dots, N. \tag{4-10}$$

As a result, high-order coefficients are mostly responsible for forming large local curvatures and have little impact on the integral-type criterion (2-8) of minimum stress variation. Second, with the identities

$$\bar{\rho} = \rho^{-1}, \quad d\rho = \rho\, d\theta, \quad dt = i\omega_j'(\rho)\rho\, d\theta, \quad d\bar{t} = -i\overline{\omega_j(\rho)'}\rho^{-1}\, d\theta, \quad t \in L_j, \tag{4-11}$$

the integration path L_j is continuously transformed into the unit circumference ρ, thus making the numerical integration easier and independent of the parameter M. In numerical simulation (Section 5) we use the simplest trapezoid rule with N_{int} equal subintervals.

In a multiply connected case, the parametrization (4-7)–(4-11) also does better numerically than the canonical simultaneous mapping [Courant 1950] of an infinite plane ζ with N slits or holes by a holomorphic function $\omega(\zeta)$. Indeed, the boundary condition in ζ [Muskhelishvili 1963]

$$-\frac{2}{\zeta^2}\overline{\omega'(\zeta)}\,\mathrm{Re}\,\Phi(\zeta)+\overline{\omega(\zeta)}\Phi'(\zeta)+\omega'(\zeta)\Psi(\zeta)=0, \qquad \zeta\in l, \tag{4-12}$$

is more complicate than its unmapped counterpart (2-4b) and, most likely, may not be simplified beyond the nice exception of the equistressness. Further, the proposed approach easily meets any given arrangement of the holes by displacing the separate maps (4-7) in the physical plane E:

$$\omega_j(z)\to\omega_j(z)+h_j, \qquad j=1,\dots,N. \tag{4-13}$$

Here the h_j are complex-valued constants. This can hardly be done by an ordinary mapping of the whole domain S as exemplified in Section 3, where the implicit relation in (3-8) between the ESS interdistance x_0 and the auxiliary parameter λ is not invertible analytically to give λ as a function of ξ_0. This is all the more true for fixed shapes. When they exist, they are necessarily involved into the usual mapping, and should be restored through a nonlinear boundary condition imposed on the holomorphic function $\omega(\zeta)$, while separate mapping simply does not touch them. Finally, we note that the parametrization works well up to closely spaced holes (see Section 5) with a relatively small number M of the Laurent terms in (4-7).

4.3. ***Fitness evaluation.*** Once the hoop stresses $\sigma_{\tau\tau}(t)$ are found through $\Phi(z)$, the fitness of the corresponding set of the holes can be next evaluated with respect to the minimum variation criterion (2-8)+(1-4). Of course, for numerical implementation, the supremum in (1-4) is replaced by the sum over only one selection of q closely spaced points $0=x_1<x_2<\dots<x_q=2\pi$ along each hole contour. We select the points x_p in the form

$$x_p=\pi(1+\beta_p^{(q)}), \qquad p=1,\dots,q, \tag{4-14}$$

where the $\beta_p^{(q)}$ are the roots of the Chebyshev polynomials of the second kind

$$U_q(x)=\prod_{p=1}^{q}\bigl(x-\beta_p^{(q)}\bigr), \qquad \beta_p^{(q)}=\arccos\frac{p\pi}{q+1}, \tag{4-15}$$

widely used in approximation theory. In the current context, their especially relevant property stems from the fact that the $U_n(x)$ are known [Abramowitz and Stegun 1964] to minimize the integral

$$\int_{-1}^{1}P_q(x)\,dx \xrightarrow[\{P_q\}]{\qquad\qquad} \int_{-1}^{1}U_q(x)\,dx \tag{4-16}$$

among all polynomials $P_q(x)$ of same degree q and same leading coefficient. On the other hand, the variation of a differentiable function $f(x)$ in an interval takes the form [Natanson 1955]

$$V_a^b(f)=\int_a^b|f'(x)|\,dx, \tag{4-17}$$

in conformity with the general definition (1-4). Comparison of (4-17) with (4-16) shows that $V_{q+1}(x)$: $V'_{q+1} \equiv U_q(x)$, $q \geq 1$, are the polynomials of the minimum variation in $[-1, 1]$. The numerical simulation (Section 5) indicate that the usage of (4-14) adds some 6 to 8 percent to the accuracy of the results obtained with the same number of uniformly distributed approximation points.

Finally (4-17) gives

$$V_a^b(f) = \int_a^b \left|f'(x)\right| dx \geq \left|\int_a^b f'(x)\,dx\right| = \left|f(b) - f(a)\right|, \tag{4-18}$$

where the equality holds if and only if $f'(x)$ has constant sign on $[a, b]$. This means that V-optimization seeks to smooth the stresses distribution by making it monotonous on the irreducible part of the contour. We have already noted that the proposed criterion, in fact, does even more. Amongst monotone distributions it tends to find a piecewise constant one, as exemplified in Section 5.

4.4. ***Evolutionary optimization scheme.*** With the mapping terms (4-7), the optimization problem is finally reformulated as follows

$$V[\sigma_{\theta\theta}(L)] \xrightarrow[\{b_m^{(j)}\}]{} \min\bigl(\hat{b}_m^{(j)},\ m = 1, \dots, M,\ j = 0, \dots, N\bigr). \tag{4-19}$$

Put another way, the search space for each shape L_j is reduced to a M-dimensional rectangular parallelepiped with edges of length $2/\sqrt{m}$, $m = 1, \dots, M$, as defined by bilateral inequalities (4-9). They form a set of linear constraints on the definition domain of the nonlinear minimized function $V(b_1^{(0)}, \dots, b_M^{(N)})$, thus completing the problem formulation.

Our previous experience [Vigdergauz 2008; 2010] suggests that the computational process of shape optimization (4-19)+(4-9) can be effectively conducted by evolutionary genetic algorithms (GAs), which have been well-accepted in the last two decades (see, for instance, [Goldberg and Sastry 2010] and references therein). They perform a gradientless optimization in a large search space by mimicking the Darwinian process of natural selection over successive generations through crossover and mutation operations. The efficient direct solver and the time-saving shape encoding numerically simplify the parametrized optimization problem (4-19), allowing the use of an ordinary genetic algorithm configuration, as detailed in our papers just cited. A set $\{L\}$ of shapes is stochastically generated into a "chromosome" encoding $M \times (n+1)$ mapping parameters (4-7) as signed 16-bit integers r_j^m, in conformity with (4-9):

$$b_j^{(m)} = \frac{r_j^m}{I\sqrt{m}} \quad \text{with } I = 2^{15} - 1,\ \ -I \leq r_j^m \leq I, \quad j = 0, \dots, n,\ \ m = 1, 2, \dots. \tag{4-20}$$

The proposed direct solver permits evaluating the fitness of the chromosome that is the stresses variation for the decoded shapes $L(b_j^{(m)})$. An initial family of N_{chr} chromosomes is then subject to genetic operations of recombination, crossover and mutation performed over the integers $\{r_j^m\}$ rather then over $\{b_j^{(m)})\}$. In doing so, the best individuals with the minimal fitness have the highest chance of surviving in the offspring which in turn is passed to the fitness evaluation stage, and the cycle continues until the search is terminated. The number N_{iter} of iterations should be taken sufficiently large to ensure close proximity of the solution to the global minimum. As is customary in iterative optimization, we indirectly estimate the proximity by the inner stability of the process when the obtained minimum remains unchanged through a number of successive evolutionary steps. In general, the efficiency of GAs strongly depends on the parameters involved, which, when chosen poorly, may slow convergence or even result in failure.

Of course, the scheme above described is not the only possible way to solve the shape optimization problem at hand. For instance, Waldman et al. [2003] combine the finite element analysis with the specially designed gradientless scheme of shape optimization by the M-equistress criterion (1-7) when the elastic material is added at regions of high stress and/or removed where the hoop stress is low. In contrast to our approach, this procedure needs an initial guess for the shapes to start with. As a result, a given mutual arrangement of the holes is generally not preserved after optimization. Besides, the authors use a time-consuming remeshing between iterations to avoid mesh distortion. Qualitatively, their results fully agree with ours, though quantitative discrepancies are rather significant for two closely spaced optimal holes in a plane under shear dominating far load. The details are discussed in Section 5.3.

5. Numerical results

As already noted, the evaluation of the variation under the proposed optimization scheme depends on a number of parameters such as the probabilities of the GA operations, the truncated system size N_{syst}, and the numbers N_{int}, M, and q of, respectively, integration points, mapping terms, and Chebyshev polynomial roots. All must be pre-adjusted to obtain stable and reliable solutions. We do it here using a rare opportunity of comparing the numerical results with the corresponding closed solution (3-8) for two equistress holes (Section 5.1). Further, in order to validate the approach, we numerically simulated a number of yet unsolved two-dimensional cases.

5.1. ***Two equistress holes in an infinite plate under unibiaxial tension*** **($B = 1,\ \Gamma = 0$).** Here our aim is to identify the ESS numerically with the minimum variation criterion (2-8) instead of using the equistress principle (3-1)+(3-2) as a prerequisite.

Let two identical holes be located symmetrically with respect to the Cartesian axes. Then $\Phi(z)$ is even and takes conjugate values at complex conjugate points [Muskhelishvili 1963]:

$$\Phi(z) = \Phi(-z), \quad \Phi(\bar{z}) = \overline{\Phi(z)}, \quad z \in S + L \tag{5-1}$$

With this in view, the Laurent expansion (4-5) simplifies to

$$\Phi(z) = \sum_{k=2}^{\infty} d_k^{(1)} \left(\frac{1}{(z-a_1)^k} + \frac{(-1)^k}{(z+a_1)^k} \right), \quad z \in S + L, \quad a_1 \in S_1; \quad \operatorname{Im} d_k^{(1)}, \quad k = 2, 3, \dots, \tag{5-2}$$

and the system (4-6) takes the form

$$A_{kl} = 2l \int_{L_1} \operatorname{Re}(\rho_{l+1}(t,c))\rho_k(t,c)\, d\bar{t} + l(l+1) \int_{L_1} \bar{t} \rho_{l+2}(t,c)\rho_k(t,c)\, dt, \tag{5-3a}$$

$$D_k = -4B \int_{L_1} \rho_k(t,c)\, d\bar{t}, \quad k = 0, 1, 2, \tag{5-3b}$$

$$\rho_0(t,z) \equiv \frac{1}{t-z} + \frac{1}{t+z}, \quad z \in S_1, \tag{5-3c}$$

$$\rho_k(t,c) \equiv \frac{1}{k!} \frac{\partial^k \rho_0(t,z)}{\partial z^k}\Big|_{z=a_1} = \frac{1}{(t-a_1)^{k+1}} + \frac{(-1)^k}{(t+a_1)^{k+1}}, \tag{5-3d}$$

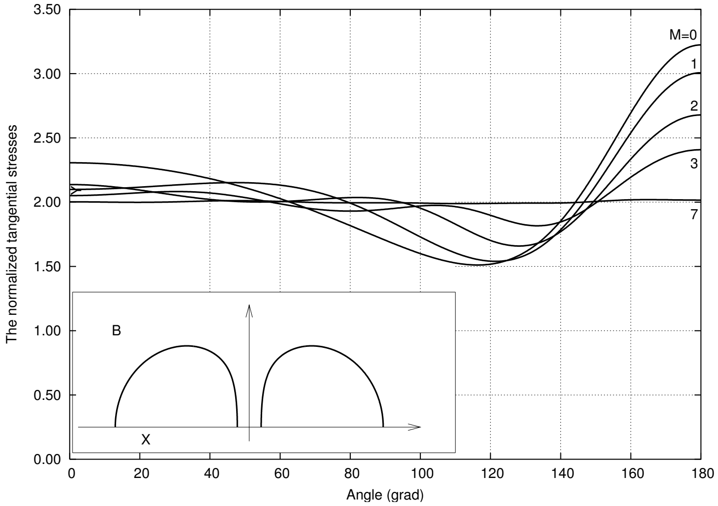

Figure 2. Two holes under remote bulk loading: the V-optimal hoop stresses $\sigma_{\tau\tau}(\theta)$ as a function of the mapping size M at $\lambda = 0.2$.

Finally, when replacing $t \in L_1$ by its map (4-7)+(4-8), we define the scaling factor C and the displacement (4-13) (separately for each generated shape) to keep a given geometrical parameter λ from (3-9). By virtue of symmetry, the mapping terms $b_m^{(1)}$, $m = 1, \dots, M$ are also real and the integration in (5-3) is performed only along the upper half of $L_1 : 0 \leq \theta \leq \pi$.

Figure 2 depicts the convergence of the resultant hoop stresses on the optimized contour L_1 to the uniform distribution (3-2) at $\lambda = 0.2$ in dependence on the mapping problem size M, beginning with a circle $M = 0$. As one would expect, the largest local deviation of the hoop stresses is observed near the point x_0, $(\theta = \pi)$ closest to the opposite hole. Figure 3 shows the optimally smoothed stresses at $M = 9$

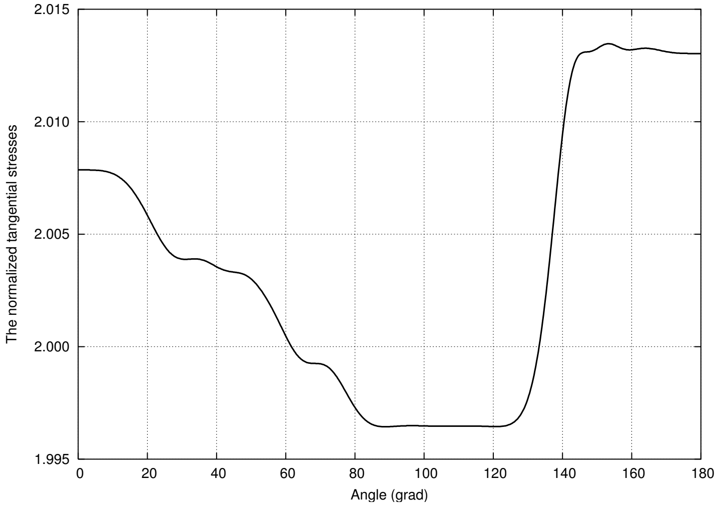

Figure 3. Two holes under remote bulk loading: the V-optimal hoop stresses for $M = 9$ in an enlarged scale.

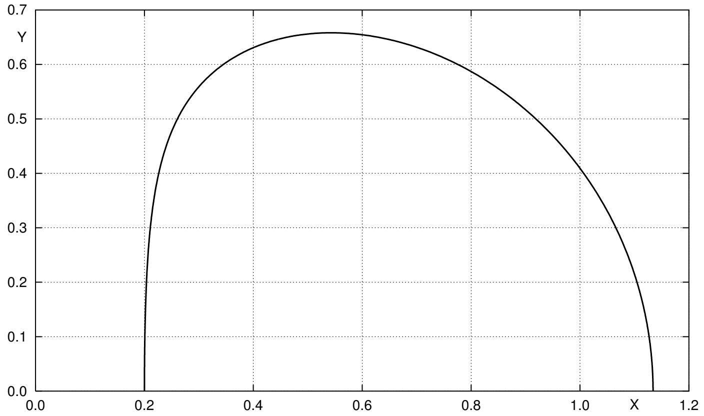

Figure 4. Two holes under remote bulk loading: the upper half of the right V-optimal hole at $\lambda = 0.2$.

in an enlarged scale. The maximum relative error of $\sigma_{\theta\theta}$ is approximately 0.65%. We believe that the error can be further reduced at the expense of increasing the computational cost but it is not our current aim. Figure 4 depicts the numerically obtained optimal shape which is compared with the parametric equations (3-8) taken at the computed value $\xi_0 \approx 0.0024051725$, $\lambda(\xi_0) = 0.2$. The mutual deviations are too small to be seen here. This closeness provides empirical grounds for adjusting the parameters listed at the beginning of the section. Table 1 gives their calibrated values used in further calculations.

GA parameter	Parameter value(s)
Gene	Integer in [−32767; 32767]
Individual	Interface shape
Population size	800
Number of genes, M	up to 9
Initial population	800 random individuals
Selection	Tournament
Elitism	Four best individuals
Crossover	1-point
Crossover rate	0.90
Creep mutation	By randomly changing a bit
Creep mutation rate	0.35
Jump mutation	By adding a random integer, typically in the range [−4; 4]
Jump mutation rate	0.35
Stopping criterion	After 1200 iterations
Resolving system size K	36
Number of integration points N_p	720 (in the interval $[0, \pi]$)
Number q of sample points on contour	1440

Table 1. GA operator types, their probability rates and related parameters typically used in further optimizations.

5.2. ***A single V-optimal hole in infinite plate under remote shear* ($B = 0$, $\Gamma = 1$).** Here, the rotational properties of the problem imply that $\Phi(iz) = -\Phi(z)$ and hence

$$\Phi(z)=\sum_{k=1}^{\infty}\frac{a^{(1)}_{4k-2}}{z^{4k-2}};\qquad \frac{\omega_1(\zeta)}{C}=\zeta+\sum_{m=1}^{M}\frac{b^{(1)}_{4m-1}}{\zeta^{4m-1}},\quad |\zeta|\ge 1, \tag{5-4}$$

while the right-hand side of the system (4-6) takes the form

$$D_0=-2\Gamma_0,\quad D_k=0,\quad k=1,2,\dots \tag{5-5}$$

In conformity with (3-10) and (5-4) we have

$$\sigma_{\theta\theta}(e^{i\pi/2}\zeta)=-\sigma_{\theta\theta}(\zeta),\quad \widehat{\sigma_{\theta\theta}(\zeta)}=0. \tag{5-6}$$

Remarkably, for a single hole an M-term finite mapping expansion generates *exactly* a finite $M \times M$ system [Vigdergauz 2006]. This allows one to avoid additional truncation error by explicitly summing the infinite tail of the series (5-4) through a finite difference scheme. As a result, the hoop stresses along any hole are obtained as rational functions of the nonzero mapping terms $b^{(1)}_{4m-1}$, $m = 1, \dots, M$. In particular, for $M = 1$ we have [Vigdergauz 2006]

$$\sigma_{\theta\theta}(\xi)=\frac{4(1-3b_3)\cos 2\theta}{(1-b_3)(1-6b_3\cos 4\theta+9b_3^2)},\quad b_3=b_3^{(1)}. \tag{5-7}$$

This makes the fitness evaluation equally easy and accurate for any criterion of optimality. Table 2 compares the computed V- and $\mathcal{H}$-optima and the corresponding mapping terms for various M. The $\mathcal{H}$-related values, in parentheses, are taken from [Vigdergauz 2006]. It is seen that with increasing M, both sets come closer and closer together; this is further illustrated in Figure 5. The V- and $\mathcal{H}$-optimal stress

N	$b_3^{(1)}$	$b_7^{(1)}$	$b_{11}^{(1)}$	$b_{15}^{(1)}$	$b_{19}^{(1)}$	$b_{23}^{(1)}$	$V_{\min}$	$\mathcal{H}_{\min}$
3	−0.07110 (−0.09000)						3.15744	3.11765 (3.07165)
7	−0.09681 (−0.11162)	0.00444 (0.00751)					2.96826	2.95683 (2.90563)
11	−0.10987 (−0.12182)	0.00733 (0.01044)	−0.00090 (−0.00200)				2.88768	2.88003 (2.84110)
15	−0.11748 (−0.12732)	0.00918 (0.01210)	−0.00165 (−0.00293)	0.00027 (0.00076)			2.84435	2.84159 (2.80824)
19	−0.12991 (−0.13049)	0.01055 (0.01293)	−0.00221 (−0.00340)	0.00055 (0.00112)	−0.00011 (−0.00032)		2.81818	2.81517 (2.78843)
23	−0.12498 (−0.13059)	0.01093 (0.01292)	−0.00239 (−0.00338)	0.00064 (0.00116)	−0.00017 (−0.00041)	0.00003 (0.00010)	2.80387	2.80262 (2.77936)

Table 2. A single square symmetric hole under remote shear: conformal mapping coefficients and the V-criterion resulting from the GA optimization process for different values of N. The $\mathcal{H}$-related values are also shown for comparison, in parentheses.

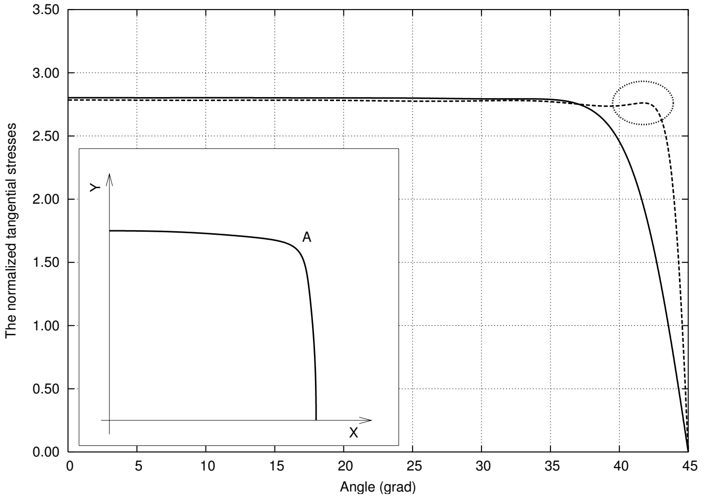

Figure 5. A single square symmetric hole under remote shear: tangential stress distribution along the V- and $\mathcal{H}$-optimal holes (solid and dashed lines, respectively) for $M = 23$. The local nonmonotonicity of the $\mathcal{H}$-related curve is marked with an ellipse.

distributions at $M = 23$ are very similar except for a vicinity of the angular point ($\theta = \pi/4$) where the criteria work differently. As explained at the end of Section 4.3, the V-optimal stress distribution tends to be monotonous while the $\mathcal{H}$-criterion further diminishes the stress maximum with some sacrifice in monotonicity. In any case, the difference between two maxima is hardly greater than the computational errors. This favors in the V-criterion ability. We may conservatively conclude that again, as in the equistress case, the $\mathcal{H}$- and V-optimal single holes under pure shear are very similar to each other, if not the same. Figure 6 depicts the evolution of the V-optimal shape with increasing M. One clearly sees the smooth formation of an angular point with higher mapping coefficients.

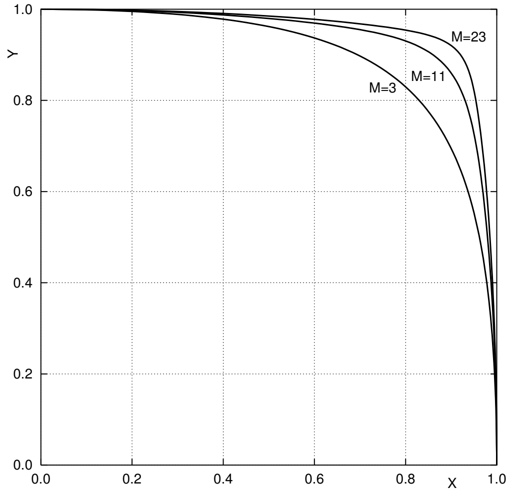

Figure 6. A single square symmetric hole under remote shear: the M-related evolution of the V-optimal hole.

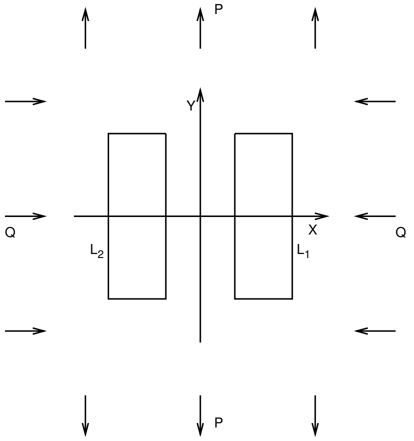

Figure 7. An infinite plate with two identical holes under pure shear. The hole shapes are symmetric about the x-axis and may have a finite number of angular points.

5.3. ***Two V-optimal holes in an infinite plate under remote shear*** **($B = 0$, $\Gamma = 1$).** The corresponding setup is shown in Figure 7. The only computational difference from the equistress case (Section 5.1) is in the right-hand side (5-3b) of the resolving system (5-3). Now it has the form (5-5) [Vigdergauz 2008].

It is worth noting the following. Our previous experience [Vigdergauz 2008; 2010] shows that, by contrast to (5-3b), the shear-type loading vector (5-5) results in low stability and accuracy of computing the local stresses which are polluted with spurious oscillations. The reason is that the shear-type optimal problem is no more elliptic as (3-2), and hence its solution looses some regular properties. For a single hole (Section 5.2) it was compensated by an analytical summation of the infinite series in (5-4). Here, as before, the numerically implemented V-criterion works equally well. Figure 8 illustrates this

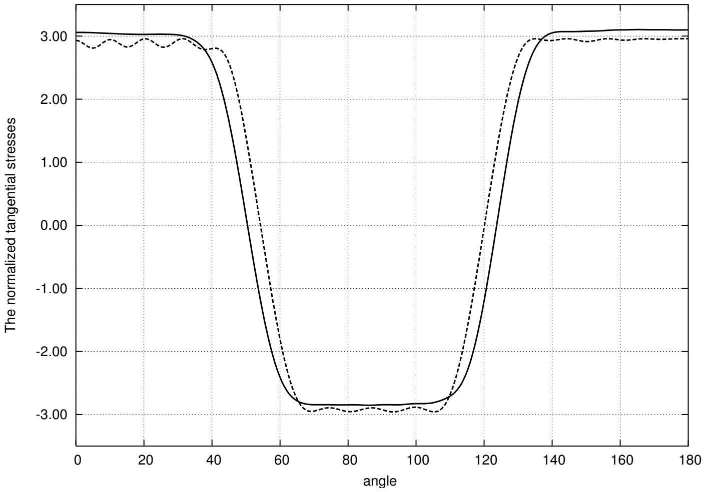

Figure 8. An infinite plate with two identical holes under pure shear: the V- and $\mathcal{H}$-optimal stresses (the dashed line) obtained by the same numerical scheme at $\lambda = 0.2$ are compared to demonstrate the distinctive V-related smoothing effect.

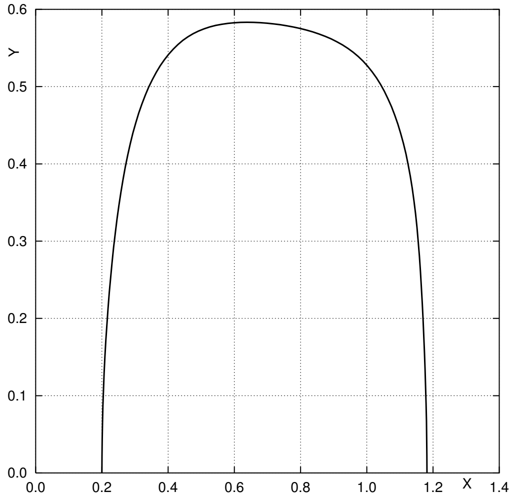

Figure 9. An infinite plate with two identical holes under pure shear: the upper half of the right V-optimal hole at $\lambda = 0.2$.

conclusion, exemplifying the V-related filtering effect for two closely spaced holes at $\lambda = 0.2$ whose shape is given in Figure 9. In contrast to the square symmetric V-optimal single hole, they are elongated in the y-direction as was previously found by Waldman et al. [2003]. However, these authors further obtained that the piecewise-constant hoop stresses for two holes under shear-dominating loading are *exactly* the same as in the single hole case *independently* of the separation distance. In other words, the shear-loaded optimal shapes also fully eliminate the holes interaction like in the equistress case. In contrast, our stresses extrema $\max \sigma_{\theta\theta}(\theta) \approx 3.10$ and $\min \sigma_{\theta\theta}(\theta) \approx -2.85$ on Figure 8 are higher than the single-hole level $\sigma_{\theta\theta}(\theta) \approx 2.78843$ (the right-bottom cell of Table 2) and differ in their absolute values. The difference is too large to be attributed completely to numerical accuracy and, therefore, the above-mentioned conclusion is not entirely supported in the quantitative analysis.

5.4. ***Two V-optimal holes in a circular disk under uniform pressure*** **($\sigma_{nn} = P,\ \sigma_{n\tau} = 0$).** As the last example, we consider a uniformly compressed disk with two identical traction-free side holes. Here, again, the symmetry relations (5-1) are obeyed, so that $\Phi(z)$ is written as

$$\Phi(z) = \sum_{k=1}^{\infty} d_{2k}^{(0)} z^{2k} + \sum_{k=1}^{\infty} d_k^{(1)} \left(\frac{1}{(z-a_1)^k} - \frac{(-1)^k}{(z+a_1)^k} \right), \tag{5-8}$$

$$z \in S + L, \qquad a_1 \in S_1, \qquad \operatorname{Im} d_k^{(0,1)},\ k = 2, 3, \ldots$$

In contrast to the equistress case (Section 5.1), the elastic domain is now finite and described by two dimensionless parameters, namely the relative area $f_{1,2} = f_{1,2}/\pi R^2 < 0.5$ of the hole and its displacement $x_0 < R$ from the center of the disk, where R is the disk radius.

Figure 10 depicts the identified V-optimal holes against their circular counterparts. Qualitatively, the resultant shape is rather predictable because at given $f_{1,2}$ and x_0 the V-optimization strives to move the hole away from the fixed outer boundary at the expense of the inner disk part. The corresponding

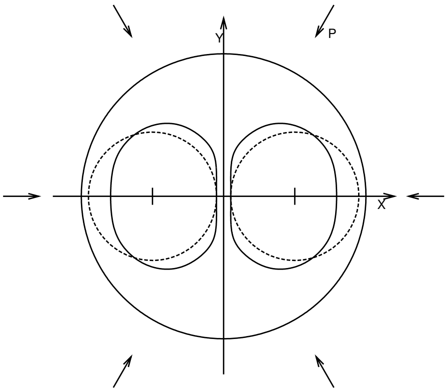

Figure 10. A uniformly compressed disk with two V-optimal holes at $x_0 = 0.05$ and $f_{1,2} = 0.2025$. The circular holes of the same location and area (dashed lines) are also shown for comparison.

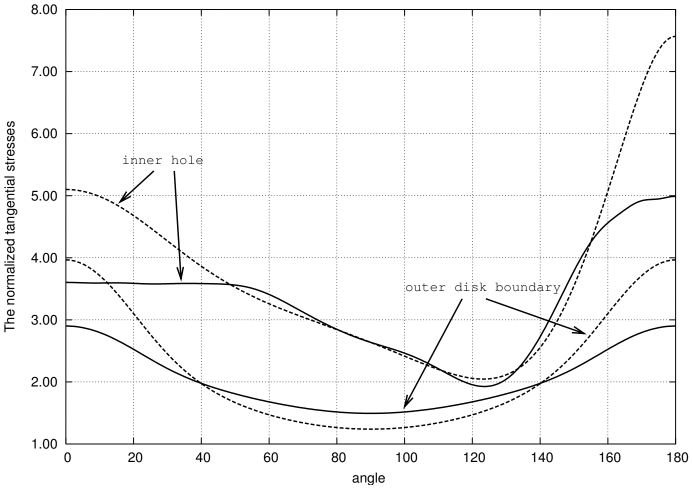

Figure 11. A uniformly compressed disk with two V-optimal holes at $x_0 = 0.05$ and $f_{1,2} = 0.2025$. The resultant tangential stress distributions (solid lines) versus their counterparts for circular holes (dashed lines).

stress distributions are shown in Figure 11. As one might expect, the V-criterion not only smooths the hoop stresses but also drastically reduces them as compared to the standard circular holes. The observed deviations of the V-optimal distributions from the equistress value $\sigma_{\theta\theta} \equiv 2$ measure the influence of the disk's circular boundary.

6. Concluding remarks

A new optimality criterion of smoothing the hoop stresses along holes in a perforated two-dimensional elastic body has been proposed to extend the equistress principle (3-1) for the general case when neither the equi- nor M-equistress shapes exist. For efficient numerical simulations, the criterion was combined with a complex variable-base direct solver and an economical shape encoding scheme as the main ingredients of an evolutionary optimization process, each especially tailored for the problem at hand. Of them, only the stresses variation criterion is really novel. Though related to the local stress distributions, it has an integral form thus offering substantial numerical advantages. Within the proposed simulation approach the V-criterion runs as a powerful filter of spurious oscillations of the hoop stresses thus permitting to effectively smooth and reduce them at moderate computational cost. It is worthy to note again that the V-optimal distribution tends to be piecewise constant what is absolutely a nontrivial solution. The results presented demonstrate the promise of applying it to shape optimization in other fields of continuum mechanics.

References

[Abramowitz and Stegun 1964] M. Abramowitz and I. A. Stegun (editors), *Handbook of mathematical functions with formulas, graphs, and mathematical tables*, National Bureau of Standards Applied Mathematics Series **55**, U.S. Government Printing Office, Washington, DC, 1964.

[Ahlfors 1978] L. V. Ahlfors, *Complex analysis: An introduction to the theory of analytic functions of one complex variable*, 3rd ed., McGraw-Hill, New York, 1978.

[Banichuk 1977] N. V. Banichuk, “Optimality conditions in the problem of seeking the hole shapes in elastic bodies”, *Prik. Matem. Mekhan.* **41**:5 (1977), 920–925. In Russian; translation in *J. Appl. Math. Mech.*, **41**:5, 946–951.

[Cherepanov 1974] G. P. Cherepanov, “Inverse problems of the plane theory of elasticity”, *Prikl. Mat. Mekh.* **38**:6 (1974), 963–979. In Russian; translated in *J. Appl. Math. Mech.* **38**:6 (1974), 915–931.

[Courant 1950] R. Courant, *Dirichlet’s principle, conformal mapping, and minimal surfaces*, Interscience, New York, 1950. Reprinted Dover, New York, 2005.

[Goldberg and Sastry 2010] D. Goldberg and K. Sastry, *Genetic algorithms: the design of innovation*, Springer, New York, 2010.

[Milton 2002] G. W. Milton, *The theory of composites*, Cambridge Monographs on Applied and Computational Mathematics **6**, Cambridge University Press, Cambridge, 2002.

[Muskhelishvili 1963] N. I. Muskhelishvili, *Some basic problems of the mathematical theory of elasticity: fundamental equations, plane theory of elasticity, torsion and bending*, 2nd ed., Noordhoff, Leiden, 1963. Reprinted 1975.

[Natanson 1955] I. P. Natanson, *Theory of functions of a real variable*, Frederick Ungar, New York, 1955.

[Vigdergauz 1976] S. B. Vigdergauz, “Integral equation of the inverse problem of the plane theory of elasticity”, *Prikl. Mat. Mekh.* **40**:3 (1976), 566–569. In Russian; translated in *J. Appl. Math. Mech.* **40**:3 (1976), 518–522.

[Vigdergauz 2006] S. B. Vigdergauz, “Energy-minimizing hole in an elastic plate under remote shear”, *J. Mech. Mater. Struct.* **1**:2 (2006), 387–406.

[Vigdergauz 2008] S. B. Vigdergauz, “Shape optimization in an elastic plate under remote shear: from single to interacting holes”, *J. Mech. Mater. Struct.* **3**:7 (2008), 1341–1363.

[Vigdergauz 2010] S. B. Vigdergauz, “Energy-minimizing openings around a fixed hole in an elastic plate”, *J. Mech. Mater. Struct.* **5**:4 (2010), 661–677.

[Vigdergauz and Cherkaev 1986] S. B. Vigdergauz and A. V. Cherkaev, “A hole in a plate optimal for its biaxial extension-compression”, *Prikl. Mat. Mekh.* **50**:3 (1986), 524–528. In Russian; translated in *J. Appl. Math. Mech.* **50**:3 (1986), 401–404.

[Waldman et al. 2003] W. Waldman, M. Heller, and L. F. Rose, “Shape optimisation of two closely spaced holes for fatigue life extension”, Report DSTO-RR-0253, Defence Science and Technology Organization, Australian Department of Defence, 2003, Available at http://www.dsto.defence.gov.au/publications/2558/.

Received 30 May 2010. Revised 11 Oct 2010. Accepted 13 Oct 2010.

SHMUEL VIGDERGAUZ: `smuel@iec.co.il`
Research and Development Division, The Israel Electric Corp. Ltd., P.O.Box 10, 31000 Haifa, Israel

JOURNAL OF MECHANICS OF MATERIALS AND STRUCTURES
Vol. 5, No. 6, 2010

NUMERICAL SIMULATION OF FAILED ZONE PROPAGATION PROCESS AND ANOMALIES RELATED TO THE RELEASED ENERGY DURING A COMPRESSIVE JOG INTERSECTION

XUE-BIN WANG, JIN MA AND LI-QIANG LIU

A compressive echelon fault structure is modeled using an explicit finite difference code (FLAC). The Weibull distribution is used to reflect the heterogeneity of elemental parameters. The released elastic strain energies due to shear and tensile failures are calculated using FISH functions. We examine the failed zone propagation process and the temporal and spatial distribution of the released strain energy, emphasizing those during the jog intersection.

A specimen including two parallel faults with an overlap is divided into square elements. Rock and faults are considered as nonhomogeneous materials with uncorrelated mechanical parameters (elastic modulus, tensile strength and cohesion). A Mohr–Coulomb criterion with tension cut-off and a post-peak brittle law are used. During the jog intersection, high values of released *tensile* strain energy are found at wing failure zones and at fault tips, while high values of released *shear* strain energy are found at faults. Despite the jog intersection, the released strain energy in the jog is not high.

We also introduce a quantity b_0 describing the slope of the curve connecting the number of failed elements and the energy released. This is similar to the quantity b found in the literature, but is expressed in units of J^{-1}. Before the jog intersection, some anomalies associated with shear sliding of rock blocks along faults can be observed from the number of failed elements (in shear, in tension and in either), the accumulated released strain energy due to shear and tensile failures, the strain energy release rates in shear and in tension, and the value of b_0. As deformation proceeds, the evolution of b_0 is calculated according to two kinds of the released energy: total energy due to shear and tensile failures and shear strain energy. The two exhibit similar behavior, suggesting that the released strain energy in shear is much higher than in tension.

1. Introduction

Echelon fault structures can be observed in a wide range of length scales: they can be some 20 km long in the San Andreas fault [Segall and Pollard 1980], while in mining-induced normal faults observed in South Africa gold mines [Gay and Ortlepp 1979], echelon faults measured in centimeters can be found. The observed echelon cracks are even smaller in rock samples stressed in laboratory [Ewy and Cook 1990; Saimoto et al. 2003]. Seismologic evidence indicates that some earthquakes tend to cluster near echelon faults or in jogs [Segall and Pollard 1980; Sibson 1985]. Geologic evidence indicates that some basins and ranges can be formed in jogs [Aydin and Schultz 1990; Zachariasen and Sieh 1995]. Therefore, considerable attention has been given to the problems of deformation, failure process and stability of echelon fault structures [Bombolakis 1973; Segall and Pollard 1980; Sibson 1985; Ma et al. 1986; Aydin

Keywords: compressive echelon fault structure, jog intersection, failed zone, released strain energy, heterogeneity, shear failure.

and Schultz 1990; Du and Aydin 1991; Harris and Day 1993; Thomas and Pollard 1993; Zachariasen and Sieh 1995; Jiang et al. 2002; Chen et al. 2005; Ma et al. 2007; 2008; 2010].

Echelon fault structures fall into two categories, compressive and extensional, according to the stress state in the jog. For a compressive echelon fault structure, the jog is also called anti-dilatation or compressive, while for an extensional one, the jog is called a dilatation jog. Extensive evidence shows a marked difference between the two kinds, in stress distribution, secondary fracturing and magnitude of earthquakes [Segall and Pollard 1980; Sibson 1985; Aydin and Schultz 1990]. For a compressive echelon fault structure, the elastic interaction between two faults increases both the mean compressive stress between them and the frictional resistance at fault tips, inhibiting slip transfer across the jog. The compressive jog is a "pinned" area where much strain and strain energy can be stored [Segall and Pollard 1980; Sibson 1985; Ma et al. 2007; 2008; 2010]. Such a pinned jog is a potential nucleation site for moderate to large earthquakes. In contrast, in the extensional echelon fault structure, the frictional resistance at fault tips decreases, facilitating sliding [Segall and Pollard 1980; Sibson 1985]. For this reason, the present study is limited to compressive echelon structures.

Laboratory experiments, using transducers to measure displacement, strain, acoustic emissions (AE), and so on, have contributed greatly to ongoing research on faulting and rock failure, and have provided a vast amount of data, including waveforms, AEs and displacements on and around artificial faults [Paterson and Wong 2005]. Even with transducers, however, no accurate results are guaranteed. Narrow faults have been modeled physically by weak materials, such as gypsum mixture and wax paper [Shen et al. 1995]. It is often difficult to make precise direct measurements using transducers on and adjacent to faults. Therefore, energy accumulation and release are not clear in faults. Location errors in AE events may lead to inaccurate results — even that AE sources are located outside the sample boundaries [Lockner et al. 1991; Jiang et al. 2002]. For most experimental systems, insufficient AE data have been provided [Lei et al. 2000]. In addition, in AE tests, the released strain energy in shear and tensile failures cannot be distinguished from the total energy; and the individual sizes of failed zones in shear and in tension cannot be determined.

Stress and secondary fracturing distribution near jogs of two kinds of echelon fault structures were analyzed theoretically in [Segall and Pollard 1980]. A marked difference in behavior between them was found. However, this was a two-dimensional quasistatic study. In quasistatic analyses, some critical elements cannot be included, such as stress waves and time-dependent stress concentrations [Harris and Day 1993]. Therefore, dynamic rupture propagation analyses were advocated by Harris and Day. However, their model is purely elastic, in which the rupture cannot break through into the rock medium surrounding faults.

The studies mentioned mainly focus on the interaction between faults and the distribution of stress and displacement. The following problems are left untouched: the temporal and spatial distribution of the released elastic strain energy during the jog intersection and the corresponding change in macroscopic mechanical behavior, precursors to the jog intersection or the consequent unstable sliding of rock blocks along faults and the relation between the number of events and the released energy.

The principal objective of this paper is to examine these problems numerically by use of FLAC ("Fast Lagrangian Analysis of Continua"), an explicit finite-difference code that can be used to model geologic structures [Strayer and Hudleston 1997; McKinnon and de la Barra 1998; Erickson et al. 2001], rock specimens with imperfections and joints, [Wang 2005; Wang 2007a; Wang 2007b; Wang 2007c; Wang

2008; Wang et al. 2009] and heterogeneous rock specimens [Cundall 1989; Fang and Harrison 2002; Wang and Pan 2008; Wang and Zhang 2009].

2. Introduction of heterogeneity and calculation of released energy

Weibull's theory is known to be useful for tensile fractures. There are still arguments on whether it is also appropriate for fracturing in compression [Paterson and Wong 2005]. For brittle materials, the Weibull distribution function has been used in considering the distribution of microdefects [Tang and Kou 1998; Liu et al. 2004]. Here it is still used to describe the heterogeneity in an elemental parameter:

$$f(u)=\frac{m}{u_0}\Big(\frac{u}{u_0}\Big)^{m-1}\exp\Big(-\Big(\frac{u}{u_0}\Big)^{m}\Big) \tag{1}$$

where u is the elemental parameter, with mean u_0, and m is the shape parameter describing the scatter of u, Higher values of m mean the material is more homogeneous.

FLAC includes a programming language, FISH, which allows the definition of new functions, thus providing great flexibility. In [Wang 2007b; 2008; Wang et al. 2009] we used FISH functions to introduce random material imperfections with the same strength within rock specimens. A similar method is used in the present paper to consider the heterogeneity in an elemental parameter satisfying the statistical distribution above.

If an element undergoes shear or tensile failure, the stored elastic strain energy is given by

$$W=\frac{V}{2E}\left(\sigma_1^2+\sigma_2^2+\sigma_3^2-2\nu(\sigma_1\sigma_2+\sigma_1\sigma_3+\sigma_2\sigma_3)\right), \tag{2}$$

where E is the elastic modulus, σ_1, σ_2 and σ_3 are the principal stresses, ν is the Poisson's ratio and V is the volume of the element.

This equation is applied as follows. Once an element is found to fail in shear, the value given by the formula is the stored shear strain energy, and likewise for an element undergoing tensile failure. Equation (2) is applied once every 10 timesteps. Once the stored shear or tensile strain energy for an element is found to decrease, the change in the energy is remembered for the element. This part of the energy is the released elastic strain energy in shear or in tension. In any 10 timesteps, summing the released elastic strain energy of all elements leads to the elastic strain energy release rate whose units are still J. Then, for the time interval of interest (from a beginning to an ending timestep), we sum the elastic strain energy release rate to obtain the accumulated released elastic strain energy.

We next introduce a quantity we call b_0, which is the negative of the slope of the line relating the log of the number of failed elements and the released energy. Here is how b_0 is calculated. In a given timestep interval, the element releasing the maximum elastic strain energy $E_{\max}$ is found among all elements. We find that the elements releasing higher strain energy are fewer than those releasing lower energy. If all data about energy are used to obtain the relation between the number of failed elements and the released elastic strain energy, then possibly the relation is not monotonic. Therefore, a part of the data may need to be omitted. For this we introduce two factors: the cut-off factor P and the classification factor Q (Figure 1). All data higher than $E_0 = E_{\max} \cdot P$ are discarded. The remaining energy interval, from 0 to E_0, is divided into Q subintervals. The calculation of b_0 is made from the residual data sorted according to subinterval. For each subinterval, the average released average strain energy can be calculated according

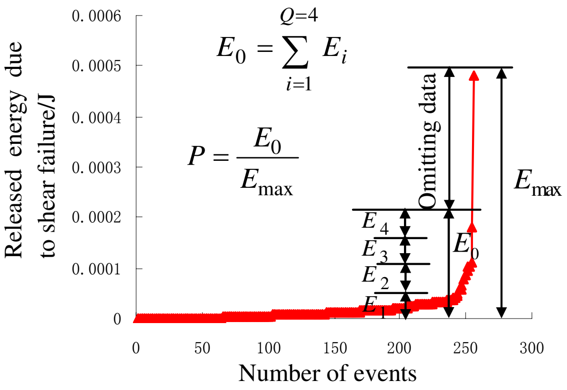

Figure 1. Definitions of the cut-off factor and classification factor.

to the upper and lower limits of the released energy. The number of failed elements in each level and its logarithm need to be determined. For each level, the same operation is executed. Thus, the relation between the logarithm of the number and the average released energy can be determined. Linearly fitting the relation and multiplying the slope by -1 yields b_0, whose units are J^{-1}, different from the common b-value [Lockner et al. 1991; Main et al. 1992; Sammonds et al. 1992; Lei et al. 2000].

3. Numerical model and constitutive parameters

3.1. ***Constitutive models.*** For elements in elastic stage, an isotropic model is used:

$$\Delta\sigma_{ij} = 2G\Delta\epsilon_{ij} + \left(K - \tfrac{2}{3}G\right)\Delta\epsilon_{kk}\delta_{ij} \tag{3}$$

where $\Delta\sigma_{ij}$ is the stress tensor, $\Delta\epsilon_{ij}$ is the strain tensor, G is the shear modulus, K is the bulk modulus and δ_{ij} is the Kronecker sign. G and K are related to two elastic parameters: elastic modulus and Poisson's ratio.

As is known, the Mohr–Coulomb criterion can overestimate the tensile strength of brittle materials. Therefore, a tension cut-off is needed. For the Mohr–Coulomb criterion with tension cut-off, the initial yield function includes two parts: the shear yield function

$$f^s = \sigma_1 - \sigma_3 N_\phi + 2c\sqrt{N_\phi} = 0, \tag{4}$$

depending on the the initial cohesion c and the initial internal friction angle ϕ, via $N_\phi = \dfrac{1+\sin\phi}{1-\sin\phi}$, and the tensile yield function

$$f^t = \sigma_3 - \sigma_t = 0, \tag{5}$$

depending on the initial tensile strength σ_t.

Accordingly, the plastic potential function governing plastic flows is composed of two parts: the shear potential function

$$g^s = \sigma_1 - \sigma_3 N_\psi \tag{6}$$

and the tensile potential function

$$g^t = \sigma_3. \tag{7}$$

In (6), ψ is the dilatation angle; the functional dependence of N_ψ on ψ is the same as that of N_ϕ on ϕ.

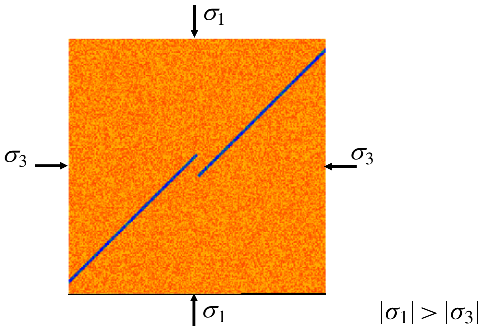

Figure 2. Computational model for the compressive echelon fault structure.

Once an element fails as deformation proceeds, the stress state will not reside on the initial yield surface and will drop to the yield surfaces determined by the present cohesion, internal friction angle and tensile strength. These yield surfaces lie below the initial yield surface. Eventually, as deformation proceeds, the stress state will stop on the residual yield surface controlled by the residual strength parameters.

3.2. ***Computational model and parameters.*** Figure 2 shows the computational model of a specimen whose size is 0.3 m × 0.3 m. The specimen is composed of a rock block and two faults. Two faults form an echelon fault structure, which are oriented at 45° from the horizontal direction. The fault overlap is equal to the distance between two faults, i.e., 1.84×10^{-2} m. The specimen is divided into 300 × 300 elements and faults are composed of 1.493×10^3 elements. Elements in faults are determined through their centroid coordinates by use of a written FISH function for identifying a joint in rock specimens [Wang 2005; 2007a]. The present numerical model represents a plane strain problem and only a small strain mode is permitted.

Two steps of calculation are carried out. In the first step, a hydrostatic pressure of 2 MPa is applied to four specimen boundaries. This step consumes 2×10^4 timesteps. A timestep (or step, computational step) in FLAC is a cycle in which constitutive equations for elements and equations of motion for gridpoints or nodes are executed one time. Large complex problem can require tens of thousands of timesteps to reach a steady state. During computation stepping, information is propagated across the elements in the finite difference grid. After calculating 2×10^4 cycles, the maximum unbalanced force among nodes has been found to be small enough, and the specimen is considered to have reached a static equilibrium state. In FLAC, each gridpoint is surrounded by elements that contribute forces to the gridpoint. At equilibrium, the algebraic sum of these forces is almost zero. When failure and plastic flow are occurring within a model, the unbalanced force of some nodes can be nonzero, among which the maximum value is usually called the maximum unbalanced force that can be displayed in FLAC. It is a good tool for assessing the state of a model, such as equilibrium or plastic flow.

In the second step, a displacement-controlled loading is conducted in the vertical direction (σ_1 direction in Figure 2 in which $\sigma_3 = 2$ MPa) with a small compressive velocity of $v = 1 \times 10^{-9}$ m/timestep. According to the stress state in the jog, the echelon fault structure belongs to a compressive one.

In this paper, three mechanical parameters (elastic modulus, initial cohesion and initial tensile strength) are declared to obey the Weibull distribution, and a value of $m = 9$ is used. The three parameters are *a priori* uncorrelated. This suggests that for an element, if its initial cohesion is higher, then its elastic modulus or initial tensile strength is possibly lower. The point of assigning uncorrelated parameters is to increase the complexity of elemental mechanical parameters with position variation.

The reported values of Poisson's ratio for marble and gypsum are 0.25 and 0.2, respectively [Chen et al. 2005]. These values are used in the isotropic elastic model. The reported values of elastic modulus for marble and gypsum are 55 GPa and 5.1 GPa, respectively [Chen et al. 2005]. These values are adopted as average values in the isotropic elastic model. For rock and fault elements, average values of initial cohesion are assumed to be 37.5 MPa and 5 MPa, respectively; average values of initial tensile strength are 12 MPa and 1.2 MPa, respectively; initial internal friction angles are 50° and 10°, respectively. The dilatation angle is 0° for two kinds of materials.

In fact, for most rock materials, the post-peak behavior exhibits apparent brittle nature at low confining pressures [Wawersik and Fairhurst 1970]. Once elements fail, they are assumed to undergo a linear strain-softening behavior followed by a residual deformation stage. For both kinds of elements, we assume that the residual strength will be reached immediately after failures occur. This means that the plastic strain corresponding to the beginning of the residual deformation stage is extremely low. In the present paper, the values of residual tensile strength and cohesion of rock elements are assumed to be zero. When the plastic strain exceeds 5×10^{-6} (an extremely low value to reflect the brittle nature of rock elements), it is assumed that rock element completely loses its cohesion and tensile strength. For fault elements, the values for residual tensile strength and cohesion are assumed to be zero. When the plastic strain is larger than 5×10^{-7} (0.1 times the value for rock elements), it is assumed that fault elements have completely lost their cohesion and tensile strength. For rock and fault elements, a small residual internal friction angle of 1° is used to model the relative weak fault gouge and to create an obvious response in the macroscopic mechanical behavior (stress-timestep curve) during the jog intersection.

4. Results and discussion

4.1. ***Stress-timestep curve and propagation process of failed zones.*** Figure 3 shows the stress-timestep curve of the specimen including a compressive jog and the relation between the maximum unbalanced force and the timestep. The stress-timestep curve is basically the same as the stress-strain curve. The

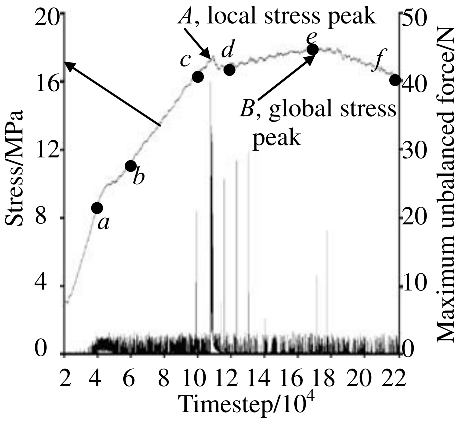

Figure 3. Stress-timestep curve and maximum unbalanced force-timestep curve.

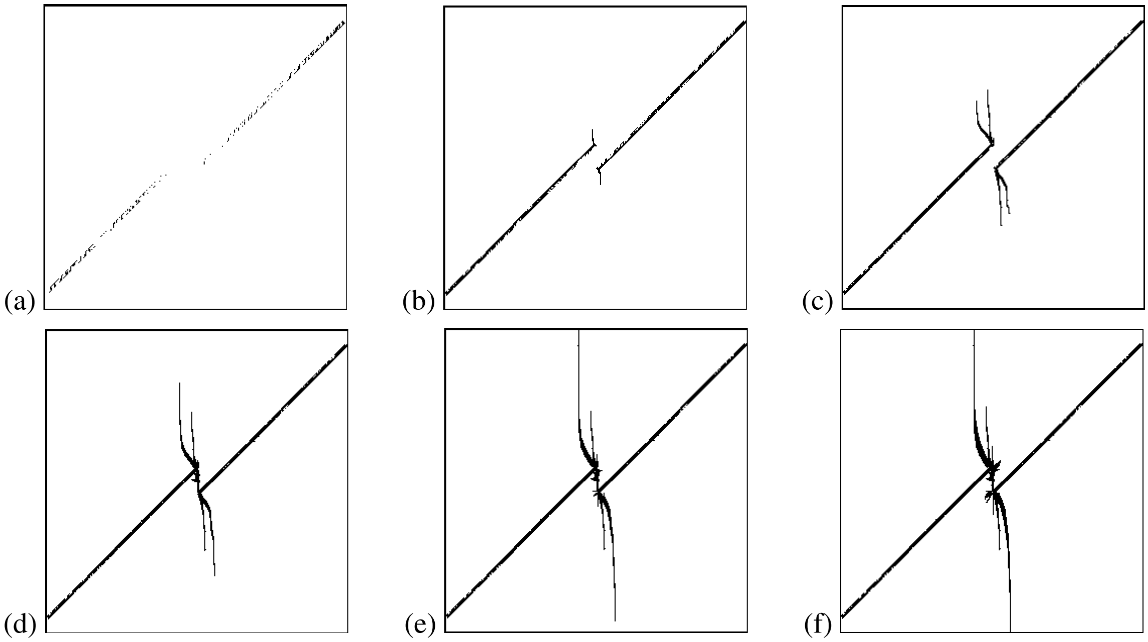

Figure 4. Failure patterns at different timesteps: (a) = 4×10^4, (b) = 6×10^4, (c) = 1×10^5, (d) = 1.2×10^5, (e) = 1.7×10^5, (f) = 2.2×10^5.

formula $\epsilon_a = vt/L$ can be used to convert ϵ_a (axial strain) from t (timestep) and L (height of the specimen). Figure 4 shows the failure process of the echelon fault structure. Black elements are failed elements. The stress-timestep curve can be roughly divided into four stages based on its slope.

Let's consider Figure 4 in light of the stress-timestep graph in Figure 3. Points a–f in the latter correspond to parts (a)–(f) of the former. In the first stage, the stress-timestep graph has a fairly high slope, and is relatively smooth and straight. In this stage, the failed elements are at the faults — see Figure 4(a) — due to the weakness of faults.

In the second stage, the graph becomes less smooth and its slope decreases. At this stage, failed zones extend outwards from the fault tips. In Figure 4(b), there are two failed zones pointing up and down, while in Figure 4(c), the two failed zones become even longer and two wing failure zones also extend outwards from two fault tips. Cracks formed toward the outside of the jog can be observed in tests [Jiang et al. 2002; Chen et al. 2005; Ma et al. 2008], in steeply dipping-mining-induced normal faults in South Africa [Gay and Ortlepp 1979] and in granitic rocks of the Sierra Nevada [Segall and Pollard 1980]. Based on the elastic model, tensile cracks are formed at fault tips and propagate outwards [Segall and Pollard 1980]. The present numerical results agree with these observations and theoretical results.

In the third stage, a local stress peak is formed (point A in Figure 3) and the jog is intersected by elements arranged in a vertical direction. After that, the stress increases slightly in a long timestep interval until a global stress peak is reached (point B in Figure 3). Failed zones outside the jog become even longer. We see in Figure 4(d,e) that the vertical failure zones have stopped, while the wing failure zones continuously extend toward loading ends of the specimen. In Figure 4(e), they have reached the loading ends.

In the fourth stage, the load-carrying capacity of the specimen is slowly decreased and the specimen will collapse. The failure patterns of the specimen do not change; see Figure 4(f).

It is noted that the vertical failure zones outside the jog stop during the propagation of wing failure zones. The reason will be discussed in the next section.

4.2. ***Intersection process of the jog.*** Figure 5 shows the propagation of failed zones in the jog intersection process: black elements have failed in shear or in tension, while the scale of yellows and reds represents the magnitude of tensile strength for an unfailed element (redder or darker = higher tensile strength). Figure 6 shows the corresponding timesteps as points a, b, c, d. Thus, Figure 5(c) corresponds to the local stress peak (point A in Figure 3). Parts (a) and (b) of Figure 5 represent the situation pre-peak, while part (d) is post-peak.

It is found from Figure 5(a) that wing failure zones are more curved near fault tips, which are perpendicular to faults. They tend to grow in the vertical direction with an increase of their length, parallel to the vertical failure zones. These two kinds of failed zones nearly have the same distance from their tips to loading ends. In part (a) of the figure, the jog has not been bisected and the maximum unbalanced force among nodes is low. In part (b), the jog is bisected and tips of wing failure zones have exceeded those of the vertical failure zones. At about 1.0745×10^5 timesteps (Figure 6), the maximum unbalanced

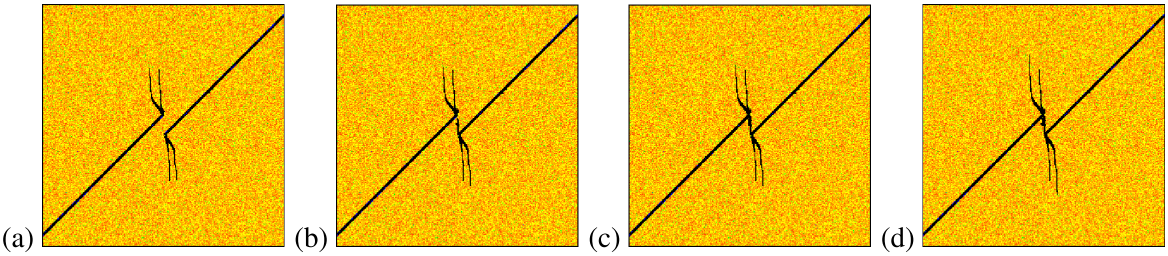

Figure 5. Jog intersection process at different timesteps: (a) = 1.06×10^5, (b) = 1.08×10^5, (c) = 1.09×10^5, (d) = 1.12×10^5.

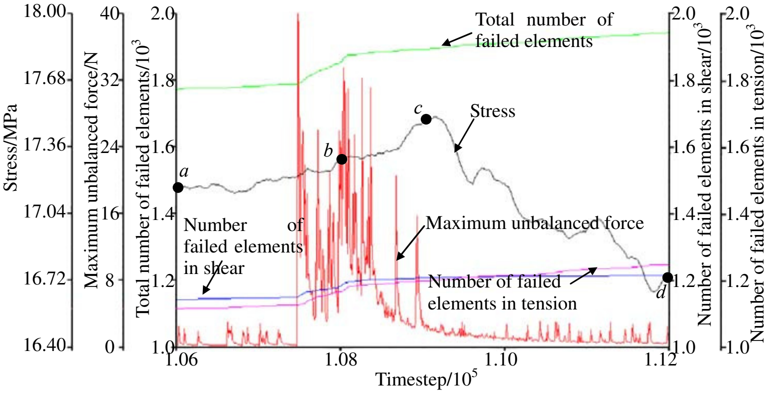

Figure 6. Evolution of stress, maximum unbalanced force, and number of failed elements (in shear, in tension, and in either) during the jog intersection. Note clipped vertical scales. For the horizontal scale, 10^5 timesteps equal axial strains of 3.33×10^{-4}.

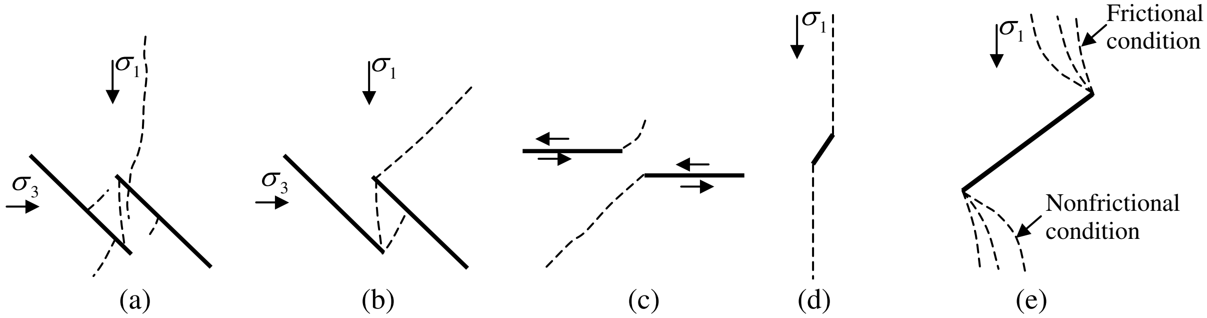

Figure 7. Observed cracks extending outwards and inwards from fault tips (a,c) and some straight and wing cracks (d,e). Part (a) from [Jiang et al. 2002], (b) from [Chen et al. 2005], (c) from [Segall and Pollard 1980], (d) from [Ewy and Cook 1990], (e) from [Shen et al. 1995].

force begins to increase rapidly. This phenomenon ends at about 1.084×10^5 timesteps. During the rapid increase in the maximum unbalanced force, the jog is bisected. In parts (c) and (d) of Figure 5, the wing failure zones become even longer. Beyond timesteps of 1.084×10^5, the maximum unbalanced force exhibits a deceasing tendency. However, there are two major peaks (at 1.09×10^5 and 1.093×10^5 timesteps) in the maximum unbalanced force; beyond the local stress peak, many minor peaks can be observed.

Parts (a)–(c) of Figure 7 show experimental failure modes of compressive echelon fault structures [Jiang et al. 2002; Chen et al. 2005] and field observation [Segall and Pollard 1980]. Two kinds of cracks (dotted lines) can be found: cracks extending outwards, not linking faults, and those linking fault tips. These observed cracks are similar in geometry to those in the present numerical study results. The vertical failure zones outside the jog, which are observed in the present numerical results, are especially similar to splitting cracks from a slip interface in the simplified model of [Ewy and Cook 1990]; see Figure 7(d). Wing fractures originating from a preexisting fracture were also observed in many experiments [Horii and Nemat-Nasser 1985; Shen et al. 1995; Dyskin et al. 1999; Saimoto et al. 2003]. Using a displacement discontinuous method, Shen and Stephansson found that a stiff contact condition (high normal fracture stiffness and high shear fracture stiffness) produces straight wing fractures similar to the present vertical failure zones, while a noncontact condition (zero normal fracture stiffness and zero shear fracture stiffness) leads to curved wing fractures analogous to the present wing failure zones. Both types are shown in Figure 7(e).

It is found from the present numerical results that the vertical failure zones stop when their length reach a critical value. After wing failure zones appear, they extend continuously. This phenomenon may be due to the change in the internal friction angle of the faults beyond failure: when elements in faults just fail, their internal friction angles are high, but when elements in faults enter the residual deformational stage, lower internal frictional angles are expected. Following [Shen et al. 1995], we can say that in the first case the fault is similar to a frictional fracture, resulting in straight failed zones, while in the second case, the behavior of the fault is equivalent to that of a nonfrictional fracture, thus inducing curved wing failure zones.

4.3. ***Temporal and spatial distribution of the released energy in the jog intersection process.*** Figure 8 shows the temporal and spatial distribution of the released elastic strain energy before the jog intersection and beyond. Green color regions denote faults. The radii of black and red circles denote magnitudes of the released shear and tensile strain energy, respectively. The four images at the bottom are close-ups of the four at the top, emphasizing the jog. The markers *a–d* in Figure 6 correspond to (a)–(d) and (aa)–(dd) in Figure 8.

It is found from (a) and (aa) that the released shear strain energy is high at faults, while the released tensile strain energy is high at fault tips. Parts (b) and (bb) reveal that, after the jog intersection, failed zones linking fault tips in the jog liberate both strain energy in shear and in tension. The latter is lower.

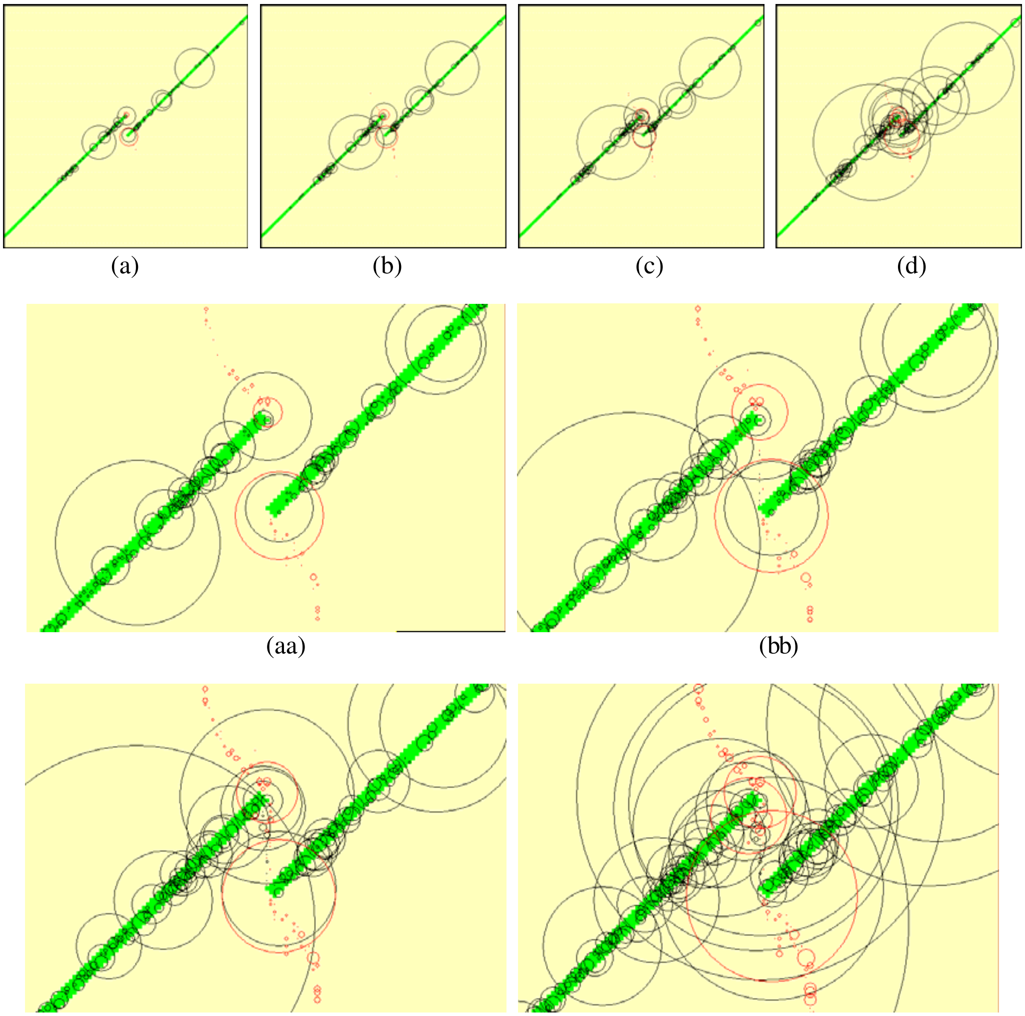
(a) (b) (c) (d)

(aa) (bb)

(cc) (dd)

Figure 8. Spatial and temporal distribution of the liberated energy in the jog intersection process. Timesteps are 1.06×10^5 for (a) and (aa), 1.08×10^5 for (b) and (bb), 1.09×10^5 for (c) and (cc), and 1.12×10^5 for (d) and (dd).

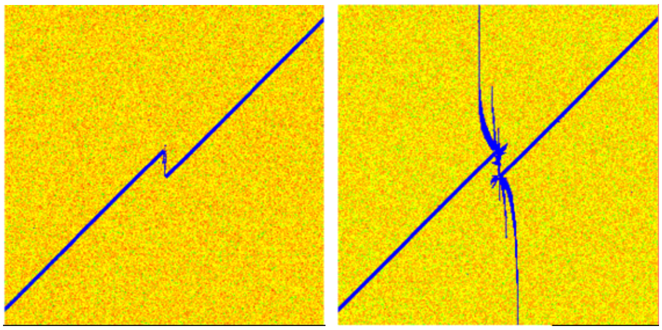

Figure 9. Failed zones in shear (left) and in tension (right).

The remaining images suggest that in the strain-softening stage beyond the local stress peak, many sites in faults release a great deal of elastic strain energy, implying occurrence of many events associated with abrupt shear sliding of rock blocks along faults.

Note that a relatively small amount of strain energy is released in the vertical failure zones in the jog and outside, while a large amount is liberated in wing failure zones and at fault tips. Much strain energy in shear is released at faults, especially at their tips.

4.4. ***Evolution of the number of failed elements.*** Figure 9 shows the location of failed elements (blue) at 2.2×10^5 timesteps. The figure reveals that shear and tension failures occur at faults, also in the vertical failed zone in the jog. Failures in the vertical failure zones outside the jog and in wing failure zones are due to tension. The elastic model predicts that antithetic shear fractures bisect the jog [Segall and Pollard 1980], which is consistent with the present numerical results. However, the jog is subjected to both shear and tensile failures in the present simulation.

In Figure 6 we showed the evolution of the number of failed elements. (Since some elements fail both in shear and in tension, the topmost curve, showing the number of failed elements in either shear or tension, does not equal the sum of the two lowest curves, showing the number of elements failing in each mode.)

To better clarify this evolution, the figure also shows stress and maximum unbalanced force as function of timestep. One sees that before the maximum unbalanced force begins to increase rapidly (at about 1.0745×10^5 timesteps) the numbers of failed elements (in shear, in tension, or in either) increase steadily. During the rapid increase in the maximum unbalanced force, these numbers increase rapidly. These phenomena occur prior to the local stress peak. Beyond the peak, there is little change in the number of failed elements in shear, while the other two numbers continue to increase significantly. The reason for this is the extending wing failure zones where tensile failure propagates continuously beyond the jog intersection.

4.5. ***Evolution of the accumulated released energy and the energy release rate.*** The top graph in Figure 10 shows the evolution of the released energy due to shear failure and the energy release rate in shear (i.e., the released energy due to shear failure per 10 timesteps, whose units are still J). As can be seen from the figure, before the maximum unbalanced force rapidly increases (at about 1.0745×10^5 timesteps), the released energy in shear increases linearly. Afterwards, the released shear strain energy-timestep

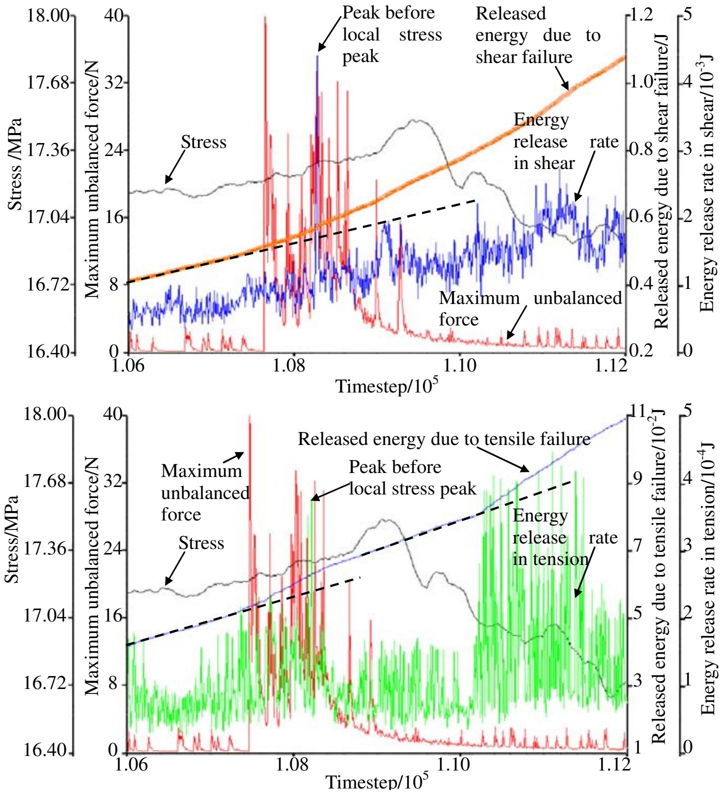

Figure 10. Evolution of the released strain energy and the strain energy release rate with timestep during the jog intersection for the case of shear strain energy (top) and tensile strain energy (bottom).

curve exhibits an apparent change in slope, deviating from the dotted line. (In fact some deviation from linearity occurs even prior to the local stress peak: the curve exhibits a concave-upward behavior.)

The energy release rate in shear is relatively low before the rapid increase in the maximum unbalanced force and the fluctuating amplitude is also low. Next, a peak of the energy release rate is formed. Afterwards, although the energy release rate in shear is lower than the peak, it is higher than before the rapid increase in the maximum unbalanced force. Moreover, the fluctuation is more obvious.

The bottom graph in Figure 10 shows the evolution of the released energy due to tensile failure and the energy release rate in tension. Two apparent slope changes occur in the released energy in tension (the dotted lines show the slope before each change). The first change corresponds to the rapid increase in the maximum unbalanced force, in which a high energy release rate in tension can be observed. This change is caused by a large amount of energy release in tension due to the jog intersection. The second change begins at about 1.102×10^5 timesteps, and is due to extension of wing failure zones. The energy release rate in tension is higher and fluctuates greatly.

4.6. ***Evolution of b_0 using two kinds of energy.*** Eighty timestep intervals, each 500 timesteps long, are taken covering the range from timestep 8.75×10^4 to 1.275×10^5. The value of b_0 for each interval

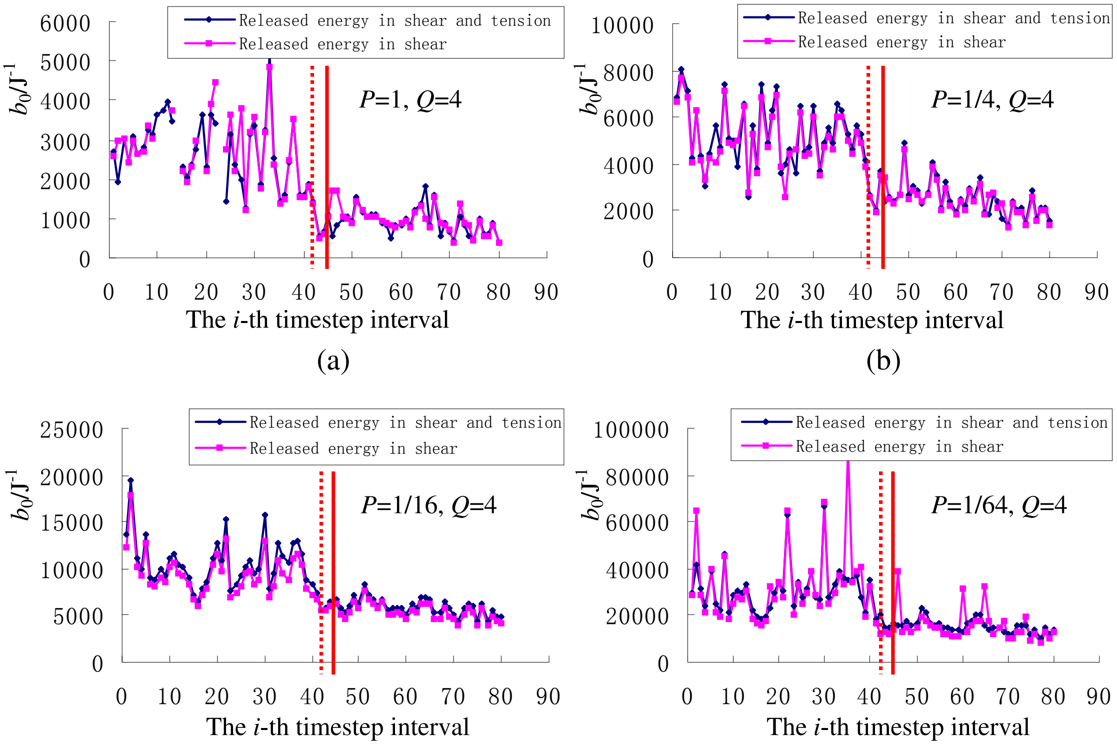

Figure 11. Evolution of b_0 according to the released energy due to shear failure and the released energy due to shear and tensile failures from 87500 to 127500 timesteps at different cut-off factors P. The dotted vertical line denotes the jog intersection and the solid one corresponds to the local stress peak.

is calculated as described on page 1009 and plotted in Figure 11. At the 41st interval (dotted vertical line), the jog is intersected. Local stress peak appears in the 44th interval (solid line). Figure 11 shows the evolution of b_0 according to two kinds of the released energy: energy due to failures and that solely due to tensile failure. These results reveal that b_0 fluctuates at a higher level and then decreases to a lower level. Transition between the two levels can be found at timestep roughly corresponding to the local stress peak. For a low cut-off factor P (omitting many big data), the fluctuation in b_0 is apparent. Experimental results show that the related variable b decreases to a single minimum or double minimum before fault nucleation [Lockner et al. 1991; Lei et al. 2000] and before rapid stress drop [Main et al. 1992; Sammonds et al. 1992]. The present numerical results support these findings. However, the recovery for b_0 from the minimum cannot be observed in Figure 11.

Only a small difference exists in b_0 according to two kinds of energy. This suggests that the released energy due to shear failure is much higher than that due to tensile failure. For the sake of simplicity of calculation, seemingly, the released energy in shear is sufficient in calculating the evolution of b_0. No value for b_0 is calculated in some timestep intervals in Figure 11(a) since big events are greater and small events are fewer, leading to a nonmonotonic relation between the log of the number of failed elements and the released elastic strain energy. Therefore, an appropriate selection of the cut-off factor P is necessary.

5. Conclusions

Two kinds of failed zones initiated from fault tips are observed in the process of the compressive jog intersection. The vertical failed zones outside the jog occur earlier and then stop. The wing failure zones appear later and then extend continuously toward the outside of the jog. The possible reason for this phenomenon stems from the decreasing internal friction angle of faults at post-peak. During the jog intersection, high released tensile strain energy is found at wing failure zones and at fault tips, while high released shear strain energy is at faults. Despite the jog intersection, the released strain energy in the jog is not high. After the jog intersection, a local stress peak is reached and then much shear strain energy is released at faults, indicating that a number of events related to abrupt shear sliding of rock blocks along faults occur.

Before the jog intersection, some anomalies associated with shear sliding of rock blocks along faults can be observed: rapid increases in the numbers of failed elements in shear and in tension, rapid increases in the accumulated strain energy released due to shear and tensile failures, peak values of strain energy release rates in shear and in tension, and b_0-value transition from higher values with higher fluctuating amplitude to lower values with lower fluctuating amplitude. As deformation proceeds, the evolution of b_0 is calculated according to two kinds of energy exhibits similar behavior. This suggests that the released strain energy in shear is much higher than that in tension, facilitating the calculation of b_0 with timestep or exerted strain in the displacement-controlled direction.

Acknowledgements

We are grateful to an anonymous reviewer for his helpful comments and suggestions in improving the manuscript. This work was supported by the National Natural Science Foundation of China (50974069) and the open research fund (LED2010B04) of State Key Laboratory of Earthquake Dynamics, Institute of Geology, China Earthquake Administration.

References

[Aydin and Schultz 1990] A. Aydin and R. A. Schultz, "Effect of mechanical interaction on the development of strike-slip faults with echelon patterns", *J. Struct. Geol.* **12**:1 (1990), 123–129.

[Bombolakis 1973] E. G. Bombolakis, "Study of the brittle fracture process under uniaxial compression", *Tectonophys.* **18**:3–4 (1973), 231–248.

[Chen et al. 2005] J.-D. Chen, S.-P. Ma, S.-J. Liu, and G.-C. Jin, "An experimental study of the failure process of en-echelon fault structure using the digital speckle correlation method", *Chin. J. Geophys.* **48**:6 (2005), 1350–1356. In Chinese.

[Cundall 1989] P. A. Cundall, "Numerical experiments on localization in frictional materials", *Ing. Arch.* **59**:2 (1989), 148–159.

[Du and Aydin 1991] Y. Du and A. Aydin, "Interaction of multiple cracks and formation of echelon crack arrays", *Int. J. Numer. Anal. Methods Geomech.* **15**:3 (1991), 205–218.

[Dyskin et al. 1999] A. V. Dyskin, L. N. Germanovich, and K. B. Ustinov, "A 3-D model of wing crack growth and interaction", *Eng. Fract. Mech.* **63**:1 (1999), 81–110.

[Erickson et al. 2001] S. G. Erickson, L. M. Strayer, and J. Suppe, "Initiation and reactivation of faults during movement over a thrust-fault ramp: numerical mechanical models", *J. Struct. Geol.* **23**:1 (2001), 11–23.

[Ewy and Cook 1990] R. T. Ewy and N. G. W. Cook, "Deformation and fracture around cylindrical openings in rock, II: initiation, growth and interaction of fractures", *Int. J. Rock Mech. Min.* **27**:5 (1990), 409–427.

[Fang and Harrison 2002] Z. Fang and J. P. Harrison, "Development of a local degradation approach to the modelling of brittle fracture in heterogeneous rocks", *Int. J. Rock Mech. Min.* **39**:4 (2002), 443–457.

[Gay and Ortlepp 1979] N. C. Gay and W. D. Ortlepp, "Anatomy of a mining-induced fault zone", *Geol. Soc. Am. Bull.* **90**:1 (1979), 47–58.

[Harris and Day 1993] R. A. Harris and S. M. Day, "Dynamic of fault interaction: parallel strike-slip faults", *J. Geophys. Res.* **98**:B3 (1993), 4461–4472.

[Horii and Nemat-Nasser 1985] H. Horii and S. Nemat-Nasser, "Compression-induced microcrack growth in brittle solids: axial splitting and shear failure", *J. Geophys. Res.* **90**:B4 (1985), 3105–3125.

[Jiang et al. 2002] H.-K. Jiang, S.-L. Ma, L. Zhang, H.-F. Hou, and W.-H. Cao, "Spatio-temporal characteristics of acoustic emission during the deformation of rock samples with compressional and extensional en-echelon fault pattern", *Acta Seismol. Sin.* **4** (2002), 385–396. In Chinese; translated in *Acta. Seismol. Sin.* **15**:4 (2002), 402–413.

[Lei et al. 2000] X. Lei, K. Kusunose, M. V. M. S. Rao, O. Nishizawa, and T. Satoh, "Quasi-static fault growth and cracking in homogeneous brittle rock under triaxial compression using acoustic emission monitoring", *J. Geophys. Res.* **105**:B3 (2000), 6127–6139.

[Liu et al. 2004] H. Y. Liu, S. Q. Kou, P.-A. Lindqvist, and C. A. Tang, "Numerical studies on the failure process and associated microseismicity in rock under triaxial compression", *Tectonophys.* **384**:1–4 (2004), 149–174.

[Lockner et al. 1991] D. A. Lockner, J. D. Byerlee, V. Kuksenko, A. Ponomarev, and A. Sidorin, "Quasi-static fault growth and shear fracture energy in granite", *Nature* **350** (1991), 39–42.

[Ma et al. 1986] J. Ma, Y. Du, and L. Liu, "The instability of en-echelon cracks and its precursors", *J. Phys. Earth* **34** (1986), S141–S157.

[Ma et al. 2007] J. Ma, L.-Q. Liu, P.-X. Liu, and S.-L. Ma, "Thermal precursory pattern of fault unstable sliding: an experimental study of en echelon faults", *Chin. J. Geophys.* **50**:4 (2007), 1141–1149. In Chinese.

[Ma et al. 2008] S. L. Ma, S. Y. Chen, P. X. Liu, X. Y. Hu, K. Y. Wang, and Y. M. Huang, "Effect of fault jogs on frictional behavior: an experimental study", *Sci. Chin. D* **51**:10 (2008), 1436–1445.

[Ma et al. 2010] J. Ma, S. P. Ma, L. Liu, and P. X. Liu, "Experimental study of thermal and strain fields during deformation of en echelon faults and its geological implications", *Geodyn. Tectonophys.* **1**:1 (2010), 24–35.

[Main et al. 1992] I. G. Main, P. G. Meredith, and P. R. Sammonds, "Temporal variations in seismic event rate and *b*-values from stress corrosion constitutive laws", *Tectonophys.* **211**:1–4 (1992), 233–246.

[McKinnon and de la Barra 1998] S. D. McKinnon and I. G. de la Barra, "Fracture initiation, growth and effect on stress field: a numerical investigation", *J. Struct. Geol.* **20**:12 (1998), 1673–1689.

[Paterson and Wong 2005] M. S. Paterson and T.-F. Wong, *Experimental rock deformation: the brittle field*, 2nd ed., Springer, Berlin, 2005.

[Saimoto et al. 2003] A. Saimoto, Y. Imai, and T. Hashida, "The genesis of echelon-mode-I cracks in the neighbourhood of a mode-II-crack tip under uniaxial compression", *Key Eng. Mater.* **251–252** (2003), 327–332.

[Sammonds et al. 1992] P. R. Sammonds, P. G. Meredith, and I. G. Main, "Role of pore fluids in the generation of seismic precursors to shear fracture", *Nature* **359** (1992), 228–230.

[Segall and Pollard 1980] P. Segall and D. D. Pollard, "Mechanics of discontinuous faults", *J. Geophys. Res.* **85**:B8 (1980), 4337–4350.

[Shen et al. 1995] B. Shen, O. Stephansson, H. H. Einstein, and B. Ghahreman, "Coalescence of fractures under shear stresses in experiments", *J. Geophys. Res.* **100**:B4 (1995), 5975–5990.

[Sibson 1985] R. H. Sibson, "Stopping of earthquake ruptures at dilational fault jogs", *Nature* **316** (1985), 248–251.

[Strayer and Hudleston 1997] L. M. Strayer and P. J. Hudleston, "Numerical modeling of fold initiation at thrust ramps", *J. Struct. Geol.* **19**:3–4 (1997), 551–566.

[Tang and Kou 1998] C. A. Tang and S. Q. Kou, "Crack propagation and coalescence in brittle materials under compression", *Eng. Fract. Mech.* **61**:3–4 (1998), 311–324.

[Thomas and Pollard 1993] A. L. Thomas and D. D. Pollard, "The geometry of echelon fractures in rock: implications from laboratory and numerical experiments", *J. Struct. Geol.* **15**:3–5 (1993), 323–334.

[Wang 2005] X. B. Wang, "Joint inclination effect on strength, stress-strain curve and strain localization of rock in plane strain compression", *Mater. Sci. Forum* **495–497** (2005), 69–76.

[Wang 2007a] X. B. Wang, "Effects of joint width on strength, stress-strain curve and strain localization of rock mass in uniaxial plane strain compression", *Key Eng. Mater.* **353–358** (2007), 1129–1132.

[Wang 2007b] X. B. Wang, "Failure process and stress-strain curve of plane strain rock specimen with initially random material imperfections", *Key Eng. Mater.* **353–358** (2007), 1133–1136.

[Wang 2007c] X. B. Wang, "Prediction of height effect, plastic deformation and fracture energy for high-strength concrete by linear shear softening constitutive relation based on energy conservation method", *Mag. Concr. Res.* **59**:5 (2007), 341–350.

[Wang 2008] X.-B. Wang, "Influence of imperfection number on acoustic emissions and elastic strain energy decrease of rock specimens with initially random imperfections", *Chin. J. Nonferr. Met.* **18**:8 (2008), 1541–1549. In Chinese.

[Wang and Pan 2008] X.-B. Wang and Y.-S. Pan, "Preliminary failure process modeling of strain-softening rocks with heterogeneity and stiffness deterioration", pp. 767–771 in *Proceedings of the 3rd International Symposium on Modern Mining and Safety Technology* (Fuxin, 2008), Coal Industry Publishing House, Beijing, 2008.

[Wang and Zhang 2009] X.-B. Wang and J. Zhang, "Numerical simulation of failure process of three-point bending concrete beam considering heterogeneity of tensile strength and post-peak softening curve", *Eng. Mech.* **26**:12 (2009), 155–160. In Chinese.

[Wang et al. 2009] X.-B. Wang, D. Wu, F.-C. Zhao, and Y.-S. Pan, "Simulation of failure processes, precursors and overall deformation of rock specimens with different numbers of initially random imperfections", *Prog. Geophys.* **24**:5 (2009), 1874–1881. In Chinese.

[Wawersik and Fairhurst 1970] W. R. Wawersik and C. Fairhurst, "A study of brittle rock fracture in laboratory compression experiments", *Int. J. Rock Mech. Min.* **7**:5 (1970), 561–575.

[Zachariasen and Sieh 1995] J. Zachariasen and K. Sieh, "The transfer of slip between two en echelon strike-slip faults: a case study from the 1992 Landers earthquake, southern California", *J. Geophys. Res.* **100**:B8 (1995), 15281–15301.

Received 22 Jul 2010. Revised 13 Oct 2010. Accepted 14 Oct 2010.

XUE-BIN WANG: `wxbbb@263.net`
State Key Laboratory of Earthquake Dynamics, Institute of Geology, China Earthquake Administration, Beijing, 100029, China

and

College of Mechanics and Engineering, Liaoning Technical University, Fuxin, 123000, China

JIN MA: `majin@ies.ac.cn`
State Key Laboratory of Earthquake Dynamics, Institute of Geology, China Earthquake Administration, Beijing, 100029, China

LI-QIANG LIU: `liulq-sohu@sohu.com`
State Key Laboratory of Earthquake Dynamics, Institute of Geology, China Earthquake Administration, Beijing, 100029, China

JOURNAL OF MECHANICS OF MATERIALS AND STRUCTURES
Vol. 5, No. 6, 2010

REVISITING THE HULT–MCCLINTOCK CLOSED-FORM SOLUTION FOR MODE III CRACKS

ZHI-JIAN YI

The well-known closed-form solution given by Hult and McClintock for an antiplane crack in an elastic-perfectly plastic material is reconsidered using the crack line analysis method. A precise elastic-plastic solution near the crack line region, different from Hult and McClintock's, is deduced by matching the general solution of the plastic field with that of the exact elastic field. It is verified from the deduction that the Hult–McClintock elastic-plastic solution is inadequate for many purposes.

Introduction

The Hult–McClintock closed-form solution [1957] for an antiplane crack in an elastic-perfectly plastic material was a significant achievement in the development of fracture mechanics. Its importance lies not only in being the first closed-from elastic-plastic solution in fracture mechanics, but also in that the two usual assumptions of small-scale yielding originate from it: (1) the plastic zone ahead of the crack tip is so small that the elastic field out of the plastic zone is the K-dominant elastic singular field for the crack; and (2) the crack tip of the K-dominant elastic singular field effectively behaves as if it lies a distance x_e ahead of the actual crack tip, along the crack line, giving rise to the notion of an "imaginary crack" (see Figure 1). These assumptions were preserved in many subsequent works on the problem, such as [Koshinen 1963; Rice 1966; 1967; Edmunds and Willis 1976; Hutchinson 1979].

Because of the authority of the Hult–McClintock elastic-plastic solution, its limitations have largely gone unaddressed. These shortcomings are difficult to verify directly by conventional crack tip asymptotic

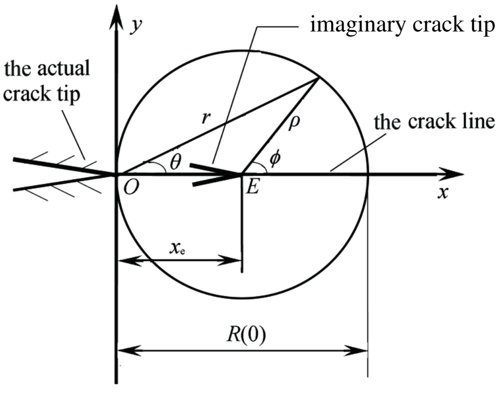

Figure 1. The crack-tip plastic zone [Hult and McClintock 1957].

Keywords: crack, crack line, elastic-plastic solution, Hult–McClintock solution.
Supported by the National Natural Science Foundation of China (Fund No. 10672196).

analysis under small-scale yielding. However, if the crack line analysis method is used, the method's inadequacy becomes apparent, and already in [Yi 1993; 1994] we were compelled to find more reasonable solutions. In this paper we continue these investigations by deducing an elastic-plastic solution near the crack line region, different from Hult and McClintock's. We do this by matching the general solution of the plastic field to that of the exact elastic field, to discuss the validity of the Hult–McClintock solution.

1. Review of the Hult–McClintock solution

General assumptions. For an antiplane crack in an elastic-perfectly plastic solid, the displacement w and stress components τ_{xz} and τ_{yz} are assumed to depend only on x and y. The crack tip region is shown in Figure 1. The equilibrium equation is

$$\frac{\partial \tau_{xz}}{\partial x}+\frac{\partial \tau_{yz}}{\partial y}=0 \tag{1}$$

and the Huber–von Mises yield criterion is

$$\tau_{xz}^2+\tau_{yz}^2=k^2, \tag{2}$$

where k is the yield stress in pure shear. The strain is given by $\gamma_{xz}=\dfrac{\partial w}{\partial x}$ and $\gamma_{yz}=\dfrac{\partial w}{\partial y}$. For a stationary crack, the Hencky deformation constitutive relations are

$$\frac{\partial w}{\partial x}=\frac{1}{G}\tau_{xz}+\lambda\tau_{xz}, \qquad \frac{\partial w}{\partial y}=\frac{1}{G}\tau_{yz}+\lambda\tau_{yz}, \tag{3}$$

where G is the elastic shear modulus and λ a nonnegative factor.

Statement of the Hult–McClintock solution. In an (r,θ) polar coordinate system, Hult and McClintock suggested that the stresses in the plastic zone are

$$\tau_{xz}=-k\sin\theta, \qquad \tau_{yz}=k\cos\theta. \tag{4}$$

They then obtained the displacement in the plastic zone, the strains in the plastic zone, and the elastic-plastic boundary by matching the plastic stress field (4) and its corresponding displacement field for the actual crack with the usual crack tip K-dominant elastic singular field of an "imaginary crack" (see Figure 1) at the elastic-plastic boundary. The Hult–McClintock solutions are

$$w=\frac{K_{\mathrm{III}}^2}{G\pi k}\sin\theta, \quad \gamma_{xz}=-\frac{K_{\mathrm{III}}^2}{G\pi k}\frac{\sin\theta\cos\theta}{r}, \quad \gamma_{yz}=\frac{K_{\mathrm{III}}^2}{G\pi k}\frac{\cos^2\theta}{r}, \quad R(\theta)=\frac{1}{\pi}\Bigl(\frac{K_{\mathrm{III}}}{k}\Bigr)^2\cos\theta, \tag{5}$$

where K_{III} is the stress intensity factor. The strain $(5)_{2,3}$ in the plastic zone has a $1/r$ singularity.

According to $(5)_4$, the plastic zone is a circle tangent to the actual crack tip, having diameter $d=R(0)=K_{\mathrm{III}}^2/(\pi k^2)$. The imaginary crack tip of the K-dominant elastic singular field lies at the center of the plastic zone, at a distance $x_e=d/2$ ahead of the actual tip.

Beyond the Hult–McClintock plastic field. Solutions satisfying the equilibrium equations (1) and the Huber–von Mises yield criterion (2) are countless: the Hult–McClintock plastic stress field (4) is just a particular solution, not a general one. What are its limitations? A fruitful approach to this question is to use the crack line analysis method and expansion in power series of θ, reducing the solution of the partial differential equations to that of ordinary differential equations, through which a description of the general solution for the plastic field near the crack line region can be obtained.

The crack line analysis method only focuses on the field near the crack line. The method has been used for an antiplane crack before [Achenbach and Li 1984; Guo and Li 1987; Yi 1992]. The elastic-plastic solutions obtained in those references are the same as those given by Hult and McClintock near the crack line, but any such solution is still inadequate and is still confined by the small-scale yielding assumptions.

The crack line analysis method was improved in [Yi 1993; 1994; Yi et al. 1996; 1997; Yi and Yan 2001], and has been used to solve other crack problems [Wu and Wang 1996; Wang and Zhang 1998; Wang and Wu 2003; Wang and Zhou 2004; Zhou and Wang 2005; Zhou and Ling 2006]. The method also applies well to linear elastic fracture mechanics and has been developed into an effective way of solving the stress intensity factors of cracks [Yi 1991; 1992; Wang 1996; 2002]. The significance of the improved crack line method is that the general solution in power series of the plastic field near the crack line can be obtained exactly. By matching the general power series form solution of the plastic field with the precise elastic field outside the plastic zone, the assumptions of the usual small-scale yielding condition can be completely given up. Thus, a more reasonable elastic-plastic solution can be obtained.

2. Introduction to the crack line analysis method: General power series solution for the plastic field near the crack line

To proceed, consider the region near the crack line, shown in Figure 2 and corresponding to $\theta = 0$. The stress components and the displacement are continuous across the crack line. So in the plastic zone near the crack line region, τ_{xz}, τ_{yz}, and w can be expressed in polar coordinates as power series up to second order in θ as

$$\begin{aligned} \tau_{xz} &= \tau_1(r)\theta + O(\theta^3), & w &= w_1(r)\theta + O(\theta^3), \\ \tau_{yz} &= \tau_0(r) + \tau_2(r)\theta^2 + O(\theta^4), & \lambda &= \lambda_0(r) + \lambda_2(r)\theta^2 + O(\theta^4), \end{aligned} \tag{6}$$

where λ is the nonnegative factor in (3). Here we have taken into account that τ_{xz} and w are antisymmetric, while τ_{yz} and λ are symmetric with respect to $\theta = 0$. (In [Guo and Li 1987; Yi 1992] the corresponding expressions in rectangular coordinates are considered.)

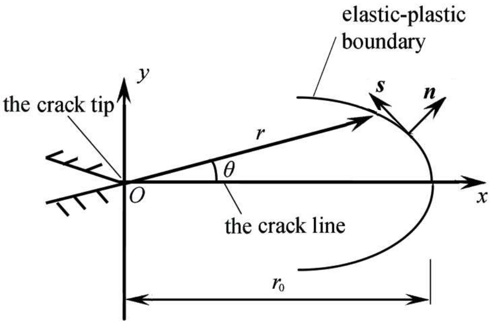

Figure 2. The region near the crack line.

Substituting (6) into (1)–(3) by using the relationships $r^2 = x^2 + y^2$ and $\theta = \arctan \frac{y}{x}$ and collecting terms of the same order θ yields

$$\begin{gathered}\frac{d\tau_1}{dr} + \frac{d\tau_0}{dr} - \frac{\tau_1}{r} + \frac{2\tau_2}{r} = 0, \qquad \tau_0^2 = k^2, \qquad \tau_1^2 + 2\tau_0\tau_2 = 0, \\ \frac{dw_1}{dr} - \frac{w_1}{r} = \Big(\frac{1}{G} + \lambda_0\Big)\tau_1, \qquad \frac{w_1}{r} = \Big(\frac{1}{G} + \lambda_0\Big)\tau_0.\end{gathered} \tag{7}$$

Thus the system of partial differential equations (1)–(3) has been transformed into a system of ordinary differential equations. We can solve the equations (7) to obtain *in closed form* the coefficients τ_0, τ_1, τ_2, and w_1 appearing in (6). We find

$$\tau_0 = k, \quad \tau_1 = -\frac{kr}{r+L}, \quad \tau_2 = -\frac{kr^2}{2(r+L)^2}, \quad w_1 = \frac{Cr}{r+L}, \tag{8}$$

where L and C are constants of integration. Thus we have

$$\tau_{xz} = -\frac{kr}{r+L}\theta + O(\theta^3), \quad \tau_{yz} = k - \frac{kr^2}{2(r+L)^2}\theta^2 + O(\theta^4), \quad w = \frac{Cr}{r+L}\theta + O(\theta^3). \tag{9}$$

When converted to rectangular coordinates, the solutions (9) are the same as those given in [Yi 1994].

The strains corresponding to (9) are

$$\gamma_{xz} = -\frac{Cr}{(r+L)^2}\theta + O(\theta^3), \quad \gamma_{yz} = \frac{C}{r+L} + O(\theta^2), \tag{10}$$

which have no singularities as $r \to 0$ if $L > 0$.

Remark. Although the preceding discussion only considered terms up to θ^2, it can be extended to a higher-order analysis using the same idea. Suppose, for example, that we wish to go up to θ^4, writing

$$\begin{aligned}\tau_{xz} &= \tau_1(r)\theta + \tau_3(r)\theta^3 + O(\theta^5), \\ \tau_{yz} &= \tau_0(r) + \tau_2(r)\theta^2 + \tau_4(r)\theta^4 + O(\theta^6).\end{aligned} \tag{11}$$

Substituting these equalities into (1) and (2) and collecting terms of the same order in θ yields two new equations besides the ones appearing on the first line of (7):

$$-\frac{1}{6}\frac{d\tau_0}{dr} - \frac{1}{2}\frac{d\tau_1}{dr} + \frac{1}{6}\frac{\tau_1}{r} + \frac{d\tau_2}{dr} - \frac{\tau_2}{r} + \frac{d\tau_3}{dr} - 3\frac{\tau_3}{r} + 4\frac{\tau_4}{r} = 0, \quad 2\tau_1\tau_3 + \tau_2^2 + 2\tau_0\tau_4 = 0.$$

The number of equations and unknowns has increased from three to five, but we can still use the same method to solve the system of five equations, obtaining, besides the first three equations in (8), the expressions

$$\begin{aligned}\tau_3 &= \frac{k}{6}\frac{r}{r+L} - \frac{k}{2}\Big(\frac{r}{r+L}\Big)^2 + \Big(\frac{k}{2} + \frac{D}{r+L}\Big)\Big(\frac{r}{r+L}\Big)^3, \\ \tau_4 &= \frac{k}{6}\Big(\frac{r}{r+L}\Big)^2 - \frac{k}{2}\Big(\frac{r}{r+L}\Big)^3 + \Big(\frac{3k}{8} + \frac{D}{r+L}\Big)\Big(\frac{r}{r+L}\Big)^4,\end{aligned}$$

which are then plugged into (11) to give explicit expressions for the stress components to order four. The displacement is handled similarly.

Further, the elastic-plastic boundary is assumed to be continuous across the crack line and to have equation $r = r_p(\theta)$ (Figure 2). Again by symmetry, the function r_p is even, and we have, to second order,

$$r_p(\theta) = r_0 + r_2\theta^2 + O(\theta^4), \tag{12}$$

where r_0 is the length of the plastic zone along the crack line [Yi 1994]. The values of r_0 and r_2 can be determined by matching the plastic field with the elastic field at the elastic-plastic boundary.

It follows from (12) that the unit normal vector $\boldsymbol{n} = (n_x, n_y)$ of the elastic-plastic boundary is

$$n_x = 1 - \tfrac{1}{2}B_1^2\theta^2 + O(\theta^4), \quad n_y = B_1\theta + (\theta^3), \qquad \text{where } B_1 = 1 - 2\frac{r_2}{r_0}. \tag{13}$$

Returning to the analysis to second order, the idea now is to match (9) and (10) with a sufficiently precise elastic field near the crack line. Before doing this, we recall the derivation of the Hult–McClintock equations in the context of our analysis, to understand its limitations and set the scenario for our solution.

3. Further discussion of the Hult–McClintock matching result

Rederivation of the Hult–McClintock elastic-plastic boundary. In polar coordinates (ρ, ϕ) centered at the point $x = x_e$, $y = 0$ (the "imaginary crack tip"), let the elastic-plastic boundary be written as

$$\rho_p(\phi) = \rho_0 + \rho_2\phi^2 + O(\phi^4), \tag{14}$$

(see Figure 3). The unit normal vector $\boldsymbol{n} = (n_x, n_y)$ of the boundary is then

$$n_x = 1 - \tfrac{1}{2}\beta_1^2\phi^2 + O(\phi^4), \quad n_y = \beta_1\phi + O(\phi^3), \qquad \text{where } \beta_1 = 1 - 2\frac{\rho_2}{\rho_0} \tag{15}$$

(compare (13)), and the equations relating the two polar coordinate systems are

$$\theta = \arctan\frac{\rho\sin\phi}{x_e + \rho\cos\phi}, \qquad r^2 = x_e^2 + \rho^2 - 2\rho x_e\cos(\pi - \phi). \tag{16}$$

In the Hult–McClintock solution, the usual K-dominant elastic stress field for the imaginary crack in polar coordinates (ρ, ϕ) (see Figure 1 or Figure 3) is

$$\tau_{xz} = -\frac{K_{\mathrm{III}}}{\sqrt{2\pi\rho}}\sin\frac{\phi}{2}, \qquad \tau_{yz} = \frac{K_{\mathrm{III}}}{\sqrt{2\pi\rho}}\cos\frac{\phi}{2}, \tag{17}$$

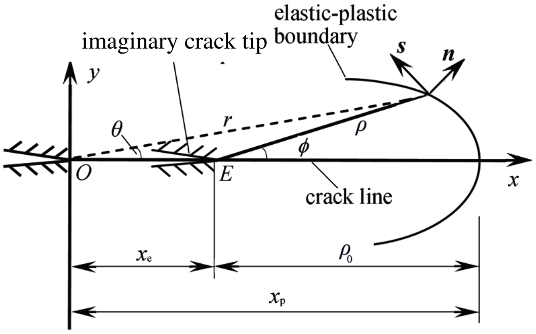

Figure 3. The region near the crack according to [Hult and McClintock 1957].

where the second assumption of small scale yielding is adopted.

Expanding (17) to second order gives

$$\tau_{xz}=-\frac{1}{2}\frac{K_{\mathrm{III}}}{\sqrt{2\pi\rho}}\phi+O(\phi^3),\quad \tau_{yz}=\frac{K_{\mathrm{III}}}{\sqrt{2\pi\rho}}\Big(1-\tfrac{1}{8}\phi^2\Big)+O(\phi^4). \tag{18}$$

The corresponding displacement is

$$w=\sqrt{\frac{\rho}{2\pi}}\cdot\frac{K_{\mathrm{III}}}{G}\phi+O(\phi^3). \tag{19}$$

Substituting (14) into (18) and (19), we get for the elastic stresses and displacement at the elastic-plastic boundary the expressions

$$\tau^e_{xz}=-\frac{1}{2}\frac{K_{\mathrm{III}}}{\sqrt{2\pi\rho_0}}\phi+O(\phi^3),\quad \tau^e_{yz}=\frac{K_{\mathrm{III}}}{\sqrt{2\pi\rho_0}}\bigg(1-\Big(\frac{1}{2}\frac{\rho_2}{\rho_0}+\frac{1}{8}\Big)\phi^2\bigg)+O(\phi^4), \tag{20}$$

$$w=\sqrt{\frac{\rho_0}{2\pi}}\cdot\frac{K_{\mathrm{III}}}{G}\phi+O(\phi^3). \tag{21}$$

The Hult–McClintock plastic stresses (4) have the expansion

$$\tau_{xz}=-k\theta+O(\theta^3),\quad \tau_{yz}=k-\tfrac{1}{2}k\theta^2+O(\theta^4). \tag{22}$$

The expansion of the Hult–McClintock displacement in the plastic zone is

$$w=C\theta+O(\theta^3), \tag{23}$$

where C is a constant, and the expansion of the strain is

$$\gamma_{xz}=-\frac{C}{r}\theta+O(\theta^3),\quad \gamma_{yz}=\frac{C}{r}+O(\theta^2), \tag{24}$$

Combining (14) with (22), (23) and (16), we obtain the plastic stresses and displacement of the real crack at the elastic-plastic boundary:

$$\tau^p_{xz}=-k\frac{\rho_0}{x_e+\rho_0}\phi+O(\phi^3),\quad \tau^p_{yz}=k-\frac{k}{2}\Big(\frac{\rho_0}{x_e+\rho_0}\Big)^2\phi^2+O(\phi^4), \tag{25}$$

$$w^p=C\frac{\rho_0}{x_e+\rho_0}\phi+O(\phi^3). \tag{26}$$

Now the plastic stresses (25) are made to match the crack tip K-dominant elastic stresses (20) at the elastic-plastic boundary (14), and likewise for the displacements (26) and (21). In the normal local coordinate frame $(\boldsymbol{n},\boldsymbol{s})$ along the elastic-plastic boundary (see Figure 1), let σ_{nz} and σ_{sz} denote the stress components, so

$$\sigma_{nz}=\tau_{xz}n_x+\tau_{yz}n_y,\quad \sigma_{sz}=\tau_{xz}n_y-\tau_{yz}n_x. \tag{27}$$

Then the matching conditions for the stresses are

$$\sigma^e_{nz}=\sigma^p_{nz},\quad \sigma^e_{sz}=\sigma^p_{sz}\qquad \text{along the elastic-plastic boundary.} \tag{28}$$

where superscript e and p represent the elastic and plastic sides of the boundary. The right-hand sides of $(28)_{1,2}$ can be obtained by substituting (25) and (15) into (27), and the left-hand sides by substituting (20) and (15) into (27). In this way we obtain three matching equations:

$$\frac{K_{\mathrm{III}}}{\sqrt{2\pi\rho_0}}=k,\quad \frac{1}{2}\frac{K_{\mathrm{III}}}{\sqrt{2\pi\rho_0}}=k\frac{\rho_0}{x_e+\rho_0},\quad \frac{K_{\mathrm{III}}}{\sqrt{2\pi\rho_0}}\Big(\frac{1}{2}\frac{\rho_2}{\rho_0}+\frac{1}{8}\Big)=\frac{1}{2}k\Big(\frac{\rho_0}{x_e+\rho_0}\Big)^2. \tag{29}$$

Solving the system (29) yields

$$\rho_0=\frac{K_{\mathrm{III}}^2}{2\pi k^2},\quad \rho_2=0,\quad x_e=\frac{K_{\mathrm{III}}^2}{2\pi k^2}. \tag{30}$$

Thus $\rho_0=x_e$, expressing that the imaginary crack tip moves to the center of the plastic zone along the crack line. The length of the plastic zone is $x_p=x_e+\rho_0=K_{\mathrm{III}}^2/(\pi k^2)$, in agreement with the case $\theta=0$ of $(5)_4$. The result $\rho_2=0$ in $(30)_2$ agrees with Hult–McClintock's elastic-plastic solution, in which the elastic-plastic boundary is a circle. Similarly, the constant C in (23) and (24) can be obtained by comparing (21) with (26) and using (29):

$$C=\frac{k}{G}(\rho_0+x_e), \tag{31}$$

leading to the following expression for the strain (24) in the plastic zone:

$$\gamma_{xz}=-\frac{k}{G}\frac{\rho_0+x_e}{r}\theta+O(\theta^3),\quad \gamma_{yz}=\frac{k}{G}\frac{\rho_0+x_e}{r}+O(\theta^2); \tag{32}$$

this again agrees with the Hult–McClintock solution in $(5)_{2,3}$.

It follows that, to second order in θ, the Hult–McClintock elastic-plastic solution is a necessary consequence of the underlying assumptions.

Critique of the assumptions underlying the Hult–McClintock elastic-plastic solution. Nevertheless, we must inquire whether the assumptions are reasonable. If the plastic zone is small enough, the first assumption — that the dominant elastic field matches the plastic field at the elastic-plastic boundary — is acceptable. However, the second assumption, concerning the "imaginary crack tip", is questionable on several grounds. First, it has no clear physical meaning. Second, it is arbitrary; it is introduced essentially in order to gain one free parameter, the distance x_e. Finally, according to the Hult–McClintock elastic-plastic solution, the strain in the plastic zone, given by (32) or (24), has a singularity. Such a result is incorrect even under small-scale yielding, as will be explained later.

In the alternative formulation we started to develop in Section 2, there is no singularity in the corresponding expression for the strain, (10), unless the parameter L is taken equal to 0 (which corresponds to the Hult–McClintock situation).

4. Abandoning the second assumption

We saw in Section 2 that the three matching equations in (29) involve three constants, ρ_0, ρ_2 and x_e. If we let $x_e=0$, thus giving up the second assumption of small scale yielding (under which condition the coordinates (ρ,ϕ) coincide with (r,θ)), a conflict inevitably occurs in that the three independent matching equations (29) involve only two unknowns ρ_0 and ρ_2. But if the general solution (9) is used in the matching, the constant L can replace the artificial x_e in providing the additional degree of freedom necessary for a natural match at the actual elastic-plastic boundary. Thus, the second assumption of small-scale yielding becomes unnecessary, and a more natural matching solution can be obtained even under small-scale yielding.

The crack tip K-dominant elastic singular field for the actual crack (see Figure 2) is

$$\tau_{xz} = -\frac{K_{\text{III}}}{\sqrt{2\pi r}} \sin\frac{\theta}{2}, \quad \tau_{yz} = \frac{K_{\text{III}}}{\sqrt{2\pi r}} \cos\frac{\theta}{2}, \tag{33}$$

(compare (17)). The power series expansion of (33) to second order is

$$\tau_{xz} = -\frac{1}{2}\frac{K_{\text{III}}}{\sqrt{2\pi r}}\theta + O(\theta^3), \quad \tau_{yz} = \frac{K_{\text{III}}}{\sqrt{2\pi r}}\Big(1 - \frac{1}{8}\theta^2\Big) + O(\theta^4) \tag{34}$$

(compare with (18), which expresses the same relationship but for the imaginary crack tip). The corresponding displacement is

$$w = \sqrt{\frac{r}{2\pi}} \cdot \frac{K_{\text{III}}}{G}\theta + O(\theta^3). \tag{35}$$

The expression (9) of the plastic field is now required to match that of the crack-tip elastic dominant field, (34). In the same vein as in Section 3, we can do this by taking the expressions for σ_{nz}^{p} and σ_{sz}^{p} obtained by combining (9), (12), (13) and (27), and equating it, coefficient-wise, to the expressions for σ_{nz}^{e} and σ_{sz}^{e} obtained by combining (34), (12), (13) and (27) (see (28)). Solving the resulting equations yields

$$r_0 = \frac{1}{2\pi}\Big(\frac{K_{\text{III}}}{k}\Big)^2, \quad r_2 = 0, \quad L = \frac{1}{2\pi}\Big(\frac{K_{\text{III}}}{k}\Big)^2. \tag{36}$$

According to $(36)_1$ and Figure 2, the length of the plastic zone along the crack line is r_0, or half the length of the plastic zone

$$x_p = x_e + \rho_0 = 2\rho_0 = \frac{K_{\text{III}}^2}{\pi k^2}$$

obtained in the Hult–McClintock solution.

From the continuity condition $w^e = w^p$ for the displacement at the elastic-plastic boundary, the constant C in (9) can be obtained from (35), (36), and (12) as

$$C = \frac{k}{G}(r_0 + L). \tag{37}$$

The strain near the crack line can be deduced as

$$\gamma_{xz} = -\frac{k}{G}\frac{(r_0 + L)r}{(r + L)^2}\theta + O(\theta^3), \quad \gamma_{yz} = \frac{k}{G}\frac{r_0 + L}{r + L} + O(\theta^2). \tag{38}$$

Thus no singularity is present in the plastic zone, in contrast with the Hult–McClintock strain, (32).

5. Abandoning the first assumption

In Section 4, we kept the first assumption usually made for small-scale yielding. Although the results are more natural than the Hult–McClintock solution (Section 3), they are still confined by small-scale yielding.

The crack line analysis method allows us to abandon also the first assumption. In this section we go over an example of how this can be done in special cases. The general idea is this: the general solution

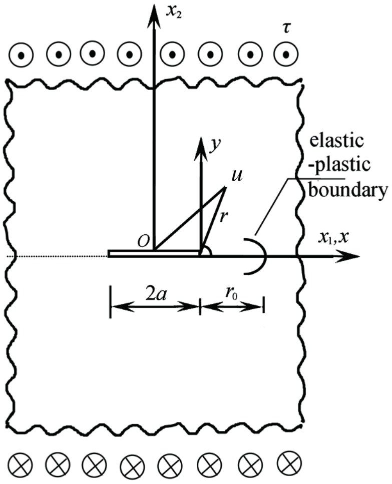

Figure 4. An antiplane crack in an infinite plate.

(9)–(10) for the plastic stress field near the crack line is correct to second order in the plastic zone, whether it be small or large. Hence, if a sufficiently accurate elastic field is known outside the plastic zone, the small-scale yielding assumptions can be relaxed by matching the elastic field with the general plastic field. The key, therefore, is to obtain the precise elastic field, and this can be done with sufficient accuracy near the crack line for some problems.

Our example involves an antiplane crack in an infinite body; see Figure 4. As discussed in [Yi 1994], the exact elastic stresses satisfying the far field boundary condition and the boundary condition that the crack surface is traction-free can be shown to be (see [Paris and Sih 1965; Gdoutos 2005, pp. 25–27])

$$\tau_{xz} = \operatorname{Im} Z_{\mathrm{III}}(u), \qquad \tau_{yz} = \operatorname{Re} Z_{\mathrm{III}}(u), \tag{39}$$

where $u = x + iy$ and $Z_{\mathrm{III}}(u) = \tau u/\sqrt{u^2 - a^2}$ is the Westergaard complex stress function. The corresponding displacement is $w = \operatorname{Im} \tilde{Z}_{\mathrm{III}}(u)/G$, where $\tilde{Z}_{\mathrm{III}}(u) = \int Z_{\mathrm{III}}(u)\,du$, the integral being over the contour $u = a + re^{i\theta}$. In the polar coordinate system centered at the crack tip, when $r \to 0$, the elastic K-dominant field can be obtained from (39) as in (33). But in the following analysis we will focus not on the elastic dominant term near the crack tip where $r \to 0$, but on the terms that are sufficiently precise near the crack line region when $\theta \to 0$.

Equation (39) is a classical analytical solution satisfying the basic equations and boundary conditions for the problem, which contains nonsingular terms besides the K-dominant field. Expanding (39) as a power series in θ, we get for the elastic stresses near the crack line

$$\tau_{xz} = -\frac{\tau}{\sqrt{r(2a+r)}}\,\frac{a^2}{2a+r}\theta + O(\theta^3), \qquad \tau_{yz} = \frac{\tau}{\sqrt{r(2a+r)}}\left((a+r) - \frac{2a^2r + a^3}{2(2a+r)^2}\theta^2\right) + O(\theta^4). \tag{40}$$

As $r \to 0$, this degenerates into (34); but note that (40) is sufficiently precise near the crack line, while (34) is valid only within a tiny area around the crack tip near the crack line.

Matching the elastic stress (40) and its corresponding displacement with the plastic stress and displacement, given in (9), one can obtain an accurate matching solution without the small-scale yielding assumptions. For details, see [Yi 1994].

Comparison between the general matching results and Hult and McClintock's results. In the example just given, elastic stresses precise enough near the crack line are obtained. By matching the general solution of the plastic stress (9) (and the corresponding plastic displacement) with the precise elastic stress (40) (and the corresponding elastic displacement) at the elastic-plastic boundary (12), the small-scale yielding assumptions can be completely abandoned and the matching results are correct, whether the plastic zone is small or large.

The matching results of the example for the infinite cracked plate are

$$r_0 = a\left(\sqrt{\frac{k^2}{k^2-\tau^2}} - 1\right), \quad \frac{r_2}{r_0} = \frac{1}{2}\sqrt{\frac{k^2-\tau^2}{k^2}} - \frac{k}{k+\sqrt{k^2-\tau^2}}, \quad L = a\left(1 + \frac{2\tau^2-k^2}{k^2-\tau^2}\sqrt{\frac{k^2}{k^2-\tau^2}}\right), \tag{41}$$

$$C = \frac{k}{G}(r_0+L), \qquad \gamma_{xz} = -\frac{k}{G}\frac{(r_0+L)r}{(r+L)^2}\theta + O(\theta^3), \qquad \gamma_{yz} = \frac{k}{G}\frac{r_0+L}{r+L} + O(\theta^2). \tag{42}$$

Expanding the first of these equations in a power series of τ/k, when $\tau/k \ll 1$, we have

$$r_0 = a\left(\sqrt{\frac{1}{1-\tau^2/k^2}} - 1\right) = \frac{a}{2}\left(\frac{\tau}{k}\right)^2 + O\left(\frac{\tau}{k}\right)^4 = \frac{1}{2\pi}\left(\frac{\tau^2 a\pi}{k^2}\right) = \frac{1}{2\pi}\left(\frac{K_{\mathrm{III}}}{k}\right)^2. \tag{43}$$

Similarly, when $\tau/k \ll 1$, we have to second order

$$\frac{r_2}{r_0} = 0, \quad L = \frac{1}{2\pi}\left(\frac{K_{\mathrm{III}}}{k}\right)^2. \tag{44}$$

Equations (43) and (44) say the same as (36), where $K_{\mathrm{III}} = \tau(\pi a)^{1/2}$.

It is obvious that when the first assumption of small-scale yielding is introduced, the matching results (41) reduce to (43) and (44).

Figure 5 compares the plastic zone lengths for three solutions: the present solution (41), obtained after abandoning the two small-scale yielding assumptions; the solution (43) or $(36)_1$, obtained by maintaining first assumption of small-scale yielding reserved; and Hult and McClintock's solution $(5)_4$, which relies on both the small-scale yielding assumptions.

We see that the result (41) is not confined by the yielding scale: when $\tau \to k$ the length of the plastic zone in (41) approaches ∞, which is reasonable for a plate with infinite width. By contrast, (43) and

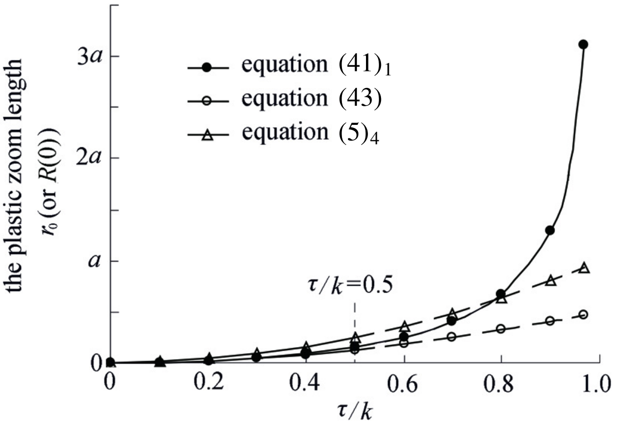

Figure 5. Comparison of the plastic zone lengths.

$(36)_1$ behave correctly only when τ/k is relatively small ($\tau/k \leq 0.5$), while Hult and McClintock's result $(5)_4$, also meant for τ/k small, lies some distance from either of the above.

However, when focusing on the plastic strain, neither our solution $(42)_{2,3}$ nor the small-scale yielding solution (38) have any singularities. In contrast, Hult and McClintock's solution (32) shows a physically unreasonable singularity $1/r$.

6. Conclusions

Three elastic-plastic matching solutions are given in the present paper.

The first matching solution is exhibited by the crack line analysis method to demonstrate the crack-tip elastic-plastic solution given by Hult and McClintock, where the particular plastic stresses (4) and the corresponding plastic strains suggested by Hult and McClintock are expanded in power series forms, (22) and (24), to match with the crack tip K-dominant elastic singular fields. The two small-scale yielding assumptions have to be used during deduction and the resultant plastic strains (32) have singularities. Although the matching solution is obtained around the crack line, it is in fact the same crack tip asymptotic solution as that of Hult and McClintock because the crack tip K-dominant elastic singular fields are introduced in matching.

The second matching solution (Section 4) takes the general power series form (but not the above particular form) plastic stresses (9) and corresponding plastic strains (10) near the crack line, to match with the crack tip K-dominant elastic singular fields. A more rational elastic-plastic solution is obtained with only the first small-scale yielding assumption adopted, in which the plastic strains do not have singularities. Since the crack tip K-dominant elastic singular fields are still applied in matching, the resultant solution can be considered as a new crack tip asymptotic solution, distinct from Hult and McClintock's. This new solution has no singularity in the plastic strain, unlike Hult and McClintock's.

The third matching solution (Section 5) shows how to obtain the precise elastic-plastic solution near the crack line with the usual small-scale yielding assumptions completely removed; the general power series form plastic fields are used to match the precise elastic fields near the crack line. The matching results in the case of an infinite plate will degenerate to those of the second matching solution, the validity of which is strictly justified by the matching conditions and the boundary conditions of the real problem. The resultant plastic strains also have no singularities.

The following observations can be made:

- Hult and McClintock's solution is inappropriate. Firstly, the plastic stress field (4) suggested by Hult and McClintock is just one particular solution of countless solutions to the system of partial differential equations, (1) and (2), instead of a general solution. Near the crack line, the plastic stress field of the Hult–McClintock particular solution is shown in (22) while that of the author's general solution is shown in (9). A comparison between (9) and (22) indicates that the general solution (9) has one constant L but the particular solution (22) does not. Secondly, owing to the adoption of particular plastic solution (4), the assumption that the crack-tip elastic field moves a distance x_e along the crack line has to be expediently introduced in Hult and McClintock's matching solution. Thus the elastic field used to match with the real plastic field is just an imaginarily offset elastic field, not the real one. Thirdly, the plastic strain, (24) or (32), corresponding to Hult and McClintock's matching solution obtained from the particular plastic stress (22) has a singularity, which is incorrect even under small scale yielding.

- The second assumption of the usual small-scale yielding is removable. The usual small-scale yielding involves two assumptions. If the plastic zone is small enough, the first assumption can be adopted, meaning, to match the K-dominant elastic field with the plastic field is acceptable. However, to adopt the second assumption, that is, to assume that the crack tip of the elastic field moves a distance along the crack line as Hult and McClintock have done, is inappropriate and should be rationally abandoned.

- The crack line analysis method offers a precise Taylor series form general solution (that is, a general power series form solution) of the plastic field (9), and provides the possibility of completely abandoning the two small-scale yielding assumptions. Then the elastic-plastic matching solution is decided by how the two small-scale yielding assumptions are treated. If both assumptions are still embraced, as Hult and McClintock have done, the same matching solution as Hult and McClintock's will be reached, as shown in Section 3; if only the first assumption is adopted a mathematically approximate matching solution will be gained which is more appropriate than Hult and McClintock's, as shown in Section 4; finally, if both assumptions are given up, a rigorously precise matching solution will be attained, as shown in Section 5, which goes far beyond Hult and McClintock's.

- There exists an obvious difference between the crack line analysis method and the crack tip asymptotic analysis method. The crack tip area is really a crucial position in the analysis of a crack problem, but the same is true of the crack line area: the stresses, strains, and plastic length near the crack line are all crucial parameters in analysis. When the dominant order terms are used to characterize the stress or strain field, the crack tip asymptotic analysis method only gives solutions appropriate for all points infinitely approaching the crack tip, but which are inappropriate for those points beyond a certain distance from the crack tip. In the polar coordinate system with the crack tip as its origin, the crack tip analysis method is usually restricted by the condition of $r \to 0$ but not by any range of θ $(-\pi \le \theta \le \pi)$, so the solution is restricted by the small-scale yielding conditions and remains valid only when the plastic zone is small enough. While the crack line analysis method only gives solutions appropriate for all points infinitely approaching the crack line, restricted by the condition of $\theta \to 0$ but not by any range of r $(0 \le r \le \infty)$, then the results are sufficiently precise within an area close enough to the crack line and not restricted by the small-scale yielding conditions. The crack line analysis method has the following merits: it can give the precise power-series-form plastic field solution near the crack line, the precise power-series-form plastic field can match with the precise elastic field near the crack line to give sufficiently precise results with the small scale yielding conditions completely abandoned, and it bears a physical clarity of related concepts and mathematical simplicity in deduction.

References

[Achenbach and Li 1984] J. D. Achenbach and Z. L. Li, “Plane stress crack-line fields for crack growth in an elastic perfectly-plastic material”, *Eng. Fract. Mech.* **20**:3 (1984), 535–544.

[Edmunds and Willis 1976] T. M. Edmunds and J. R. Willis, “Matched asymptotic expansions in nonlinear fracture mechanics, II: Longitudinal shear of an elastic work-hardening plastic specimen”, *J. Mech. Phys. Solids* **24**:4 (1976), 225–237.

[Gdoutos 2005] E. E. Gdoutos, *Fracture mechanics: an introduction*, 2nd ed., Springer, 2005.

[Guo and Li 1987] Q. Guo and K. Li, “Plastic deformation ahead of a plane stress tensile crack growth in an elastic-perfectly-plastic solid”, *Eng. Fract. Mech.* **28**:2 (1987), 139–146.

[Hult and McClintock 1957] J. A. Hult and F. A. McClintock, “Elastic-plastic stress and strain distribution around sharp notches under repeated shear”, pp. 51–58 in *Proceedings of the 9th International Congress on Applied Mechanics* (Brussels, 1956), vol. 8, University of Brussels, 1957.

[Hutchinson 1979] J. W. Hutchinson, *A course on nonlinear fracture mechanics*, Technical University of Denmark, Copenhagen, 1979.

[Koshinen 1963] M. F. Koshinen, “Elastic-plastic deformation of a single grooved flat plate under longitudinal shear”, *J. Basic Eng.* (*ASME*) **85**:4 (1963), 585–594.

[Paris and Sih 1965] P. C. Paris and G. C. Sih, “Stress analysis of cracks”, pp. 30–81 in *Fracture toughness testing and its applications* (Chicago, 1964), Special Technical Publication **381-EB**, Amer. Soc. for Testing and Materials, Philadelphia, 1965.

[Rice 1966] J. R. Rice, “Contained plastic deformation near cracks and notches under longitudinal shear”, *Int. J. Fract.* **2**:2 (1966), 426–447.

[Rice 1967] J. R. Rice, “Stresses due to a sharp notch in a work-hardening elastic-plastic material loaded by longitudinal shear”, *J. Appl. Mech.* (*ASME*) **34**:2 (1967), 287–298.

[Wang 1996] Q.-Z. Wang, “The crack-line (plane) stress field method for estimating SIFs: a review”, *Eng. Fract. Mech.* **55**:4 (1996), 593–603.

[Wang 2002] Q.-Z. Wang, “Simple formulae for the stress concentration factor for two- and three-dimensional holes in finite domains”, *J. Strain Anal. Eng. Des.* **37**:3 (2002), 259–264.

[Wang and Wu 2003] C. Wang and C.-P. Wu, “Elastic-plastic analytical solutions for an eccentric crack loaded by two pairs of antiplane point forces”, *Appl. Math. Mech.* **24**:7 (2003), 782–790.

[Wang and Zhang 1998] C. Wang and L.-K. Zhang, “Near crack line elastic-plastic analysis for a finite plate loaded by two pairs of antiplane point forces”, *Appl. Math. Mech.* **19**:6 (1998), 547–553.

[Wang and Zhou 2004] J.-H. Wang and X.-P. Zhou, “Near crack line elastic-plastic analysis for a infinite plate loaded by two pairs of point tensile forces”, *Mech. Res. Commun.* **31**:4 (2004), 415–420.

[Wu and Wang 1996] C.-P. Wu and C. Wang, “Near crack line elastic-plastic analysis for a crack loaded by antiplane point forces”, *Appl. Math. Mech.* **17**:12 (1996), 1121–1126.

[Yi 1991] Z.-J. Yi, “A new method of determining the stress intensity factors”, *J. Chongqing Jiaotong Inst.* **10**:3 (1991), 37–41. In Chinese.

[Yi 1992] Z.-J. Yi, “The new and analytical solutions for mode III cracks in an elastic-perfectly plastic materal”, *Eng. Fract. Mech.* **42**:5 (1992), 833–840.

[Yi 1993] Z.-J. Yi, “The precise and new analysis for a mode III growing crack in an elastic-perfectly plastic solid”, *Appl. Math. Mech.* **14**:4 (1993), 345–352.

[Yi 1994] Z.-J. Yi, “The most recent solutions of near crack line fields for mode III cracks”, *Eng. Fract. Mech.* **47**:1 (1994), 147–155.

[Yi and Yan 2001] Z.-J. Yi and B. Yan, “General form of matching equation of elastic-plastic field near crack line for mode I crack under plane stress condition”, *Appl. Math. Mech.* **22**:10 (2001), 1173–1182.

[Yi et al. 1996] Z.-J. Yi, S.-J. Wang, and H.-L. Wu, “Precise elastic-plastic analysis of crack line field for mode II plane strain crack”, *Int. J. Fract.* **80**:4 (1996), 353–363.

[Yi et al. 1997] Z.-J. Yi, S.-J. Wang, and X.-J. Wang, “Precise solutions of elastic-plastic crack line fields for cracked plate loaded by antiplane point forces”, *Eng. Fract. Mech.* **57**:1 (1997), 75–83.

[Zhou and Ling 2006] X.-P. Zhou and T.-H. Ling, “Elastic-plastic analytical solution for centric crack loaded by two pairs of point shear forces in finite plate”, *Trans. Nonferr. Met. Soc. China* **16**:5 (2006), 1009–1014.

[Zhou and Wang 2005] X.-P. Zhou and J.-H. Wang, “Study on the coalescence mechanism of splitting failure of crack-weakened rock subjected to compressive loads”, *Mech. Res. Commun.* **32**:2 (2005), 161–171.

Received 30 Jul 2009. Revised 25 Nov 2009. Accepted 25 Nov 2009.

ZHI-JIAN YI: `yizjyizj@hotmail.com`
School of Civil Engineering, Chongqing Jiaotong University, Chongqing 400074, China

SUBMISSION GUIDELINES

ORIGINALITY

Authors may submit manuscripts in PDF format online at the Submissions page. Submission of a manuscript acknowledges that the manuscript is original and has neither previously, nor simultaneously, in whole or in part, been submitted elsewhere. Information regarding the preparation of manuscripts is provided below. Correspondence by email is requested for convenience and speed. For further information, write to one of the Chief Editors:

Davide Bigoni	bigoni@ing.unitn.it
Iwona Jasiuk	ijasiuk@me.concordia.ca
Yasuhide Shindo	shindo@material.tohoku.ac.jp

LANGUAGE

Manuscripts must be in English. A brief abstract of about 150 words or less must be included. The abstract should be self-contained and not make any reference to the bibliography. Also required are keywords and subject classification for the article, and, for each author, postal address, affiliation (if appropriate), and email address if available. A home-page URL is optional.

FORMAT

Authors can use their preferred manuscript-preparation software, including for example Microsoft Word or any variant of TEX. The journal itself is produced in LATEX, so accepted articles prepared using other software will be converted to LATEX at production time. Authors wishing to prepare their document in LATEX can follow the example file at www.jomms.org (but the use of other class files is acceptable). At submission time only a PDF file is required. After acceptance, authors must submit all source material (see especially Figures below).

REFERENCES

Bibliographical references should be complete, including article titles and page ranges. All references in the bibliography should be cited in the text. The use of BibTEX is preferred but not required. Tags will be converted to the house format (see a current issue for examples); however, for submission you may use the format of your choice. Links will be provided to all literature with known web locations; authors can supply their own links in addition to those provided by the editorial process.

FIGURES

Figures must be of publication quality. After acceptance, you will need to submit the original source files in vector format for all diagrams and graphs in your manuscript: vector EPS or vector PDF files are the most useful. (EPS stands for Encapsulated PostScript.)

Most drawing and graphing packages—Mathematica, Adobe Illustrator, Corel Draw, MATLAB, etc.—allow the user to save files in one of these formats. Make sure that what you're saving is vector graphics and not a bitmap. If you need help, please write to graphics@mathscipub.org with as many details as you can about how your graphics were generated.

Please also include the original data for any plots. This is particularly important if you are unable to save Excel-generated plots in vector format. Saving them as bitmaps is not useful; please send the Excel (.xls) spreadsheets instead. Bundle your figure files into a single archive (using zip, tar, rar or other format of your choice) and upload on the link you been given at acceptance time.

Each figure should be captioned and numbered so that it can float. Small figures occupying no more than three lines of vertical space can be kept in the text ("the curve looks like this:"). It is acceptable to submit a manuscript with all figures at the end, if their placement is specified in the text by means of comments such as "Place Figure 1 here". The same considerations apply to tables.

WHITE SPACE

Forced line breaks or page breaks should not be inserted in the document. There is no point in your trying to optimize line and page breaks in the original manuscript. The manuscript will be reformatted to use the journal's preferred fonts and layout.

PROOFS

Page proofs will be made available to authors (or to the designated corresponding author) at a Web site in PDF format. Failure to acknowledge the receipt of proofs or to return corrections within the requested deadline may cause publication to be postponed.

Journal of Mechanics of Materials and Structures

Volume 5, No. 6 June 2010

1559-3959(2010)5:6;1-C